CHAPTER TWO

Zeolites and Zeotypes for Oil and Gas Conversion

Eelco T.C. Vogt*,†,1,2, **Gareth T. Whiting***,
Abhishek Dutta Chowdhury*, **Bert M. Weckhuysen***,2

*Inorganic Chemistry and Catalysis Group, Debye Institute for Nanomaterials Science, Faculty of Science, Utrecht University, Utrecht, The Netherlands
†Albemarle Catalysts Company BV, Amsterdam, The Netherlands
2Corresponding authors: e-mail address: e.t.c.vogt@uu.nl; b.m.weckhuysen@uu.nl

Contents

Abstract

Zeolite-based catalyst materials are widely used in chemical industry. In this chapter, the applications of zeolites and zeotypes in the catalytic conversion of oil and gas are reviewed. After a general introduction to zeolite science and technology, we discuss refinery applications, such as fluid catalytic cracking and hydrocracking, and also a wide variety of important petrochemical processes, such as alkylation and isomerization. The fields of low-temperature zeolite-assisted methane activation and methanol-to-hydrocarbon conversion are also covered, as well as several zeolite-catalyzed organic

---

1 Copyright with respect to the contributions of Dr. Eelco Vogt owned by Albemarle.

reactions with the aim to synthesize fine chemicals and pharmaceutical intermediates. By reviewing the processes, a wide range of catalytic functionalities are discussed, including Brønsted and Lewis acid sites, basic sites as well as metal and redox sites. The chapter continues with a discussion of the effects of zeolite–binder interactions in commercial catalysts, where the zeolite is only part of the system. We show how modern microspectroscopy methods provide detailed insight into the complex structure of these catalyst materials. Finally, we present future directions, which may include new zeolite-based processes for chemicals production or energy conversion, while new synthetic and characterization tools are envisioned to contribute to the accelerated discovery of new zeolite framework structures.

ABBREVIATIONS

AAP alumina–aluminum phosphate
AlPO aluminophosphate molecular sieve
AMK acid-modified kaolin
APS aluminum–phosphate sol
ASF Anderson–Schulz–Flory product distribution in Fischer–Tropsch synthesis
ATO alcohol to olefins
CHA IUPAC structure code for Chabazite, SAPO-34, SSZ-13
CI constraint index
CMK caustic-modified kaolin
DFT density functional theory
DME dimethyl ether
DMPO 5,5-dimethylpyrrolidine-N-oxide
DRS diffuse reflectance spectroscopy
EB ethylbenzene
E-Cat equilibrium catalyst (FCC)
ED electron diffraction
EFAL extra-framework alumina or aluminum
EPR electron paramagnetic resonance
EXAFS extended X–ray absorption fine structure
FAU IUPAC structure code for faujasite, zeolite X, zeolite Y
FCC fluid catalytic cracking, fluid cracking catalyst
FER IUPAC structure code for ferrierite
FT–IR Fourier transform infrared
FTS Fischer–Tropsch synthesis
GTL gas to liquids
HAGO heavy atmospheric gas oil
HC hydrocracking
HC-PT hydrocracker-pretreating
HGO heavy gas oil
HMB hexamethylbenzene
HRTEM high-resolution transmission electron microscopy
IZA International Zeolite Association
kt kiloton
LAB linear alkyl benzene
LCO light cycle oil

LID local interatomic distances
MAS NMR magic angle spinning nuclear magnetic resonance spectroscopy
MDA methane dehydroaromatization
MFI IUPAC structure code for ZSM-5, TS-1
MgAAP magnesia–alumina–aluminum phosphate
MOF metal-organic framework
MON motor octane number
MOR IUPAC structure code for mordenite
MPVO reactions Meerwein–Ponndorf–Verley reduction of aldehydes/ketones and Oppenauer oxidation of alcohols
MR membered ring (in zeolite structures)
mt metric ton
MTBE methyl tertiary butyl ether
MTG methanol to gasoline
MTH methanol to hydrocarbons
MTO methanol to olefins
MWW IUPAC structure code for MCM-22
NMR nuclear magnetic resonance spectroscopy
PDH propane dehydrogenation
PE polyethylene
pMMO particulate methane mono-oxygenase
PP polypropylene
RE-Y rare earth-exchanged Y zeolite
RON research octane number
SAPO silicoaluminophosphate molecular sieve
SCR selective catalytic reduction (of NO_x with NH_3)
SDA structure-directing agent
SEM scanning electron microscopy
SI spaciousness index
SPA supported phosphoric acid
TAME tertiary amyl-methyl ether
TDP toluene disproportionation
TEM transmission electron microscopy
TEOM tapered element oscillating microbalance
TEOS tetraethyl orthosilicate
TOF turnover frequency
TPH temperature-programmed hydrogenation
TPO temperature-programmed oxidation
TPSR temperature-programmed surface reaction
TS-1 titanium-silicate-1 (Ti-silicalite)
USY ultra-stabilized Y zeolite
VGO vacuum gas oil
XAFS X-ray absorption fine structure
XANES X-ray absorption near edge structure
XAS X-ray absorption spectroscopy
XPS X-ray photoelectron spectroscopy
XRD X-ray diffraction
**XRF** X-ray fluorescence
ZIF zeolitic imidazolate framework

1. INTRODUCTION

Zeolites are microporous solids containing pores, channels, and cages with molecular dimensions. Their microporosity makes them highly suitable for catalysis, because the spaces in the lattice can be used to control access to active sites, and steric restrictions can be placed on reaction intermediates and transition states. As a result, zeolites and zeolite-like materials have found widespread use in a large number of commercial applications, including conversion of petrochemical feedstocks in refineries, further conversion of the obtained molecules in chemical processes, conversion of biomass–derived feedstocks (mainly synthesis gas and methanol, but also pyrolysis oils), methane conversion and C_1-chemistry, and more recently environmental catalysis.

This review will discuss the use of zeolites and zeolite-like materials in processes that have, to a large extent, found commercial application in oil and gas conversion, as outlined in Scheme 1. We will first discuss the processes of fluid catalytic cracking (FCC) and hydrocracking (HC), which are toward the front-end of the refinery and thus large in scale, followed by review of the subsequent upgrading processes in an oil refinery (Sections 3.1 and 3.2). We will complete the review of commercial applications by discussing smaller scale processes for the synthesis of (fine) chemicals (Section 3.3). We will then switch to emerging applications of zeolite catalysts (Section 4), which are the conversion of methane, including low-temperature methane activation, and the conversion of methanol and ethanol to olefins and gasoline. We will conclude with a critical review of the effects observed when incorporating zeolites in compound catalyst materials; understanding the role of binders is a field of growing importance, and new characterization tools allow us to investigate both nanoscale and mesoscale phenomena in zeolite-containing catalysts. Finally, the chapter will outline some future perspectives for the application of zeolites in catalysis.
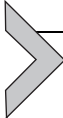
2. ZEOLITES: DEFINITION, APPLICATIONS, STRUCTURES, AND SYNTHESIS

Zeolites are crystalline microporous aluminosilicates, which are composed of corner-sharing SiO_4- and AlO_4-tetrahedra *(1)*. They are formed in nature in association with volcanic activity and can be synthesized in the laboratory. The Swedish chemist Axel Cronstedt first described zeolites in 1756. He noted that the mineral stilbite appeared to boil when heated.
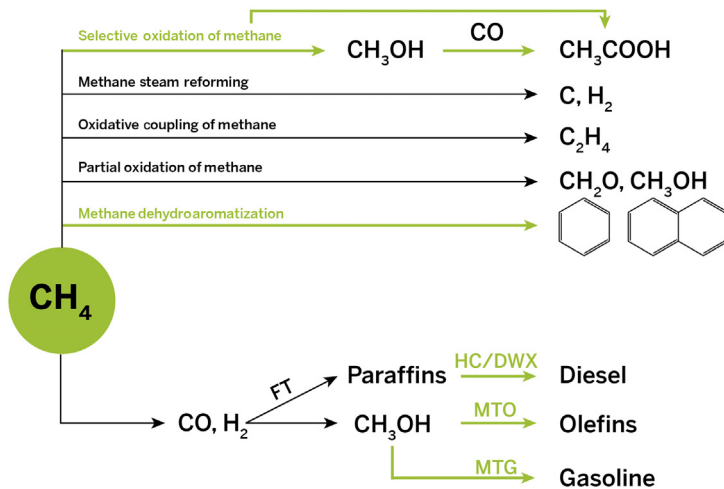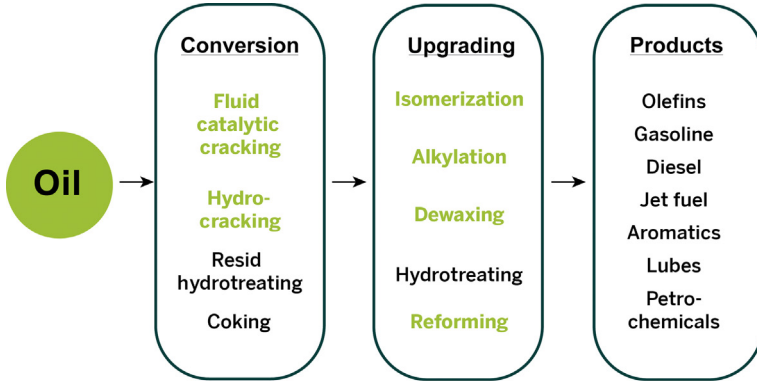
Scheme 1 Overview of this review article.

He therefore named them zeolites or "boiling stones" (from Ι ζέω—boil and λίθος—stone) *(2)*. A number of textbooks focus on zeolites and their applications. We refer the interested reader to the books by Cejka *et al.* *(3)*, Ertl *et al.* *(4)*, and van Bekkum *et al.* *(5)*.

2.1 Definition and Description

The exact definition of what zeolites are has been a matter of debate for years *(6)*. Especially the discovery of a class of aluminophosphate structures that are partly isostructural with known zeolites (i.e., the family of AlPOs and

SAPOs) *(7)*, as well as the discovery of metal–organic frameworks (MOFs) *(8)* and the related zeolitic imidazolate frameworks (ZIFs) *(9,10)* have sparked discussion. In the strictest sense, zeolites are aluminosilicates with regular micropores (i.e., pores with a diameter smaller than 2 nm). The micropores contain counterions to compensate for the negative charge introduced by each aluminum atom in the (silicate) framework. The pores typically also contain varying amounts of water, which can be removed by various procedures, among them heating, which will produce the peculiar "boiling" phenomenon observed by Cronstedt.

The size of pores in zeolites is characterized by the number of tetrahedral atoms (T–atoms) in the ring circumscribing the pores. Structures like sodalite and ZSM-39 have very small pores not exceeding rings of six T–atoms (six-membered rings, or 6-MRs), which renders them essentially useless for catalysis. These materials behave like clathrates and have been called *clathrasils (11,12)*. True zeolites would then be *porotectosilicates* with regular pores of at least 8-MRs. A large number of framework structures that are isostructural to zeolites, but with the silicon and/or aluminum in the tetra-hedral sites replaced by other atoms, are known today. The microporous *aluminophosphates* developed in the early 1980s at Union Carbide *(7)* are probably the largest group of these materials, and have been called *zeotypes (13)*. Replacement of the aluminum and phosphorus atoms in these AlPOs can create a wealth of new chemistry: introduction of silicon atoms creates Brønsted acidity, and transition metal atoms in the framework sites can introduce redox activity. Silicon and/or aluminum atoms in aluminosilicates can also be replaced by gallium and/or germanium atoms, typically in approaches to synthesize structures that would be difficult to produce in pure silica or aluminosilicate forms, since these compositions favor the formation of specific building units *(14)*. We should also mention the term *molecular sieves*. The pores in zeolites and zeotypes have the same dimensions as small- or medium-sized molecules, and these materials can thus separate molecules on the basis of their size, conformation, and/or shape.

2.2 Applications and Related Markets

Zeolites are used in large quantities in a variety of commercial processes. The largest application for synthetic zeolites is detergency, where zeolites function as ion–exchange reagents to remove calcium and magnesium ions from "hard" water. The second largest application is catalysis, with FCC and HC as the leading processes. Another large area is the use as adsorbents. There are also various uses for natural zeolites, for example, as nutrient release agent in

horticulture, odor control agent in pet litter, soil conditioner, or to remove radioactive isotopes from wastewater streams. We refer the interested reader to reviews like Refs. (15,16). The total consumption of synthetic zeolites was estimated to be 1.817 million ton per year by Janshekar et al. in 2013 (see Table 1 and Figure 1) (17). The authors note that an additional 3 million tons of natural zeolites are produced each year, 2/3 of which is mined in China and mostly used as a cement additive. The most important synthetic zeolites considering the produced volume are Linde Type A (LTA) (18) and

Table 1 Zeolite Production (Anhydrous Base)

| Use/Source	Production (kt/year)		
	2001	2004	2013
Synthetic zeolites			
Detergent builder	1188	1325	1326
Catalysts	184	241	271
Adsorbents/desiccants	92	126	220
Total synthetic zeolite production	1464	1692	1817
Natural zeolite production	3308	2555	2902

Based on data from Refs. (17,20).
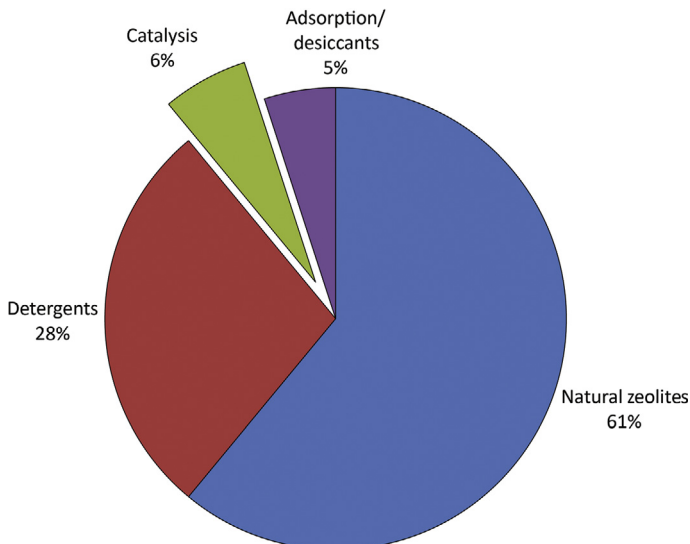
Figure 1 Application of zeolites by weight. *Based on data from Refs.* (17,20).

gismondine (Zeolite P, MAP) *(19)*, used as water softeners in detergents. In monetary value, they are surpassed by zeolite Y with the faujasite (FAU) topology, used in oil refinery catalysis. The largest producers of zeolites applied in catalysis are the three main producers of FCC catalysts: Albemarle, BASF, and W.R. Grace (other suppliers include CCIC, Petrochina, and Sinopec). These companies also produce specialty zeolites for other (catalytic) applications. Other major zeolite producers, mainly in the field of specialty zeolites, are ExxonMobil, PQ/Zeolyst/Ineos Silica, Südchemie/Tricat/Clariant, Tosoh, Uetikon/Zeochem, and UOP *(20)*.

Although there are 229 recognized zeolite and zeotype structures, only a limited number of these materials have been applied in commercial processes. Maesen *(16)* lists 17 structures that are of commercial interest based on Refs. *(15,21)* (see Table 2). Of these 17, only five are produced in significant amounts for catalytic applications; the structures of these so-called Big Five *(22)* are represented in Figure 2.

Zeolites are applied in a variety of fields. In this review, we will focus on the use of zeolite materials as catalysts for the conversion of oil (fractions) and natural gas (see Scheme 1). The largest of these applications are found in the refinery, notably FCC and HC. However, there are other applications in the refinery, such as dewaxing, reforming, isomerization, and alkylation that can be performed with zeolite-based catalysts. In the petrochemical complex, the production of cumene and ethylbenzene, and the isomerization of xylenes are good examples of zeolite-based catalytic processes. These petroleum refinery processes are depicted in the top half of Scheme 1. In addition, we will discuss the direct conversion of methane to methanol or methane to aromatics and the conversion of methanol to gasoline (MTG) next to methanol to olefins (MTO) in more detail, as shown in the bottom half of Scheme 1.

We would like to mention two more fields of application of zeolite catalysts, which will not be discussed in detail; these are car exhaust gas treatment and biomass processing.

Numerous zeolite framework types based on medium and large pores have been proposed as catalysts for removal of NO_x from car exhaust gases: ferrierite (FER, 10-MR); ZSM-5 (MFI, 10-MR); Y (FAU, 12-MR); mordenite (MOR, 12-MR); and beta (BEA–12-MR). Early success was established with both ZSM-5 and BEA zeolite types. Nowadays, small-pore chabazite zeolites and zeotypes (CHA, 8-MR) have made a breakthrough in obtaining high NO_x reduction efficiency with excellent activity at low temperature and high durability to harsh hydrothermal conditions. Since the

Table 2 Zeolites Recognized by the International Zeolite Association as of July 1, 2015 [23]

ABW	ACO	AEI	**AEL**	AEN	AET	AFG	AFI	AFN	AFO	AFR	AFS
AFT	AFV	AFX	**AFY**	AHT	ANA	APC	APD	AST	ASV	ATN	ATO
ATS	ATT	ATV	AVL	AWO	AWW	BCT	***BEA**	BEC	BIK	BOF	BOG
BOZ	BPH	BRE	BSV	CAN	CAS	CDO	CFI	CGF	CGS	**CHA**	-CHI
-CLO	CON	CSV	CZP	DAC	DDR	DFO	DFT	DOH	DON	EAB	**EDI**
EEI	EMT	EON	EPI	**ERI**	ESV	ETR	EUO	*-EWT	EZT	FAR	**FAU**
FER	FRA	**GIS**	GIU	GME	GON	GOO	HEU	IFO	IFR	IFW	IFY
IHW	IMF	IRN	IRR	-IRY	ISV	ITE	ITG	ITH	*-ITN	ITR	ITT
-ITV	ITW	IWR	IWS	IWV	IWW	JBW	JNT	JOZ	JRY	JSN	JSR
JST	JSW	KFI	LAU	LEV	LIO	-LIT	LOS	LOV	**LTA**	LTF	LTJ
LTL	LTN	MAR	MAZ	MEI	MEL	MEP	**MER**	**MFI**	MFS	MON	**MOR**
MOZ	*MRE	MSE	MSO	MTF	MTN	MTT	MTW	MVY	**MWW**	NAB	NAT
NES	NON	NPO	NPT	NSI	OBW	OFF	OKO	OSI	OSO	OWE	-PAR
PAU	PCR	PHI	PON	POS	PSI	PUN	**RHO**	-RON	RRO	RSN	RTE
RTH	RUT	RWR	RWY	SAF	SAO	SAS	SAT	SAV	SBE	SBN	SBS
SBT	SEW	SFE	SFF	SFG	SFH	SFN	SFO	SFS	*SFV	SFW	SGT
SIV	SOD	SOF	SOS	SSF	*-SSO	SSY	STF	STI	*STO	STT	STW
-SVR	SVV	SZR	TER	THO	TOL	**TON**	TSC	TUN	UEI	UFI	UOS
UOV	UOZ	USI	UTL	UWY	VET	VFI	VNI	VSV	WEI	-WEN	YUG
ZON											

Zeolites that are commercially used according to Refs. [16,20] are highlighted. Zeolites highlighted by green (gray in the print version) boxes mainly have catalytic applications, whereas zeolites highlighted by yellow (light gray in the print version) boxes mainly have applications in detergency or adsorption/separation. Bold borders represent the so-called Big Five zeolites.

early reports by Bull of BASF [24] and Andersen of Johnson Matthey [25] on the remarkable activity of copper-doped chabazites for the selective catalytic reduction (SCR) of NO_x by NH_3, these catalysts have generated a substantial amount of interest in both academia and industry [26]. Both Cu-SSZ-13 and Cu-SAPO-34 show excellent catalytic activity in large temperature windows (particularly at low temperatures) and possess superior hydrothermal stability in the NH_3-SCR reaction compared to Cu-ZSM-5 and beta zeolite catalysts [27]. Moreover, the Cu-CHA catalysts are less susceptible

Zeolites: The Big Five

FER
(ferrierite)
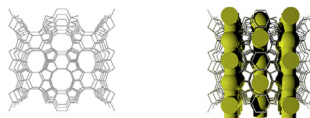
MFI
(ZSM-5)
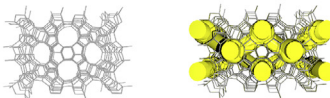
MOR
(mordenite)
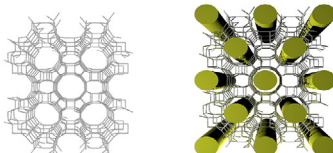
BEA
(beta polymorph A)
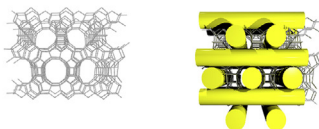
FAU
(faujasite,
zeolite Y)
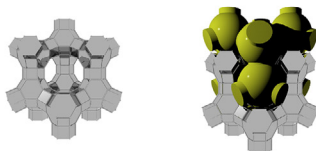
Figure 2 The "Big Five" zeolites—materials that are produced in significant amount for application in the field of catalysis.

to reaction inhibition by hydrocarbons and associated deactivation and even operate better than previously known catalysts at lower temperatures with a limited amount of NO_2 present in the feed *(28)*. However, sulfur poisoning is still an issue with these small–pore zeolites. In general, at low copper load-ings, it is proposed that Cu^{2+} ions are present at extra-framework positions near the faces of 6-MRs. In contrast, at higher loadings, it is likely that the copper ions will move to occupy 8-MRs *(29)*. The latter occurs due to Cu^{2+} interactions with H_2O and NH_3 that weaken its bond with the zeolite framework. The copper ions located at the 8-MRs are in fact proposed to undergo redox cycles (Cu^{2+}/Cu^+) more easily than those at 6-MR sites,

making them more active in NH_3 oxidation and SCR. For the subject of exhaust gas treatment, we refer the reader to the reviews by Johnson (30), Chen (31), and Brandenberger et al. (32).

Zeolites have also found numerous applications in the conversion of biomass, for instance in the conversion of biomass–derived feedstocks admixed to petroleum-derived feedstocks in FCC–like processes. Applications in this field that have proceeded beyond laboratory scale are described by Petrobras in the work of de Rezende Pinho et al., who report FCC of pyrolysis oil from woodchips mixed with vacuum gas oil (VGO) in a 150 kg/h demonstration unit (33), and by the KiOR company, who developed a catalytic pyrolysis technology using FCC–like catalysts, which are intimately mixed with finely ground biomass (34–36). We will not discuss this subject further in this review article, but rather refer to the reviews by Corma and coworkers (22,37–40), Stöcker (41), Al-Sabawi et al. (42), and Kubicka and Kikhtyanin (43).

Figure 3 gives an overview of the applications of zeolites in oil refining processes; and Figure 4 presents an overview of the major chemical processes
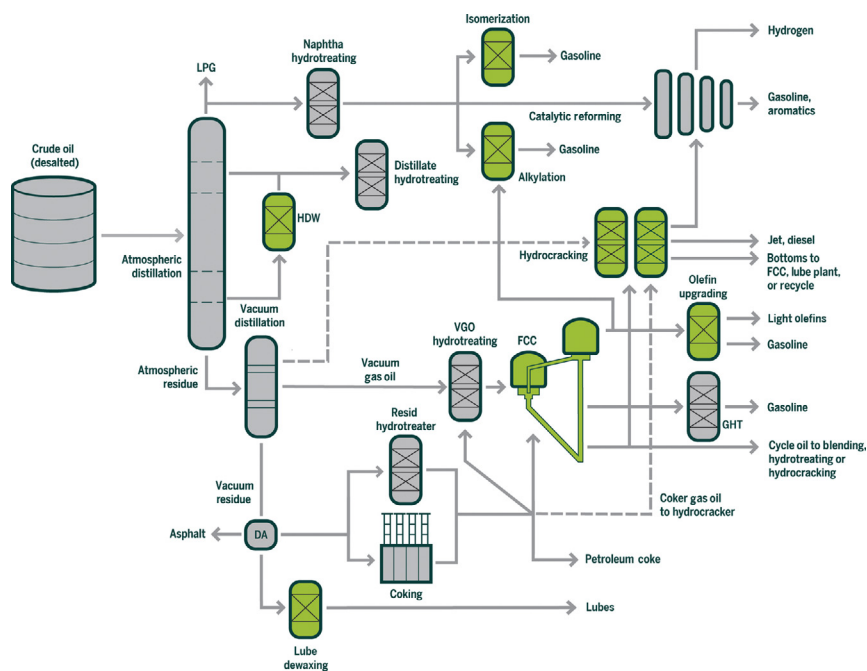
Figure 3 Applications of zeolite materials in oil refining processes. Green color (dark gray in the print version) indicates zeolite-based processes. *Partly based on Ref. (44)*.

Acid
> Brønsted
FCC (FAU, MFI)
Olefin oligomerization (MFI)
MTO, MTG (MFI, CHA)
Aromatic alkylation, acylation (FAU, MOR, BEA, MWW)
Alkylaromatic isomerization (MFI, MOR)

> Lewis
Baeyer–Villiger reaction (BEA)
Meerwein–Ponndorf–Verley reaction (BEA)
Glucose isomerization (BEA)

Base
Knoevenagel condensation (FAU)
Aldol condensation (FAU)
Transesterification (FAU)

Redox
Ammoxidation, epoxidation (Ti-MFI)
Aromatic hydroxylation (Ti-MFI , Fe-MFI)

Bifunctional
HC (FAU)
Isoparaffin/olefin alkylation (FAU)
Hydrodearomatization (FAU)
Dewaxing, isodewaxing (MFI, BEA, AEL)
Xylene isomerization (MFI)
Olefin isomerization (FER)
Naphtha isomerization (MOR)

Figure 4 Overview of the different applications of zeolites in chemical processes.

for which zeolites have been applied and provides information on the framework type used and the type of catalysis performed.

2.3 Zeolite Structures and Related Pore Systems

The *Atlas of Zeolite Structure Types* published by the International Zeolite Association (IZA) currently lists 229 distinct framework structures *(23)*. Not all of them are zeolites in the strictest sense of the definition; there are framework structures of (silico)aluminophosphates and gallogermanates (e.g., CJ63, JST *(23)*), and a variety of other materials that are conceptually isostructural to silicates. The database of the IZA shows a large variety of structures and pores; the smallest pores are delineated by rings of six tetrahedral atoms (6-MR), and the largest (ITQ-37 *(45)*) by 30 T-atoms (30-MR). An indication of the size of molecules that can be accommodated by the openings in the structure is presented in the database of the IZA: for each structure, the largest sphere that can pass through the pores in the structure is calculated, as well as the largest sphere that fits into the cages inside the structure. Figure 5 gives an overview of the pore and cage sizes of all zeolites and zeotypes listed in the IZA database *(23)*. The largest pore as defined by a sphere that can pass through is found in ITQ-44 (with a diameter of 12.12 Å) *(46)*, the largest internal cage as defined by a sphere that can
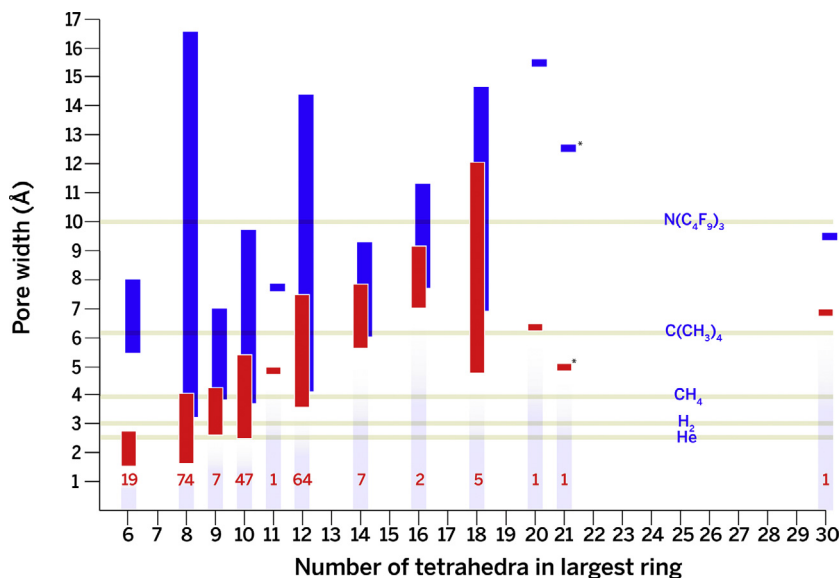
Figure 5 Overview of the pore sizes and cage sizes of all known zeolites. Red bars (dark gray in the print version): largest sphere that can pass through the structures. Blue bars (black in the print version): largest sphere that fits in the structure (cages). Numbers at the bottom of the bars represent number of structures with listed number of T-atoms in the largest ring. The horizontal orange bars (light gray in the print version) represent the size of typical molecules that could pass through the pores for comparison. *Data from Ref.* (23).

be included (16.45 Å) is found in tschörtnerite, a mineral found in the Eiffel region of Germany *(47)*.

Zeolite structures are usually determined by X-ray diffraction (XRD). Since in some cases only small crystallites and only small quantities are available, various tools have been developed to solve zeolite structures based on powder diffraction rather than single crystal refinement. Rietveld refinement of synchrotron powder XRD is the first tool of choice. The diffractograms are usually better defined, e.g., with sharper peaks and characterized by a high signal–to–noise ratio, but even with synchrotron powder diffraction, special techniques are sometimes needed to solve the structures of more complex frameworks with low symmetry (Charge Flipping *(48,49)*, FOCUS *(50)*), or structures with intergrowths (DIFFAX *(51)*). In some cases, imaging the structure with high-resolution transmission electron microscopy (HRTEM), sometimes combined with electron diffraction (ED) *(52,53)*, can give a good starting point for structure refinement. These techniques have been reviewed in Refs. *(54,55)*.

While XRD structure refinement unambiguously defines the framework structure, catalytic tests can also provide information on pore dimensions and connectivity of the structures and, in addition, characterize the acidity.

Cracking of *n*-hexane at a temperature of 534 °C is called the Alpha test *(56)*. The test, developed by Haag *et al.*, is a simple gas–phase reaction that can determine the intrinsic activity of a zeolite material, and with minor modifications, also its deactivation behavior. The Alpha value is determined from the activity after 5 min on stream. Miale *et al.* *(57)* noted that with zeolites that express high molecular shape selectivity, so-called superactivity can be achieved. Thus, even this simple test can already give insight in the crystal structure. The other implication, not readily recognized, is that an exact fit of the molecule to the zeolite pore leads to unexpectedly high activity. Derouane *et al.* *(58,59)* elegantly described the effect of this "confinement" of molecules in the pore system on the observed activity.

The constraint index (CI), also developed by Haag *et al.* in the Mobil laboratories *(60)*, is based on the relative rates observed during simultaneous cracking of straight chain *n*-hexane (HEX) and its bulky isomer 3-methylpentane (3MP). The CI is defined as

$$CI = \log\left(1 - HEX\,conversion\right)/\log\left(1 - 3MP\,conversion\right)$$

A high CI indicates the presence of steric hindrance or reactant shape selectivity, since the straight chain molecules crack faster than the bulky isomer. A modified version of the CI, the modified constraint index, which is based on the hydroisomerization of *n*-decane, and the spaciousness index (SI), which is based on the product distribution in the HC of butylcyclohexane, were later employed to refine these tests *(61)*. Frequently, proposals on the pore size and connectivity were published before the structures of molecular sieves were solved, and ranges in the reactivity patterns observed in tests like the above have been used to identify zeolite structures in process patent claims (see, e.g., Refs. *(62,63)*).

Constraint indices for small-pore (8-MR) zeolites are very high, typically above 12; for medium-pore (10-MR) zeolites, they are typically between 1 and 12; and for large-pore (12-MR or larger) zeolites, they are below 1 (see Table 3). Figure 6 shows the variation of the CI with the diameter of the largest passable sphere as taken from Table 3. Various structures are color coded according to their largest pores (as determined by the number of T-atoms in the ring).

Table 3 Constraint Indices for a Number of Zeolite Structures

Zeolite	IZA Framework Code	Largest Pore (Ring Size)	Constraint Index	Largest Passable Sphere (Å)
SSZ–13	CHA	8	100	3.72
Erionite	ERI	8	38	3.42
ZSM–23	MTT	10	10.6	5.07
SSZ–20	TON	10	6.9	5.11
ZSM–5	MFI	10	6.9	4.7
EU–1	EUO	10	3.7	4.99
SSZ–23	STT	9	3.2	2.76
ZSM–12	MTW	12	2.1	5.68
IM–5	IMF	10	1.8	5.44
SSZ–36	ITE/RTH	8	1.1	4.17
SSZ–57	SFV	12	1.1	5.3
SSZ–31	*STO	12	0.9	6.09
SSZ–25	MWW	10	0.8	4.92
SSZ–35	STF	10	0.6	5.44
CIT–5	CFI	14	0.4	7.26
LZY–82	FAU	12	0.4	7.35
SSZ–24	AFI	12	0.3	7.42
UTD–1	DON	14	0.3	8.07

*The asterisk in the code indicates that the structure is disordered.
Data from Refs. (64,65).

From Table 3 and Figure 6, it is obvious that relatively simple catalytic cracking and isomerization tests can already provide a wealth of information on zeolite structures. However, there are significant deviations from the general rules of thumb, as Figure 6 clearly shows. Zones et al. note that SSZ-23 and SSZ-35 show deviating behavior in the CI test, because their structures contain 9-MR or 10-MR arrangements that open into large cages (65). The same explanation should then hold for SSZ-25 with the MWW structure. It is likely that SSZ-36 deviates from ideal behavior in the CI test because it is a highly faulted structure containing ITE and
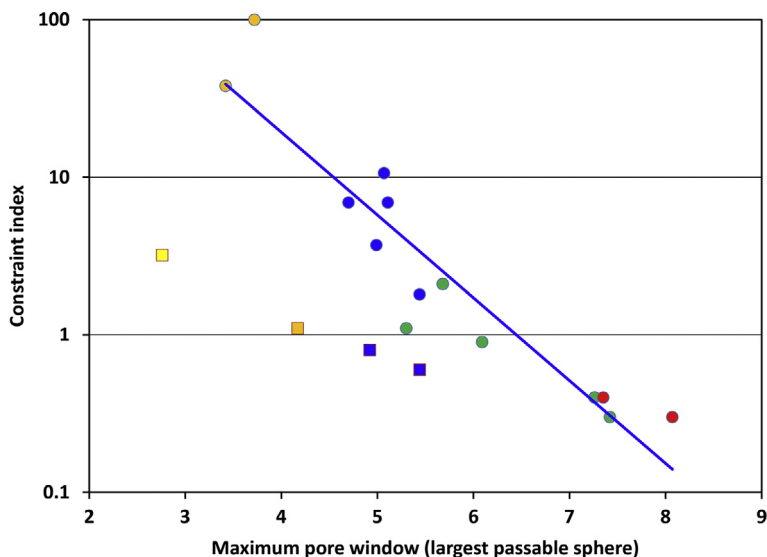
Figure 6 Constraint index as a function of pore opening (defined as the largest sphere that can pass through the structure). Green: 8-MR zeolites, yellow: 9-MR zeolites, blue: 10-MR zeolites, orange: 12-MR zeolites, red: 14-MR zeolites. Squares excluded from the regression line for reasons explained in the text. *Data from Refs.* (23,64,65).

RTH domains (66). The regression line in Figure 6 was therefore drawn excluding these four structures.

Zones *et al.* (65) demonstrated that a combination of intimate knowledge of the synthesis conditions, comparative sorption experiments (2,2,-dimethylbutane in this case), and selectivity considerations in catalytic test reactions (i.e., methanol conversion and hexane cracking) can be used to estimate the pore dimensions of unknown structures, in their case SSZ-57 and IM-5. The authors used a large set of zeolite materials for comparison and concluded correctly that both zeolites have 10-MR pores, which was confirmed by XRD measurements and structure refinement (48,67).

2.4 Synthesis Strategies for New Zeolite Materials

Even though only a small number of the 229 structure types currently recognized by the IZA structure committee are represented in catalysts actively used in industry, there is a never-ending quest to synthesize new zeolite structures in the hope of finding new activity and selectivity patterns. Over the last few years, we have seen reports of new structures with odd ring

numbers [7-MR (STT *(68)*, 9-MR (ITR *(69)*, STT, ITH *(70)*), 11-MR (JSR *(71)*, EMM-25 *(72)*), and 15-MR (−IRY *(73)*)]; structures with extra large pores [16-MR (−IRY, IFO *(74)*), 18-MR (IFO, ITQ-33 *(75)*), 20-MR (ITQ-54 *(76)*), 28-MR (ITQ-43 *(77)*), and even 30-MR (−ITV *(45)*)]; chiral structures [−ITV, STW *(78)*, JRY *(79)*, LTJ *(80)*]; and structures with interconnected mixed pore systems that are built from 10- and 12-MR systems [ITQ-39 *(81,82)*]. We refer the reader to recent review articles by Li *et al.* *(14)* and Li and Yu *(55)*.

The review by Li *et al.* describes three generally accepted strategies to create or design new zeolite structures: the use of predesigned structure-directing agents (SDAs), heteroatom substitution, and topotactic transformation *(14)*. The first technique relies on varying substituents in, for instance, a class of bulky quaternary ammonium ions or diquaternary ions. By systematic subtle changes in the SDA structures, or the distance between the two nitrogen atoms in the diquaternary ions, a variety of new structures have been created, especially by the group of Zones and coworkers (various SSZ structures, see, e.g., Ref. *(83)*), by Corma and coworkers (various ITQ structures), and at ExxonMobil (e.g., EMM-3 *(84)*).

Corma and coworkers have designed new families of SDAs based on phosphonium and phosphazene ions and synthesized the new structures ITQ-26 (IWS *(85)*), ITQ-27 (IWV *(86)*), ITQ-34 (ITR *(69)*), and ITQ-49 (IRN *(87)*), as well as the first synthetic analog of the 10–12-MR mineral boggsite (ITQ-47, BOG) *(88)*. Particularly the phophazene ions seem to offer a lot of opportunity for further discoveries. Combining nitrogen and phosphorus atoms in aminophosphines also seems viable; it has led to the new zeolite structures STF *(89)* and IFW *(90,91)*. Corma *et al.* also have described a new class of SDAs, namely bulky aromatic "proton sponges." These molecules are highly basic and are protonated at synthesis conditions, which allows for a better contact between the SDA and the silica oligomers during nucleation. ITQ-51 (IFO *(74)*), a large-pore (16-MR) aluminophosphate, was synthesized with the help of this class of SDA. Yet another class of SDAs are the imidazolium derivatives, which have been used as SDAs since the late 1980s, and have led to the synthesis of, for example, the TON, MTT, MTW, and ITW structures *(92,93)*, and more recently the UOS *(94)*, UWY structures *(95)*, and the pure silica form of the chiral STW *(96)*. Finally, metal complexes can also be used as (bulky) SDAs leading to extra large pores, as demonstrated by the synthesis of the DON, JST, and JSR structures *(97–99)*. Such SDAs were also used to prepare the Cu forms of CHA and SAPO-18, which are possibly important

candidates for the SCR of NO$_x$. In these materials, the copper was introduced via copper–amino complexes that served as (co-)SDA, thus avoiding a postsynthesis metal ion exchange step *(100–104)*.

It should be noted that many of the structures described in the previous paragraph are to a large extent not pure silicates or aluminosilicates, rather they contain germanium or boron as additional framework T-atoms. The introduction of germanium or boron into the framework allows the formation of smaller 3- and 4-MR rings in the structure, because the T—O—T bond angles can vary a little, which allows the formation of high-stress structures such as smaller rings.

In microporous aluminophosphates (AlPOs), both aluminum and phosphorus atoms can relatively easily be replaced by heteroatoms with various charges, including transition metal ions. Although many MeAPO (with Me being the heteroatom) structures have been found in which the heteroatoms replace atoms in known structures, there is also a number of new MeAPO structures that do not exist as AlPOs, in which case the heteroatoms likely stabilize the structures *(14)*. Cobalt and zinc seem to be particularly suited for this approach *(105,106)*.

Interestingly, not just the T-atoms but also the oxygen atoms in the framework can be replaced, to yield nitrido- and oxynitrido structures, such as nitrido- and oxynitrido-sodalite *(107–109)*.

The last approach, the topotactic transformation, has most likely received the most attention in conjunction with the synthesis of to MCM-22 (MWW) through transformation of a layered precursor, referred to as MCM-22P *(110)*. A number of new zeolites have been synthesized since by using the topotactic transformation of layered precursors; these are materials that are not accessible through direct hydrothermal synthesis so far. Another topotactic transformation is the conversion of the 18-MR AlPO VPI-5 (VFI) to the 14-MR AlPO$_4$-8 (AET), which unfortunately introduces so many stacking faults in the resulting structure that the one-dimensional 14-MR pores are largely inaccessible and practically useless *(111,112)*.

As is evident from the number of new structures published in recent years, the synthesis of zeolite structures is a very active field, with contributions from many academic and industrial research groups. There are a wide variety of possible approaches, and a rapid increase in computational capabilities as well, to assist the experimental synthesis approaches.

Treacy *et al. (113)* and Li *et al. (114)* have described methods to build theoretical framework model structures and provide rules on their viability. The number of unique hypothetical framework structures in the databases

(115,116) amounts to well over 2 million. A first estimate for viability is the calculated framework energy after energy minimization of the all-silica version of the structure. Low framework energy indicates a possible stable structure that could possibly be synthesized. However, this criterion has proven to be unreliable in the case of substituted frameworks. Li *et al*. *(114)* therefore propose to consider local interatomic distances (LID) rather than the global framework structure. They conclude that the average tetrahedral angles in the structure should not deviate too much from ideal tetrahedral angles; that is, there should not be too much local stress. The authors provide four criteria related to the ratios of the O—O to the T—O distance, the ratio of the T—O—T to the T—O distance, as well as the standard deviation and the ranges of the T—O, T—O—T, and O—O distances, that determine whether a hypothetical structure may be synthesized. All known zeolites appear to fit the criteria, whereas energy criteria incorrectly predict that a number of known materials could not be synthesized *(114)*.

The hypothetical structure databases can be a great help in solving structures of unknown materials, but do not provide information on possible synthetic routes to a hypothetical structure. At this point in time, we lack the knowledge of the chemistry and kinetics in the initial stages of crystallization required to predict the outcome of zeolite synthesis. Thomas and coworkers *(117,118)*, Bushuev and Sastre *(119)*, and Moliner *et al*. *(120)* have developed computational tools to assist in the design of zeolite synthesis routes. Bushuev and Sastre *(119)* take into account the effect of water in the modeling of the template (SDA) molecules in the pore system. The computations described by these authors all, to a large extent, rely on the interaction of the SDA with the final structure. Although this approach can assist in finding patterns in SDA effects and possible SDAs may be identified, the methods do not take into account the early stages of crystallization, when the template is interacting with water, mineralizing agents, other template molecules, and more or less oligomerized silicate species, usually at increased temperature and pressure. A thorough understanding of the effects of all these parameters on the kinetics of the initial stages of crystallization is required, before we can truly predict zeolite synthesis and prepare whichever of the viable hypothetic frameworks we would like.

Yu and Xu *(121)* have described a complete route for the design and the synthesis of zeolites. The route starts with a careful investigation of the desired catalytic reaction or process, which provides requirements for the zeolite structure such as favoring a transition state or allowing "molecular traffic control" *(122)* of reactants or products. The structure is

then modeled to meet the requirements, using the framework generation tools described above; candidate SDA molecules are designed for the structure(s) by using the tools described above, or by using data–mining techniques *(121)*. Synthesis is then attempted using an array of combinatorial and high–throughput experimentation tools. The structures resulting from the synthesis campaigns are identified by comparing the experimental results to those predicted by the hypothetical structure databases. Finally, the zeolites are tested in the application. The authors conclude that replacing the present trial–and–error approach by this *ab initio* design "is, in fact, a long journey from possibility to reality" *(121)*.

Moliner *et al. (123)* have reported the synthesis design and characterization of ITQ–38, a new 10–12–MR zeolite. They seem to have applied at least a number of the steps from Yu's and Xu's procedure. Their work indicates that encouraging steps on this long journey have already been taken and offers prospects that such an approach may indeed become reality.

3. CATALYTIC APPLICATIONS

3.1 Refinery Operations

3.1.1 FCC Processes

FCC is undoubtedly the largest application of zeolites in the field of catalysis. Approximately 14.5 million barrels of feedstock are treated every day in FCC units in over 300 oil refineries worldwide. Approximately 840,000 t of FCC catalysts are produced and used every year. A review by Vogt and Weckhuysen on the FCC process and related zeolite developments has recently been published *(124)*.

Houdry catalytic cracking and early FCC processes initially did not use zeolites, but rather acid–treated clay and amorphous silica–alumina. Soon after their discovery, synthetic zeolites were employed with great success in FCC processes. The first synthetic zeolites used in FCC were developed in the 1960s and 1970s in the research laboratories of Union Carbide and Mobil Oil Corporation. Breck and his team at Union Carbide invented zeolite Y or Linde Type Y *(125)*, a synthetic variant of the mineral faujasite with the framework structure FAU *(23)*. The zeolite, with various improvements, has been the major active component of FCC catalysts, since 1964 *(126)*. Another zeolite important for FCC is ZSM–5 with the framework structure MFI *(23)*, invented at Mobil's research laboratories by Argauer and Landolt *(127)*. ZSM–5 is employed in FCC mainly in additives that increase the yield of propylene *(124)*.

FCC is a process that is performed at severe conditions. Hot catalyst is mixed with hot oil (typically at a catalyst–to–oil ratio of about 5) at the bottom of a vertical riser reactor, typically at a temperature around 550 °C (see Figure 7). The catalyst–oil mixture quickly expands as a result of gas formation from the cracking reaction, and the mixture is forced up the reactor, which can be up to 40 m in height. Typical residence times in the riser are on the order of seconds or shorter. As a result of the endothermic cracking reaction, the temperature at the top of the riser drops to about 500 °C. At this point, products and the catalyst are separated, and the catalyst is stripped with steam to remove remaining product. The products receive further treatment upstream in the refinery.

Even after stripping, the catalyst will still contain carbonaceous deposits, known as coke. These coke deposits result from the direct deposition of feed molecules, or from secondary reactions in the riser reactor. The coked
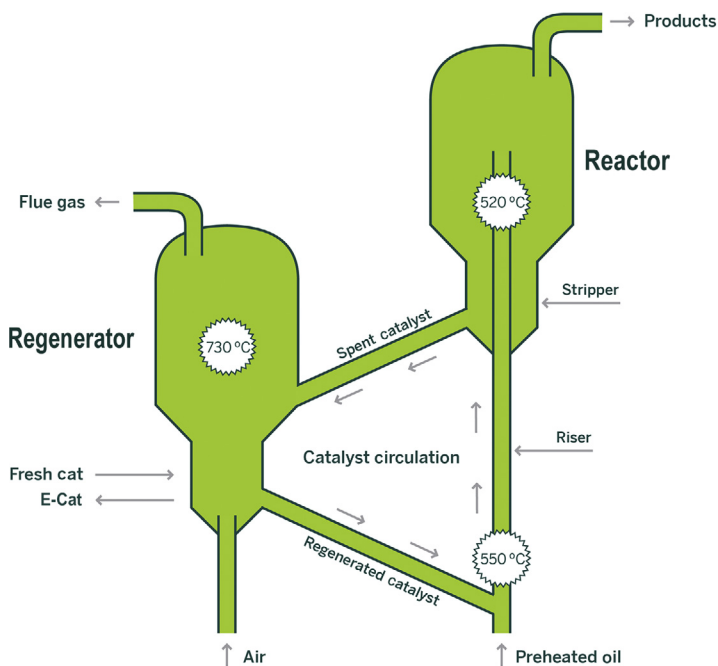
Figure 7 Schematic representation of an FCC unit. Preheated oil is fed to the bottom of the riser reactor and mixed with hot catalyst. The catalyst–oil mixture is transported up the reactor. At the top, the product is separated from the catalyst. The catalyst is stripped with steam and leaves the reactor as spent catalyst. The spent catalyst is regenerated in the regenerator and can be reused. A small portion of the inventory of the regenerator is removed and replaced with fresh catalyst at regular intervals.

catalyst is transported to a separate regenerator reactor, where the coke is removed by oxidation. In the regenerator, depending on the exact conditions, the temperature can reach up to 760 °C *(128)*.

The catalyst remains in the regenerator until it is transported back to the riser reactor for another cracking cycle. The process is continuous. It is clear that the harsh conditions in the riser and regenerator, the temperature cycles, the changes in atmosphere (reducing in the riser, oxidizing in the regenerator), the high velocities at which the catalyst particles travel (the average velocity in the riser is close to 140 km/h), and finally the presence of catalyst poisons, such as iron, nickel, and vanadium in the feedstock, will have an impact on the catalyst life. A conservative estimate would be to assume the lifetime of the catalyst is on the order of a couple of weeks. Since it is not possible to selectively remove catalyst particles that have deactivated, oil refiners remove a small portion of the regenerator inventory every day, and add fresh catalyst to replace the removed catalyst. Over time, this mode of operation creates a catalyst mixture with an age (or activity) distribution and a steady-state performance. This steady-state mixture is called equilibrium catalyst or E-Cat. Depending on the exact requirements of the FCC unit, the feedstock processed, and the size of the unit, catalyst addition rates can be between 1 and 30 t per day.

FCC is used to convert heavy feedstocks, such as heavy gas oil (HGO), VGO, or residue, into useful products, with the target of producing gasoline range molecules. The FCC unit is also a major source of alkenes, like propylene, and the process can be tailored to produce larger amounts of propylene if the refiner requires it. Although it is difficult to depict typical molecules one could find in a VGO FCC feedstock because of the large variety of molecules, some examples of the more complex molecules in VGO are described by Fu *et al*. *(129)* and Ma *et al*. *(130)* (see Figure 8).

The molecules consist of large aromatic systems with alkyl side chains and typically contain impurities, such as nitrogen, sulfur, or oxygen. Typical VGO molecules in the heavier fractions (boiling points of 456–543 °C) can have carbon numbers around 30 *(129)* and can vary with respect to number of aromatic rings, length of side chains, and impurities *(130,131)*.

Although the zeolite material is considered to be the main active component of the catalyst, these feed molecules are actually too large to enter the micropores of the zeolite, as is obvious from Figure 8. The matrix of the catalyst particle, consisting of clay, alumina, and silica compounds, will have to precrack such large feed molecules to a size range that the zeolite pores can accommodate.
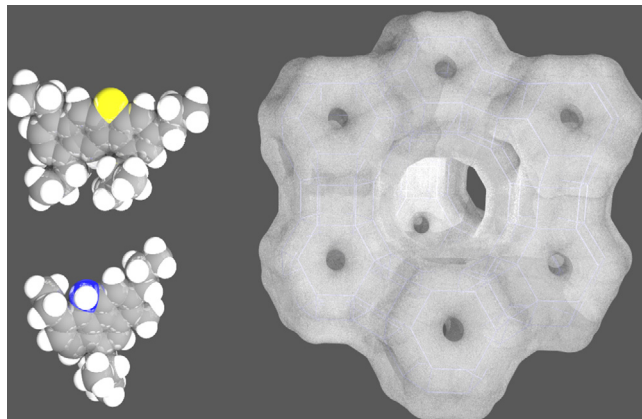
Figure 8 Typical molecules one could find in an FCC VGO feedstock contrasted with the pore openings in zeolite Y (FAU) which is used in FCC catalysts. Molecules selected from VGO-range molecules described by Fu *et al.* *(129)* and Ma *et al.* *(130)*. Carbon and hydrogen are depicted in gray and white, respectively; impurities sulfur and nitrogen are depicted in yellow and blue, respectively.

The cracking reactions in the FCC process, particularly those in the matrix, are very likely a combination of thermal and catalytic reactions, with the contribution from catalytic cracking increasing as the molecules become smaller on their way into the catalyst particle. The catalytic reaction network is acid catalyzed. Acid sites can be located in the matrix (e.g., Brønsted acid sites at the interfaces between silica and alumina regions, or Lewis acid sites on the alumina surface) or in the zeolite. Zeolite sites can be Brønsted acids (protons compensating the negative framework charge introduced by Al^{3+} ions) or Lewis sites (coordinatively unsaturated aluminum sites in damaged zeolite frameworks). Figure 9 explains the various functions.

The exact nature of the cracking mechanism has been the subject of debate since the early days of catalytic cracking *(133)*. The generally accepted theory now appears to be that acid-catalyzed cracking involves the formation of carbenium ions *(134–136)*. These can be formed on Brønsted sites by donation of a proton to an alkene, which can be present as the result of previous thermal cracking steps *(137)*. Lewis acid sites can abstract a hydride ion from alkene, which also leads to carbenium ion formation. Finally, Brønsted sites can donate a proton to an alkane, forming a penta–coordinated (zeolite-stabilized) carbonium ion. The carbonium ion can split off dihydrogen to form a carbenium ion, or it can crack to form an alkane and a carbenium ion (protolytic cracking) *(138)*. The carbenium ions formed in these processes crack through β–scission, forming alkenes and
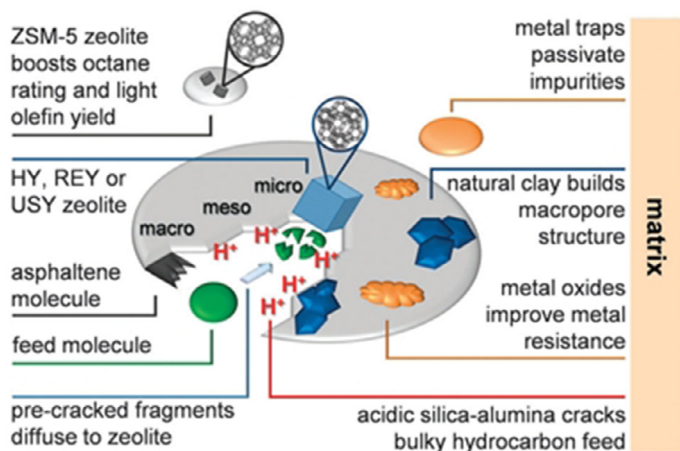
Figure 9 Schematic diagram showing the components and their functions in a spray-dried FCC catalyst particle. *Reproduced from Ref.* (132) *with permission of The Royal Society of Chemistry.*

smaller carbenium ions. Hydride-transfer processes between larger alkanes and the smaller carbenium ions allow the small carbenium ions to desorb as alkanes, while the larger alkanes are transformed to new carbenium ions, which propagate the reaction. Recovery of the hydride from a Lewis acid site will transform the carbenium ion to an alkane and terminate the reaction, as will the donation of a proton from the carbenium ion to the Brønsted acid site to form an alkene (see Figure 10).

The zeolites in FCC processing have to endure harsh conditions and certain poisons that can destroy the zeolite. During the process, the zeolite deactivates quickly. The framework aluminum atoms are dislodged, Brønsted acidity is lost, and the framework integrity is compromised. Eventually, the framework collapses, as indicated by a decline in surface area and pore volume and the disappearance of the XRD pattern. Already in the very early history of zeolite catalytic cracking, it was known that the addition of rare earth (RE) cations to the zeolite, for example, by ion exchange, increases the cracking activity and apparently stabilizes the zeolite framework structure. Plank and Rosinky (139) reported a remarkable increase in activity when using RE-stabilized Y zeolites, though it should be noted that they compared the activity of the RE-doped materials with those of amorphous SiO_2/Al_2O_3 and Na–Y. Although the increased activity and stability of the RE-exchanged zeolites are desirable, there is a less desirable effect on the selectivity: the introduction of RE cations also increases the rate of
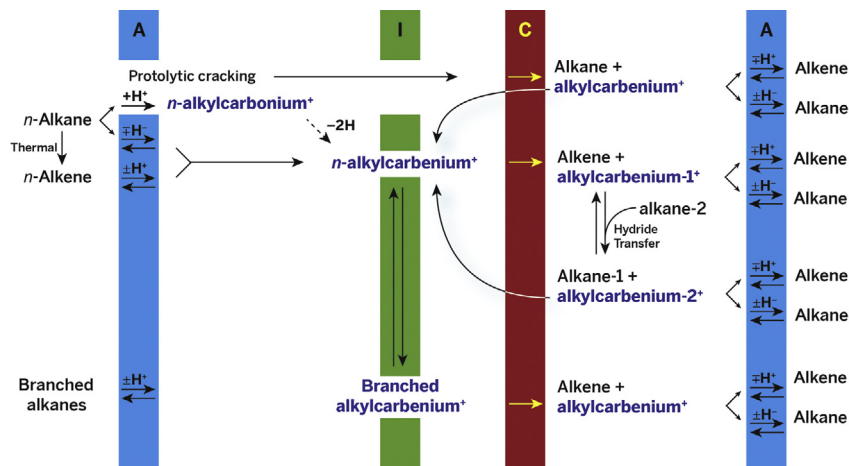
Figure 10 FCC mechanism starting from a linear alkane (*n*-alkane) or alkene (*n*-alkene). Blue (gray in the print version) bar (A): Brønsted or Lewis acid-catalyzed hydrogen transfer, green (gray in the print version) bar (I): acid-catalyzed isomerization, red bar (dark gray in the print version) (C): β-scission or protolytic cracking. Second blue bar (gray in the print version) (A): hydrogen transfer to final products. Carbenium ions in bold are stabilized by the zeolite. The mechanism is explained in more detail in the text.

hydrogen transfer, which in turn leads to a drop in research octane number and a lower olefin content in the liquefied petroleum gas (LPG) product.

To explain the effects of the RE addition, a substantial amount of work was performed already in the 1970s and 1980s. Li and Rees *(140)* noted that the thermal collapse of RE-containing zeolite Y occurs at higher temperature than that of undoped Y, thus indicating enhanced lattice stability. Flanigen *et al.* *(141)* assigned the IR bands observed for zeolite Y, and from these bands, the asymmetric stretching vibration at around 790 cm^{-1} was selected as the band best suited to determine the framework composition by Roelofsen *et al.* *(142)*. The authors investigated the dealumination with a variety of techniques, including Fourier transform infrared (FT-IR) spectroscopy, XRD, and ^{29}Si MAS NMR spectroscopy. They concluded that the trends in FT-IR and ^{29}Si MAS NMR spectra reflect the framework composition, but the standard correlation of framework alumina content with the unit cell (UC) size (the well-known Breck–Flanigen relation *(143)*) does not hold in the case of RE-stabilized Y zeolite. The correlation between the IR band positions and the framework silica–to–alumina ratio (SAR) was also noted by Scherzer *et al.* *(144,145)* and Falabella Sousa-Aguiar *et al.* *(146)*. Rabo *et al.* *(646)* focused on IR bands associated with the RE ions rather than on those associated with the zeolite framework. They

observed two types of hydroxyl bands, one at a wavenumber of 3640 cm^{-1}, which seems to be associated with OH groups exposed inside the supercages, and one at 3524 cm^{-1}, which seems to be associated with OH groups hidden in the sodalite cages. The latter band might indicate multinuclear OH-bridged RE clusters in the sodalite cages, as described in the theory-based work by Schüßler *et al.* *(147)*. van Bokhoven *et al.* *(148)* indicate that small, highly charged ions, such as RE^{3+} but also extra-framework aluminum (EFAL), can induce local electrostatic effects that alter the acidity of the framework aluminum. In addition, the presence of RE^{3+} in the lattice ion-exchange positions already causes the T—O—T angles and thus the UC size to increase. Dealumination causes shrinkage of the UC. One would normally assume that a higher UC size after steaming implies stabilization of the framework (retention of framework alumina), but in this case the UC size is altered even without any stabilization occurring. In recent years, the price volatility of RE elements has sparked renewed interest in other solutions for stabilization of zeolite Y that do not require these elements.

The other zeolite that is often applied in FCC is ZSM-5. ZSM-5 is used in additives that promote the formation of propylene. ZSM-5 was first synthesized in 1973 *(127)* in the research laboratories of Mobil Oil. It was later discovered that there is a mineral analog, called mutinaite *(149)*. ZSM-5 has a more restricted pore system than zeolite Y. Its pores are limited to 10-MRs, and there are no large cages, which means there is no room for the transition states of the bimolecular reactions. The secondary cracking of gasoline range molecules will therefore produce a relatively large amount of olefins, including the desired propylene. Of course, zeolite ZSM-5 in the FCC-additive will encounter the same conditions in the unit as the primary cracking zeolite Y. These conditions imply that ZSM-5 will also deactivate and eventually collapse. While a partial collapse of the zeolite structure may lead to mesoporosity and thus improved mass transfer, the extra room allows the undesired bimolecular cracking mechanism, and therefore ZSM-5 is also stabilized. In the case of ZSM-5, the stabilizing agent is usually a phosphorous compound. Xue *et al.* *(150)* mentioned a long list of possible compounds. It should be noted that phosphorus stabilization or activation of ZSM-5 is not limited to FCC, but can also be applied in MTO, alkylation, and ethanol dehydration *(150)*. A recent review on phosphatation of ZSM-5 has been published by van der Bij and Weckhuysen *(151)*.

While a large number of phosphorus compounds have been applied as stabilizing agents, the inorganic compounds are of particular relevance to FCC because of the scale of the operation. It does appear though as if the

nature of the phosphorus compound chosen for the activation is of less importance than the Al/P ratio, the zeolite Si/Al ratio, the crystal size, and the exact activation conditions *(150)*.

The phosphate species can enter the pore system of the zeolite and form an adduct with partially (but not completely) dislodged framework aluminum atoms. This process eliminates the Brønsted acid site associated with the aluminum atom, but may generate acidic protons on the phosphorus atoms in the adduct. The formation of the adduct seems to stabilize the framework *(151)*. Any excess phosphorus species will migrate to the outside of the zeolite crystal and may react with EFAL, or even with the binder of the catalysts, which generally also comprises alumina.

Whatever the exact atomic structure of the adduct may be, the macroscopically observable effect on the ZSM-5-containing catalysts is appreciable: The zeolite lattice is stabilized, the formation of bulky isomers is reduced, the formation of light olefins is promoted, both in FCC and MTO, as well as in ethanol dehydration, and finally, the formation of coke is reduced. The latter two effects may indicate a decreased propensity for hydrogen transfer, and the second effect may indicate that the adduct restricts the space that is available for bulky intermediates in the vicinity of the acid sites.

Van der Bij *et al.* *(152–155)* recently combined NMR spectroscopy, X-ray microscopy, and X-ray photoelectron spectroscopy (XPS) to determine the nature of the adduct (see Figure 11). They conclude that stable —$(SiO)_{3-x}$—Al—$(PO)_x$ species (SAPO species) are formed, in which the SAPO species is attached to the framework, but the aluminum is no longer in its original framework position. The exact structure of the adduct remains to be solved. The bulky SAPO species in the zeolite pores may impede the formation of carbenium ions, thus suppressing bimolecular pathways, which in turn leads to the desired increased propylene selectivity.

Historically, FCC units were optimized for the production of gasoline, or alternatively propylene. In recent years, the demand for middle distillate has been growing, and therefore middle distillate-selective FCC catalysts and processes are becoming more interesting *(156)*. Figure 12 shows the changes in product demand and highlights the increase in the diesel-to-gasoline ratio predicted over the next years.

Another option is to use HC as the primary conversion technology, since this process is usually more middle distillate selective *(158)*. Although a higher middle distillate selectivity in FCC can to some extent be achieved by operational changes to the process (e.g., by lowering cracking severity), changes to the catalyst can also be considered (e.g., lowering the zeolite
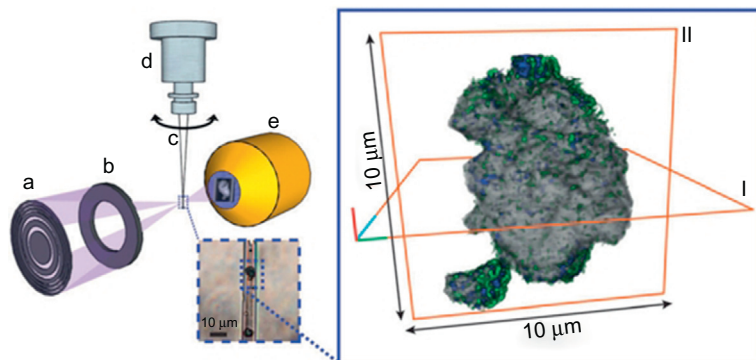
Figure 11 Left-hand side: Soft X-ray tomography setup. Monochromatic X-rays are focused by a Fresnel zone plate lens (a), while all but first-order light is blocked by an order-sorting aperture (b). The X-rays are focused to an approximate spot size of 30 nm and pass through a zeolite aggregate of about 8 mm in diameter. The aggregate is positioned in a borosilicate capillary tip (c) of 10 mm diameter, with a wall thickness of approximately 1 mm. The capillary is placed on a tomography stage (d) and can freely rotate by 360°. X-rays that have passed through the sample are collected by an X-ray detector (e). Right-hand side: 3D reconstruction of the specimen, based on X-ray tomography images. Voxel size $= 69 \times 69 \times 69$ nm^3. Gray $=$ particle density; blue $=$ aluminum; green $=$ phosphorus. *Reproduced with permission from Ref.* (154). *Copyright 2014 Wiley-VCH.*
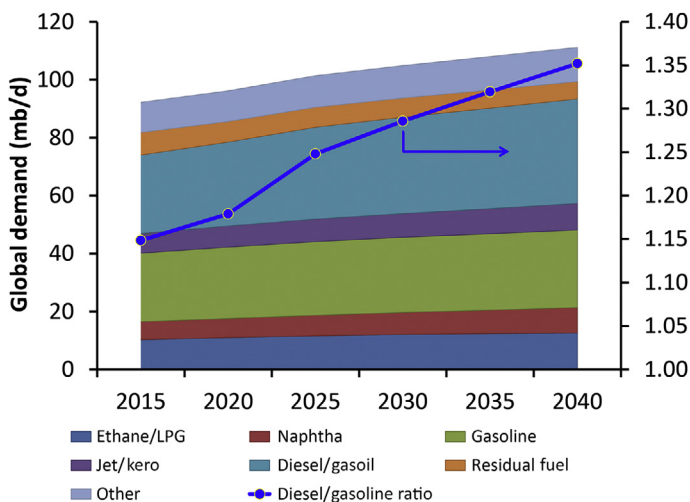
Figure 12 Liquid product demand projections. Left axis: global demand for products. Right axis: Increasing diesel-to-gasoline ratio reflects the increasing demand for diesel at the cost of gasoline. *Data from Ref.* (157).

content and increasing the matrix activity) (159). The FCC process relies on a series of consecutive primary and secondary cracking reactions, and the result of the process is to a certain extent controlled by mass transfer limitations. Therefore, it has been proposed to modify the mesoporosity of the zeolite crystals themselves, by using so-called hierarchical zeolites. The larger pore size would allow for reaction pathways that involve larger transition states, such as bimolecular or multimolecular reactions (160). Mesoporosity is already introduced by the more extreme forms of ultrastabilization, in which steaming is combined with chemical treatments such as acid leaching to remove the dislodged nonframework aluminum. This method was used to create the mesoporous 3DDM (3D-dealuminated mordenite) zeolite developed by The Dow Chemical Company for their cumene process (161,162). Li et al. (163) and Park et al. (164) have reported processes to prepare hierarchical mesoporous mordenite and ZSM-5, of which the latter was tested in propylene-selective FCC catalysis.

The ultrastabilization process lowers the total number of acid sites available and lowers the structural integrity of the zeolite crystals, but these negative effects are offset by the improved diffusion characteristics and the formation of new (types of) acid sites (165). The effects of the severe dealumination treatments are illustrated nicely in the work of Janssen et al., who performed three-dimensional transmission electron microscopy (3D-TEM) in combination with more standard techniques to investigate the mesopores (166). Mesoporosity can also be introduced by desilication, as demonstrated by Pérez-Ramírez and coworkers (167–170), who also proposed routes to recycle the waste stream from the postsynthesis treatment as a source of raw material for future zeolite crystallizations (169).

Hansen et al. (159) obtained a hierarchical mesoporous Y zeolite by recrystallization of Y zeolite at a temperature of 150 °C and a pH of 9–11 in the presence of CTAB (a micelle-forming SDA also applied in the synthesis of the mesoporous MCM-41 (171)). The treatment apparently restores both silicon and aluminum atoms in lattice positions, since NMR spectra do not show any octahedrally coordinated aluminum, and IR spectra do not show terminal silanol vibrations. An FCC catalyst containing the mesoporous hierarchical zeolite was tested in a refinery and showed higher selectivity to light cycle oil, lower rate of coke formation, and improved conversion of the heavier fractions (172).

Martens et al. describe "zeogrids" and "zeotiles," which are characterized by hierarchical pore systems and can be formed by self-assembly of MFI-building blocks in the presence of supramolecular SDAs (173). The

materials are claimed to behave different from both normal zeolites and ordered mesoporous materials. Choi *et al.* prepared nanosheets of MFI with single UC thickness and found high activity, which was explained by a high number of acid sites on the exterior surface of the sheets, combined with little coking because of improved diffusion properties *(174)*. Kim *et al.* prepared MFI "nanosponges," which are three-dimensional disordered networks of MFI nanolayers *(175)*. Ng *et al. (176)* reported the colloidal synthesis of very small zeolite EMT crystals in a template-free reaction medium. Awala *et al.* reported on the template-free synthesis of nanosized faujasite zeolites *(177)*. The authors developed a synthesis in which they control nucleation by mixing and aging freshly prepared gel components at a temperature of 4 °C prior to crystallization at 50 °C for 45 h. This protocol leads to nanometer-sized single crystals with a very narrow size distribution. Uniform crystals of a size as small as 10 nm can be prepared by this method.

Recent analytical developments have allowed detailed investigations of FCC catalysts, which have greatly increased our fundamental understanding of activity patterns and mechanisms of deactivation by metal poisons. X-ray tomographic analyses have shed light on the location of metal poisons in deactivated catalysts, the correlation in their spatial distribution, and the effects of their presence on the pore structure. An initial investigation by Ruiz-Martinez *et al. (178)* combined micro–X-ray fluorescence (μ–XRF), micro–X-ray absorption near edge structure (μ–XANES), and micro-XRD analysis of entire FCC catalyst particles at a resolution of about 5 μm. The authors present chemical maps of nickel and vanadium distributions, in which nickel is mainly located close to the surface of the particle, and vanadium largely dispersed throughout. μ–XRD analysis showed that the zeolites were dealuminated in a distorted egg-shell pattern, with the largest extent of dealumination (both seen in SiO_2–Al_2O_3 molar ratio as well as crystallinity) at the outside of the FCC particle *(178)*. Meirer *et al.* used element-specific X-ray nanotomography to investigate the three-dimensional structure and composition of integral FCC particles at 30 nm resolution *(179–181)* (Figure 13).

Details of this work are discussed in Section 3.3. When investigating the spatial correlation of metal poisons with structural markers by using multielement XRF nanotomography, Kalirai *et al.* recently found that the location of vanadium is not correlated with the zeolite particles, while confirming the correlation between iron and nickel, particularly at the outer shell of the FCC catalyst particles *(182)*.
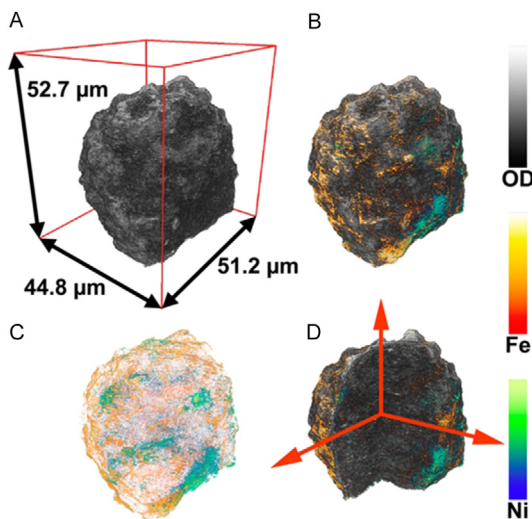
Figure 13 Three-dimensional representation of an approximately 50 µm diameter FCC particle based on TXM mosaic computed tomography with a voxel size of $64 \times 64 \times 64$ nm^3. (A) Optical density (OD) as recorded at 7060 eV. (B–D) Visualization of Fe (orange) and Ni (blue) 3D relative distributions obtained from differences of tomography data: 7160–7060 and 8400–8300 eV, respectively. (D) Cut-through of the tomography data showing the inner structure of the particle. *Reproduced with permission from Ref. (179). Published under Creative Commons Attribution CC-BY license.*

Bare *et al.* investigated larger numbers of FCC particles with combinations of X-ray microscopy and nanotomography, as well as μ–XRF and μ–XRD. They analyzed the morphology of more than 1200 FCC catalyst particles and observed large internal voids in some FCC particles. The location of nickel was confirmed to be close to the external surface of the particles, and the μ–XRD techniques allowed the determination of the zeolite lattice parameters as described above *(183)*.

Da Silva *et al.* used phase–contrast X-ray microtomography and high-resolution ptychographic X-ray tomography to investigate model FCC catalysts *(184)*. They were able to identify zeolite regions, clay regions, and open pores in their 3D reconstruction at a resolution of about 39 nm.

Buurmans *et al.* used optical techniques to investigate the dispersion of active zeolite particles in FCC catalysts, by staining them with thiophene and styrene derivatives, which oligomerize on Brønsted acid sites and form fluorescent moieties. Both the spatial distribution and the deactivation of the zeolite particles could be investigated by this method *(185)*. In a subsequent investigation, the authors compared zeolite ZSM-5 and

Y crystals in commercial FCC catalysts using the reactions of 4-fluoro- and 4-methoxy-styrene, which display different oligomerization reactivity patterns depending on the active sites. In ZSM-5, both molecules oligomerized, whereas in zeolite Y zeolite only 4-methoxy-styrene oligomerized *(186)*. Integrated laser and electron microscopy can be conducted in one setup, thus combining the strengths of both techniques in the observation of exactly the same spots in FCC catalyst particles. Karreman *et al.* used this technique to identify different structures in FCC catalysts and demonstrated that laboratory deactivation techniques such as steaming lead to different transformations in the catalyst components (clay, zeolites) compared with those observed in E-Cat samples *(187,188)*.

Sprung and Weckhuysen exploited the anisotropic nature of ZSM-5 crystals in FCC particles to refine the fluorescence microscopy and locate ZSM-5 crystals and crystal clusters in FCC particles, and determine their dispersion *(189)*. Furthermore, by analyzing the fluorescence microscopy images, they could estimate the amount of zeolite ZSM-5 within a single FCC catalyst particle, which was close to 15 wt.%. However, the confocal fluorescence techniques are limited in resolution and cannot resolve details smaller than the wavelength of the laser light, which is slightly below 1 μm (Figure 14).

Ristanovic *et al.* recently resolved this problem by using single-molecule fluorescence microscopy, which relies on measuring fluorescence "bursts" that occur in an FCC catalyst particle irradiated with a laser whenever an oligomerization reaction of furfuryl alcohol takes place at a Brønsted acid site and fluorescent moieties form *(190)*. In this way, a much higher spatial resolution can be obtained of around 25 nm, but also turnover rates can be determined accurately. The results point toward substantial variations in turnover frequencies (TOFs) among zeolite ZSM-5 aggregates embedded within an FCC catalyst particle, revealing significant intraparticle heterogeneities in the reactivity of the Brønsted sites.

The large body of recent analytical work on FCC catalysts from various groups has led to a rapid increase in the understanding of the interaction of catalyst components and the effects of poison and impurities on the deactivated catalysts. This increased understanding provides a promising basis for further catalyst development.

3.1.2 HC Processes

HC is defined as a process in which the components of gas oil fractions are (partially or completely) converted into lighter molecules under the
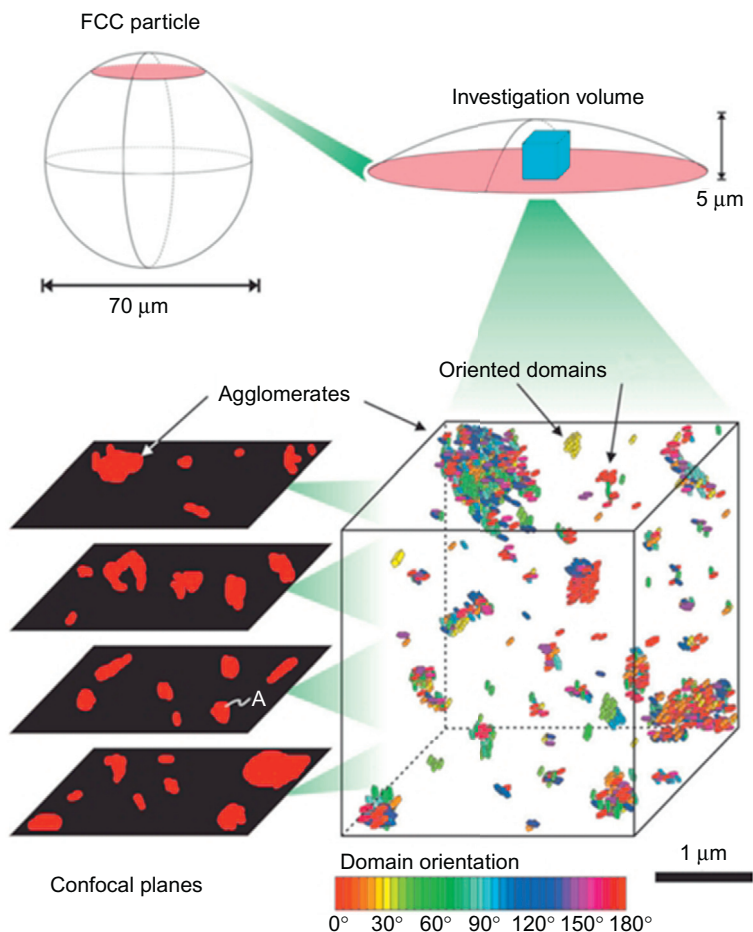
Figure 14 Schematic drawing of the investigated volume within a single industrial FCC particle: The outer layer of the particle was investigated to a depth of about 5–6 mm. Within this volume, we schematically illustrate a box (about $4 \times 4 \times 4 \ \mu m^3$) highlighting solely the zeolite component. These zeolite domains appear in a random orientation, indicated by their color. Some of the domains may be agglomerated to large or small clusters with more or fewer similarly oriented domains. The confocal planes visualize areas of fluorescence in the investigated volume. *Reproduced with permission from Ref.* (189)*. Copyright 2014 Wiley-VCH.*

influence of H_2 and in the presence of a catalyst. HC is a very versatile conversion process for transforming heavy petroleum fractions, like heavy atmospheric gas oil (HAGO) and VGO or cracked gas oils, into more valuable lighter fractions, mostly targeting middle distillates. HC is the second largest application of zeolite materials in the field of catalysis. Approximately

5.6 million barrels of feedstock are processed in HC each day, and the process is performed in at least 170 oil refineries *(191)*.

The first hydrocrackers were designed and built by I.G. Farben in Germany in the mid-1920s. The catalyst materials were nitrogen compounds (ammonia or ammonium compounds) that were added to the feedstock in the presence of other, solid, catalysts, such as clays, active silica or alumina, or sulfides, carbides, and nitrides *(192,193)*. The process was further developed in the USA in the 1930s, and with the advent of zeolite catalysts in the 1960s and 1970s, various versions (UOP/Chevron Isomax and Unocal/Esso Unicracking) became widely implemented.

HC catalysts are bifunctional. They combine a hydrogenation function, provided by either promoted transition metal sulfides, such as mixed sulfides of nickel and tungsten, or a noble metal such as platinum and palladium, with an acid function, provided by a zeolite. The zeolite is typically an ultra-stabilized Y zeolite (USY), in which a considerable fraction of the initially present framework aluminum has been removed by combining ion exchange, steaming and acid-leaching treatments. The characteristics of the obtained zeolite are strongly dependent on the starting material, as well as on the order and severity of the various treatment steps. The resulting USY zeolite has a lower number of acid sites than the zeolites typically used in fresh FCC catalysts, which results in a lower cracking activity. As a result of the severe treatment, the zeolite structure will be partially destroyed, and a certain increased mesoporosity will be generated, which is conceptually beneficial for the mass transfer of large gas oil molecules. By tuning the overall acidity of the zeolite, as well as the ratio between hydrogenation function and acid function, HC catalysts can be tailored to obtain a desired ratio of conversion to middle distillate selectivity *(194–196)*. It is this flexibility and the high middle distillate selectivity compared to FCC that will likely allow HC to claim a larger portion of the conversion processes in future refining schemes.

HC is the most severe hydrotreatment process. It is performed at high reaction temperatures and pressures, that is, 350–450 °C and 100–200 bar, though there is a lower severity process called mild HC, which operates at milder conditions (see Table 4).

It is evident from Table 4 that HC requires a large amount of hydrogen. However, if we convert the units of Nl/l to mol/mol, the number becomes less impressive. A H_2/oil ratio of 1000 for HC translates to about 12 molecules of H_2 per gas oil molecule if we assume a typical gas oil molecule to have an average molar weight of about 230 g/mol. The hydrogenation of a

Table 4 Overview of the Parameters for Mild HC and HC *(194)*

	Mild HC	HC
	Single Stage	Single or Two Stage
Conversion (%)	20–70	70–100
Temperature (°C)	350–440	350–450
H_2 pressure (bar)	30–70	100–200
WHSV (h^{-1})	0.3–1.5	0.5–2.0
H_2/oil ratio (Nl/l)	300–1000	1000–2000

few double bonds or aromatic rings will quickly consume this hydrogen. HC is thus a hydrogen addition process, in contrast to FCC, which is a carbon rejection process. Both processes aim at increasing the ratio of hydrogen to carbon from about 1.4 (in highly aromatic gas oils) to just over 2 (for fuel alkanes). This goal can obviously be achieved by increasing the hydrogen content (HC process) or lowering the carbon content (FCC process).

HC can be performed in single-stage or two-stage processes (see Figure 15) and can be preceded by a hydrotreatment step (hydrocracker pretreat, HC-PT) to remove undesired impurities before the cracking process; for example, nitrogen in the feedstock may damage the zeolite in the HC catalyst (see, e.g., Refs. *(158,197)*).

A single-stage design is easier to construct, but full conversion is usually not achieved. A two-stage design, in which unconverted feedstock from the first reactor is cracked in a second reactor after removal of H_2S and NH_3 from the stream, typically allows for full conversion.

Because the catalyst operates at high H_2 partial pressure, deactivation by coke is not as much an issue as it is in FCC, and HC catalysts will typically have a much longer lifetime (sometimes up to several years). However, since the feedstocks for HC are of similar origin as FCC feedstocks, other contaminants are present (e.g., iron and arsenic) and will slowly deactivate the catalyst material.

Both functions in the catalyst (i.e., hydrogenation and acid sites) are important for the mechanism of HC. In an initial step, the hydrocarbon molecule is activated by dehydrogenation and adsorbed on the zeolite to form a zeolite–carbenium ion complex, which subsequently isomerizes and cracks by beta-scission (i.e., isomerization precedes cracking *(198)*).
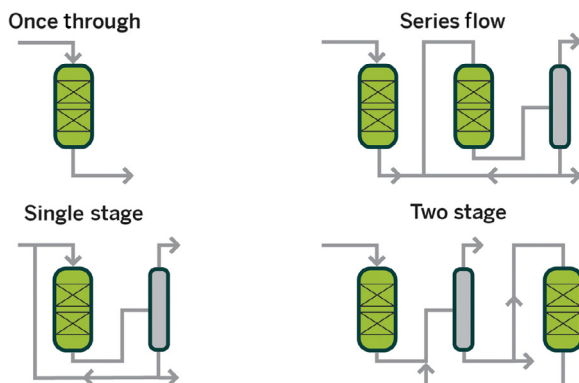
Figure 15 HC process options. A simple once-through process is easy to build, but full conversion is not easily achieved (referred to as mild HC). An expansion is the single-stage HC process with recycle. A series flow configuration offers the possibility to combine different catalyst functionalities. The two-stage configuration has a separator between the two reactors, which removes the side products NH_3 and H_2S, and full conversion is thus more easily achieved. The first stage can be a pretreatment reactor to remove nitrogen and sulfur. *Based on Ref.* (197).

Martens *et al.* *(199)* observed that secondary and tertiary alkylcarbenium ions are involved in the mechanism, and primary carbenium ion formation is avoided. The secondary and tertiary carbocations are derived from di- and tri-branched isomers of the feed molecules, indicating that at least two isomerization steps are required before cracking occurs (Figure 16).

Both the isomerized alkenes and the cracked product will be hydrogenated before leaving the catalyst surface. The high H_2 partial pressure ensures that coke formation reactions are limited *(200)*. Further control of the rate of coke formation can be achieved by controlling the relative locations of the hydrogenation function and the acid function *(158,201)*. Zhang *et al.* constructed a kinetics model for HC on NiMo–USY catalysts and concluded that the initial acid-catalyzed carbenium ion formation, alkene protonation, and hydride and metal shifts, as well as the metal-catalyzed (de)hydrogenations are fast steps in the reaction network and reach equilibrium, whereas the protonated cyclopropane isomerization, β-scissions, dealkylation of aromatics, and cyclization are kinetically controlled *(202)*.

As described above, the zeolites used in HC receive considerable postsynthesis treatment. Although the exact recipes for making HC zeolites are mostly proprietary, they will likely contain a succession of the following steps. Since the active sites for Brønsted acid–catalyzed cracking are protons
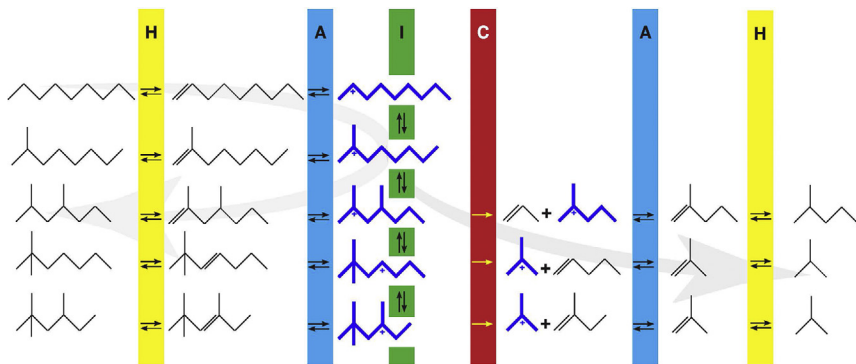
Figure 16 HC mechanism. A linear hydrocarbon is first dehydrogenated on the hydrogenation function of the catalyst (H). In a subsequent acid-catalyzed step (A), a carbenium ion is formed, which isomerizes (I) before being cracked. Hydrogen transfer on the acid sites (second A) and subsequent hydrogenation (second H) lead to saturated branched cracked products. The branched carbenium ion can also lead to uncracked branched products by returning via the A,H pathway. Carbenium ions stabilized by the zeolite are marked in bold.

associated with framework aluminum, the initial step will be a (partial) removal of the counterions used in the synthesis (typically sodium), followed by steaming to reduce the UC size of the zeolite. The bond length of the Al—O bond is longer than the Si—O bond; thus removal of framework aluminum leads to framework shrinkage. This step can be followed by further ion exchange and steaming, or acid leaching can be employed to remove EFAL. The severity of all steps (ion exchange, steaming, and leaching) as well as the order of treatments can be varied almost without limits, and the exact route followed determines the catalytic performance and stability of the zeolite *(194–196)*. Figure 17 and 18 show a comparison of different generations of catalysts, and the effect of catalyst activity on the middle distillate selectivity.

The removal of framework aluminum atoms lowers the overall acidity of the zeolite and also creates mesoporosity, as elegantly illustrated by Jansen *et al. (166)* (see Figure 19). In recent years, a large body of work has been published concerning the synthesis and characterization of so-called hierarchical zeolites, which is discussed briefly in Section 3.1.1, and in more detail in Refs. *(124,205)*.

Agudelo *et al.* investigated the effect of steaming and dealumination on NiMoP-loaded USY zeolites used for HC. They concluded that a relatively mild dealumination (performed with EDTA or mild acid leaching) removes
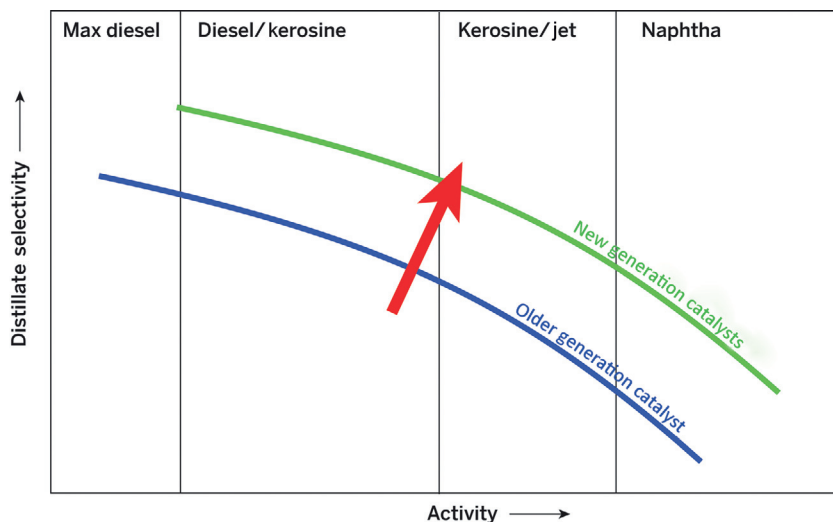
Figure 17 Selectivity in HC as a function of catalyst activity. *Based on Ref.* (203).
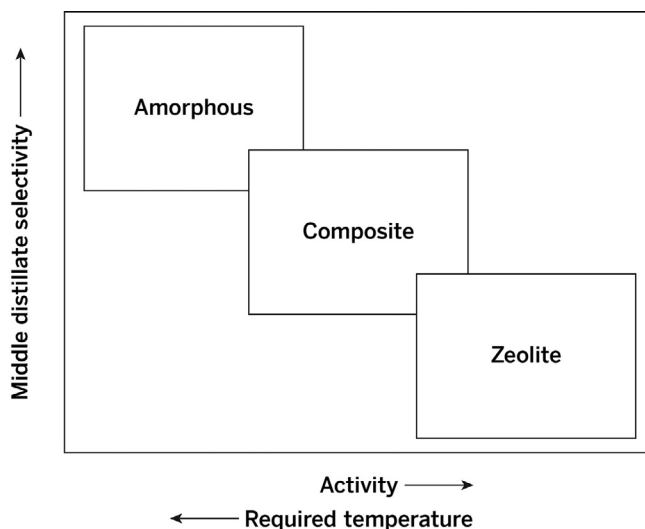

Figure 18 Activity versus selectivity depending on catalyst composition and structural properties. *Based on Ref.* (204).

EFAL that blocks the mesopores, while a portion of EFAL that is beneficial to the activity remains. A careful balance between steaming severity and very mild removal of EFAL is required to create zeolites with improved accessibility through mesopore generation, while maintaining optimized acidity (206,207).
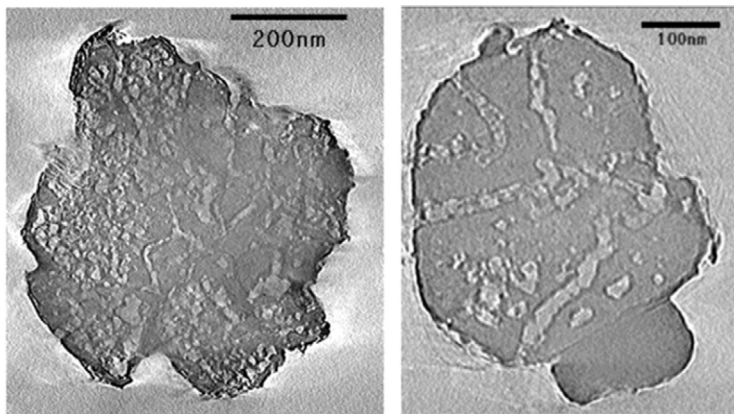
Figure 19 3D-TEM slices of two dealuminated USY crystals, showing the interconnected cylindrical mesopore system. *Reproduced with permission from Ref.* (166). *Copyright 2002 American Chemical Society.*

3.1.3 Dewaxing Processes

Catalytic dewaxing is applied to petroleum products to reduce the concentration of long linear alkanes through cracking or isomerization reactions. These molecules have high melting points, which cause them to precipitate from diesel fuels in cold winter conditions. The so-called cold flow properties, such as cloud point and pour point, are important parameters in middle distillate fuels. Figure 20 shows the dependence of melting points on carbon number for linear alkanes, 2-methyl–alkanes, and selected 5-methyl–alkanes. There are two approaches to improving the cold flow properties: isomerization and cracking.

As is evident from the figure, isomerization with retention of the overall carbon number yields a melting point decrease that can be as high as 60 K. The melting point typically appears to decrease with the distance of the methyl group from the end of the chain: the 5-methyl isomers shown all have lower melting points than the 2-methyl isomers. Branching does not appear to change the boiling point range too much (see Figure 21).

Cracking, of course, will lower the carbon number, thereby achieving the desired melting point decrease. However, the boiling point will also decrease, and care must be taken to avoid overcracking which would lower the diesel yield.

Both cracking and isomerization lower the cetane number of the feedstock. However, the resulting cetane numbers for linear alkanes and singly branched molecules are still well above the desired product cetane number range (see Figure 22).
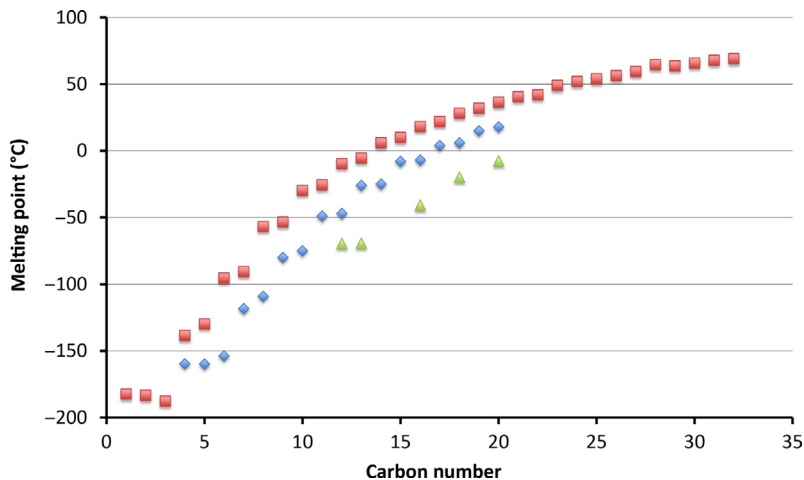
Figure 20 Dependence of the melting point of selected alkanes on carbon number. Red squares (gray in the print version): melting points of normal alkanes, blue diamonds (gray in the print version): melting points of 2-methyl-alkanes, green triangles (light gray in the print version): melting points of 5-methyl-alkanes. *Data from Refs.* (208–212).
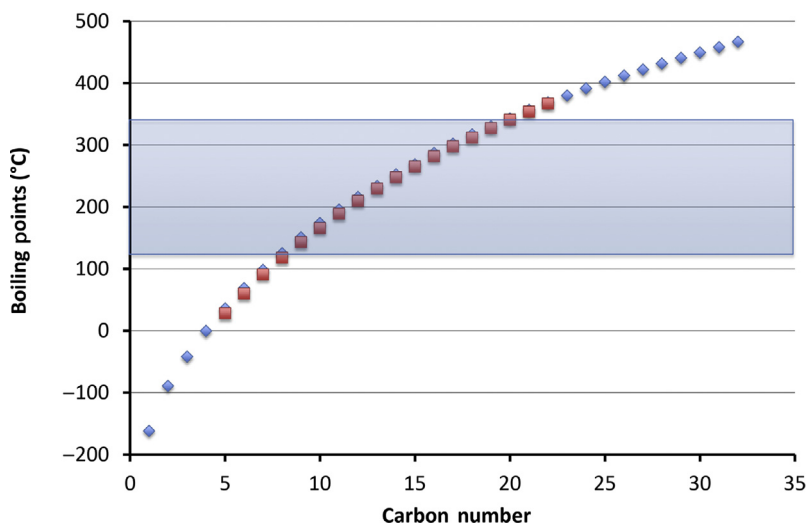
Figure 21 Dependence of the boiling point on branching and carbon number. Red squares (gray in the print version): boiling points of normal alkanes, blue diamonds (gray in the print version): boiling points of 2-methyl-alkanes. *Data from Refs.* (211,213–215).
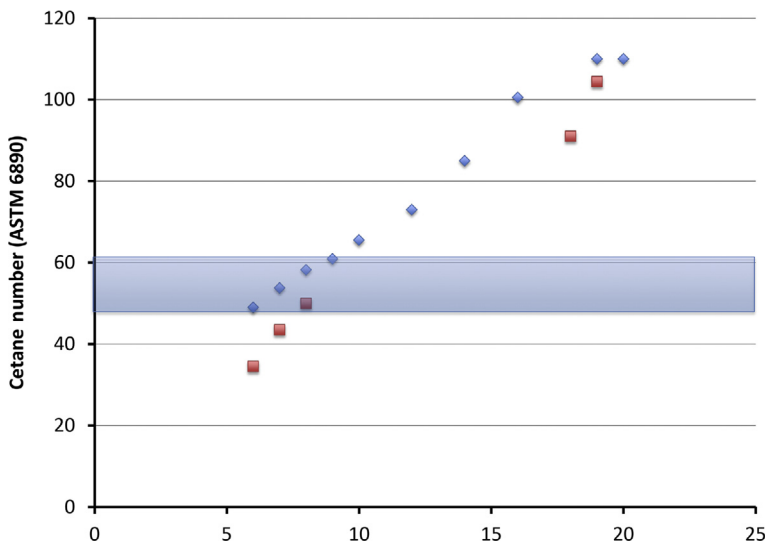
Figure 22 Cetane numbers as a function of branching and carbon number. Red squares (gray in the print version): cetane numbers of normal alkanes, blue diamonds (gray in the print version): cetane numbers of 2-methyl-alkanes. *Data from Ref.* (216).

Mobil Oil's distillate dewaxing (MDDW), which was introduced in the mid-1970s, is based on a ZSM-5 catalyst to selectively crack the longest chain linear alkanes to gasoline and LPG (217), making use of the shape selectivity imposed by the narrow pores of the ZSM-5, which preferably allow access to the straight chains. The process is performed at temperatures of 260–430 °C, at pressures of 20–50 bar, H_2-to-oil ratios of 250–450 Nl/l, or 3–5 mol H_2/mol hydrocarbon (assuming hexadecane as the average molecule in the feedstock) (218). The process concept can also be applied to dewax lube feedstock (Mobil lube dewaxing, MLDW), although it would then be operated at lower temperature (260–360 °C), because of the relatively small concentrations of poison in the lube feedstock (218). In the 1980s, Akzo (later Akzo Nobel; Akzo Nobel's catalyst business was acquired by Albemarle) and Fina (Fina was acquired by Total) introduced an improved version of the process, called cold flow improvement (CFI) (219). This process combines the dewaxing step with a desulfurization function and adds a hydrotreating step after the dewaxing catalyst in order to minimize heteroatoms and convert aromatics and olefins to saturated compounds. The Akzo–Fina process was combined with the MDDW process when the companies formed the Mobil Akzo Kellogg (MAK) alliance in 1992 (44).

Further improvements in the reactor design and the use of enhanced desulfurization techniques allow for optimal yields of gasoline and distillate, upgrading of waxy feedstocks, and production of high-quality jet fuel *(44)*.

Cracking of waxy feedstocks leads to loss of middle distillate products. Therefore, in some cases isomerization is a preferred solution. Cracking and isomerization processes are not interchangeable in the refinery, since they operate at different conditions. Cracking occurs at higher temperatures, and isomerization relies on a strong (noble) metal function, which can be more sensitive to poisons than the base metals used in cracking catalysts.

Dewaxing by isomerization has been applied by ExxonMobil in their MIDW (Mobil Isomerization Dewaxing) process, which is very likely based on a beta-zeolite *(220)* loaded with a small amount of platinum and/or palladium. *(221)*. In later versions, the hydroprocessing function seems to have been strengthened, and the process, which operates at fairly mild conditions (20–40 bar), produces low-pour-point and low-sulfur-content diesel *(44)*. Another version of a wax isomerization process was introduced by Chevron (called isodewaxing) and is based on a catalyst of specific pore geometry with oval pores, most likely SAPO-11, loaded with a metal, most likely platinum *(222)*. The oval pores would conceptually favor access to mono-methylated alkanes. The isodewaxing process and a version of the ExxonMobil process called MSDW (Mobil selective dewaxing) are also used for dewaxing lube feedstocks. Processes using shape-selective catalysts deliver products with a much better viscosity index than noncatalytic processes that use solvents for dewaxing *(44)*.

Martens *et al.* *(223)* tested the hydroisomerization and HC of more complex and bulky biomass-derived molecules, such as pristane (2,6,10,14-tetramethylpentadecane) and 2,6-lutidine (2,6-dimethylpyridine), on a hierarchical Pt-ZSM-22 (TON *(23)*), and concluded that the hierarchical system is well suited for isomerization, particularly of larger and more branched molecules.

Focused efforts have been made in the literature with respect to the HC and hydroisomerization of Fischer–Tropsch synthesis (FTS) waxes. Although these are in principle not too different from the waxes described above, we will briefly discuss some developments here. Hanaoka *et al.* optimized a platinum-loaded beta zeolite catalyst for the production of jet fuel (C_9–C_{15} fraction) and found that a low platinum loading of 0.1 wt.% provided the highest jet fuel yield at low temperature (250 °C) and 15 bar *(224)*. Seo *et al.* investigated Pt-beta and Pt-SBA-15 catalysts and found the Pt-SBA-15 catalyst to be more active for the production of gasoline at

380 °C and 60 bar *(225)*. A higher platinum loading (0.5 wt.%) and a relatively high Si/Al ratio of 14.5 were required. Pölczmann *et al.* *(226)* compared Pt/Al-SBA-15 and Pt/SAPO-11 catalysts for the hydroisomerization of FTS waxes. They observed a higher isomeric paraffin yield for the Pt/Al-SBA-15 catalyst, which they ascribed to higher acidity of Pt/Al-SBA-15 relative to Pt-SAPO-11, which would be in line with the results reported by Seo *et al.* *(225)*. At higher temperature (>325 °C), the liquid product yield for the SBA-15 catalyst dropped, because of the higher cracking activity of this material. Increasing the pressure to 80 bar and lowering the contact time improved the yield of isoparaffins *(226)*.

A special application is the combination of FTS and HC function in one catalyst system. Sartipi *et al.* *(227)* used a mesoporous ZSM-5 as the support for a cobalt FTS catalyst. The authors observed a deviation from the normal Anderson–Schulz–Flory (ASF) product distribution in FTS for cobalt supported on ZSM-5 (both for mesoporous and normal ZSM-5), which leads to improved gasoline range product yield. The mesoporosity in the ZSM-5 is required to provide sufficient surface area to keep the cobalt dispersion high. The strong interaction between cobalt and the zeolite, however, also leads to relatively high methane production *(227)*. Xing *et al.* followed a similar idea and used a hierarchical Y zeolite as support for a cobalt FT catalyst. The authors were able to tune the selectivity of the FT catalyst by tuning the dealumination procedure of the hierarchical zeolite *(228)*. Kim *et al.* reported on the use of hierarchical MFI nanosponges as supports for cobalt FTS catalysts; the obtained materials show increased branching in the gasoline product range, a result of the hydroisomerization reactions in the zeolite nanoparticles *(229)*.

3.1.4 Aromatics Reforming Processes

The standard catalyst for reforming, which increases the value of light naphtha (the C_6–C_7 stream) by conversion to high octane aromatics and H_2, is (rhenium-) promoted platinum supported on chlorinated alumina *(230)*. Several zeolite-based catalysts have been described in the literature, most notably Pt/K/Ba–zeolite L, the catalyst used in Chevron's Aromax[SM] process *(230)*.

Bernard *(231)* was the first to report the Pt/K-L catalyst; he compared a number of different platinum-loaded zeolites (K-L, Na-Y, Na-X, Na-Ω, Na-MOR) with Pt/chlorinated Al_2O_3 and found that Pt/K-L had the highest benzene selectivity. He inferred that the selectivity is not related to the nature of the alkali ions in the zeolites, since zeolite K-Y performed

worse than zeolite Na-Y. The benzene selectivity of the Pt/zeolite L was 80%, whereas it was only 49% for the conventional catalysts. The author concluded that the mechanism cannot be truly bifunctional, as described below.

The Aromax process was developed because the conventional reforming catalysts showed poor selectivity particularly in the conversion of light naphtha to aromatic molecules with high octane number, thus more or less creating an "orphan stream": the C_6–C_7 stream is on the high end of the applicability range of isomerization, and on the low end of the applicability range of reforming, and neither process is effective for these molecules (230). This observation, together with the exceptional benzene selectivity of the Pt/Ba/K-L catalyst, implies that the mechanism for reforming on the Pt/Ba/K-L catalyst must be different from the normal reforming mechanism. The normal bifunctional reforming mechanism observed for hexane on Pt/Re-chlorinated Al_2O_3 displays an intricate network of (de)hydrogenation steps and acid-catalyzed rearrangement steps (Figure 23). The key sequence in the mechanism is the ring closure, which proceeds through the formation of a methylcyclopentene structure (i.e., through a secondary carbenium ion).

The poor selectivity of the conventional catalysts for the isomerization of light naphtha then must have its origin in the relative rates of cracking and aromatization, both of which are acid catalyzed. In contrast, the Aromax catalyst effectively closes directly to six-carbon atom rings (which might imply, as Bernard suggested (231), that the ring closure is not Brønsted acid catalyzed), as illustrated by the high selectivity in converting six-membered carbon chains compared to five-membered chains (230). The ring closure to five-carbon atom rings can also occur, but the reverse reaction, methylcyclopentane (MCP) ring opening to hexane, is much faster (Figure 24). Since the acidity of the zeolitic catalyst is moderated by the potassium and barium ions, cracking reactions are not as prominent.

Lane et al. (232) have offered two possible explanations for the good performance of the Pt/Ba/K-L catalyst: the geometry of the support or the basicity of the support and its (electronic) effect on platinum. Derouane and Vanderveken (233) suggested a preorganization of the hexane in the pore system of zeolite L, leading to the formation of a pseudo-cycle (an unclosed ring confined in the zeolite pore). The hexane must then adsorb in terminal configuration on the platinum clusters, that is, via its C_1 atom. As Lane et al. note, the 1D pore structure of zeolite L is apparently ideal for the cyclization
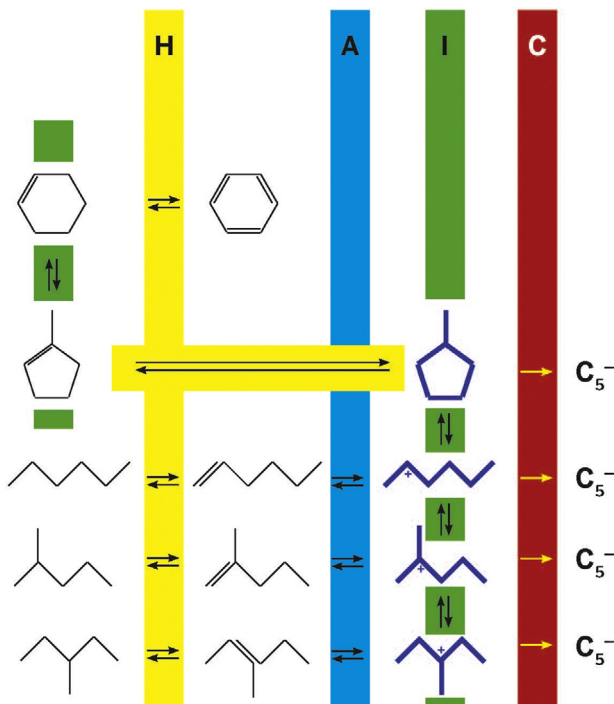
Figure 23 Normal bifunctional reforming mechanism for hexane. The reaction starts with hexane, which is dehydrogenated at the hydrogenation function (H) and subsequently is reacted to a carbenium ion on the acid function (A). This molecule can isomerize to a branched alkane (I) and can then either crack (C) or transfer hydrogen (A) followed by hydrogenation (H). Alternatively, the initial isomerization can lead to ring closure to give MCP, which can isomerize and be further dehydrogenated to benzene. Carbenium ions are represented in bold.

via the C_1 and the C_6 carbon atoms. The ratio of 1–6 ring closure over 1–5 ring closure is two times higher on Pt/K–L than on Pt/K–Y, and turnover rates are 10 times higher on Pt/K–L than on Pt/K–Y (232). Both Derouane and Vanderveken (233) and Lane et al. (232) performed modeling experiments showing the pseudo–cycle prearrangement of hexane. The pseudo–cycle can become a metallocycle by additional adsorption of the C_6-terminus, and this metallocycle can then be transformed into the C_6-ring. Tauster and Steger (234) supported this "molecular die" or "confinement" mechanism. However, in later years, Davis and Derouane (235) showed that an activity and a selectivity very similar to that of the Pt/Ba,K–L system can be observed on an amorphous Pt/Mg(Al)O system, which might suggest some relevance of the basicity as well. Vaarkamp et al. (236) investigated the platinum
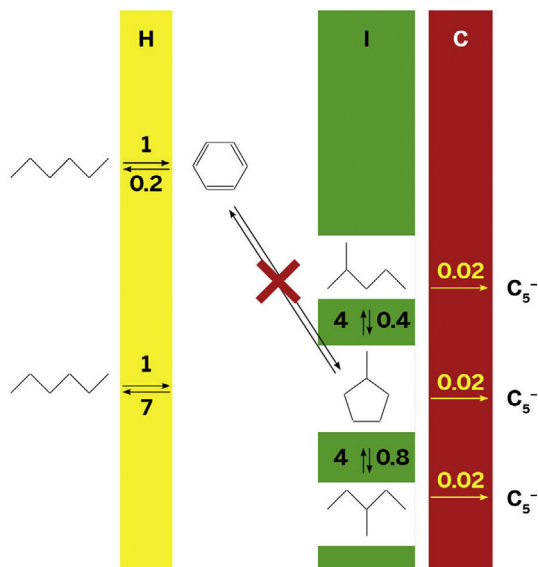
Figure 24 The reforming mechanism for hexane on zeolite Pt/K,Ba-L. In contrast to the route in Figure 23, there is effectively no isomerization route from hexane and MCP to benzene (the reaction of MCP back to hexane is too fast), but rather a direct route. The numbers indicate the relative reaction rates. *Based on Ref. (232).*

dispersion with EXAFS and TEM and noted that the Pt/Ba,K–L system is very structurally uniform and shows very high dispersion, with platinum clusters of 5–6 atoms (although these clusters grow in size upon reduction at increasing temperature *(237)*), and no platinum located outside the zeolite crystals. They also observed barium ions in close proximity to the platinum cluster. In a later investigation, Vaarkamp *et al. (238)* used X-ray absorption spectroscopy (XAS) to demonstrate the electronic effect of the support on the platinum. The authors reported that on acidic supports (Pt/γ-Al$_2$O$_3$, Pt/H–L), the platinum is more electron deficient than on neutral supports (Pt/K–L). The acidity of the support or the promoter atoms therefore influences the Pt d-band density of states and in turn the catalytic behavior in hydrogenation and dehydrogenation reactions.

Philippou *et al. (239)* described the use of zeolite ETS-10 as a possible candidate and, in line with Vaarkamp *et al. (238)*, pointed to the basicity as the main explanation for good performance. Chevron published patents on Pt/Cs-beta and large pore Pt/borosilicates (beta, SSZ-24, SSZ-31, and SSZ-33); it is not clear whether these catalysts were commercialized *(240,241)*.

3.1.5 Isomerization Processes

Isomerization increases the value of short–chain alkanes. Butane is isomerized to isobutane, which can be used in isoparaffin–olefin alkylation, or dehydrogenated to isobutene, a raw material for butyl rubber and for the gasoline additive methyl tertiary butyl ether (MTBE). Pentanes and hexanes in light straight run naphtha can be isomerized to increase octane numbers. Longer chain hydrocarbons are hydroisomerized to improve the cold flow properties, as described in Section 3.1.3 *(44,218)*.

(Hydro)Isomerization requires bifunctional catalysts. The initial steps in the mechanism are similar to those observed in HC, but clearly the final step (cracking) must be avoided, implying that a careful balance needs to be struck between the acid function and the (de)hydrogenation function. The smaller molecules are not easily cracked and can typically tolerate catalysts with higher acid strength, which in turn allow for lower operating temperatures and higher product octane numbers *(242)*. Already before 1940, aluminum halide catalysts were used in the isomerization of pentane and butane *(243)*.

Commercial catalysts for light paraffin isomerization can be divided into three classes, based on their operating temperature. Low-temperature processes rely on Pt/chlorinated alumina (120–180 °C) or Pt/sulfated zirconia (130–180 °C). Zeolite-based processes are operated at medium temperatures (250–300 °C), and fluorinated alumina is used in high-temperature processes (360–440 °C) *(244)*. Catalyst suppliers include UOP, Albemarle, and Clariant. Various authors describe the isomerization of butanes on Pt–H-mordenite (recent work includes *(245,246)*), or silicoaluminophosphates such as SAPO-11 and SAPO-5 *(247)*.

For C_5/C_6 isomerization, Pt/sulfated zirconia can be used instead of the Pt/chlorinated alumina catalysts. These catalysts are less active, but have the advantage of not requiring halide injection to retain catalyst activity. Zeolite catalysts again include Pt/mordenite *(248)* and various silicoaluminophosphates *(247)*. Shell's Hysomer process, developed in the 1960s for the isomerization of C_5/C_6 fractions, for instance, is based on a Pt/mordenite catalyst *(44)*. The process is typically combined with UOP's IsoSiv process, in which an LTA zeolite is used to separate the unconverted n-paraffins from the product for recycle to the isomerization unit. The combined process is called TIP™ (total isomerization process) *(249)* (see Figure 25).

The mechanism for isomerization of larger alkanes is fairly well established and involves the formation of alkylated cyclopropane rings,
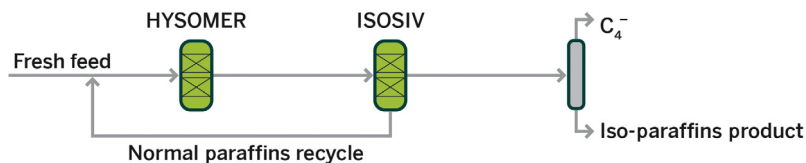
Figure 25 Schematic of the total isomerization process (TIP), a combination of the Shell Hysomer process for isomerization of C_5/C_6 fractions, and the UOP IsoSiv process, which separates unconverted *n*-paraffins from the product. *Based on Ref.* (250).

which open to a secondary carbenium ion of the isomer (251,252). For *n*-butane, the mechanism is subject to debate in the literature. The reason is that the methylcyclopropane ring cannot open without forming a primary carbenium ion, which would be energetically very unfavorable (253). Most authors therefore assume that a bimolecular mechanism should occur. However, this mechanism would lead to the formation of C_3 and C_5 species, which lower the selectivity of the process. Wulfers and Jentoft (246) have provided arguments for a monomolecular mechanism, based on isotope distributions in experiments with $1,4-{}^{13}C_2-n$-butane, and reaction orders for the different products. They concluded that a monomolecular mechanism is a relevant route for butane isomerization on Pt–H–mordenite catalysts, particularly at low butene concentrations. At higher butene concentrations, the bimolecular route, which involves alkylation of the adsorbed C_4-carbenium ion with butene, is more prevalent. Butane does not isomerize on H-mordenite in the absence of butenes or, more generally, alkenes. According to this scenario, the role of platinum and H_2 in the process is to keep the butene concentration low (Figure 26).

The monomolecular mechanism is possible because, contrary to liquid acids, free carbenium ions do not exist in zeolites, and alkoxide species are formed upon the ring opening of the cyclopropane transition state, rather than a primary carbenium ion. Boronat *et al.* (254,255) provide theoretical support for this explanation.

Butene can be isomerized on FER, which is used in processes by Shell and Texaco (44). van Donk *et al.* investigated the mechanism of skeletal isomerization of butene by IR spectroscopy (256) and concluded that a small number of Brønsted sites are responsible for the activity of the catalyst. In the initial stages, rapid deactivation occurs and a large portion of the Brønsted sites are blocked. The remaining sites, which may be located in the 10-MRs of the FER structure, display a high selectivity toward butene isomerization to isobutene, as subsequent measurements with a tapered element oscillating
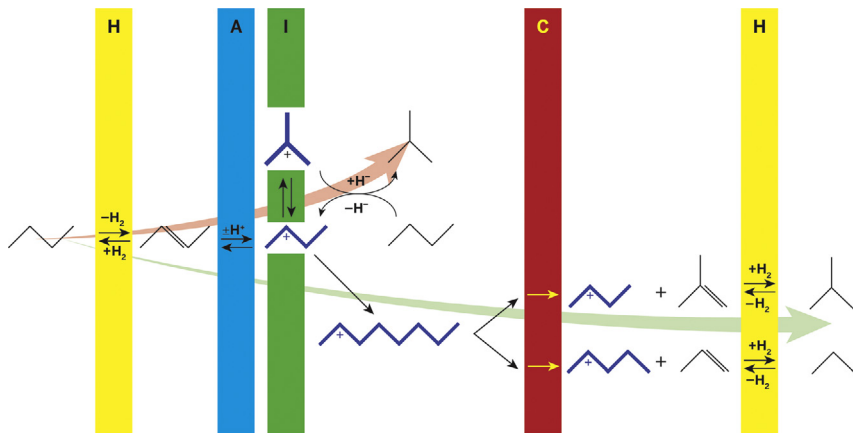
Figure 26 The monomolecular and bimolecular routes for butane isomerization. The monomolecular route (top) exclusively leads to C_4 products. The bimolecular route can also produce fragments with deviating carbon numbers. Butane is first dehydrogenated (H) and reacts on the acid site (A) to form a carbenium ion (bold). This carbenium ion then isomerizes (I) monomolecularly, or oligomerizes and isomerizes, and subsequently cracks (C) in the later stages. Carbenium ions in bold are stabilized by the zeolite. *Based on Ref.* (246).

microbalance (TEOM) indicated (257). The selectivity increase is accompanied by a loss in overall activity, as the nonselective sites are blocked. Jo *et al.* recently investigated the same reaction and concluded that a monomolecular route is responsible for the selective isomerization of butene in ferrierite (258). The authors also introduced a medium–pore size zeolite, H-HPM-1 (STW), which they report to be more effective than FER. The catalyst is active and selective from the onset of the reaction and does not deactivate rapidly. The weak acidity and low acid density of the new material are claimed to be responsible for the good performance.

3.1.6 Dimerization and Oligomerization Processes

Low-value light olefins can be oligomerized to valuable gasoline components (polymer gasoline or polygas) by a variety of acid-catalyzed reactions. The alkylation of isoparaffins with lower olefins will be treated separately in the next section.

Oligomerization processes historically have relied on supported phosphoric acid (SPA) catalysts, for example, with Kieselguhr silica as the support. An example of a process with this catalyst technology is UOP's CatPoly process. A number of zeolite-based alternatives have been developed (259).

ExxonMobil's olefin-to-gasoline process (MOG™) relies on ZSM–5 to convert olefins by a number of consecutive reactions including acid-catalyzed oligomerization, aromatization, hydrogen transfer, and isomerization. The products can have very good properties depending on the process conditions and the feedstock. The MOG process consists of a combination of a dense-fluid bed reactor and a regenerator reactor, not unlike the FCC process, though the reaction chemistry is different (44).

Improvements to the MOG process are the EMOGAS™ (ExxonMobil olefin-to-gasoline) and ODG™ (olefins to diesel and gasoline) processes developed by ExxonMobil. These processes allow for a wider range of olefins to be used and offer greater product flexibility between gasoline, kerosine, and diesel. It is believed that ZSM–5 is no longer used as the catalyst in the EMOGAS process, but rather MFS or TON-based catalysts (260).

Shell has a similar process based on Ni/mordenite, called SPGK (Shell PolyGasoline and Kero). This process is carried out at pressures of 10–50 bar and temperatures of 200–280 °C and converts C_2 to C_5 olefins to gasoline, kerosine (jet fuel), and middle distillate fractions. The product contains mostly iso-olefins and only a small amount of aromatics, regardless of the role of aromatization in the mechanism (261,262).

Finiels et al. (263) recently reviewed the literature that focuses on the oligomerization of ethylene to longer olefins on nickel-containing zeolites. Other non-zeolite-based catalysts for this reaction are known, but we will not treat them in the context of this review, which focuses on zeolite-based catalysts. The application has been known since the early 1970s, when Lapidus et al. (264) described the use of nickel supported on zeolite Y or mordenite as catalysts for ethylene oligomerization and compared the activity of these catalysts to that of catalysts with amorphous, porous supports (265). Heveling et al. (266) showed that ethylene can be oligomerized to diesel-range molecules on nickel-exchanged zeolite Y. Lallemand et al. tuned the Y zeolites with respect to accessibility and mild acidity and demonstrated positive effects of these alterations on the performance (267). In a subsequent paper (268), the authors reported on the use of nickel–exchanged MCM–36 and MCM–22 for ethylene oligomerization. The microporosity and high acidity of MCM–22 limit its applicability in this process. Hulea and Fajula (269) tested Ni–MCM–41 as a bifunctional catalyst for the oligomerization. They concluded that both acid sites and metal sites are required, whereby lower-acidity samples retain their high activity better. The ordered mesoporosity of the MCM–41 was found to be beneficial. Dutta et al. (270) combined the conversion of methanol to olefins with olefin oligomerization; they employed heteropolyacids for the first step, and

various (in liquid phase) alkylaluminum-based catalysts for the second step. In the vapor phase, they also tested zeolites and report H-ZSM-5 as the preferred catalyst within their set. The selectivity toward higher olefins was observed to be lower in the gas–phase process than in the liquid–phase process. In their review, Finiels *et al. (263)* conclude that nickel-exchanged porous materials are the preferred catalysts for the oligomerization of ethylene. Isolated ionic species like Ni^+ and dehydrated Ni^{2+} sites are very likely the active species in these catalysts. Mesoporous catalysts show the best results both in terms of TOF and productivity. The authors emphasize that the oligomerization of ethylene on nickel-exchanged zeolites is a very versatile process, because the variation of the zeolite properties such as pore and cage size, acidity distribution, mesoporosity, and nickel site concentration can be used to tune the selectivity toward higher olefins.

3.1.7 Isoparaffin–Olefin Alkylation Processes

The alkylation of relatively low value C_4 and C_5 olefins with C_4 and C_5 isoparaffins to high octane (number) gasoline components is one way refiners increase the volume of useful products from their operations. Alkylation of lower olefins with isoparaffins yields products that are very good gasoline components: the products have high research and motor octane numbers (RON/MON), no aromatics, no volatile olefins, generally contain no nitrogen or sulfur, and have low vapor pressure *(271)* (see Table 5).

Table 5 Characteristics of Gasoline Components from Various Gasoline Production Processes *(272,273)*

Specification for Euro Super 95 (Euro V)

Aromatics	Max. 35 vol.% (benzene max. 1 vol.%)			
Olefins	Max. 18 vol.%			
Sulfur	Max. 10 ppm			
RON/MON	Min. 95/85			
	Alkylate	**FCC**	**Reformate**	**Polygas**
Aromatics (wt.%)	0	29	63	0
Olefins (wt.%)	0	29	1	95
Sulfur (ppm)	≈ 0	756	≈ 0	≈ 0
MON	92–94	81	87	82
RON	94–98	92	98	94

Alkylation is a process that has been performed in the refinery for many decades and accounts for more than 10% of the gasoline pool products *(274)*. The conventional processes were based on HF or H_2SO_4 as catalysts. Although containment and other safety measures are usually in place to prevent major problems in case of process upsets, the risks of these processes either in the direct process or in the transport (fresh/spent H_2SO_4 transport can amount to 200–400 truckloads per month at 1000 t per day alkylate capacity) related to the process are obvious. The search for a safe solid acid-based process has therefore already been ongoing for decades *(271,275)*. Increasingly tight legislation may force refiners to find alternatives for HF-catalyzed alkylation *(276)*.

The benefits of a zeolite-based true solid acid alkylation process are obvious (see Table 6): the spent catalyst production is approximately 10 times lower than in the case of HF (and 1000 times less than in the case of H_2SO_4) *(279)*, no acid removal from the product and hence no wastewater treatment is needed, no product is lost with the liquid acid, there are no corrosion issues, much lower maintenance costs; and moreover, the process is inherently safe, and no special precautions for the refinery and adjacent neighborhoods are needed *(279)*.

Of course, the alkylation equilibrium is the same as the cracking equilibrium, which is why conceptually the same catalysts can be used, albeit at much lower temperatures. The difficulties in creating a successful process arise from the rapid deactivation of the catalyst as a result of coke deposition.

In the reaction mechanism (Figure 27), the desired alkylation of isobutane with olefins competes with the oligomerization or polymerization of the olefins, which leads to coke formation. The undesired reaction is second order in olefin concentration, whereas the desired reaction is first order.

The reaction orders dictate the high isobutane/olefin ratios that are used in all processes. Yet the formation of oligomers is the essence of the

Table 6 Comparison of Liquid Acid-Catalyzed and Solid Acid (i.e., Zeolite)-Catalyzed Alkylation Processes *(277,278)*

|	H_2SO_4	HF	Zeolite
Catalyst	Liquid	Gas	Solid
Isobutane/alkene feed ratio	8–10	12–15	8–10
Temperature (°C)	4–10	32–38	50–90
Catalyst use per ton alkylate (kg)	78–180	1.15	0.14
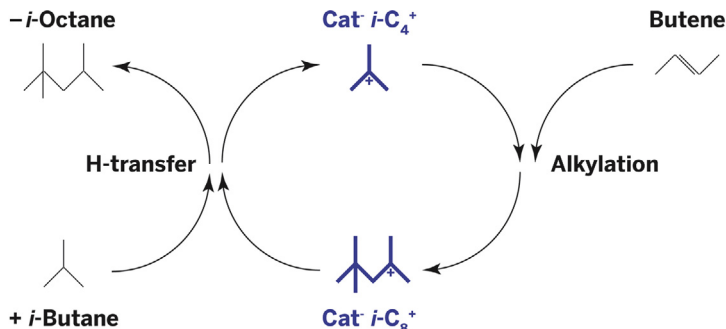
Figure 27 Mechanism of isobutane–butene alkylation *(279,280)*.

alkylation process, and a careful balance needs to be struck in catalyst and process design to allow for a commercially successful process. It should be noted that the olefins used are rarely pure *n*-butenes, but rather mixtures of 1-butene, 2-butene, and isobutene, sometimes also pentenes, branched butenes and pentenes (although they can also be converted to MTBE and tertiary amyl–methyl ether (TAME)), and even propylene is applied *(276)*.

The development of a solid acid alkylation process started at Sun Oil in the 1970s. The researchers concluded that zeolites are effective catalysts for this type of alkylation, but could not solve the rapid deactivation. Typically, the catalysts lasted for a couple of hours *(281)*. In later years, Catalytica with Conoco and Neste developed a process with BF_3/Al_2O_3 as the catalyst *(282)*. Haldor Topsoe developed a solid catalyst containing immobilized triflic acid (i.e., trifluoromethanesulfonic acid) *(283,284)*. Shell worked on a process based on zeolite beta *(285)*, and Lurgi and the group of Lercher collaborated on a process presumably operating with zeolite Y (Lurgi Eurofuel) *(286)*. Another solid acid process, called ExSact, is presumably based on zeolite catalysts and was developed by Exelus *(287)*. The UOP Alkylene process, likely based on alumina–supported $AlCl_3$ promoted with platinum, is another solid acid alkylation process, but the catalyst is not zeolite based *(288,289)*. To the best of our knowledge, for none of these processes, a commercial license has been sold that has resulted in a process in operation.

The only true halogen-free solid acid alkylation process that did reach commercial maturity is Albemarle and Lummus's AlkyClean® process *(290)*. Fundamental catalyst developments for this process started in the mid-1980s in the Amsterdam Research facilities of Akzo Chemicals' Catalyst Division (later Albemarle Catalysts Company BV). For the development

of the process, cooperation with Lummus was initiated in 1996, and in 2001, Neste Oil joined the team for a technology demonstration unit at their Porvoo refinery. This three-reactor demo unit (capacity roughly 4 barrels per day) successfully ran for a number of years and demonstrated the reliability and robustness of the process.

The AlkyClean process is based on a proprietary noble metal–promoted zeolite catalyst *(292,293)*. Problems through rapid deactivation of the catalyst are circumvented by a system of reactors that can be switched between different modes. The design is illustrated in Figure 28. In the continuously switched system, one reactor is in alkylation mode, and one reactor is in mild regeneration mode. A third reactor (not shown) allows for an occasional more severe regeneration at 250 °C in H_2 atmosphere. In this way, a continuous process is made possible, and the catalyst lifetime is extended from months to years, far exceeding the few hours in the original Sun Oil process *(281)*.

A commercial 100,000 t/a new AlkyClean alkylate unit was announced by Shandong Wonfull Petrochemical Group Co. in China *(294)*.

3.2 Petrochemicals Manufacturing

3.2.1 para-*Xylene Production*

para-Xylene (*p*-xylene) is an intermediate in the production of terephthalic acid and dimethylterephthalate, which are in turn intermediates for the production of polyethylene terephthalate (PET) polyester. *p*-Xylene is present in certain refinery streams and can be extracted by (shape)-selective
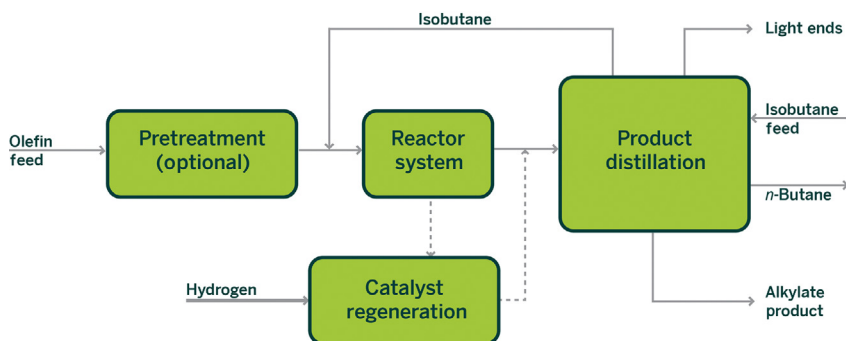
Figure 28 The AlkyClean process design. Olefin feedstock (pretreated depending on contaminant level) enters the reactor with isobutane recycle. The reactants are in the liquid state at temperatures of 50–90 °C. Multiple reactors are used to allow for continuous alkylate production, while reactors cycle between alkylation and rejuvenation *(279,291)*.

adsorption. The other xylene isomers are isomerized on ZSM-5 catalysts *(218)*. This zeolite exhibits excellent shape selectivity for this reaction. The xylene isomer mixture may contain high concentrations of ethylbenzene, which can be removed by hydroisomerization (i.e., conversion to xylenes) or by dealkylation to benzene and ethylene.

p-Xylene can also be produced by transalkylation of toluene with C_9^+-aromatics or by alkylation of toluene with methanol. A variety of zeolites are employed in these reactions, the former is conducted using zeolite mordenite, the latter using catalysts on the basis of ZSM-5, lanthanum-modified MWW, SAPO-11, MOR, or FAU. A final option is to produce *p*-xylene from the disproportionation of toluene. For this transalkylation process, ZSM-5 seems to be an obvious catalyst choice *(22)*.

UOP provides a range of processes that can be combined in a complex to make *p*-xylene: for example, PX-Plus™-XP, based on toluene disproportionation (TDP) (PX-Plus) combined with a *p*-xylene crystallization step developed by Badger/Niro; Isomar™, based on C_8-isomerization *(295)*; and the Parex™ process, a version of the Sorbex process, for extraction of *p*-xylene from a mixed C_8-stream. Axens provides an array of processes similar to the UOP range called Paramax™ *(296)*.

3.2.2 Processes for the Alkylation of Aromatics

3.2.2.1 Ethylbenzene Production

Ethylbenzene (EB) is the key intermediate in the production of styrene, which is a monomer produced in very large volumes. Ethylbenzene is obtained through acid-catalyzed alkylation of benzene with ethylene *(297)*. Original catalysts were Friedel–Crafts-type catalysts $AlCl_3$–HCl and BF_3/Al_2O_3, and silica-SPA. The alkylation of benzene with ethylene produces ethylbenzene as the primary product, but subsequent alkylation of EB produces a variety of polyethylbenzenes. These have to be transalkylated with benzene after recycle. In commercial operation, the benzene-to-ethylene ratio is kept high to avoid polyalkylation and polymerization of ethylene as far as possible *(297,298)*. The transalkylation step is an important feature in all commercial EB production processes. The supported catalysts originally proposed (BF_3/Al_2O_3 and SPA) are not active for transalkylation and therefore did not play a major role in commercial application *(298)*.

Zeolites were applied in research on new EB processes from the mid-1960s, but a commercial process based on zeolites did not mature until 1980. The so-called Mobil–Badger process relied on zeolite ZSM-5-based

catalysts; this gas–phase process was conducted at temperatures of 320–420 °C *(297,299)*. The process allowed for recycling of polyalkylated benzene and transalkylation in the main reactor. A third-generation process had a second reactor dedicated to transalkylation *(298)*. Liquid–phase processes, operating at lower temperature, were developed in the 1980s and commercialized in the early 1990s. Lummus Crest/Unocal/UOP were the first to introduce a zeolite-catalyzed process, based on zeolite Y *(297,298)*. Various researchers worked on improvements, and it was soon reported that zeolite beta gave better performance than zeolite Y *(298)*. MCM-22, however, was the catalyst of choice for the Mobil–Raytheon EBMax™ process in 1995 *(297,298,300)*. MCM-22, a 10-MR zeolite structure, unexpectedly shows very good catalytic performance, explained by the characteristics of its pore structure *(22)*.

An improved version of the Lummus/UOP process called EBOne comprises a two-reactor system in which the initial alkylation catalyst is likely zeolite beta *(297,298)*. CDTech introduced a process based on catalytic distillation, in which the catalyst is introduced in a distillation column. Although the production of polyalkylated benzene can be suppressed by this mode of operation, a transalkylation step is still required. The alkylation catalyst in this process is very likely also zeolite beta *(298)*. Perego and Ingallini reported that in 2002, approximately 75% of the EB in the world was produced by zeolite-based processes, indicating that the remaining amount is still obtained by using Friedel–Crafts catalysts *(298)*.

3.2.2.2 Cumene Production

Cumene has been used as a blending component in gasoline during the Second World War. These days, it is mostly an intermediate in the production of phenol and acetone *(297,298)*.

The first commercial processes employed sulfuric acid as the catalyst, which was fairly quickly replaced by SPA. This technology was first introduced in the 1940s and is still in use as a main production route today. Similar to the production of EB, polyalkylation is an issue and SPA does not catalyze transalkylation. Therefore, again, the ratio of benzene to olefin is kept high.

Unlike EB, cumene cannot be synthesized by alkylation of benzene (with propylene instead of ethylene) using zeolite ZSM-5. One of the problems proved to be isomerization of the product to *n*-propylbenzene; another problem was the rapid deactivation of the catalyst.

The Dow Chemical Company solved this problem by introducing a severely dealuminated mordenite catalyst, which was claimed to have a 3D structure that allows molecular traffic control of benzene and propylene (3DDM) *(161)*. The Mobil–Raytheon process for cumene is very likely based on the same principles as their EB process, which implies MCM-22 may be the catalyst. CDTech also commercialized a catalytic distillation process for cumene, likely employing zeolite Y. UOP and Eni developed a process which is likely relying on zeolite beta *(298)*. Degnan *et al.* have reported that UOP was working on an improved catalyst containing MgAPSO-31, which would reportedly eliminate the formation of *n*-propylbenzene *(297)*.

3.2.2.3 Linear Alkyl Benzene Production

Linear alkyl benzene (LAB) is a raw material for making the detergent intermediate LAB sulfonate *(298)*. According to Perego and Ingallina, the process for making LABs comprises the alkylation of benzene with linear internal olefins, and most of the installed capacity is probably based on HF catalysts *(298)*. According to the authors, solid acid catalysts have been tried, but apparently only a UOP/CEPSA process (Detal™), in which a fluorinated silica–alumina catalyst is employed, made it to a commercial stage. The application of zeolites for this application has not yet been successful.

3.3 Bulk and Fine Chemicals Manufacturing

Zeolites are active and selective catalyst materials for the production of organic bulk and fine chemicals, and their use has been continuously increasing over the last few decades. The topological variety, tunability of acidic (and/or basic) sites, and the shape selectivity of zeolite materials are responsible for their increasing popularity in the syntheses of fine chemicals. In this section, some noteworthy organic reactions will be highlighted.

3.3.1 Reactions with Carbonyl Compounds

Among the most important zeolite-catalyzed processes are the reactions with versatile carbonyl compounds, ranging from aromatic functionalization to synthesis of heteroaromatic compounds, and protection of carbonyl groups.

The synthesis of pyridine derivatives from ammonia and aldehydes (Chichibabin pyridine synthesis) can be carried out by using H–ZSM-5 (including its thallium-, lead-, or cobalt-exchanged analogs), H-beta, and H-Y zeolites (Scheme 2(a)) *(301–303)*. However, the most commonly
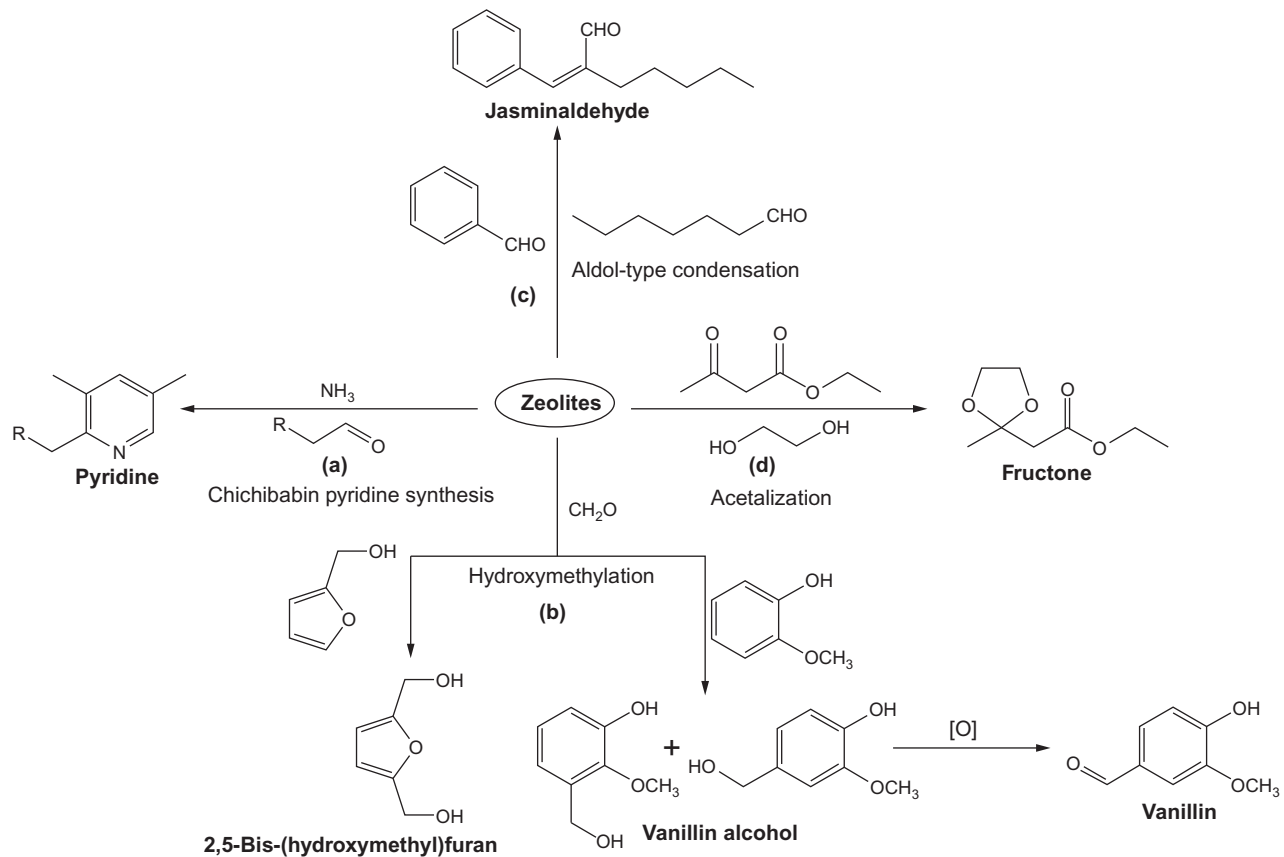
**Scheme 2** Zeolite-catalyzed reactions involving carbonyl compounds.

performed zeolite-catalyzed reaction with a carbonyl compound is the aromatic hydroxymethylation with formaldehyde because it provides a versatile range of fine chemicals (Scheme 2B) *(304)*. Pioneering work on this reaction was reported by Venuto and Landis in 1966, who used zeolite H–Y as a catalyst at a temperature of 180 °C *(305)*. Later, various aromatic molecules were used as substrates for hydroxymethylation, among them toluene, phenol, anisole, benzaldehyde, and acetophenone. Another interesting example in this class of reactions is the hydroxymethylation of guaiacol with H-mordenite as catalyst. The reason is that the product *para*-hydroxymethylguaiacol is the precursor for an important food additive, vanillin (Scheme 2(b)) *(304,306)*. Furfuryl alcohol can be similarly hydroxymethylated with an excess of aqueous formaldehyde to 2,5-bis-(hydroxymethyl)furan at 40 °C by using dealuminated mordenite as a catalyst (Scheme 2(b)) *(307)*. 2,5-Bis-(hydroxymethyl)furan is currently regarded as one of the most important organic intermediates for the production of drugs, crown ethers, polyurethane foams, and other polymers *(304)*.

Zeolites are also considered as potential catalysts for aldol-type condensation reactions. The reaction between benzaldehyde and 1-heptanal, which can be catalyzed by MCM–41 and beta-zeolite, yielded a well-known "natural fragrance" jasminaldehyde (α–pentyl cinnamaldehyde) (Scheme 2(c)) *(308)*. This chemistry was also applied to the acetalization of carbonyl compounds, as it is essential for the protection of reactive carbonyl functionalities during organic and natural product synthesis. Moreover, acetals are renowned for their applications as flavors and fragrances, mainly in the liquor industry. The synthesis of fructone (which is characterized by apple scent) is presented in Scheme 2(d) as an example. Fructone can be easily synthesized by acetalization of ethyl acetoacetate with ethylene glycol using different acid zeolites, for example H–beta, H–Y, and H–ZSM–5 (Scheme 2(d)) *(309)*.

3.3.2 Isomerization Reactions

Similar to the isomerization of xylenes and other aliphatic substrates, the isomerization of α–pinene and α–pinene oxide can be catalyzed by zeolites, and various zeolites are currently being employed (Scheme 3). Both processes are highly important for the fine chemicals industries, as all the isomerized products are high–value substrates (Scheme 3) in the production of various fragrances, cosmetics, and pharmaceuticals.

Traditionally, TiO_2 catalysts are used for the isomerization of α–pinene at atmospheric pressure and a temperature of 200 °C, but very slow

A

B
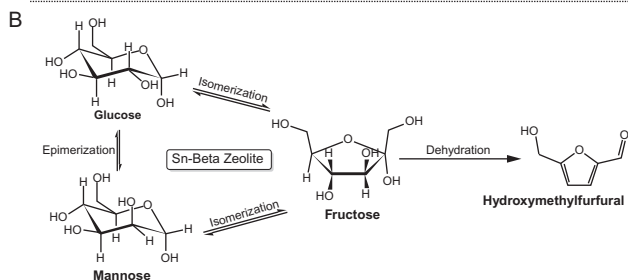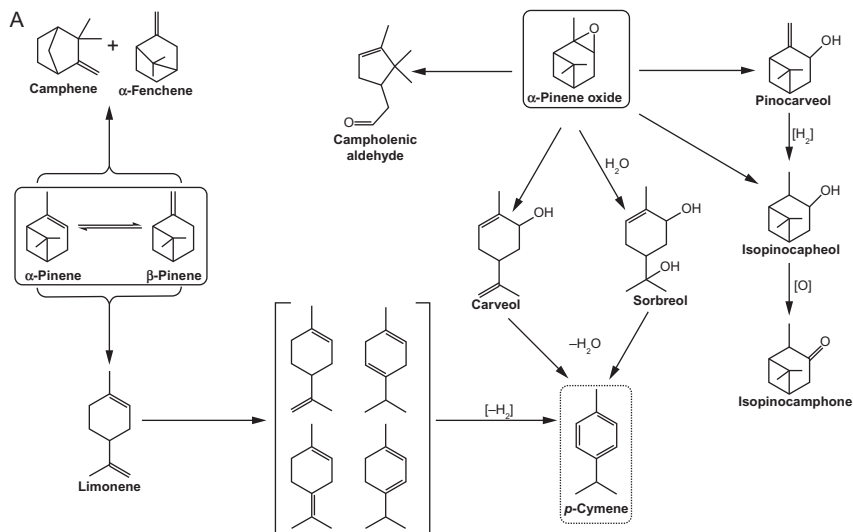
Scheme 3 Zeolite-catalyzed isomerization reactions.

isomerization rates are a concern in this process *(304)*. Among the various isomerization products from α-pinene (as depicted in Scheme 3), camphene is the most desirable product. Camphene is the precursor substrate for camphor, which has several industrial and other applications; there are explosives-related, culinary, and medicinal uses of this compound (Scheme 3) *(310)*. In order to achieve better reactivity at a reasonable isomerization rate, along with higher selectivity, various zeolites have been employed in this process over the years. Usually boron-, titanium-, or vanadium-modified beta-zeolites provide higher camphene selectivity than TiO_2-based traditional catalytic systems at 0 °C in the liquid-phase isomerization of α-pinene *(304,311,312)*. Such modified zeolites (also ZSM-5, mordenite, MCM-41) with a Si/Al ratio of 27–33 are reported to exhibit higher catalytic activity and better selectivity toward the desired

products than TiO_2-based traditional catalytic systems for such isomerization reactions *(304,311)*.

Zinc halides (ZnX_2, X=Cl, Br) are considered to be the *state-of-the-art* catalysts for the isomerization of α-pinene oxide *(313)*. Industrially, campholenic aldehyde is the most important product of the isomerization of α-pinene oxide (Scheme 3A) *(310)*. The campholenic aldehyde is a well-known fine chemical intermediate for the production of a terpenoid with a sandalwood-like smell, which is a crucial component in a variety of fragrances, perfumes, and even pharmaceuticals *(310,313)*. However, the zinc halide-catalyzed isomerization process also suffers from several inherent limitations, including fast catalyst deactivation, low turnover numbers (implying high catalyst loading), and generation of large quantities of waste containing heavy metals *(313)*. To overcome these drawbacks, zeolites are gradually gaining popularity for the isomerization of α-pinene oxide. Among various zeolite catalysts for the isomerization of α-pinene oxide, zeolite USY is well known for its high conversions and selectivity (up to 75%) toward campholenic aldehyde within 24 h at 0 °C using toluene as solvent *(310,314)*. The well-dispersed Lewis acid sites are believed to be the key behind the success of this process. Other zeolites and mesoporous materials, such as zeolite Ti-beta, H-Y, and Zn–MCM-41, are also reported to be effective catalysts for the isomerization of α-pinene oxide *(313,315)*.

Another important class of reactions that can be catalyzed by zeolites is a subcategory of isomerizations, namely carbohydrate isomerization and epimerization *(316–318)*. These types of transformation are key reactions in the health and food industry and rely on enzymes as catalysts. Among these transformations, the isomerization of glucose into fructose constitutes one of the largest biocatalytic processes in the USA *(316)*. This particular transformation is also becoming important in the field of biomass conversion, as it is an intermediate step from biomass to chemicals and fuels. The Lewis–acidic large-pore Sn–beta zeolite was proven to be a very efficient catalyst for the isomerization of glucose to fructose, with high activity and selectivity as reported by Moliner *et al.* *(316)*. The large-pore zeolites are essential for this transformation, as medium-pore zeolites are completely ineffective. Also, basic zeolites may degrade glucose. The strong and non-destructive interaction between the tin and the hydroxyl-/carbonyl-moieties of hexoses is presumably the reason for this catalyst's reactivity (Scheme 3B) *(319)*. The crucial role of tin in this isomerization is obvious from the poor performances of other catalysts of similar type, such as

Ti-beta, Sn–MCM-41, and TS-1 *(316)*. Later, this methodology was extended to synthesize hydroxymethylfurfural (HMF) directly from glucose using a "one-pot" biphasic water/THF reactor system (Scheme 3B) *(317)*. Moreover, Nikolla *et al.*, attempting to synthesize HMF in the "one-pot" fashion, achieved high conversion of glucose by using Sn-beta zeolite and an additional acid catalyst (HCl), in the above-mentioned biphasic reaction mixture *(317)*. The authors proposed that tin atoms act as isolated, Lewis-acidic catalytic centers for the initial isomerization of glucose to fructose *(317)*. The exact role of Sn-beta in the final dehydration step is not yet clear. The robustness of Sn-beta zeolites in these processes opens up a variety of possibilities in carbohydrate chemistry. For instance, Gunter *et al.* reported that Sn-beta is also an efficient catalyst for the selective epimerization of various aldoses (e.g., glucose, xylose, or arabinose) in the presence of an additional inorganic borate salt in aqueous media (Scheme 3B) *(318)*.

3.3.3 Acylation Reactions

Like aromatic alkylation, aromatic acylation also plays a crucial role in chemical industries, as acylated aromatics are versatile intermediates in pharmaceutical, agricultural, fragrance, and fine chemicals industries *(320)*. Inorganic acids (i.e., HF, H_2SO_4, and $AlCl_3$) are traditionally used as catalysts in Friedel–Crafts processes *(320)*. However, these processes have severe inherent limitations, including halide impurities in the aromatic product (contamination by HX where X = Cl or F depending on catalyst), corrosion, toxicity, and waste disposability issues with the used catalyst after the reaction. To overcome these limitations and to improve the selectivity and environmental tolerance, the inorganic Lewis acid catalysts have been increasingly replaced by various zeolites in acylation processes over the last few decades *(304,320)*. Pioneering work in zeolite-catalyzed aromatic acylation chemistry was performed by Venuto and Landis in 1968, who used various faujasites as catalysts *(321)*. Unfortunately, these catalysts suffer from moderate reactivity and poor selectivity. Almost two decades later, in 1986, Chiche *et al.* reported very high *para*-selectivity in the acylation of toluene when using Ce^{3+}-exchanged Na–Y zeolite as catalysts *(322)*. This work by Chiche *et al.* encouraged other researchers to test a wide variety of zeolites for aromatic acylation chemistry using carboxylic acids or their anhydrides or chlorides as acylating agents (Scheme 4). Among them, acetyl chloride and acetic anhydride are emerging as better acylating agents than carboxylic acid, because of their higher reactivity and better *para*-selectivity *(304)*. Among the different zeolites employed for this
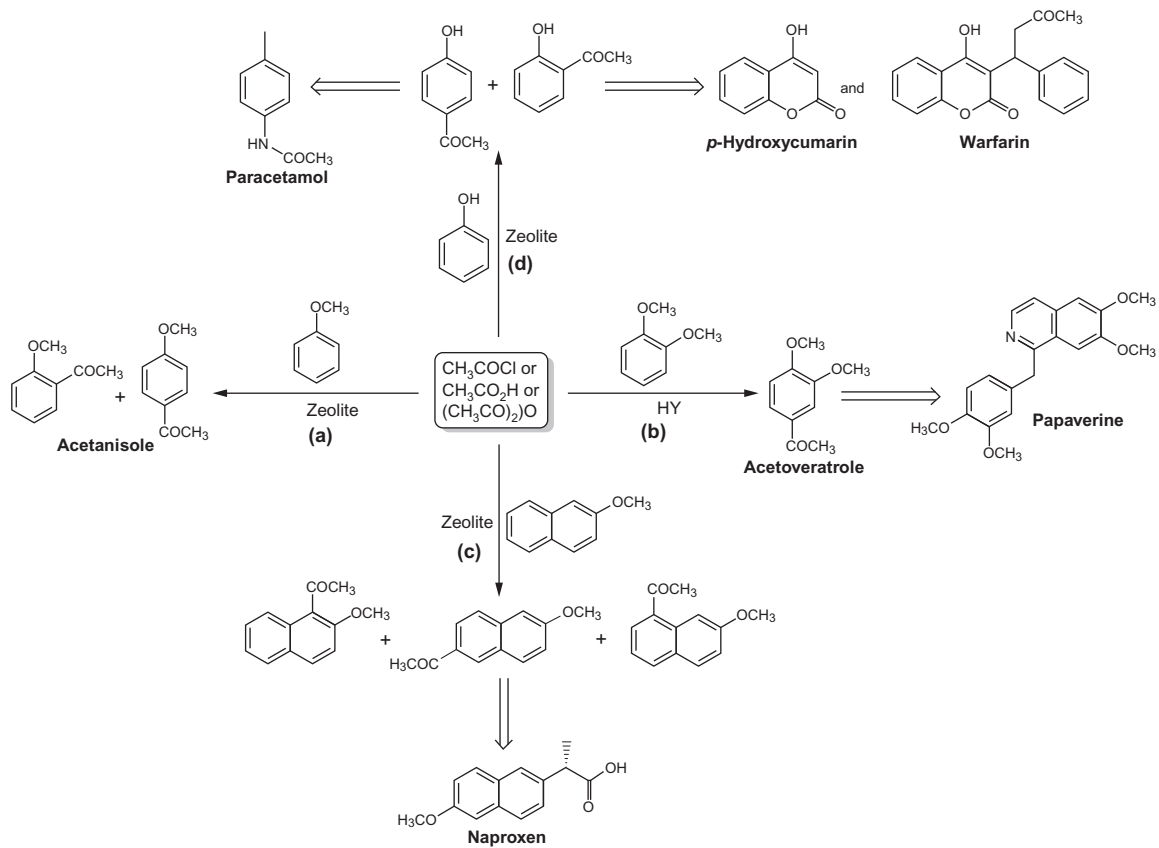
Scheme 4 Zeolite-catalyzed acylation of various aromatics.

catalytic reaction, the order of reactivity was reported as follows: ZSM–5 $\approx$ mordenite $>$ Y $>$ beta *(304)*. Regarding substrates for zeolite–catalyzed aromatic acylation, anisole receives considerable attention because it is an activated aromatic substrate and the desired product, *para*-acetanisole (characterized by a caramel smell), is an important chemical in the food, flavor, and beverage industry (Scheme 4(a)) *(323)*. Remarkable findings in the acylation of anisole were reported by Smith *et al.* in 1998; full conversation with 98% of *para*-selectivity was observed using zeolite H–beta as the catalyst and acetic anhydride as an acylating agent at 100 °C *(324)*. Very similar technology was employed by the Rhône-Poulenc company (now part of Sanofi, Solvay and Bayer); fixed-bed reactors were used for the acylation of anisole and veratrole (1,2-dimethoxybenzene) (Scheme 4(b)) *(304,325)*. In this Rhône-Poulenc process, the zeolite H–FAU was the catalyst, and the acylation of veratrole led to the production of acetoveratrole, which is an intermediate for the synthesis of a very essential antispasmodic drug, papaverine (Scheme 4(b)) *(325)*.

Another thoroughly investigated reaction in this field is the acylation of 2-methoxynaphthalene, because the acylated product, 2-acetyl-6-methoxynaphthalene, is an important intermediate for the production of nonsteroidal anti-inflammatory drugs, such as naproxen (Scheme 4(c)) *(304,323)*. Unlike anisole acylation, the acylation of 2-methoxynaphthalene is usually carried out in the presence of a solvent, because of the higher melting points of 2-methoxynaphthalene and its acylation product. The large size of the reactant and product molecules makes large-pore zeolites (e.g., H-mordenite, ITQ-7, and H-beta) the preferred catalysts *(326)*. Acetic anhydride is proven to be a better acylating agent in this process than acetic acid or acetyl chloride. Owing to the success of such liquid-phase acylations of naphthalenes, various heteroaromatics, that is thiophenes, pyrroles, and furans, have been acylated using zeolite H-beta as a catalyst and acetic anhydride as an acylating agent *(304,313,327)*. P moreover, phenol acylation is another pharmaceutically important reaction (Scheme 4(d)) *(313,328)*. The reason is that *ortho*-hydroxyacetophenol is an important intermediate for the synthesis of a very popular analgesic and antipyretic drug, paracetamol. *para*-Hydroxyacetophenol is a key intermediate for the synthesis of two important anticoagulant drugs, *para*-hydroxycoumarin and warfarin.

3.3.4 Cyclization Reactions

As highlighted above, zeolites have high potential to replace inorganic Lewis acids in organic syntheses. In this context, zeolites have also been found to be
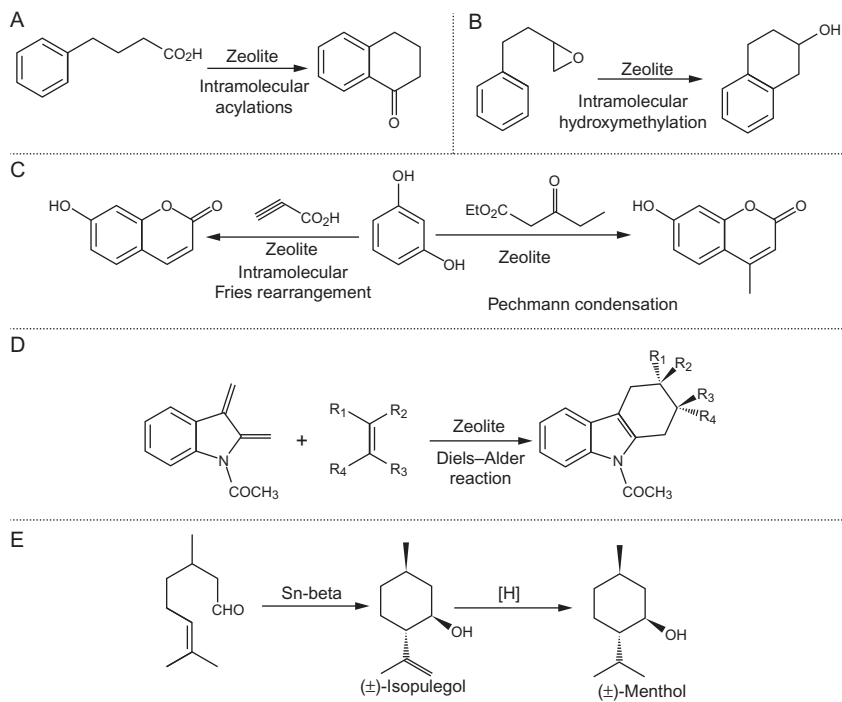
Scheme 5 Zeolite-catalyzed cyclization reactions.

catalytically active for various kinds of cyclization reactions as illustrated in Scheme 5 *(329)*. H–Y and H-beta were successfully applied for intramolecular cycliacylation of 4-phenylbutyric acid to α-tetralone (Scheme 5A) *(329,330)*. Similarly, H-beta and H-mordenite were found to catalyze intramolecular cyclihydroxymethylation of 4-phenyl–1-butene oxide to 1,2,3,4-tetrahydronaphthalen–2-ol (Scheme 5B) *(329,331)*. The synthesis of coumarin derivatives from resorcinol or phenol using ethyl acetoacetate involves (i) intramolecular hydroxyalkylation, (ii) transesterification, and (iii) subsequent dehydration *(329)*. Zeolite H-beta was reported as an effective catalyst for all three steps and potentially can replace sulfuric acid in industry. A reaction of this type with resorcinol and ethyl acetoacetate as reactants (via Pechmann-type condensation) led to a choleretic and antispasmodic drug, hymecromone (Scheme 5C) *(329)*. H-beta is also known to catalyze the reaction between α,β-unsaturated acids to various molecules of the coumarin family, which have uses as perfumes, chemicals, and dyes *(332)*.

The most important zeolite-catalyzed cyclization is probably the Diels–Alder reaction, the reaction between a dienophile (e.g., an olefin) and a

conjugated diene (e.g., 1,3-butadiene or furan) *(333)* as shown in Scheme 5D. The reaction was first described by Otto Paul Hermann Diels and Kurt Alder in 1928. In principle, the Diels–Alder reaction can proceed even without any catalyst, but often Lewis acids (AlCl$_3$ or BF$_3$·OEt$_2$) are employed in a stoichiometric amount to tune the reactivity and selectivity. Since these Lewis acids generate a lot of unnecessary waste, zeolites have been used as catalysts in this process since 1968, particularly with less reactive or thermally unstable reactants. Pioneering contributions were made by Landis of Mobil Oil Corporation, who used zeolite X as a catalyst for the reaction between butadiene and maleic anhydride and obtained an excellent product yield of 93% after 3 h at 60 °C *(334)*. Y zeolite exchanged with either copper, cerium, or zinc, H-beta, and H-Y modified with ZnCl$_2$ are among the most successful zeolite catalysts for the Diels–Alder reaction *(304,335)*. Another important Diels–Alder-type reaction is the reaction shown in Scheme 5E, which involves a double bond and a carbonyl group and results in a new C—C bond (Scheme 5E) *(336)*. The intramolecular cyclization of *rac*-citronellal (which contains both a double bond and a carbonyl group) to (±)-isopulegol is an industrially relevant example of this type of reaction. (±)-Isopulegol is valuable because it can easily be transformed into (±)-menthol through hydrogenation. As was reported by Corma and Renz, Sn-beta is currently the most active catalyst for this transformation, with >98% selectivity toward the four pulegol products at >99% conversion of citronellal and, most notably, 85% diastereoselectivity for (−)-isopulegol with respect to the three other isopulegol products *(337)*.

3.3.5 (Ep)Oxidation Reactions

Epoxides are key intermediates in the fine chemical industry for the production of a variety of alcohols, diols, ketones, ethers, and amino alcohols. Conventionally, organic peracids were used to synthesize these epoxides, but the stoichiometric amounts needed generate huge amounts of waste, which leads to cumbersome purification procedures *(333)*. Hydrogen peroxide (H$_2$O$_2$) as an oxidant in epoxidation reactions is possibly the most environmentally benign choice. Various heterogeneous catalysts have already been reported, including metals supported on, enclosed in, or exchanged into microporous or mesoporous materials *(338)*. The most noteworthy, effective, and well-understood catalyst in this regard is titanium-silicate-1 (TS-1), owing to its shape-selective oxidation properties (Scheme 6A and B) *(338,339)*. The microporous crystalline TS-1 has an
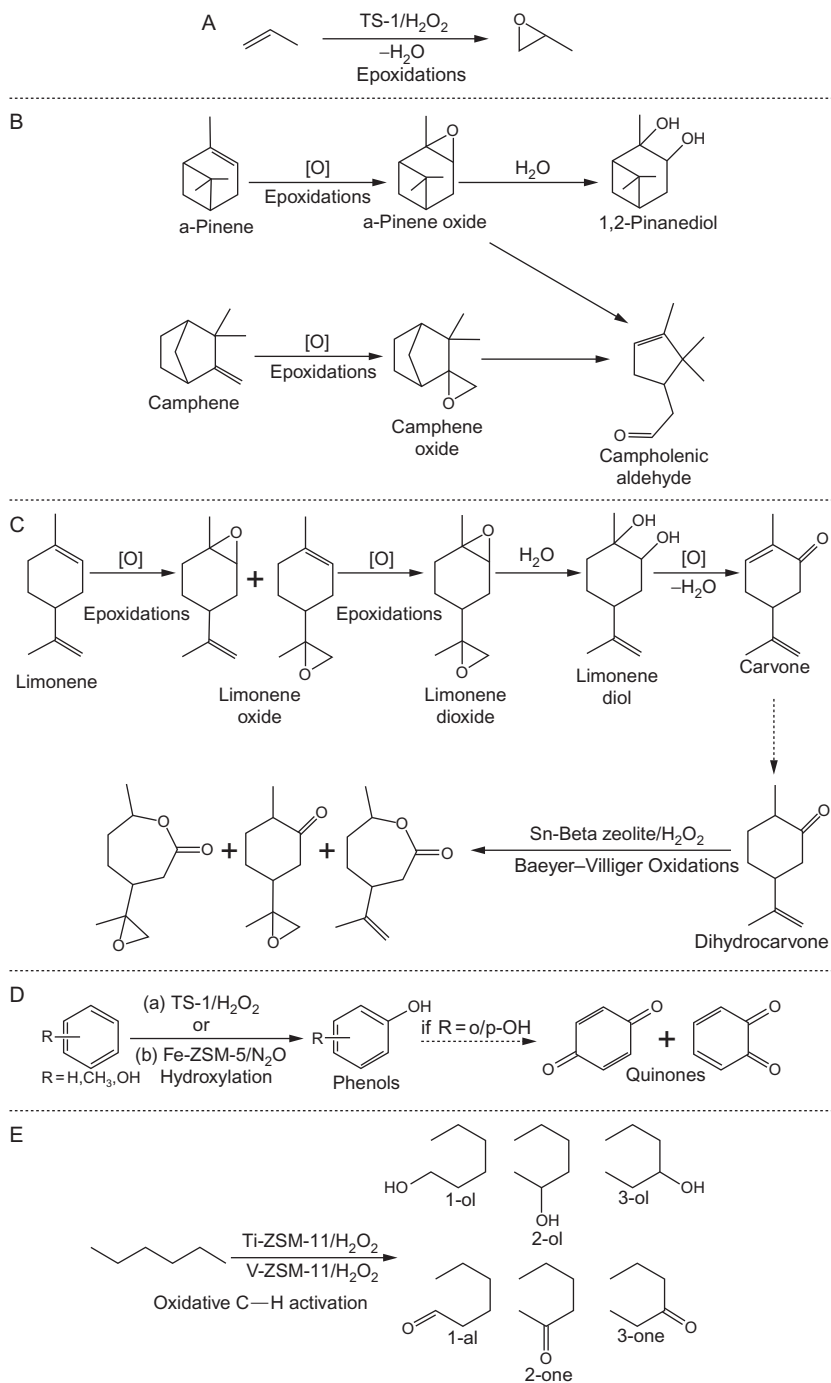
**Scheme 6** Zeolite-catalyzed oxidation reactions.
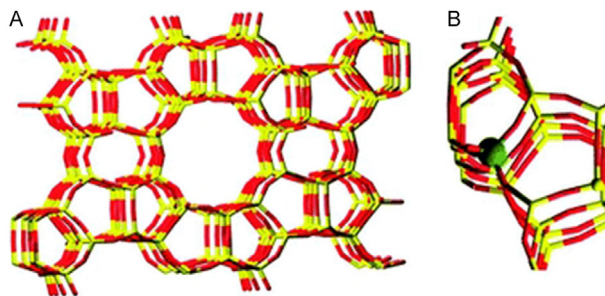
Figure 29 (A) Stick representation of the MFI framework of silicalite-1 viewed along the [010] direction. Silicon atoms are shown in yellow (light gray in the print version), oxygen atoms in red (dark gray in the print version). (B) Schematic representation of Ti(IV) insertion in the MFI framework. The titanium atom is reported in green (gray in the print version). *Reproduced from Ref. (343), published by The Royal Society of Chemistry.*

MFI-type structure and has been employed in industrial slurry–phase oxidation processes for the last three decades. The catalytic centers are isolated titanium sites with tetrahedral coordination within the silicate–1 framework. As shown in Figure 29, Ti^{4+} replaces Si^{4+}. Titanium preferentially occupies one or more specific sites in the silicalite framework; that is, it is not randomly distributed *(340)*. Because of its hydrophobic nature, TS-1 eventually became a useful suitable liquid–phase oxidation catalyst in combination with H_2O_2 (in water solution) for a variety of oxidative transformations of organic molecules in industry. Pertinent examples are presented in the report by Clerici *et al.* on the epoxidation of linear olefins ($\geq C_4$), allyl chloride, and allyl alcohol; TS-1, in combination with H_2O_2 as an oxidant and methanol as a solvent, is highly selective (72–97%) for these epoxidation reactions *(341)*. Such hydrophobicity-dependent reactivity is presumably the explanation for the inactiveness of TS-1 in the presence of molecular oxygen as an oxidant *(342)*. For a detailed account of TS-1-based catalysts for liquid–phase oxidation processes, the reader is referred to a review by Bellussi *et al.* *(339)*.

The epoxidation of propylene is arguably one of the most demanding reactions in chemical industry. Propylene oxide is traditionally produced from propylene by the chlorohydrin process, which unfortunately generates large quantities of waste associated with the brine used. The first propylene oxide plant with a different technology was implemented by EniChem in Italy in 2002; this plant incorporated the catalytic oxidation chemistry of TS-1/H_2O_2 in aqueous methanol *(342)*. The TS-1-mediated epoxidation of propylene is kinetically controlled and proceeds with almost quantitative

yields in a dilute (1–10 wt.%) solution of H_2O_2 under moderate propylene pressure *(342)*. Four years later, BASF and Dow jointly constructed a 300 kt/year propylene oxide plant in Antwerp, Belgium, using a TS-1/H_2O_2-based fixed–bed–type reactor technology *(342)*. However, the deactivation of the TS–1 catalyst during epoxidation is a subject of concern in this process *(344)*. The deactivation was attributed to the blocking of micropores by bulky organic by–products, formed through the dimerization or oligomerization of propylene oxide. Clerici *et al.* investigated the deactivation behavior and found that the yield and product distribution are almost constant with time during the epoxidation of propylene, although the overall catalytic activity decreases *(344)*. This problem can be addressed by regeneration of the catalyst through calcination in air or a solvent wash, or by using a continuous epoxidation process with hydrogen peroxide *(340)*. While the mechanism of epoxidation of propylene to propylene oxide with H_2O_2 on TS-1 is well understood, there is debate about the structures of the active species on the zeolite catalyst (Figure 30). The proposed mechanisms are based on the following active intermediates: (i) Ti-peroxide (η^2-O_2) where both oxygen atoms of the peroxo group bind in a side-on mode
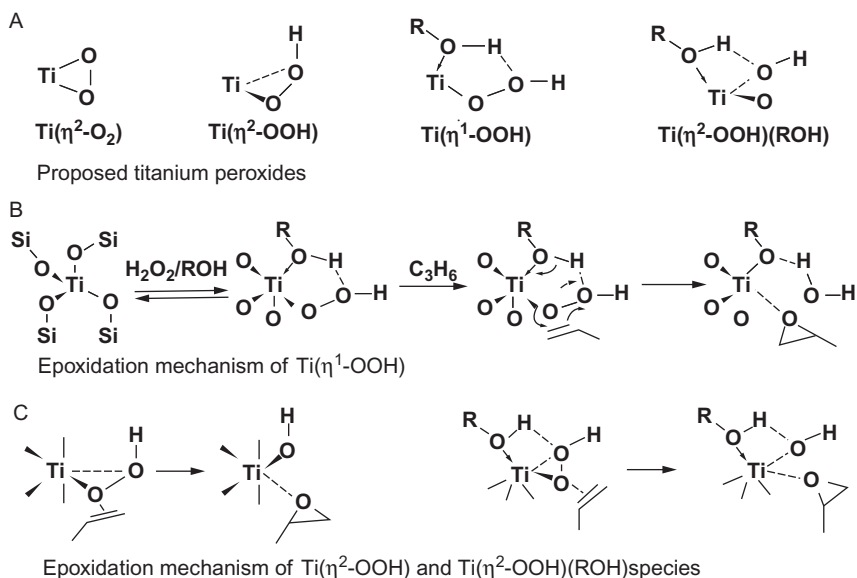
Figure 30 Structure and reactivity of various proposed titanium peroxides in TS-1. (A) Proposed titanium peroxide structures. (B and C) Mechanisms for the epoxidation of propylene formulated with three of the structures presented in (A). *Reproduced with permission from Ref.* (340).

to titanium, (ii) Ti—OOH (either an η^2 or η^1 configuration), and (iii) an η^2-coordinated —OOH group, stabilized by an additional alcohol (as solvent) molecule (Figure 30A, left to right) *(340,345,346)*.

Inspired by the successful use of TS-1 for the epoxidation of propylene, researchers have screened TS-1 for conversion of various other industrially relevant substrates. In addition to TS-1, catalysts such as Ti-beta or titanium incorporated in a mesoporous material (like MCM or SBA) are also well investigated zeotype catalysts for the epoxidation of olefins, whereby environmentally benign hydrogen peroxide or *tert*-butyl hydrogen peroxide is used as an oxidant *(304,338)*. The reports of using molecular oxygen as an oxidant are few and limited to some transition metal (Fe, Co, Mn, Mo)-exchanged Na–Y zeolites *(304,338)*. Three of the most investigated and important substrates (aside from small olefins) for epoxidation using zeotype catalysts are α-pinene, camphene, and limonene (Scheme 6B) *(338,339)*. The epoxide products from α-pinene and camphene are α-pinene oxide and camphene oxide, respectively, and they both easily isomerize into campholenic aldehyde, an industrially important chemical intermediate (*vide infra*). An even more challenging substrate is limonene, because epoxidation of both double bonds is feasible, though limonene (mono)oxide is usually the major product. Among the possible products, limonene 1,2-oxide is more important, as it can be easily hydrated to the corresponding diol, which subsequently can be transformed into another important terpenoid, carvone. Silylated Ti-MCM-41 and methyltrioxorhenium-loaded Na–Y zeolites are highly effective catalysts for this type of transformation *(304,338,347)*. Methyltrioxorhenium is a well-known oxo-transfer agent in homogeneous organometallic catalysis, and consistently, methyltrioxorhenium-modified zeolites are active catalysts for epoxidations *(348)*. Linalool and geraniol are other important and challenging substrates for epoxidation using zeotype catalysts *(349,350)*.

Another important zeolite–catalyzed reaction is the Baeyer–Villiger oxidation, which converts ketones to lactones and esters. The use of zeolites as catalysts is of high industrial significance because organic peracids can then be avoided as oxidants. TS-1, ZSM-5, Sn-beta, and Ti-beta are efficient catalysts for this process *(304,351,352)*. Selectivity can be tuned by using different zeotype catalysts. In the oxidation of dihydrocarvone with hydrogen peroxide, Sn-beta exclusively produces the corresponding lactones, whereas Ti-beta exhibits higher selectivity toward epoxide formation without any lactone formation (Scheme 6C) *(353)*. The use of Sn-beta as a catalyst by Corma *et al.* is noteworthy since other heterogeneous catalysts (i.e., TS-1

or H–beta) show poor selectivity because of their preference for epoxidation, and homogeneous Baeyer–Villiger oxidation catalysts exhibit very poor reactivity *(353)*. Here, the selective and preferential activation of the carbonyl group (over alkene) by Lewis–acidic Sn–beta zeolite catalysts in the presence of the oxidant H_2O_2 is the key reason behind the success of this process. The choice of tin for substitution into the framework is also a critical decision, as other available Lewis–acidic metals, such as titanium, vanadium, chromium or iron, have a tendency to activate the oxidant instead of the carbonyl group, which leads to either unwanted (ep)oxidation processes or decomposition of the oxidant *(353)*. The initial findings of Corma *et al.* regarding carbonyl group activation by Sn–beta have prompted researchers to screen Sn–beta catalysts for the isomerization of carbonyl-containing compounds (Section 3.3.2) as well as for the selective reduction of carbonyl groups (Section 3.3.7) *(316,319)*.

Another important class of TS-1-catalyzed oxidation reactions is the hydroxylation of aromatic compounds *(340)*. Phenols are versatile organic intermediates and have a variety of industrial applications, (mostly) in wood and plastics processing. Phenol is largely produced from cumene after aromatic alkylation of benzene using propylene as an alkylating agent. The limitations of this process are as follows: (i) it produces a stoichiometric amount of acetone as side product and (ii) it is an indirect route, which depends on many fossil fuel derivatives and their (fluctuating) prices. An environmentally benign and economically viable alternative approach would be attractive, such as the direct production of phenol by hydroxylation of benzene via oxidative (using O_2, H_2O_2, O_3, or N_2O as oxidants) aromatic C—H activation pathways *(340)*. To avoid side-product formation, transition metal-containing zeolites are potentially suitable catalyst materials for such hydroxylation processes. Nonarguably, the best zeolitic oxidation catalyst so far reported is TS-1. The first description of its ability to perform the liquid–phase hydroxylation of benzene using H_2O_2 as an oxidant was published in 1986 *(354,355)*. An additional cosolvent is necessary to obtain a homogeneous reaction medium containing both the liquid oxidant and the aromatic substrate (Scheme 6D) *(354)*. In fact, the first industrial application of TS-1 was the hydroxylation of phenol to hydroquinone and catechol by EniChem (10,000 t/year), which is carried out in a slurry reactor *(342)*. The optimum reaction temperature in this EniChem process is around 100 °C, and an excess of phenolic substrates is used to avoid further oxidations to tarry products *(342)*. Two other materials, Ti–mordenite *(356)* and Ti–beta *(357)*, were also reported as efficient catalysts for this process.

In addition to H_2O_2, N_2O has also shown good results in zeolite-catalyzed hydroxylation processes. N_2O can be easily derived from the waste streams of other processes. Noteworthy are the results by Panov and coworkers, who demonstrated high selectivity of an iron-containing ZSM-5–type catalyst with N_2O as an oxidant *(358–361)*. Specifically, the phenol selectivity for the gas-phase oxidation of benzene to phenol was 98% *(358–361)*. Several other metal-containing MFI zeolites (with metals Ti, V, Sb, As, Co, Cr, Cu, Fe, Ni, Zn, etc.) have already been evaluated for the aromatic hydroxylation using N_2O as an oxidant (Scheme 6C) *(340)*. Also, Fe-beta, Fe-TNU-9, and Fe-TNU-10 have shown similar reactivity *(362,363)*.

In general, the catalyst–oxidant combination TS-1/H_2O_2 has been reported to exhibit higher conversion and moderate selectivity, whereas the combination Fe-ZSM-5/N_2O has shown lower conversion and very high selectivity. In addition to the hydroxylation of aromatic hydrocarbons, the hydroxylation of phenol is also an industrially very important reaction because the products, catechol and hydroquinone, are well known for their biological and medicinal activity (Scheme 6C). However, phenol is a much easier substrate to hydroxylate than aromatic hydrocarbons. TS-1 and Ti-MCM-41 are noteworthy catalysts, whereby TS-1 exhibits much better selectivity *(364)*. The very recent review by Nemeth and Bare on oxidation reactions catalyzed by metal-containing zeolites is highly recommended to learn more about the technological aspects of these kinds of oxidative processes *(340)*.

In principle, the TS-1-catalyzed epoxidation and hydroxylation chemistry can be extended to more difficult and challenging chemical reactions, namely oxidative functionalization of aliphatic C—H bonds. The report by Ramaswamy *et al.* is pioneering in this field; the authors used Ti-ZSM-11 or V-ZSM-11 materials as catalysts and H_2O_2 as an oxidant (Scheme 6E) *(365)*. However, this process is still nonselective, and all the possible products were formed in various quantities (Scheme 6D). More attention should be devoted to this chemistry, to ultimately provide more selective routes for the oxidative aliphatic C—H functionalization, with the help of zeolite-based (or other) catalysts.

3.3.6 Heterocycle Synthesis Reactions

Nitrogen heterocycles are important structural units in the fine chemical industry, for the production of various drugs. Moreover, they are a very

important class of chemicals in organic synthesis *(333)*. Traditionally, nitrogen heterocycles are derived from the coal–tar fraction, but this source does not suffice, considering the gradually increasing demand. This gap prompted the chemical industry to look for alternative and sustainable routes. As highlighted in previous sections, zeolites are gradually replacing inorganic Lewis acids in organic syntheses. In the early 1980s, Mobil patented the direct amination of formaldehyde or acetaldehyde to picolines (methyl pyridines) with H–ZSM–5 as a catalyst (Scheme 7A) *(366)*. Among all picolines, 2–picoline is the most pharmaceutically important chemical, as it is the backbone of heteroaromatics such as pyridoxal or pyridoxine, which are vitamin B$_6$ supplements (Scheme 7A). A few years later in 1983, Mobil patented an alternate and very selective route for the synthesis of 2–picoline via isomerization of aniline; for this reaction, ZSM–5 catalysts were used at high temperature and ammonia pressure (Scheme 7A) *(367)*. A conceptually similar process was reported for the production of pyrrole from furan with moderate to high yield and selectivity, again with a ZSM–5–type catalyst *(368)*.

The industrial significance of caprolactam for the synthesis of Nylon–6 is well known. Industrially, caprolactam is currently produced by converting cyclohexanone in the presence of hydroxylamine and sulfuric acid to the corresponding oxime via a noncatalyzed route *(333)*. The oxime is then transformed into caprolactam in the presence of sulfuric acid. The process generates tons of waste, about ≈ 4.5 kg/kg of caprolactam, mostly ammonium sulfate *(329)*. EniChem developed a more environmentally benign route to caprolactam by using zeotype heterogeneous catalysts *(369)*. In their process, the oxime was synthesized (12,000 t/year) via liquid–phase ammoximation of cyclohexanone (Scheme 7B) using TS–1 as catalyst and H$_2$O$_2$ as oxidant *(342)*. Ti—OOH moieties are believed to be the active species on the zeolite catalyst that facilitate the conversion of ammonia to hydroxylamine (Scheme 8). The hydroxylamine is then released and oxidizes cyclohexanone to cyclohexanone oxime *(370)*. The oxime can then be transformed at a temperature of 350 °C into caprolactam (via Beckmann rearrangement) with very high selectivity, by exploiting the highly acidic nature of zeolite catalysts (Scheme 7B) *(369,371)*. Processes for this Beckmann rearrangement were developed independently by Sumitomo (60,000 t/year), who used ZSM–5 with a high Si/Al ratio, and by Union Carbide, who used SAPO–11 *(329,371)*. The main advantages of the zeolite–catalyzed process over noncatalyzed routes are (i) its atom economy and (ii) no formation of large quantities of ammonium sulfate.
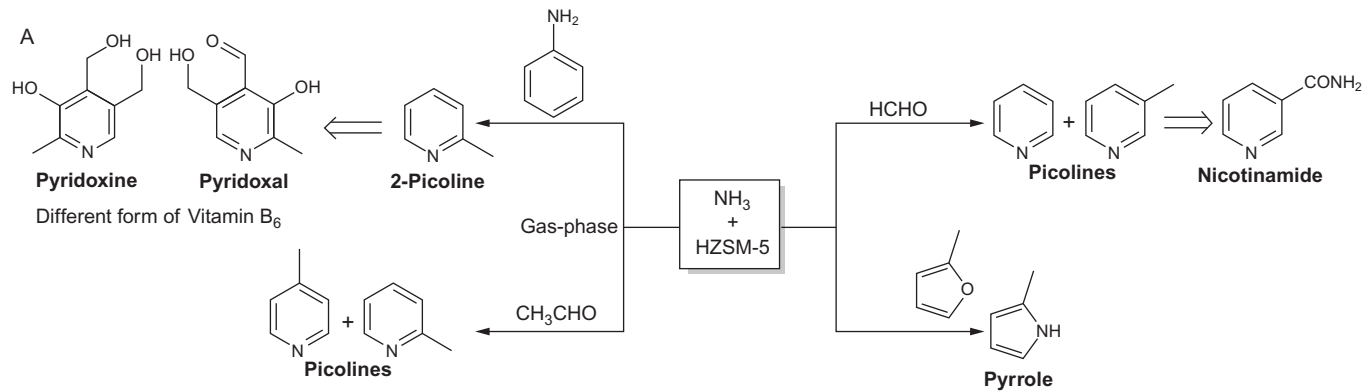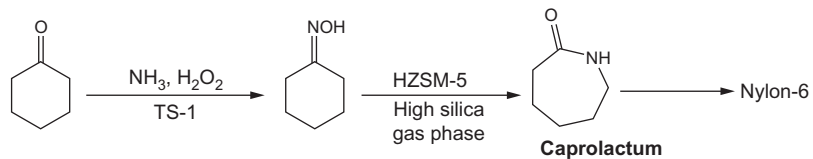
**Scheme 7** Zeolite-catalyzed heterocycle synthesis.
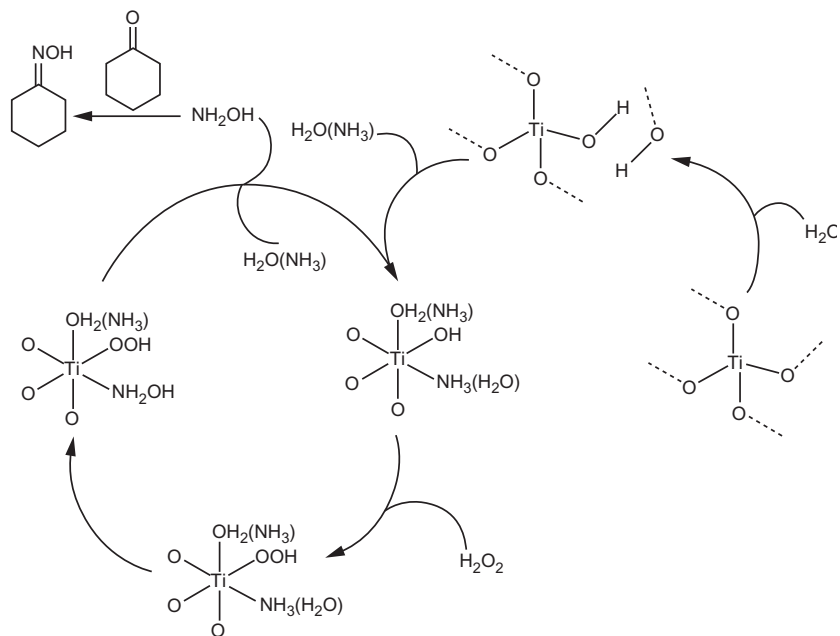
Scheme 8 Proposed mechanism for the ammoximation reaction of cyclohexanone to cyclohexanone oxime catalyzed by TS-1, with focus on the chemistry at the active titanium site. *Adapted from Refs.* (340,370).

3.3.7 Other Reactions

3.3.7.1 Knoevenagel Condensation

Most of the chemical reactions discussed in the preceding Sections (3.3.1–3.3.6) can be classified as "acid" zeolite catalysis. Similarly, basic zeolites are potentially very effective catalysts for various other organic transformations. Basic zeolites are synthesized either by ion exchange with alkali metal cations (creating weak basic sites) or by generation of alkali metal oxides or alkaline earth metal oxides within the zeolite pores (creating strong basic sites) (372). These kinds of zeolites are well known for C—C bond formation via Knoevenagel condensation between aldehyde or ketone and active methylene compounds (characterized by a CH$_2$ group between electron-withdrawing groups). Normally, simple organic bases, like amines, suffice as catalysts for this condensation. Thus, the zeolites Na–X, NaGeX, and Cs–exchanged X as well as Rb/Nb–MCM-41 are used as catalysts for different Knoevenagel condensation reactions (Scheme 9A) (373,374). As depicted in Scheme 9A, NaGeX can catalyze the condensation between

A

(Basic) zeolite catalyst
Knoevenagel condensation

EWG: electron-withdrawing group

Hantzsch ester

B

"Basic" zeolite
Michael addition

"Basic" zeolite
Michael addition

C

"Basic" zeolite
Claisen–Schmidt condensation

Chalcone

Flavone

D

Sn-Beta zeolite

R = alkyl, R^1 = alkyl or H, R^2 = alkyl or H
Meerwein–Ponndorf–Verley reduction

E

Zeolite
N_2O_5

Aromatic nitration

F

MFI nanosponge
Pechmann condensation

R = OH

Scheme 9 Some other relevant zeolite-catalyzed reactions: (A) Knoevenagel condensation, (B) Micheal addition, (C) Claisen–Schmidt condensation, (D) Meerwein–Ponndorf–Verley reaction, (E) aromatic nitration, and (F) Pechmann condensation.

deactivated benzaldehyde and ethyl acetoacetate to form 2-acetyl-3-phenylacrylic acid ester, which can be further converted to a type of compound classified as Hantzsch ester (characterized by an attached dihydropyridine) *(375)*. Hantzsch esters are very versatile organic molecules that are used in rocket fuel and photographic materials and exhibit important pharmacological activities (including antihypertensive, antibiotic, antioxidants, anti–inflammatory, and antifungal). Moreover, they have wide applications in asymmetric transfer hydrogenations in organic synthesis *(333)*.

3.3.7.2 Michael Addition

In addition to the condensation reactions already discussed, various other C—C bond-forming reactions are catalyzed by zeolites and zeotype materials. The Michael addition is a nucleophilic addition of a carbanion or another nucleophile to an acceptor, usually an activated alkene. The reaction can be catalyzed by various types of alkali metal- or alkaline earth metal-exchanged zeolites, such as Na–Y/K–Y, Li–X, Cs–beta, Cs–MCM-41, and CsLa MCM-41 *(304,329,333)*. As depicted in Scheme 9B, CsLa MCM-41 catalyzes double Michael addition between ethyl acrylate and ethyl cyanoacetate *(376)*.

3.3.7.3 Claisen–Schmidt Condensation

Sodium-, cesium-, and magnesium-exchanged zeolites are basic in nature and are very effective catalysts for the Claisen–Schmidt condensation, which is a type of cross-aldol condensation *(377)*. For example, the reaction between benzaldehyde and 2-hydroxyacetophenone gives the biologically active compound chalcone, which undergoes cyclization to flavone (Scheme 9C). Flavone-type molecules are also chemical intermediates for anti–inflammatory, antibacterial, anticancer, and anti–AIDS pharmaceuticals *(304)*. In the synthesis of various aldol condensation products, zeolites also replace conventional inorganic and organic bases to transition to more environmentally benign operation. As mentioned earlier, the ability of Sn–beta to activate the carbonyl bond has encouraged Corma *et al.* to use similar strategies in other relevant chemistries *(319)*.

3.3.7.4 Meerwein–Ponndorf–Verley Reaction

Sn–beta is also an efficient catalyst for the Meerwein–Ponndorf–Verley reaction (Scheme 9D). A very high yield (of 95%) and perfect selectivity to the desired product has been reported for the Meerwein–Ponndorf–Verley reaction between cyclohexanone and 2-propanol *(319)*. The Meerwein–Ponndorf–Verley reduction of aldehydes or ketones and the Oppenauer oxidation of alcohols (MPVO reaction) are highly chemoselective reactions that are traditionally catalyzed by aluminum alkoxide. Lewis–acidic metal centers are simultaneously interacting with both reactants to facilitate the hydride transfer from the alcohol to the carbonyl group. In addition to Sn–beta, Al– and Ti–beta have been reported as efficient MPVO catalysts *(378,379)*.

3.3.7.5 Aromatic Nitration

The industrial gas–phase nitration of aromatic compounds has increased significantly in the last decade. Aromatic nitration is a class of industrially important reactions for the synthesis of chemical intermediates with direct relevance to dyes, plastics, and pharmaceuticals. The nitration reagent is a mixture of concentrated nitric and concentrated sulfuric acid *(333)*. Obviously, a more benign route would be desirable. Various solid acids including zeolites have already been screened for nitration with N_2O_5 or NO_2/O_3 as reagent, but poor selectivity because of overnitration to di–nitro aromatics is a problem *(380,381)*. Since these observations were made, researchers have been trying to optimize the selectivity toward mono–nitrated products. Recently, Ma *et al.* observed high *para*-selectivity using H-beta as the catalyst and N_2O_5 as the nitrating agent (Scheme 9E) *(382)*. In this case, the *ortho–/ para*-selectivity could simply be tuned by changing the order of reagent addition.

3.3.7.6 Pechmann Condensation

The Pechmann condensation is the most efficient way to produce coumarins from activated phenols by reaction with β–ketoesters or unsaturated carboxylic acids. Inorganic and organic acids have traditionally been used as catalysts, though the drawbacks of such processes are numerous and include high acid use, corrosion, toxicity, and difficult separation of the product *(333)*. Obviously, zeolites can be employed as catalysts to perform this condensation reaction in a more efficient and environmentally benign manner. Zeolites MFI, BEA, and USY are usually used as catalysts for the Pechmann condensation. A very recent report from Kim *et al.* is noteworthy in this context. The authors have used a newly synthesized zeolite nanosponge with MFI framework as catalyst for the Pechmann condensation between phenols (pyrogallol and resorcinol) and ethyl acetoacetate (Scheme 9F) *(383)*. According to Kim *et al.*, the large number of acid sites located on the external surface is probably the origin of the excellent catalytic performance of this mesoporous MFI zeolite nanosponge (compared to that of bulk zeolites).

   In conclusion, zeolites are transforming organic reactions that are mediated by stoichiometric amounts of inorganic or organic acid/base to catalytic processes. This changeover (i) reduces the dependency on hazardous chemicals (e.g., inorganic acids or acetic anhydride), (ii) prevents the generation of unwanted by-products (such as ammonium sulfate in caprolactam synthesis, or di- or explosive tri-nitrated products in aromatic nitration), and

most importantly (iii) decreases or eliminates the formation of waste from the overall process with the additional option of catalyst recyclability.

4. (RE)EMERGING APPLICATIONS OF ZEOLITES

4.1 Direct Methane Activation Routes

The decreasing supply of crude oil, coupled with environmental concerns, has led to new ambitions to replace this feedstock with abundant, cheap, and cleaner sources for the production of valuable aliphatic and aromatic hydrocarbons. Methane represents an ideal alternative feedstock to crude oil, being naturally abundant in the forms of natural gas, biogas, coal-bed gas, methane hydrates, and even shale gas *(384)*. In quantitative terms, for example, the natural gas reserves amount to about 180 trillion m^3 *(385)*. The recent discovery of substantial amounts of shale gas deposits in China, South Africa, Australia, the United Kingdom, and particularly in the USA has shaken up the energy market *(386)*. These discoveries make the total amount of available methane staggeringly high in comparison to that of crude oil, therefore motivating the use of methane as a feedstock to produce valuable chemicals.

While methane, particularly in the form of natural gas, is abundant and widely distributed globally, it is often (to about 30–60%) isolated in remote regions, which means it currently has to be transported from the source to a plant for further valorization processes. Compressing natural gas (to obtain the liquid form) is the only viable method established to date to allow for economic transport. Indirect methane conversion is currently the only commercial means to convert methane (from natural gas) into valuable chemicals. Indirect conversion refers to a two-step process: First, methane is converted to synthesis gas via steam reforming, autothermal reforming, or partial oxidation. Then, in the second step, the synthesis gas is converted to diesel fuel, gasoline, aromatics, higher alcohols, and light olefins via FTS or the methanol-to-hydrocarbon (MTH) process, with the variants of MTO and MTG, and methanol to dimethylether/gasoline. However, drawbacks of methane liquefaction, transport, and subsequent formation of synthesis gas are the substantial capital investment costs (60–70%) and the energy needed to activate the stable methane C—H bond and the resulting severe reaction *(387)*. Therefore, commercial synthesis gas plants are located in the proximity of natural gas sources, for example, in South Africa (Sasol plants), Malaysia (Shell Middle Distillate Synthesis, SMDS plant), Qatar (Oryx, gas

to liquids (GTL) plant, Shell Pearl GTL), Nigeria (GTL plant), and Oklahoma (Syntroleum).

Given these drawbacks, it would be convenient to convert methane directly to valuable chemicals, avoiding transport and compression costs as well as the complications associated with additional reaction steps. Of course, this endeavor is not straightforward considering the fact that methane conversion to hydrocarbons is thermodynamically limited, requiring high reaction temperatures, but at least some costs can be cut in comparison to the indirect route. A number of processes have been proposed for direct methane conversion, based on either oxidative or nonoxidative routes. The oxidative coupling of methane, first reported by Keller and Bhasin, produces ethane and ethylene, and the direct partial oxidation produces methanol and formaldehyde. These processes have received a high degree of interest, since the inclusion of oxidants reduces the thermodynamic limitations of methane conversion *(388)*. The focus of this chapter is the production of methanol and aromatics from methane. Further details on the various routes of methane activation can be found in the above-mentioned articles (and references therein) as well as in the reviews by Holmen *(389)*, Lunsford *(390)*, Choudhary *et al.* *(391)*, and Horn and Schlögl *(392)*.

4.1.1 Oxidative Routes for Methane Activation

The direct conversion of methane into oxygenates, such as methanol, is a long-standing scientific and technological challenge in the field of catalysis *(393)*. In the past two decades, several research groups have shown that zeolites containing first row transition metal ions, such as iron, copper, cobalt, nickel, or zinc in the ion exchange positions, can selectively activate methane at low temperatures. Several routes have been developed. The first one is conducted in the gas phase and comprises a first step in which oxygen is added to the zeolite material by using either N_2O or O_2 (air) as reagents. The second route makes use of H_2O_2 as the oxygen donor and is conducted in the liquid phase. Both approaches will be discussed in the next two Sections (4.1.1.1 and 4.1.1.2).

4.1.1.1 Methane Activation in the Gas Phase

Panov and coworkers were the first to report low-temperature methane oxidation activity of a zeolite-based material *(394,395)*. The catalyst, Fe–ZSM-5, should first be activated with N_2O as an oxidant, to create an iron–oxo compound, which is then able to activate methane. More specifically, N_2O is decomposed at a temperature of about 200 °C and an oxygen species is

formed that is characterized by a particular reactivity and has been named α–oxygen. It is this α–oxygen that has been proposed to react with methane to form methanol, which has to be extracted in a follow-up step with water or an aqueous solution of acetonitrile. In this context, it is important to remark that the same catalytic system (i.e., the combination of Fe-ZSM-5 and N_2O) can also oxidize benzene to phenol, as well as convert CO into CO_2. (The reader is referred to Section 3.3.5 for further details on the oxidation of benzene to phenol.)

In a follow-up investigation, it was shown that α–oxygen is an anion-radical species $O\alpha^{\bullet-}$. The radical nature of this species may explain its high reactivity, although one may argue that such species are typically considered to be active for deep oxidation of hydrocarbons. In a seminal paper, Dubkov *et al.* have reported on the use of *in situ* Mößbauer spectroscopy and proposed that the active sites in Fe/ZSM-5 consist of a bis(μ-oxo)diiron core *(396)*. This structure is considered to be present in the soluble methane mono-oxygenase (sMMO) enzyme, which is also known to selectively activate methane to produce methanol at room temperature. Since this initial proposal of the structural motif in Fe/ZSM-5, a wide range of research efforts have been made by many groups. It is now generally accepted that the active sites of Fe/ZSM-5, generally known as α–sites, perform the oxidation of methane via a reversible redox transition $Fe^{2+} \leftrightarrow Fe^{3+}$, although the exact structure of the α–sites remains elusive as there are many arguments in favor of both binuclear and mononuclear active sites. Interestingly, The Mößbauer results of Dubkov *et al.* have been confirmed by other groups *(397,398)*, although kinetics experiments indicate that each iron atom of the methane activation complex is operating as an independent active site. These observations suggest that α–sites, while being mononuclear species, have a paired arrangement in the zeolite matrix, which would appear in spectroscopic fingerprinting as if they would constitute a binuclear complex. Interestingly, Gao *et al.* showed that the activation of Fe/ZSM-5 with molecular oxygen followed by the exposure to methane did only result in full combustion products, namely water and carbon dioxide *(399)*, illustrating the essential role of N_2O as an oxidant in combination with Fe-ZSM-5.

In recent years, Panov and coworkers have extended their investigation to explore whether truly catalytic operation is possible with Fe/ZSM-5. Starokon *et al.* report on the selective oxidation of methane to mainly methanol, DME, and some traces of acetaldehyde, extracted from the material after reaction, with a turnover number of ≈ 3 *(400)*. This nonstoichiometric ratio of the number of methane converted to the number of α–sites, as

titrated with N_2O, was explained by a spillover mechanism in which the methanol formed is liberated from the α-sites, which allows the regenerated α-sites to react again with N_2O, with subsequent formation of oxidation products. Inspired by this work conducted in a static vacuum unit, Parfenov *et al.* reported that Fe/ZSM-5 could reach a turnover number of ≈ 7 in a 4-h test at a temperature of 200 °C or below *(401)*. This finding, obtained with a conventional flow-type catalytic reactor, was explained by the fact that methanol, formed via methane oxidation by α-oxygen, migrated from the α-sites, initiating new reaction cycles. This mode of operating was denoted as "quasi-catalytic," as the products, namely methanol and dimethyl ether, still had to be removed via an extraction procedure. Above 500 °C, the methane activation reaction moved to a truly catalytic mode, with product desorption into the gas phase. Water addition strongly decreased the formation of coke, while increasing the selectivity toward methanol, which was $\approx 62\%$ at a reaction temperature of 275 °C for a still very modest methane conversion of 0.19%. This concept of quasi-catalytic and catalytic oxidation of methane on Fe/ZSM-5 is illustrated in Scheme 10, demonstrating the potential of this methane activation route.

Inspired by the innovative research work of Panov and coworkers, as well as by the fact that copper-containing enzymes are associated with the particulate methane mono-oxygenase (pMMO) system, Schoonheydt and coworkers were the first to report that copper-based catalysts, including Cu/ZSM-5 and Cu/mordenite, can also activate methane with formation of methanol. In a seminal contribution, Groothaert *et al.* reported on the selective oxidation of methane into methanol on Cu/ZSM-5 and
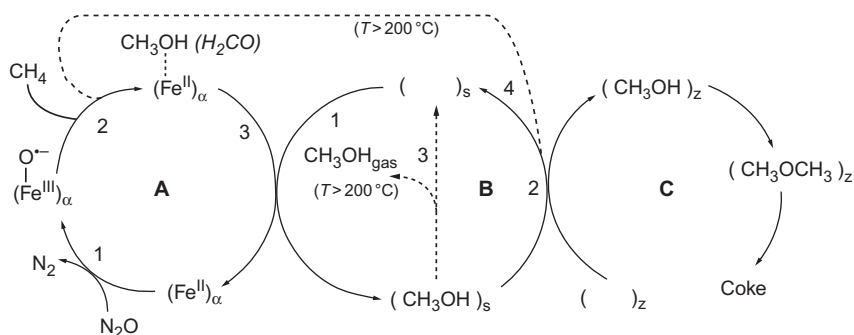

Scheme 10 Mechanistic scheme of quasi-catalytic and catalytic oxidation of methane. Solid lines indicate the steps that are present in both the quasi-catalytic and catalytic modes of reaction. Dotted lines display the steps that are present only in the catalytic mode. *Reproduced with permission from Ref. (401).*
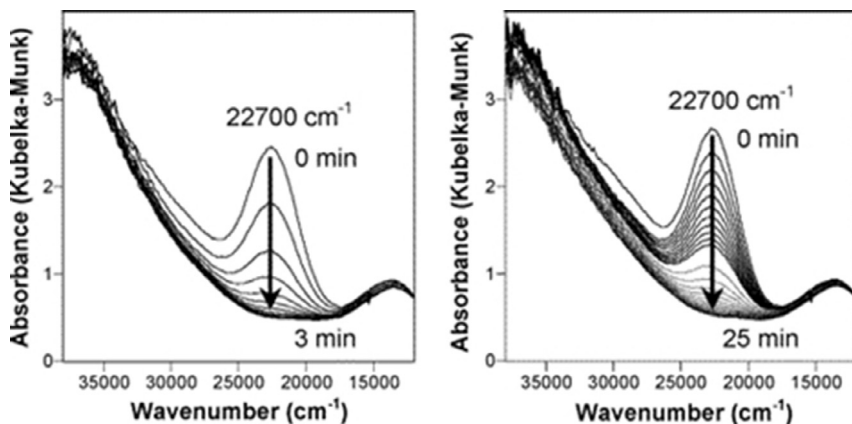
Figure 31 Fiber-optic UV–vis spectra of O_2-activated Cu/ZSM-5 (Cu/Al 0.58 and Si/Al 12) during reaction with CH_4 (5% in N_2; 25 ml/min) at temperatures of 175 °C (left) and 125 °C (right). Time interval between two spectra represented as solid lines is 25 s; time interval between two spectra represented as dashed lines is 125 s. *Reprinted with permission from Ref.* (402). *Copyright (2005) American Chemical Society.*

Cu/mordenite (402). Figure 31 shows a set of *in situ* UV–vis spectra of O_2-activated Cu/ZSM–5 (Cu/Al 0.58 and Si/Al 12) during reaction with methane, in which a characteristic band at $\sim$22,700 cm^{-1} (interpretation discussed below) decreased in intensity with increasing reaction time at a temperature of 175 °C. GC analysis of the effluent showed no product formation, whereas heating the zeolite in a helium flow resulted in the detection of CO_2.

By using a 1:1 water:acetonitrile mixture after reaction with CH_4 at 175 °C, it was possible to confirm the formation of methanol as the only reaction product by GC, GC-MS, ^{13}C NMR, and ^1H NMR. Reaction with ^{18}O-labeled O_2 and ^{13}C-labeled CH_4 yielded ^{18}O- and ^{13}C-labeled CH_3OH, respectively. Moreover, by plotting the amount of extracted methanol and the UV–vis spectra for a series of Cu/ZSM–5 as a function of the Cu/Al ratio, as illustrated in Figure 32, it was found that the 22,700 cm^{-1} absorption band appears in a sample with a Cu/Al ratio of 0.25 and then gradually increases in intensity with increasing Cu/Al ratio. The appearance of the 22,700 cm^{-1} absorption matched with the sharp increase in CH_3OH formation in the $0.2 < Cu/Al$ ratio < 0.3 region, demonstrating that a specific copper complex has first to be formed before methane activation can occur. It was proposed that this copper complex should be a dinuclear bis(μ-oxo)dicopper species, although no spectroscopic proof was provided for this active site proposal. It was mainly the analogy with the
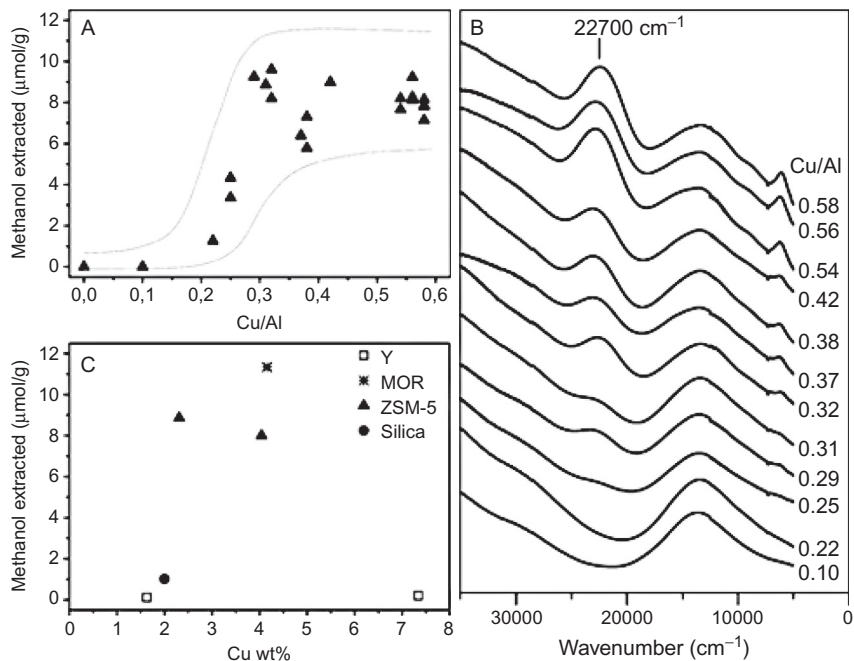
Figure 32 (A) Amount of methanol extracted per gram of Cu-ZSM-5 sample, as a function of the Cu/Al ratio of the CZ-12 samples. (B) Stacked UV–vis–NIR absorption spectra (in a.u.) of the CZ-12 samples activated in O_2 at 450 °C. (C) Amount of methanol extracted per gram of Cu-ZSM-5 sample, as a function of the copper content (in wt.%) of the sample. *Reprinted with permission from Ref.* (402). *Copyright (2005) American Chemical Society.*

active site considered to be present in the pMMO enzyme system *(403)* that led to this conclusion. Interestingly, the authors also showed that the same Cu/ZSM-5 system could activate ethane, with ethanol and acetaldehyde as the sole products extracted after reaction. Finally, by comparing different catalysts, including zeolite Y, mordenite, and amorphous silica, it was found that Cu/mordenite showed an even higher methanol yield than Cu/ZSM-5, while the UV–vis absorption band shifted from 22,700 to 22,200 cm^{-1}. This finding demonstrates that other zeolite topologies, when loaded with copper, are able to convert methane into methanol via the formation of a highly activated oxygen species.

In a follow-up article, Smeets *et al.* compared a wide variety of Cu^{2+}-zeolites, as well as Cu^{2+}-impregnated SiO_2 and Al_2O_3, for their activity in methane activation *(404)*. It was found that only in Cu/ZSM-5 and Cu/mordenite, the species with the characteristic UV–vis band at around

$\approx 22{,}500 \text{ cm}^{-1}$ were formed, whereas other materials, also active for the activation of methanol, such as Cu/ferrierite and Cu/beta, did not show such spectroscopic features. Interestingly, whereas Cu/mordenite and Cu/ZSM-5 showed activity already at a reaction temperature of 150 °C and below, Cu/ferrierite and Cu-beta started to be active at around 200 °C. The activity of Cu/mordenite increased further at the higher reaction temperatures. All other copper-based materials that were tested only showed marginal activities. These findings clearly show that other copper–oxygen species capable of activating methane are present in zeolites with FER, BEA, and MOR topologies at higher reaction temperatures.

As mentioned before, by making the analogy with the pMMO enzyme system, the methane-activating complex in Cu/ZSM-5, characterized by the 22,700 cm^{-1} absorption band, was initially thought to be a bis(μ-oxo)dicopper species, although no unambiguous spectroscopic evidence was provided. In a series of breakthrough articles by Schoonheydt, Sels, Solomon, and coworkers, the methane-activating "core" was proposed to be a mono(μ-oxo)dicopper(II) species, in the following denoted as the $[Cu_2O]^{2+}$ core (405,406). The geometric and electronic structure of this reactive core was identified by using resonance Raman spectroscopy and DFT calculations. DFT calculations reproduced the low reaction barrier as well as results of kinetic isotope effect (KIE) measurements, which had delivered a KIE value of 4.0–2.0 at 115–200 °C, clearly demonstrating that C—H bond breaking was rate limiting. It was found that the low barrier for H-atom abstraction from methane is the result of a strong $[Cu_2O{-}H]^{2+}$ bond in the initial product and a frontier molecular orbital that polarizes to an oxyl ($O^{\bullet-}$) radical along the reaction coordinate. The transition state consists of a cupric-oxyl intermediate, shown in Figure 33, that is highly activated for H-atom abstraction, thus explaining the reactive nature of the bent mono-μ-oxo dicupric core in Cu/ZSM-5.

In a follow-up investigation, Smeets *et al.* were able to identify a reactive intermediate in the pores of Cu/ZSM-5 while converting methane into methanol (407). More specifically, results from UV–vis and resonance Raman spectroscopy allowed the proposal of a reaction scheme, as outlined in Scheme 11, in which a precursor species is identified as $\mu(\eta^2{:}\eta^2)$ peroxo dicopper (II), characterized by an absorption band at around 29,000 cm^{-1}, which is readily converted into the reactive $[Cu_2O]^{2+}$ core, characterized by the absorption band at $\approx 22{,}700 \text{ cm}^{-1}$. Furthermore, ^{18}O TPD experiments demonstrated that the second ^{18}O atom is incorporated into the zeolite lattice when the $[Cu_2O]^{2+}$ core is formed.
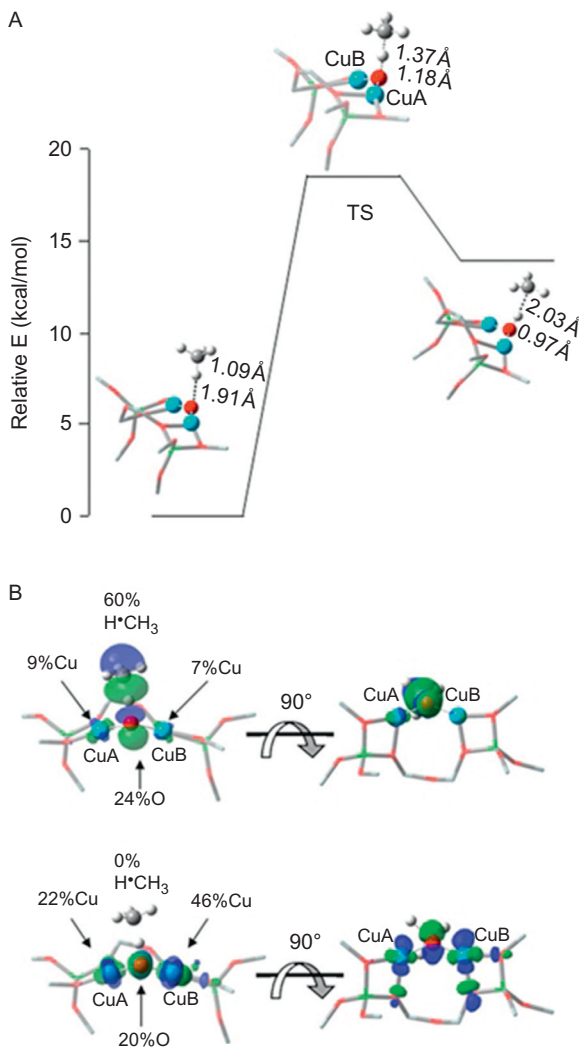
Figure 33 DFT-calculated reactivity of L-Cu$_2^{II}$O with CH$_4$. (A) Reaction coordinate of H-atom abstraction from CH$_4$ by L-Cu$_2^{II}$O. (B) Singly occupied molecular orbitals (SOMOs) at the transition state (TS) shown with the line of the CH$_4$ approach in the plane (left) and behind the plane of the figure (right). *Reproduced with permission from Ref.* (405).

The question remains as to why only a fraction of the ion-exchanged copper is active in the conversion of methane to methanol, and where other copper species are located in the zeolite material. Beznis *et al.* pursued this question and prepared a series of Cu/ZSM-5 materials, by systematically

varying the nature of the charge–compensating cation, copper precursor, copper loading, and pH of the ion-exchange solution (408). A linear relationship between the amount of methanol produced and the 22,700 cm^{-1} absorption band intensity was found irrespective of the synthesis method applied. At least two species were found, the $[Cu_2O]^{2+}$ core, responsible for methane activation, highly dispersed in the zeolite framework structure; and Cu—O clusters dispersed on the outer surface of zeolite ZSM-5. FT-IR spectroscopy in combination with pivalonitrile and NO as probe molecules was used to discriminate between these two families of copper species, leading to the conclusion that Cu—O species at the outer surface are not involved in the methane activation process. The active core however represents a minority species, and a linear relationship was obtained between the amount of methanol produced and the number of Cu—O species as probed with NO. This correlation was extracted from the changing FT-IR intensities of the bands of adsorbed NO located at 1813 and 1905 cm^{-1}, after first adsorbing pivalonitrile, which selectively titrates the Cu-species at the outer surface of zeolite ZSM-5. The correlation of methanol production with the FT–IR band intensities is shown in Figure 34.

Vanelderen et al. performed detailed reactivity, spectroscopic and theoretical investigations on Cu/mordenite, thus extending the work on Cu-ZSM-5 to other zeolites (409). Two distinct, albeit very similar, $[Cu—O—Cu]^{2+}$ sites were identified, both of which exhibited methane
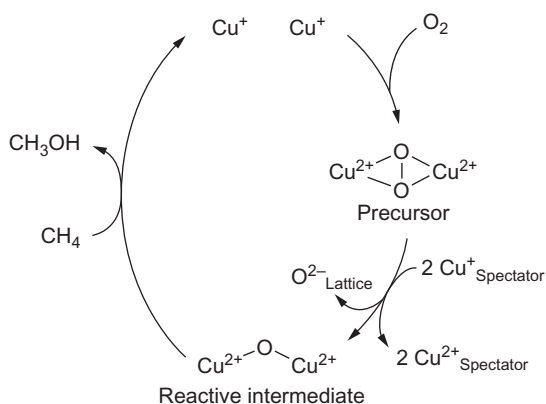
Scheme 11 Proposed reaction scheme based on UV–vis absorption and resonance Raman spectra by Smeets et al. summarizing that "a precursor is a μ-(η^2:η^2) peroxo dicopper (II) core (absorption band at 29,000 cm^{-1})" and that this species converts directly into the $[Cu_2O]^{2+}$ reactive intermediate (absorption band at 22,700 cm^{-1}). Reprinted with permission from Ref. (407). Copyright (2010) American Chemical Society.
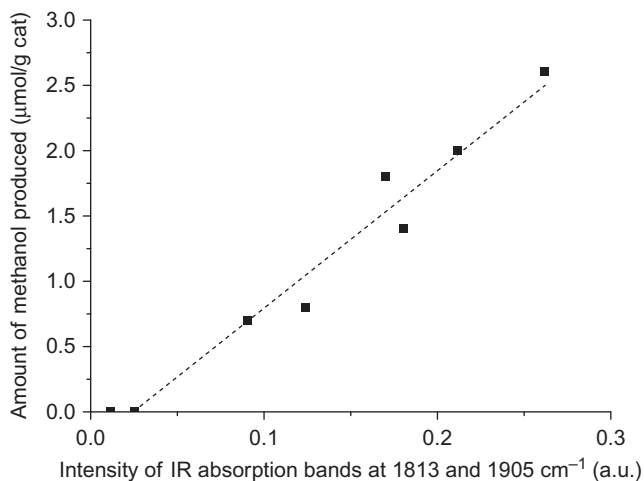
Figure 34 The amount of methanol produced on Cu-ZSM-5 zeolites as a function of the intensity of the IR bands at 1813 and 1907 cm^{-1}. *Reproduced with permission from Ref.* (408).

activation behavior. One of the two sites was characterized by an absorption band at 21,900 cm^{-1}, while the other was characterized by an absorption band at 23,100 cm^{-1}. Interestingly, the latter species was found to exhibit a 3.6–4.6 kcal/mol lower activation enthalpy ΔH for methane activation, which was suggested to be related to substrate confinement in the zeolite structure, as the framework may influence the trajectory of methane approaching the active site. In contrast to Cu/ZSM-5 where only one [Cu—O—Cu]$^{2+}$ active site could be observed at the intersection of the two 10 MR rings, Cu/mordenite provided two distinct local structures, one situated at the intersection of the side pocket with the 12-MR channel and the other situated at the intersection of the side pocket with the 8-MR channel, as illustrated in Figure 35. This figure also includes a structural comparison with the [Cu$_2$O]$^{2+}$ core in ZSM-5.

Another important contribution to this field of research was made by Alayon *et al.* who presented a two-step process to produce methanol from methane on a preoxidized Cu/mordenite, consisting of methane activation and subsequent hydration by using a wet helium stream at a temperature of 200 °C (410). The authors made use of on-line mass spectrometry and detected CO$_2$ after methane interaction at 200 °C and subsequent heating in a dry stream of helium. In contrast, if after methane interaction a wet stream of helium was allowed to flow through the catalyst bed, methanol

was observed in the gas phase. Subsequent heating in helium after methanol had been desorbed did not show any desorption of CO_2.

In a further paper, Alayon *et al.* investigated the dynamics of the structure of Cu in Cu/mordenite during methane activation with XAS and DFT calculations *(411)*. It was found that a large fraction of oxygen–activated Cu^{2+} ($\approx 40\%$) reacts with methane and is reduced to Cu^+, while activated methane intermediates are formed. On the basis of DFT calculations, these intermediates have been proposed to be of the following nature: $[Cu^+—OCH_3—Cu^{2+}]$ and $[Cu^+—OH—Cu^{2+}]$. When these intermediates were reacted with steam and methanol was released into the gas phase, Cu^+ was reoxidized to Cu^{2+}, illustrating that methane activation involves a change in the oxidation state of copper. Moreover, it was found that the
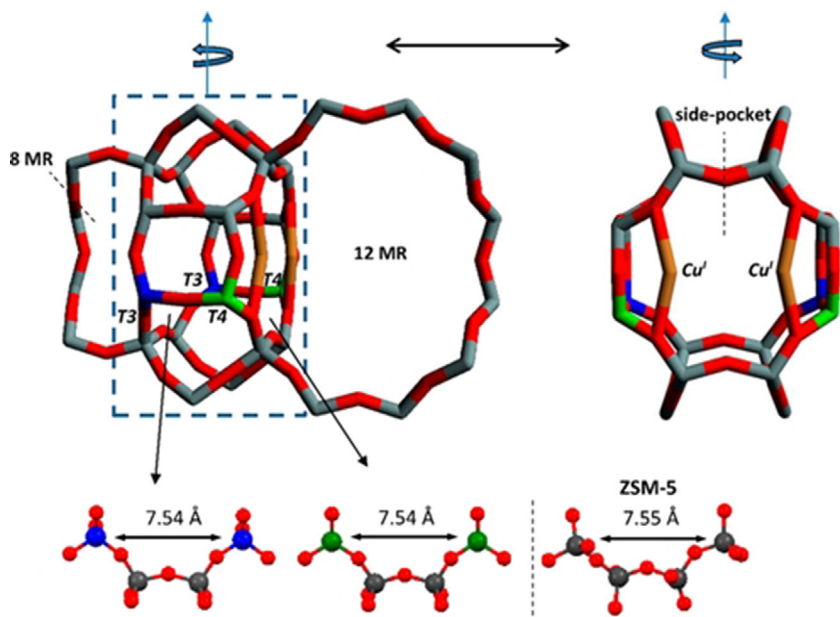
Figure 35 Top: Local structures of the MOR framework at the intersection of the side pocket with the 12-MR and 8-MR channels. T4 and T3 atoms of a possible Al—Si—Si—Al configuration for Cu—O—Cu coordination are indicated, respectively, in green (light gray in the print version) and blue (black in the print version). A pair of Cu^I atoms (yellow; light gray in the print version) with bite angles of 150° is placed at two T4 sites. Oxygen atoms at the outside of the 8-MRs and 12-MRs are omitted for clarity. Bottom: Comparison of the local structure stabilizing the Cu—O—Cu site in ZSM-5 with T4–T2–T2–T4 and T3–T2–T2–T3 sequences in MOR. The distance between two T-atoms with hypothetical Al substitution is indicated. *Reprinted with permission from Ref. (409). Copyright (2015) American Chemical Society.*

structure of the active Cu^{2+} species changes as a function of operating conditions. In a dry pretreatment environment, copper was found to be present as mono(μ–oxo) and bis(μ–oxo) dicopper species. However, under wet conditions, the dicopper species was destabilized to form a hydrated Cu^{2+} species, although a small amount of water-stable Cu^{2+} oxide remained that was also found to be active for the activation of methane. A hydrated reaction environment is required to release methanol into the gas phase and close the catalytic cycle. Hence, it has been suggested that more efforts should be directed to the investigation of this water-stable Cu^{2+} species, which is able to partially oxidize methane to methanol.

In a follow-up investigation, Alayon *et al.* reported detailed X–ray absorption data on the electronic and geometric structure of copper sites in mordenite during exposure to oxygen, helium, and subsequently methane and proposed that about 50% of all copper atoms changed their structure upon interaction with methane *(412)*. These findings were corroborated later by the same group with the help of DFT calculations and *in situ* time-resolved XAS *(413)*. In this investigation, Alayon *et al.* focused on the genesis of the reactive copper cores during treatments prior to methane activation, in an effort to obtain additional insights in the mechanisms of dehydration, autoreduction, and activation of molecular oxygen. The results of Alayon *et al.* are summarized in Figure 36, which shows the genesis of the methane–activating site via the steps of dehydration (completed at $\approx 200\ °C$), activation in oxygen (up to $\approx 400\ °C$), and autoreduction (in helium), leading to the final formation of a mono-(μ–oxo)dicopper complex with a bis-(μ–oxo)dicopper complex as intermediate formed upon oxygen activation at $400\ °C$. The work also cautions the reader on the interpretation of XAS data, as it measures an average structure of the total population of copper complexes.

More recently, Grundner *et al.* investigated Cu/mordenite as a viable system for the selective conversion of methane to methanol *(414)*. In conflict with the above proposals for the active sites on Cu/mordenite by Schoonheydt, Sels, Solomon and coworkers, and Alayon *et al.*, Grundner *et al.* propose a trinuclear copper–oxygen cluster as the active species for methane activation. Evidence for this conclusion comes from catalytic experiments, XAS, and DFT calculations, and comparison with the pMMO enzyme. Further characterization of the pMMO enzyme has led Chan *et al.* to recently propose that tricopper clusters are the active cores for the oxidation of methane to methanol with O_2 *(415)*. Grundner *et al.* used copper acetate as the precursor at a pH of 5.7 to maximize the concentration of
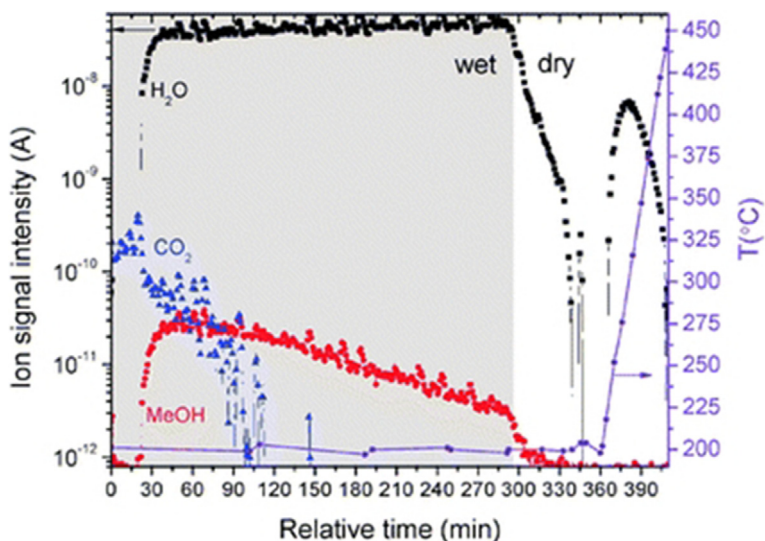
Figure 36 Mass spectrometer-detected signals of H_2O ($m/z = 18$), CO_2 ($m/z = 44$) and MeOH ($m/z = 31$) during the treatment of Cu-MOR in wet helium at 200 °C after methane interaction, and subsequent heating in dry helium at 5 K/min. *Reproduced with permission from Ref.* (410).

partially hydrolyzed $Cu(OH)^+$ ions to be ion exchanged with mordenite (414). By activating their catalyst at a temperature of 500 °C in O_2, it was possible to convert methane into methanol at 300 °C, which could be released by purging the reactor with water. In addition to methanol, DME was observed. The total yield of methanol per gram of zeolite catalyst was an order of magnitude higher than the maximum methanol yields reported initially by Groothaert *et al.* (160 vs. ≈11 µmol/g). A linear dependency of the activity on the Cu^{2+} concentration was found, as shown in Figure 37, suggesting that only one type of active site was formed. Furthermore, the slope was around 0.3, which was taken as evidence that three copper centers were involved in the oxidation of one methane molecule. With this finding in hand, combined with investigations on the siting of copper–oxo species indicating that the copper clusters were balancing the charge of two aluminum sites in the 8-MR of the side pockets of mordenite, the authors developed a series of model structures for trinuclear copper clusters in mordenite on the basis of DFT calculations. The proposed copper–oxo cluster predicted by DFT calculations was then used for detailed analysis of X-ray absorption spectra, leading to the structure and location of the $[Cu_3(\mu\text{-}O)_3]^{2+}$ cluster as shown in Figure 38. Interestingly, this copper
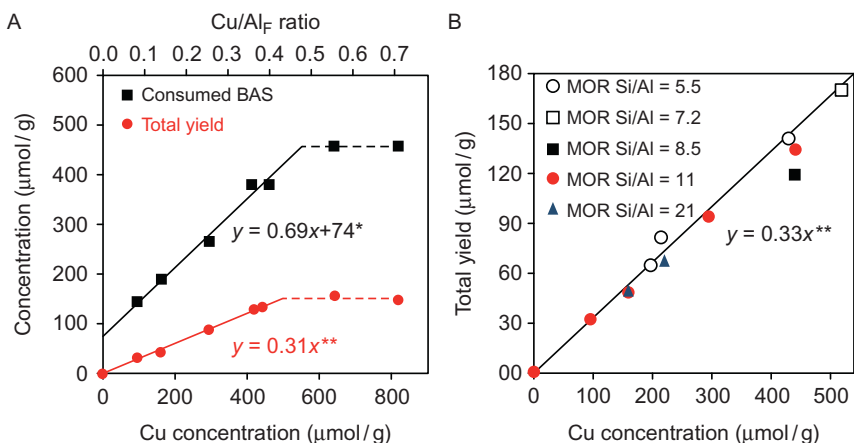
Figure 37 (A) The concentration of tetrahedrally coordinated aluminum acting as an ion exchange site for Cu^{2+} (detected as Brønsted acid sites, BAS, in the H-form) and the total yield of methanol as a function of Cu concentration in Cu-MOR with Si/Al $=11$ and (B) total yield of methanol as a function of Cu concentration in Cu-MOR for various Si/Al ratios. *The slope of 0.69 indicates an exchange stoichiometry of 2/3, meaning that two H^+ are substituted by three Cu^{2+} (forming a trinuclear complex with oxygen with an overall charge of +2). The offset of 74 µmol/g shows slight dealumination of the framework ($\approx 5\%$) during Cu exchange. **The slopes of 0.31 and 0.33, respectively, indicate that three Cu centers are involved in the oxidation of one methane molecule. *Reproduced with permission from Ref.* (414).
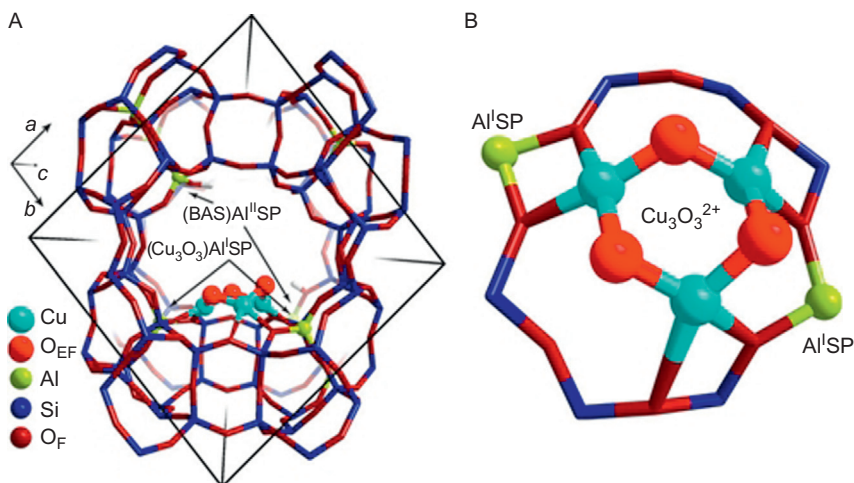
Figure 38 Model of the $Cu_2O_3^{2+}$ cluster inside mordenite. The zeolite model contains paired (type I) and isolated (type II) aluminum atoms located at the pore mouth of the side pocket. The cluster is stabilized by two anionic centers associated with the Al_{SP}^I lattice sites at the entrance of the MOR side pocket (B) such that the extra-framework oxygens responsible for the initial C—H activation are pointing toward the main channel of MOR (A). The charge due to the remaining Al_{SP}^{II} is compensated by protons resulting in BAS formation. *Reproduced with permission from Ref.* (414).

cluster did not exhibit a strong absorption band at 22,200 cm^{-1}; instead, a relatively weak and broad band at 31,000 cm^{-1} was detected, which gradually decreased in intensity upon reaction with methane. In light of this work, one should conclude that a number of distinct types of copper species, accommodated in the mordenite structure, can activate methane and, probably, more are still to be identified in the near future.

It has been demonstrated that in addition to the showcase systems, Cu/ZSM-5 and Cu/mordenite, many other zeolite structures are able to activate methane for conversion to methanol, first in the work by Smeets *et al.*, as discussed above, and more recently by Wulfers *et al.* *(416)*. The authors reported various copper–containing small-pore zeolites and zeotypes, including Cu/SSZ-13, Cu/SSZ-16, Cu/SSZ-39, and Cu/SAPO-34, as active systems, and compared the activity of these 8-MR materials with those of Cu/ZSM-5 and Cu/mordenite. It was found that the methanol yield, expressed in µmol/g catalyst, decreases in the order: Cu/SSZ-16 (39 µmol/g) > Cu/SSZ-39 (36 µmol/g) > Cu/SSZ-13 (31 µmol/g) > Cu/Mordenite (31 µmol/g) > Cu/ZSM-5 (16 µmol/g) > Cu/SAPO-34 (15 µmol/g). The authors also explored the role of the copper salt and found that zeolites exchanged with copper (II) acetate produced more methanol per gram of zeolite and more methanol per mole of copper than zeolites exchanged with copper (I) chloride. However, Cu/mordenite and Cu/SAPO-34 deviated from this rule and produced much more methanol when exchanged with Cu^{2+} than when exchanged with Cu^{+}. Taking into account that the space in the cages of the CHA structure is rather limited, the fundamental question arises as to whether the proposed active dinuclear (or trinuclear) copper species can reside in these 8-MR materials. If not, then other active copper species have to be inferred.

The nature of the medium that is used to extract the methanol product has been found to be very important. Extraction with a water–acetonitrile mixture was found to be less effective than extraction with water vapor. For example, Groothaert *et al.* observed that Cu/ZSM-5 released ≈8 µmol/g of methanol when extracted with liquid water, although 22 µmol/g CO$_2$ was formed when heating the sample in helium. Beznis *et al.* demonstrated that the amount of methanol extracted from a Cu-ZSM-5 material increases in the following order depending on the type of solvent: hexane < acetonitrile < acetonitrile/water < ethanol (see Figure 39). This sequence clearly indicates that the more polar or protic the solvent is, the higher the amounts of methanol produced.
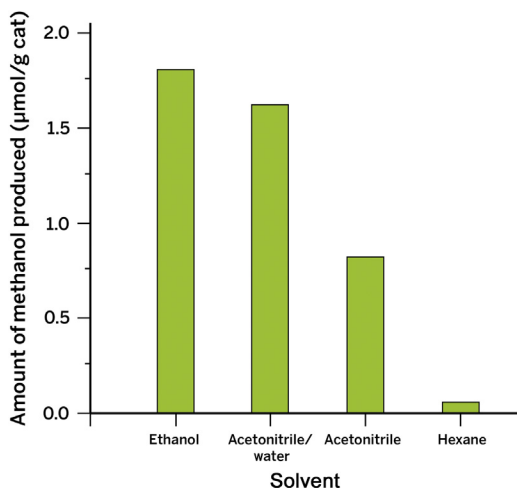
Figure 39 Influence of the extraction solvent on the amount of methanol produced for a ZSM-5 sample with 2.4 wt.% copper introduced via ion exchange using copper acetate. *Adapted from Ref. (408).*

It was proposed that the role of the solvent is not only to dissolve the reaction product but also to provide protons to the reaction intermediate so that it can be liberated from the surface. In this context, it is important to refer to the research work of Shappard *et al.*, who recently reported that the amount of methanol extracted from Cu/ZSM-5 was about 2–6 times higher when water vapor was used to perform the extraction, relative to the use of liquid water *(417)*. The authors developed a low temperature, isothermal, gas–phase, recyclable process to convert methane to methanol on Cu/ZSM-5 by conducting the methane reaction and steam extraction both at 150 °C; though it must be mentioned that they used NO instead of O_2 at 150 °C to create the required active copper species. The recyclability of the catalyst was demonstrated by three successful consecutive tests. Similarly, N_2O can be used to activate the copper species, but the temperature has then to be raised to 200 °C.

Interestingly, the reactivity of metal ion–exchanged zeolites for direct methane activation is not limited to copper and iron; in fact, cobalt, nickel, and zinc have also been found to catalyze this reaction. Beznis *et al.* were the first to show that Co/ZSM-5 can oxidize methane to methanol and to formaldehyde *(418)*. It turned out that the preparation route strongly influenced the catalytic activity and selectivity. Co/ZSM-5 materials, prepared by ion exchange at room temperature and thus having most of the cobalt in ion

exchange positions, turned out to be the most selective toward formaldehyde, whereas impregnated samples, which contained more oxidic cobalt species, were more selective toward methanol. In a follow-up article, Beznis explored the role of mesoporosity by treating zeolite ZSM-5 with alkaline solutions *(419)*. A linear relationship between the ZSM-5 surface area for alkaline-treated samples loaded with cobalt and the amount of methanol produced from methane and O_2 at 150 °C on these Co/ZSM-5 samples was observed. Subsequent acid treatment, to remove the EFAL species, led to an increased amount of highly dispersed Co^{2+} species inside the ZSM-5 channels, which resulted in a higher selectivity toward formaldehyde. Also the nature of the cation matters; Co/H-ZSM-5 was found to be more selective toward formaldehyde than Co/Na-ZSM-5. Kung *et al.* later confirmed the main findings by Beznis *et al.* and provided additional insights into the working principle of Co/ZSM-5 *(420)*. More specifically, by using *in situ* IR spectroscopy, Kung *et al.* could demonstrate that in addition to methanol and formaldehyde, formate was formed on Co/ZSM-5. It was shown that cobalt formate species can be produced by direct oxidation of methane and by the Cannizzaro reaction (i.e., a nonoxidative disproportionation) of formaldehyde at 200 °C. In addition to the IR absorption bands assigned to adsorbed methoxide and formate, the spectroscopic fingerprints of polyoxymethylene were found. Continued formation of surface formate was observed during purging in helium, providing evidence that a substantial fraction of the formaldehyde was stored in the surface polyoxymethylene phase. On the other hand, the thermal stability of the surface cobalt formate may prevent the continuous operation with Co/ZSM-5 as a selective methane oxidation catalyst, and alternative methods have to be developed to remove the formate species, or their formation has to be prevented.

Shan *et al.* recently demonstrated that also Ni/ZSM-5, activated at 650 °C in pure O_2, can oxidize methane at 175 °C with a total yield of methanol (main product), formic acid, and ethylene glycol of 14.9 μmol/g catalyst *(421)*. Based on XPS, UV–vis spectroscopy, and XAFS data, it was concluded that the active site was a bent mono-(μ-oxo)dinickel complex. The complex was characterized by an absorption band at around $22,800 \text{ cm}^{-1}$, which decreased in intensity when methane was flowing over the zeolite material. The formation of ethylene glycol was explained by the intermediate formation of ethylene oxide, which was hydrolyzed with water to form ethylene glycol. Ethylene oxide was proposed to be formed from ethylene via dehydrogenation of ethane, which could result from coupling

of two methyl radicals. Xu *et al.* reported on Zn/ZSM-5 materials, which are able to activate methane at room temperature *(422)*. It was found that a homolytic C—H bond cleavage took place when methane was interacting with an oxygen-containing di-zinc cluster, and the resulting methyl radicals were trapped by the zeolite matrix, leading to the formation of surface methoxy intermediates. In parallel to this homolytic dissociation reaction, a heterolytic pathway occurred, leading to the formation of zinc methyl species when methane interacted with isolated Zn^{2+} ions in the ZSM-5 framework. The conclusion emerging from this work is that for each of the above-mentioned catalysts and conditions, we should further inspect whether a heterolytic or homolytic pathway is operating, and what the exact role of the zeolite matrix is in stabilizing the reaction intermediates that form.

In a another recent investigation, Narsimhan *et al.* achieved the direct conversion of methane to acetic acid more favorably on Cu/mordenite than on Cu/ZSM-5, by coupling methane oxidation with subsequent carbonylation of surface methoxy groups *(423)*. More specifically, it was found that two sites exist in partially acidic Cu/mordenite: a methane activation site and a carbonylation site, as illustrated in Scheme 12. Similar to the above-described spillover process on Fe/ZSM-5 formulated by Panov and coworkers, activated methoxy species can migrate from the methane-activating species to a carbonylation site, enabling the step-wise generation of acetic acid. The availability of both sites proved to be crucial, as in Cu/Na-mordenite without Brønsted acid sites, it was found by using
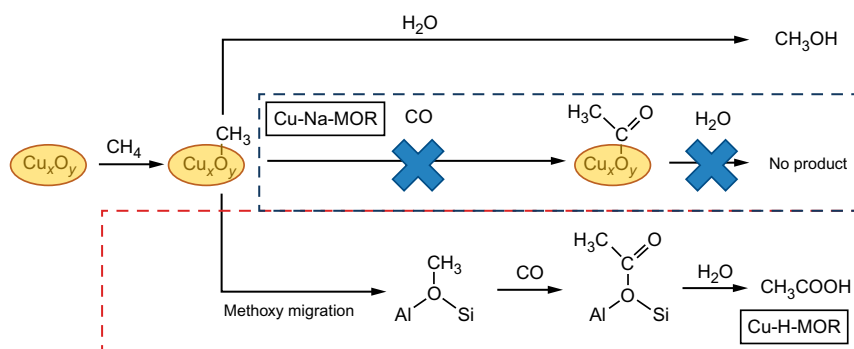

Scheme 12 Scheme representing methane oxidation and carbonylation on Cu/mordenite obtained by exchange from acid or sodium precursors as proposed by Narsimhan *et al. Reprinted with permission from Ref. (423). Copyright (2015) American Chemical Society.*

spectroscopy that a methane-activating species, characterized by a band at 22,200 cm^{-1}, was present, but not a carbonylation site. In contrast, Cu/H-mordenite with a small amount of Brønsted acid sites was much more active for carbonylation, and a new Cu^{2+} site was found, active for methane activation. The coupled methane and carbonylation reactions showed that when trace amounts of Brønsted acidity were present, an increased carbonylation activity could be noticed resulting in a higher amount of acetic acid. Wu *et al.* reported on a similar approach with a Zn/H–ZSM-5 catalyst *(424)*. It was found that methane and carbon dioxide were converted into acetic acid at temperatures between 250 and 500 °C. Zinc sites were able to activate methane to form zinc methyl species, which reacted further with CO_2 to form a zinc surface acetate. The Brønsted acid sites of the zeolite were thought to be involved in the proton transfer reaction toward the surface zinc acetate, enabling its release as acetic acid.

4.1.1.2 Methane Activation in the Liquid Phase

Inspired by the initial reports on the reaction of iron- or copper-containing zeolites with methane at low temperature after activation with N_2O or O_2 at high temperature, Hammond *et al.* explored the oxidation of methane to methanol in aqueous conditions using hydrogen peroxide *(425)*. Catalytic, theoretical, and spectroscopic experiments led to the proposal of a reaction cycle, as shown in Figure 40. In the first step, H_2O_2 reacts at the iron site to produce a species able to activate methane; subsequently, methyl hydroperoxide is formed as the primary product, which can be further converted to methanol, as well as formate and CO_2. The active species in Fe/ZSM-5 was proposed to consist of a binuclear iron–oxo species. In a detailed follow-up investigation, Hammond *et al.* further elucidated the nature of the active species and the associated reaction pathways *(426)*. Methane conversion on Fe/ZSM-5 was found to occur with a TOF of 14,200 h^{-1}, and removal of the catalyst material in a hot filtration test halted the reaction, indicating that iron was not leaching in appreciable amounts into the reaction solution. In other words, the catalyst was truly heterogeneous in nature. Time-resolved catalytic experiments confirmed that the primary oxidation product was methyl hydroperoxide (MeOOH), and subsequently, methanol, formic acid, and CO_2 were formed with formic acid as the main reaction product (selectivity of 70% after 2 h of reaction). Interestingly, formaldehyde was not observed, although higher oxidized products were detected. Addition of copper to Fe/ZSM-5 led to a selectivity change, and formic acid was no longer the dominant reaction product; instead, methanol was found in high
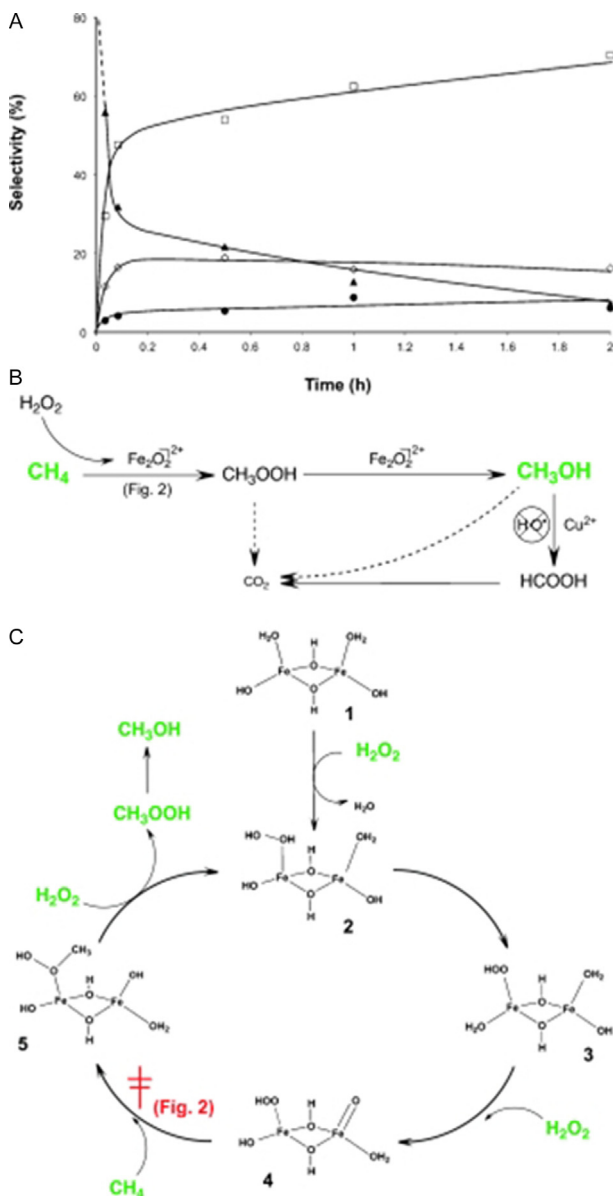
Figure 40 (A) Time-on-line profile for the liquid-phase oxidation of methane with hydrogen peroxide and ZSM-5 *(30)*. Key: Triangles = methyl hydroperoxide (MeOOH); diamonds = methanol (MeOH); squares = formic acid (HCOOH); circles = carbon dioxide (CO_2). (B) A potential reaction scheme for the oxidation of methane based on the time-on-line profile. Methanol is formed through the conversion of the methyl hydroperoxide intermediate on the iron sites present in the catalyst. ˙OH radicals produced during the reaction are later responsible for the overoxidation of methanol. (C) Catalytic cycle for the oxidation of methane to CH_3OOH using H_2O_2, catalyzed by a binuclear iron species in ZSM-5. The overall charge in each case is formally +2, as the species acts as an extra-framework cation within the zeolite. *Reproduced with permission from Ref.* (425).

amounts (>80% selectivity after 30 min of reaction). The Cu^{2+} ions in the Cu–Fe/ZSM-5 catalyst were proposed to be scavengers of hydroxyl radicals ($OH^{\bullet}$) that prevent the liberation of $OH^{\bullet}$ radicals during H_2O_2 decomposition. Several intriguing questions were to be answered, regarding the nature of the active sites and the related reaction mechanism, and the possible involvement of Fenton's chemistry. Hammond *et al.* hypothesized that hydrogen peroxide is decomposed to give a hydroxyl radical ($2\ H_2O_2 \rightarrow OH^{\bullet} + {}^{\bullet}OOH + H_2O$), which abstracts a hydrogen atom from methane to give methyl radicals. This methyl radical can then react with the cogenerated hydroperoxyl radical to form methyl hydroperoxide. To verify this hypothesis, the catalytic performance of Fe/ZSM-5 was compared with that of the Fenton's reagent for the activation of methane in the presence of H_2O_2. Although the Fenton system was able to oxidize methane, it was much less active than the Fe/ZSM-5 catalyst. Moreover, the selectivity toward CO_2 was more than 50% with Fenton's reagent, whereas it was only 5% in the case of Fe/ZSM-5. To further rule out the possibility that Fenton-type radical chemistry was responsible for the observed main catalytic findings, the authors used an inorganic hydroxyl radical scavenger, namely Na_2SO_3. It was found that this scavenger significantly decreased the activity of the homogeneous catalyst of Fenton's reagent, whereas no decrease in activity was observed for Fe/ZSM-5. Based on these experiments, it was concluded that the activation of methane on Fe/ZSM-5 does not proceed via a homolytic decomposition of H_2O_2 and a subsequent free-radical chain mechanism involving highly reactive methyl, hydroxyl, and hydroperoxyl radicals. To further strengthen this conclusion, EPR spectroscopy, together with a spin-trapping agent 5,5-dimethylpyrrolidine–N–oxide (DMPO), was used. Whereas radical species were detected in the presence of Fenton's reagent, no methyl- or other carbon-centered radical species were observed when Fe/ZSM-5 was used.

In a subsequent investigation, Hammond *et al.* explored the influence of the method of iron deposition and concluded that, although postsynthetic routes to deposit Fe^{3+} into ZSM-5 result in active catalysts, the extraction of Fe^{3+} from zeolite framework sites leads to much more active catalysts *(427)*. More specifically, optimal activity and selectivity were obtained by pretreating Fe-silicalite-1 at a temperature of 750 °C, ensuring the generation of a sufficient amount of extra-framework oligomeric iron species, which are considered to be the active species. Pretreatments at higher temperatures lead to the formation of bulk iron oxide, and hence excessive H_2O_2 decomposition and CO_2 conversion. Furthermore, Hammond *et al.*

found a peculiar promotion effect when Al^{3+} or Ga^{3+} were incorporated into the silicalite–1 framework *(428)*. Although both aluminum and gallium were not identified as part of the active site, they were inferred to facilitate the extraction of iron species from the zeolite framework upon heating, as well as the stabilization and dispersion of the generated extra-framework iron species. By optimizing the overall composition, it was possible to obtain the most highly active methane activation catalyst so far reported. This ZSM–5 catalyst contained 0.095 wt.% Fe and 2.2 wt.% Al.

More recently, Hammond *et al.* thoroughly characterized Fe–silicalite–1 and Fe–ZSM–5 by using resonance-enhanced Raman spectroscopy *(429)*. It was found that several framework and extra-framework Fe^{3+}-species could be present. The most characteristic Raman band appeared at $\tilde{v} = 521$ cm^{-1}, and its intensity was found to be correlated with the catalytic activity of the Fe–zeolite. Comparison of this Raman band with literature data on reference model compounds, DFT calculations, and the above-described UV–vis and XAS data, let the authors conclude that this feature is due to a binuclear extra-framework iron species and represents an Fe—O(H)—Fe stretching vibration. The Raman band disappeared when H_2O_2 was added to the reaction mixture, although its removal and some heating led to a complete regeneration of the 521 cm^{-1} feature. By *in situ* monitoring of the reaction of methane with Fe/ZSM–5 in the presence of either H_2O_2 or *tert*-butyl hydroperoxide, the authors were able to identify the generation of corresponding Fe—OOH and Fe—OO*t*Bu intermediate species. This finding further corroborates the reaction cycle, as outlined in Scheme 13.
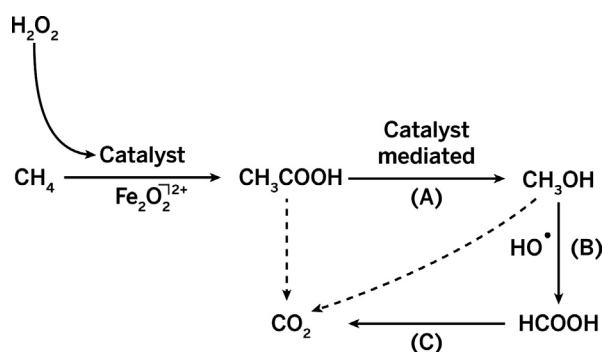
Scheme 13 Proposed reaction network for the oxidation of methane on ZSM-5 *(30)*. The primary reaction product, MeOOH, undergoes selective conversion to MeOH (A) or non-selective conversion to HCOOH. HCOOH (B) and CO_2 (C) are formed by the subsequent overoxidation of MeOH. Steps (B) and (C) are eliminated upon the addition of Cu^{2+} to the catalyst. *Reproduced with permission from Ref.* (426).

It is emphasized that Hammond *et al.* found an iron—oxygen stretching vibration, v(Fe—O), at 631 cm^{-1}, which is characteristic of Fe^{III}—OOH, but the accompanying peroxo stretching vibration, v(O—O), which is expected at around 750–800 cm^{-1}, was not observed. Both the possible overlap of these bands with the spectral features of the MFI framework and the short lifetime of the oxo species were put forward as potential reasons for the absence of the v(O—O) Raman band.

Forde *et al.* successfully extended the work of Hammond *et al.* on methane-to-methanol conversion to the oxidation of ethane using hydrogen peroxide as oxidant *(430)*. It was found that both Fe/ZSM-5 and Fe–Cu/ZSM-5 are able to activate ethane, and as a result, a range of C$_2$ as well as C$_1$ oxygenates could be produced at a temperature of 50 °C. For example, a 2.5% Fe/ZSM-5 material was able to achieve a conversion of $\approx 56\%$ with selectivities toward acetic acid, formic acid, and ethanol of about 70%, 21%, and 5%, respectively. Ethylhydroperoxide was considered as a second primary oxidation product, which together with ethanol was subsequently converted to acetaldehyde and acetic acid, while C—C scission reactions led to the formation of a mixture of C$_1$ oxygenates, including methylhydroperoxide, methanol, formic acid, and CO/CO$_2$. Interestingly, in the presence of a 2.5–2.5% Cu–Fe/ZSM-5 material at a limited ethane conversion of approximately 1.5%, ethylene was found in the gas phase, with the selectivity being around 38%. A complex reaction network was proposed, involving carbon-based radicals, which gives the observed range of C$_2$ oxygenates, with sequential C—C bond cleaving generating various C$_1$ oxygenates. In a follow-up investigation, Armstrong *et al.* further explored the potential of these catalysts and used a continuous flow reactor in an attempt to maximize the yields toward acetic acid (with the Fe/ZSM-5 catalyst) or ethylene (with the Cu–Fe/ZSM-5 catalyst) and minimize the overoxidation to CO$_2$ as well as the occurrence of C—C scission reactions *(431)*. The catalytic data collected under steady-state conditions at various pressures, temperatures, and reactant concentrations revealed that under optimal conditions (at a temperature of 50 °C and 20 bar), a 0.4% Fe/ZSM-5 catalyst could convert 22% ethane per single pass, reaching 16% yield of acetic acid, with only very small amounts of iron leaching.

4.1.2 Nonoxidative Routes for Methane Activation

Although the nonoxidative route for methane conversion is thermodynamically unfavorable compared with the oxidative route, the absence of oxidants in the reaction environment can reduce the amount of CO$_x$

formed. Since Wang *et al.* discovered in 1993 that methane can be directly converted to benzene and other aromatics *(432)*, there has been a significant interest in this reaction, termed methane dehydroaromatization (MDA), from both an academic and an industrial point of view. Wang *et al.* used a metal-modified H–ZSM-5 catalyst at reaction temperatures above 700 °C and achieved low conversion (<2%) and high benzene selectivity (~100%). One of the main advantages of this process is that no other reactants are required, and it can be performed at or near the methane source. Since a significant amount of H_2 (9 molecules) is produced per benzene molecule during the reaction, many research groups and industries were initially interested in the conversion of methane to H_2 from sources such as shale gas *(433)*. Given the increasing use of H_2 as an alternative energy source, namely in fuel cells, the MDA reaction could serve many different purposes, but it is currently mainly used for its high selectivity toward aromatic compounds. However, the MDA process has its disadvantages; in particular, the high reaction temperatures (>650 °C) favor the formation of coke, which causes problems with catalyst stability. Hence, a viable industrial interest is lacking.

Together with metal-doped zeolites, metals supported on metal oxides have also been reported as effective catalysts for the conversion of methane to aromatics. In 1991, Ismailov *et al.* observed that the high-temperature contact of methane with Re/Al_2O_3 catalysts generated new surface sites active for the formation of benzene *(434)*. Moderate conversion and aromatic selectivities were obtained by Abasov *et al.* *(435)* using Ni/ Al_2O_3 catalysts (75% methane conversion, 75% benzene selectivity) and Claridge *et al.* *(436)* using $K/BaCO_3$ and/or $NaCl/MnO_2$ (13% conversion, 18–23% selectivity). Recently, Guo *et al.* showed that silica–supported iron materials are also excellent catalysts for the production of aromatics via the direct, nonoxidative conversion of methane *(437)*. In a breakthrough discovery, they were able to demonstrate that isolated iron atoms (coordinated with one silicon and two carbon atoms) embedded in a silica matrix achieve high methane conversion and high hydrocarbon selectivity (99%). Ethylene, benzene, naphthalene, and H_2 were produced during reaction at a temperature of 1090 °C. Coke formation was insignificant, making this an atom-economical process. The absence of adjacent iron sites proved essential in avoiding C—C coupling at the catalyst surface, which suppressed the deposition of coke, even after 60 h of reaction *(438)*. Given the nature of this review article, we will focus on the remarkable progress made regarding

metal–impregnated zeolite-based MDA catalysts and related reactor designs for the activation of methane to aromatics (387,439).

As stated above, Wang et al. were the first group to report that modifying zeolite ZSM-5 with metal ions produces a catalyst capable of converting methane to aromatic products (432). By impregnating ZSM-5 with either molybdenum or zinc (2 wt.%), the catalytic activity was improved (7.2% and 2.3% conversion, respectively), in comparison to that of the unmodified ZSM-5 (1.0%). High benzene selectivity (100%) was achieved in all cases at a reaction temperature of 700 °C. In a temperature–programmed experiment, they noted that the starting temperature of the dehydroaromatization of methane was 50 K lower for Mo-ZSM-5 than for Zn-ZSM-5, with ethane and H_2 detected at the same time as benzene started to evolve. It was suggested that the catalytic reaction takes place via a carbenium ion mechanism. Wang et al. proposed that Mo^{6+} species present in the zeolite could have a role as hydride acceptors, leading to formation of $[Mo–H]^{5+}$.

Since the discovery by Wang et al., numerous variations of the catalyst have been presented. Catalyst design parameters varied include framework type of the zeolite support, Si/Al ratio of the zeolite, nature of incorporated metal, metal loading, preparation conditions, as well as addition of other metals as promoters. Ions of transition metals ions other than molybdenum also show appreciable activity for the nonoxidative methane conversion to aromatics. In the late 1990s, Weckhuysen et al. showed that Fe-, V-, W-, and Cr-ZSM-5 catalysts are also able to activate methane, but their activity is strongly determined by preparation and treatment conditions (440). Weckhuysen et al. reported that the activity of CO-prereduced H-ZSM-5 catalysts containing 2–4 wt.% transition metal ion decreased in the order: Mo (18.3) > W (10. 8) > Fe (5.7) > V (3.9) > Cr (1.5). The numbers in parentheses specify the rate of methane conversion as molec. reacted/(metal atom*h) after 3 h on stream. The method of metal introduction was important; catalysts prepared by impregnation consistently achieved higher activity and shorter initial induction periods than catalysts prepared by solid-state ion exchange (441).

In a further investigation, it was discovered with the help of XPS that if the metal ions were introduced by impregnation, and reacted at temperatures of 750 °C during MDA, suboxides formed at the external surface, except in the case of molybdenum, which formed Mo_2C species. Samples prepared by ion exchange were more active after treatment with CO at 500 °C, which causes the metal ions to migrate to the external surface of

the zeolite. Collectively, these results demonstrate that various phases are able to activate methane at high temperatures *(442)*.

Given the high activity and selectivity of molybdenum, we need to understand why the Mo/ZSM-5 materials reported by Wang *et al.* and Weckhuysen *et al.* work particularly well for this reaction. Several reaction mechanisms have been proposed by various research groups, yet there is no agreement as to which one represents the entire mechanism correctly. However, there is a general consensus that methane initially reacts with MoO_x species to give MoC_x species *(443, 444)*. Solymosi *et al. (445)* and Wang *et al. (446, 447)* characterized the materials by XPS and noted that exposure of calcined Mo/ZSM-5 to methane resulted in a reduction of molybdenum oxide to Mo_2C. The formation of Mo_2C and the loss of Mo^{6+} were complete after
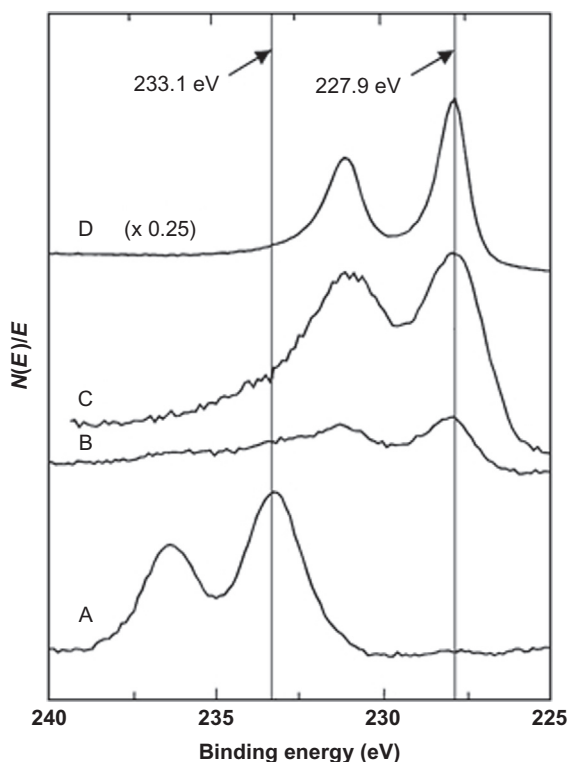
Figure 41 XP spectra of 2 wt.% Mo/ZSM-5 and Mo_2C in the Mo3d region. (A) Mo/ZSM-5 after calcination in O_2 at 700 °C; (B) after subsequent exposure to CH_4 at 700 °C for 2 h; (C) fresh sample pretreated at 700 °C in 20% CH_4/H_2 for 12 h and then in 10% CH_4/H_2 for 4 h, following treatment in O_2 at 700 °C; (D) unsupported Mo_2C, made by calcining MoO_3 at 700 °C in flowing O_2 and then treating at 700 °C in 20% CH_4/H_2 for 12 h and in 10% CH_4/H_2 for 4 h. *Reproduced with permission from Ref. (447).*

exposure for 2 h, which fits well with the induction period observed in the MDA reaction (Figure 41). These MoC_x species are then the centers that activate methane and form C—C bonds, thus producing molecules such as ethylene. Finally, ethylene intermediates migrate to Brønsted acid sites of the zeolite and undergo oligomerization and aromatization, yielding benzene, toluene, and naphthalene (448,449). This mechanism implies that Mo/ZSM-5 is a bifunctional catalyst. Moreover, its structure has advantages in that it permits shape selectivity, as well as high metal dispersion.

Considering that both the molybdenum and the zeolite contribute to the MDA reaction, the catalyst preparation conditions play a major role for its final performance. Although a significant number of different preparation methods exist in the literature, we would like to focus on the most commonly used method: incipient wetness impregnation. Given that the first reaction step in MDA takes place on MoO_x species, it is vital that a high dispersion is obtained in the host zeolite. However, impregnation with aqueous ammonium heptamolybdate ($(NH_4)_6Mo_7O_{24} \cdot 4H_2O$) solution results in bulky molybdate anions ($Mo_7O_{24}^{6-}$) on the external surface of the zeolites (450). Therefore, calcination is employed, to decompose the precursor into dispersed MoO_3 crystallites. The calcination temperature and time are critical at this point, to determine the location and size of the molybdenum species in or on the zeolite. Low calcination temperatures (of 240 °C) produce large crystallites that remain on the external surface of the zeolite (as they are too large to enter the zeolite micropore system). However, too high a calcination temperature (e.g., 700 °C) leads to the formation of aluminum molybdate ($Al_2(MoO_4)_3$), as a result of the reaction of EFAL atoms of the zeolite with the molybdenum precursor (451,452). Xu et al., by combining FT-IR spectroscopy and differential thermal analysis, determined that the optimum temperature is 500 °C. These conditions lead to only a small amount of finely dispersed molybdenum oxide crystallites on the external surface, and the majority of the species are small enough to migrate (as $(MoO_x)_n$ oligomers) into the zeolite micropore system (453).

While inside the zeolite micropore channels, MoO_x species react with H^+ atoms of Brønsted acid sites and form strong Mo—O—Al bonds. The $[MoO_2(OH)]^+$ species connected to Brønsted acid sites subsequently condense (when two $[MoO_2(OH)]^+$ species are in close proximity) to produce $[Mo_2O_5]^{2+}$ dimers and water (Scheme 14, Equation 1) (454–457). The formation of dimers is favored by a high Si/Al ratio of the zeolite, whereas a high Brønsted acid site concentration (low Si/Al ratio) favors the formation of monomeric species (MoO_2^{2+}) (458,459). Two alternative reactions/interactions are also plausible: A second Brønsted acid site can react with
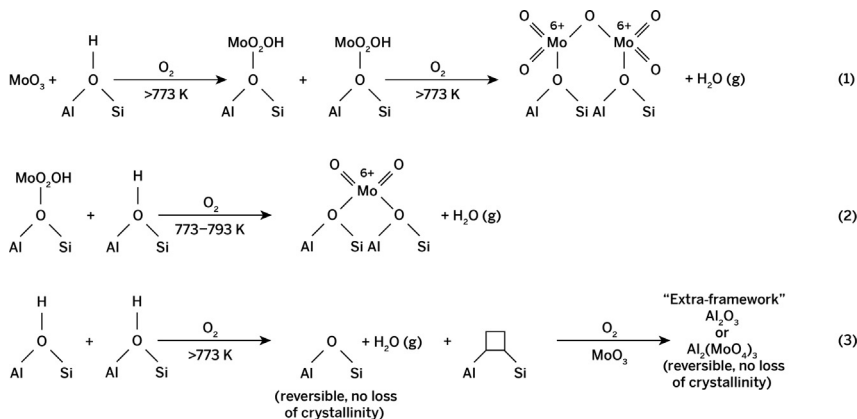
Scheme 14 Interactions between MoO_x species and Brønsted acid sites of H-ZSM-5. *Reproduced with permission from Ref.* (387).

$[MoO_2(OH)]^+$ species to form a $[MoO_2]^{2+}$-bridging cation (Scheme 14, Equation 2). Aluminum extraction from the zeolite framework can also take place, via condensation of two adjacent Brønsted acid sites, leading to an effective loss of two Brønsted acid sites (Scheme 14, Equation 3) (387).

Of course, the interaction of molybdenum with Brønsted acid sites will affect the zeolite acidity, which is needed for the conversion of ethylene intermediates to aromatics during the MDA reaction; therefore, the molybdenum loading needs to be regulated such that the Brønsted acid site concentration is not significantly decreased. Also, Chen et al. discovered that at a molybdenum loading above 5 wt.%, isolated MoO_x species decrease the surface area of the catalyst dramatically (460). Therefore, the molybdenum concentration needs to be carefully optimized. It is now generally accepted that dimeric species are precursors for the active centers in methane conversion on Mo/ZSM-5 bifunctional catalysts.

A fascinating aspect of the MDA reaction on Mo–ZSM-5–based catalysts is the appearance of an induction period, during which no aromatics are formed. In early reports in 1995, Chen et al. (460) and Xu et al. (461) proposed that methyl radicals ($CH_3^{\bullet}$) formed after methane activation on MoO_x sites would dimerize to form C_2 hydrocarbons, prior to migration and aromatization on zeolite acid sites. This reaction mechanism has been contested.

Although the exact pathway is not known, there is consensus that the carburization of MoO_x through reaction with methane creates the active MoC_x sites required to form hydrocarbon (i.e., ethylene) intermediates.
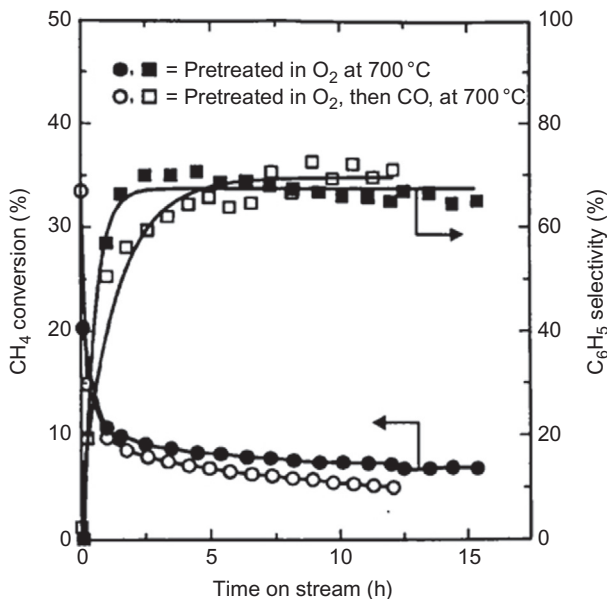
Figure 42 Methane conversion and benzene selectivity results for CH_4 conversion on 2 wt.% Mo/ZSM-5 at a temperature of 700 °C, a pressure of 1 atm, and a GHSV of 800 h^{-1}. *Reproduced with permission from Ref. (462).*

Wang *et al.* were the first to report an induction period (see Figure 42), noting that Mo^{6+} species at the external surface of the zeolite are reduced by methane to yield Mo_2C, with CO_x and H_2O formed as the only gas-phase products *(462)*. An essential step is the gradual deposition of carbonaceous species, which interact with the reduced molybdenum species to form the active sites required for methane activation *(463)*. However, too extensive formation of carbonaceous deposits, either on the acid sites or on the MoC_x active sites, is a major drawback of this reaction, since it leads to significant deactivation of the catalyst over time.

The location and nature of the active site(s) is hotly debated, considering that they may be on the external surface of the zeolite, inside the micropore channels, or in both locations. Solymosi *et al.* suggested that highly dispersed Mo_2C resides on the external surface of the zeolite and provides the active centers for methane activation *(464)*. Li *et al.* noted that MoO_x species are present on the zeolite external surface and inside the pores *(465)*. The authors reported that the MoO_x species are transformed to a mixture of MoO_xC_y, $[Mo_5O_xC_y{}^{n+}]$, and Mo_2C at 700 °C during the MDA reaction, and all species were believed to be active for methane activation. Liu *et al.*

found that molybdenum species present on the external surface were reduced by methane to β–Mo$_2$C, whereas β–MoO$_x$C$_y$ is formed inside the zeolite pore system *(466,467)*. Again, both species were proposed to be active in the MDA reaction. Ding *et al.* proposed that the reduction of Mo$_2$O$_5^{2+}$ sites by methane leads to the formation of small (i.e., <1.0 nm) MoC$_x$ clusters, which regenerates the bridging OH groups lost when forming the MoO$_x$ species during Mo–ZSM-5 preparation. This reaction is highly beneficial for the performance, because of the need for both MoC$_x$ species and Brønsted acid sites for the MDA reaction.

Summarizing the current state of our understanding, it is most common to find active molybdenum species both on the external surface and inside the zeolite micropore system, with those on the external surface less active and less stable for the MDA reaction than those inside *(468)*. There is general agreement that carburized molybdenum species are indeed the active sites during the induction period of the MDA reaction. Methane is converted to hydrocarbon intermediates (i.e., ethylene), before cyclizing and aromatizing on nearby Brønsted acid sites of the zeolite. Benzene is the main product, and the high selectivity is brought about by the shape-selective nature of the ZSM-5 pore dimensions, which are similar to the kinetic diameter of a benzene molecule (0.59 nm) *(450)*.

Although high reaction temperatures (needed to overcome thermodynamic limitations) lead to a better aromatics yield, coke deposition on the catalyst is highly detrimental to its performance, and catalyst lifetimes are extremely poor *(469–472)*. This problem is the largest challenge that researchers face and needs to be overcome before this reaction can be commercialized.

The nature of the active sites of this catalyst is also its own downfall, as these sites promote the formation of carbonaceous deposits. The dehydrogenating nature of the metal and the condensation–polymerization character of the acid sites are key in converting the olefins and aromatics into polyaromatic or graphitic-type coke *(473,474)*. The coke formed has been characterized and categorized into two types by several researchers *(463,471,475,476)*. Weckhuysen *et al.* investigated the formation of carbonaceous deposits on an Mo–ZSM-5 catalyst during 13 h on stream at 700 °C by employing XPS analysis *(471)*. Pregraphitic carbonaceous deposits (i.e., hydrogen-poor sp-type carbon) are situated on the external surface of the zeolite, whereas graphitic carbon deposits are produced inside the zeolite micropores. Carbidic carbon associated with Mo$_2$C, located in the zeolite channels, was also detected. It was discovered that the amount of sp-type

carbon increases with time on stream, and both the zeolite and the Mo_2C active sites are covered, causing deactivation. Ma *et al.* employed the methods of temperature–programmed oxidation, temperature–programmed surface reaction, and temperature–programmed hydrogenation, to observe the nature of the carbonaceous deposits on molybdenum–loaded zeolite catalysts *(472)*. Three types of carbon were identified, in general agreement with the findings of Weckhuysen *et al.*: (1) carbon associated with molybdenum sites on the external surface of the zeolite; (2) polyaromatic carbon on Brønsted acid sites; and (3) carbon associated with molybdenum in the zeolite micropores (Figure 43).

The application of various reactive gas feeds, such as O_2, CO/CO_2, N_2/NO, air, and H_2, has been investigated to seek for means to regenerate the deactivated or spent catalysts, by removing the carbonaceous deposits. There is of course difficulty in regenerating spent catalysts, because of the high temperatures that are sometimes required to "burn off" the coke deposits. High temperature could have an impact on the structure of the host and could, for example, lead to dealumination of the zeolite or cause sintering of metal particles; both phenomena would reduce catalytic performance.
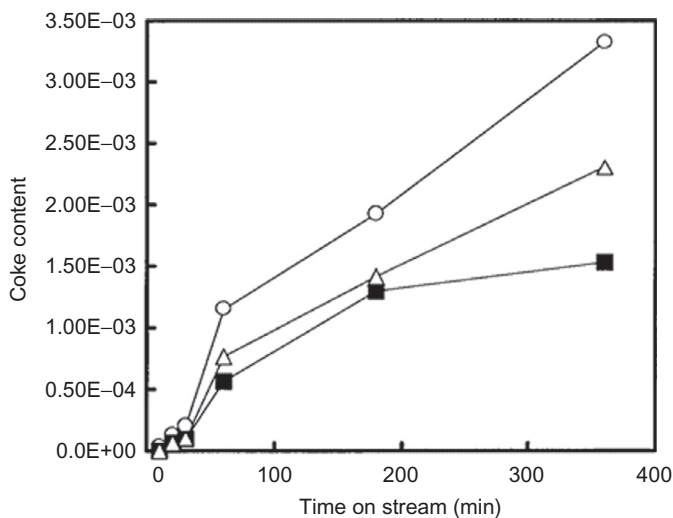
Figure 43 Variation of the content of different kinds of coke with time on stream. Circles = molybdenum-associated coke; squares and triangles = low-temperature and high-temperature aromatic-type cokes, respectively, on a Mo-H-MCM-22 catalyst. *Reproduced with permission from Ref.* (472).

Lu *et al.* showed that heating a spent catalyst in H_2 to a temperature of 900 °C produces a catalyst with lower stability than regeneration in an O_2 atmosphere at 550 °C, though both treatments were in principle successful *(477)*. The difference was thought to be due to sintering of Mo_2C microcrystals or residual coke on the catalyst. Gao *et al.* recently showed that the catalytic activity can be completely restored by using a gas–phase O_2 treatment, which recreates the isolated MoO_x species that were present before formation of MoC_x *(478)*. By using a combination of quantum chemical calculations and several spectroscopic techniques, a better understanding of the identity and anchoring sites of the initial molybdenum oxide nanostructures was obtained. A catalyst composed of 2 wt.% molybdenum supported on ZSM-5 was analyzed with diffuse reflectance UV–vis spectroscopy, and an edge energy of 4.8 eV was associated with isolated MoO_x nanostructures, with a single molybdenum atom (Figure 44). This interpretation was in good agreement with Raman spectra that showed bands of crystalline MoO_3 nanoparticles and $Al_2(MoO_4)_3$, indicating complete dispersion of molybdenum oxide. DFT calculations showed that aluminum sites are required for anchoring molybdenum oxide species; specifically, two adjacent aluminum atoms are associated with one $Mo(=O_2)_2^{2+}$ dioxo species. Adhering to Lowenstein's rule, the authors propose that "an arrangement of Al—O—$(Si—O)_2$—Al with two Al atoms as third neighbors must be the only possible double Al-atom anchoring sites for Mo dioxo species." Therefore, the number of aluminum sites, which depends on the Si/Al ratio of the zeolite, influences the distribution of molybdenum species. In general, the number of aluminum atoms that act as double-anchoring sites (i.e., two Al-atom anchoring one $Mo(=O_2)_2^{2+}$ species) decreases (but not proportionally) with an increase in Si/Al ratio. For example, at a Si/Al ratio of 140 (1.3 wt.% Mo loading, Al/Mo = 0.8), there are not enough single aluminum sites to stabilize all molybdenum atoms. DFT calculations confirmed this finding; in the absence of aluminum sites, $(Si—O—)_2Mo(=O_2)$ species are located on the external surface of the zeolite (instead of isolated $Mo(=O)_2$ dioxo species). In fact, molybdenum species populate sites in a preferred order: first double aluminum atom sites, then single aluminum atom sites, and finally silicon sites situated at the external surface of the zeolite. Performing *operando* analysis allowed the determination of regeneration possibilities of Mo–ZSM-5 catalysts. Through treatment in O_2, molybdenum carbide (formed during initial reduction with methane) is reverted to molybdenum oxide, which is redispersed to isolated nanostructures that are stabilized by anchoring on aluminum sites.
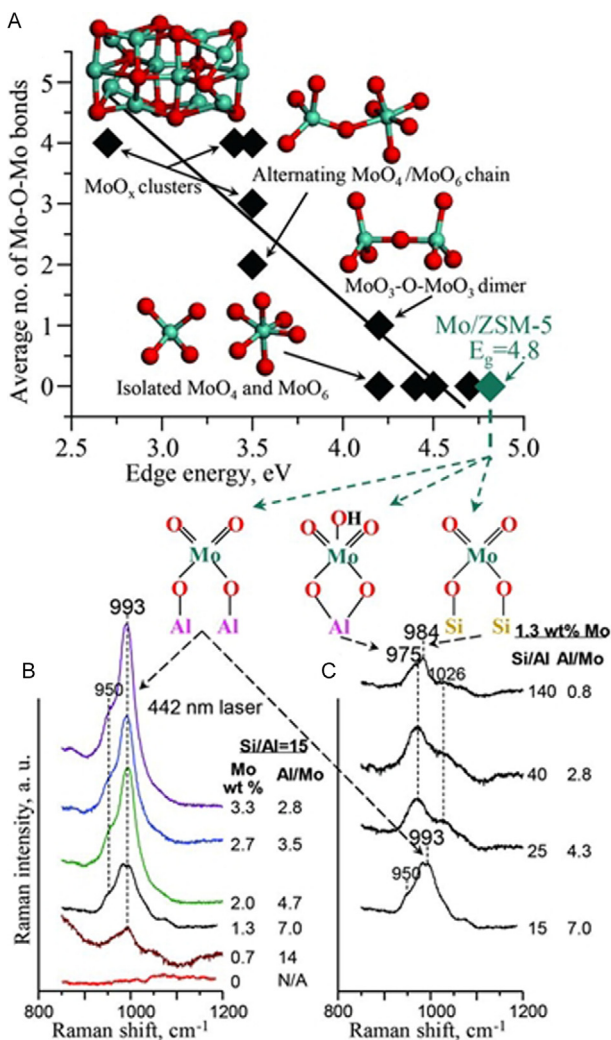
Figure 44 (A) Electronic edge energy values obtained from *in situ* UV–vis spectra of reference molybdenum oxide compounds exhibit a linear correlation with the number of bridging Mo—O—Mo covalent bonds around the central molybdenum cation. The value of 4.8 eV for 2 wt.% Mo-ZSM-5 (Si/Al = 15) corresponds to oxo-molybdenum species with a single molybdenum atom. (B and C) *In situ* Raman spectra of Mo-ZSM-5 catalysts in O_2 flow at a temperature of 500 °C as a function of (B) molybdenum loading for a constant Si/Al ratio of 15 and (C) Si/Al ratio for a constant Mo loading of 1.3 wt.% with band assignments to molybdenum oxide species based on DFT calculations; a.u. arbitrary units. *Reproduced with permission from Ref.* (478).

Ma *et al.* also investigated the use of air and air containing a small amount of NO (2%) to potentially regenerate a used Mo–ZSM-5 MDA catalyst *(479)*. They reported that the addition of NO to the flow lowered the temperature of coke removal, obtaining a more stable catalyst during regeneration cycles, compared to treatment with air alone. This type of treatment limits the sublimation of MoO_x species, which in turn contributes to the recovery of catalyst activity and selectivity.

Periodic switching between regeneration gas and methane has also been shown to reduce the amount of coke formed on the MDA catalyst. By regenerating after 6 h on stream, Ismagilov *et al.* were able to fully regenerate the catalyst; however, if the catalyst was operated for extended periods of time (>15 h), it was not possible to regenerate the catalyst to its full activity, which was thought to be related to the amount and type of residual coke species *(480)*. Shu *et al.* reported a similar result; switching between methane and H_2 or CO_2 after 30-min cycles led to full regeneration of the catalyst, whereby regeneration in H_2 produced a more stable performance in comparison with regeneration in CO_2 *(481)*.

As stated previously, MDA catalyst deactivation caused by deposition of carbonaceous species is a major hurdle, which needs to be overcome to make MDA a viable industrial process. Therefore, a vast amount of effort is directed toward limiting coking either by improving catalyst design or by adjusting the process conditions.

One of the main advantages of using the zeolite ZSM-5 as a support for the MDA catalyst is its unique pore structure and the associated shape selectivity, which allows benzene to form and diffuse relatively easily, while the formation of larger (poly)aromatic molecules is sterically hindered. Recently, ZSM-5 has received competition by MCM-22 (MWW topology) as the catalyst of choice, because MCM-22 is less prone to deactivation. MCM-22 has a unique pore structure. Two independent pore systems exist, the first consisting of 12-MRs forming cages (of dimensions $1.8 \times 0.71 \times 0.71$ nm), which are connected through 10-MR windows. The second system consists of 2D 10-MRs without any cages. No connection exists between the two pore systems *(439)*. The larger micropores of the MCM-22 zeolite allow a higher dispersion of molybdenum species accompanied by improved molecular transport, which decreases the accumulation of large (poly)aromatic compounds. However, ZSM-5 is still the preferred catalyst, given the high cost of preparing the MCM-22 zeolite. Other zeolites and zeotypes have also been tested, namely MCM-41 and SAPO-34, USY, MOR, and FSM-16, but all were less active than ZSM-5, ZSM-8,

Table 7 The Activity of 3% MoO$_3$-Zeolite Catalysts (Reaction Temperature 700 °C, Methane Space Velocity 1600 ml/g/h, SiO$_2$/Al$_2$O$_3$ = 50)

Zeolite Support	Methane Conversion[a] (%)	Selectivity[a] (%)		
		Benzene	C$_2$	CO
H–ZSM-5	5.9	91.3	4.5	4.2
H–ZSM-5[b]	6.9	90.8	4.3	4.9
H–ZSM-8[c]	4.11	86.7	3.9	9.4
H–ZSM-11[b]	8.0	90.9	5.5	3.6
H–ZSM-11	7.61	91.6	5.3	3.1
H–β[d]	3.11	80.4	8.8	10.8
H–MCM-41	0.9	80.1	8.7	11.2
H–SAPO-34[e]	0.6	72.9	10.1	17
H–MOR	0.8	0	72.3	27.7
H–X	0.7	0	70.1	29.9
H–Y	0.7	0	80.2	19.8
H–SAPO-5	–	–	–	–
H–SAPO-11	–	–	–	–

[a]Without accounting for coking.
[b]SiO$_2$/Al$_2$O$_3$ = 25.
[c]MoO$_3$ loading: 6 wt.%.
[d]MoO$_3$ loading: 7 wt.%.
[e]Reaction temperature is 650 °C.
Reproduced with permission from Ref. *(482)*.

and ZSM-11 *(482)* with their two-dimensional structure and pore diameters equaling the kinetic diameter of benzene molecules (Table 7).

Given that altering the framework type of the zeolite support can be costly and sometimes ineffective, additional metals have been investigated as promoters of Mo-ZSM-5. Numerous metals are reported to improve the performance, among them cobalt *(483)*, zinc *(484)*, iron *(485)*, ruthenium *(486)*, gallium *(487)*, and tin *(488)*. These promoters either enhance benzene selectivity and methane conversion or limit deactivation. Abdelsayed *et al.* investigated the effect of adding either iron or zinc (or both) to Mo-ZSM-5 catalysts on their performance in the MDA reaction at a temperature of 700 °C and atmospheric pressure *(489)*. Promoting with iron alone increased the benzene formation rate by 35% in comparison to the

unpromoted catalyst after 12 h on stream. Zinc promotion resulted in a slight increase in benzene formation rate at short time on stream relative to the unpromoted catalyst, but no advantage was observed after 3 h on stream. Furthermore, a higher rate of formation of ethylene was discovered. However, combining iron and zinc led to a significant decrease in benzene formation rate (by 31%), ascribed to deactivation of the catalyst by unhydrogenated carbon. Further investigation showed that two types of zinc species exist, weakly bound ZnO and more strongly bound zinc anchored to Brønsted acid sites. Results regarding zinc as a "promoter" are contradictory when analyzing its effect on the catalytic performance of Mo-ZSM-5. Xu et al. noted no improvement in catalyst stability *(483,490)*, whereas Zeng et al. reported increased benzene selectivity and increased stability *(491)*. There is also no universal agreement regarding the promotional effect of iron, with some researchers reporting an increase in benzene formation rate after prolonged time on stream *(492)*, others witnessing an overwhelming enhancement in catalyst stability *(483)*, and some even noting a negative effect on catalyst activity, thought to be due to the alteration of electronic properties of the catalyst surface, leading to stronger methane adsorption and coke formation *(485)*.

It is obvious that the promotional effects of the various metals are highly dependent on the catalyst composition and preparation conditions (i.e., metal loading, method of loading, calcination temperature, etc.), as well as on the reaction conditions (flow rates, temperature, pressure, amount of catalyst used, etc.). The parameters space is large and the reported results are difficult to assess, leading discussion of this aspect outside the scope of this chapter.

Since it is known that coke deposition occurs mainly on the active sites of the zeolite support and that only a small number of acid sites are required for the conversion of hydrocarbons to aromatics, dealumination is a viable option to reduce coke deactivation *(493)*. Dealumination is an effective means to reduce the number of acid sites on the zeolite and can be achieved by steam pretreatment of the ZSM-5 catalyst. Liu et al. observed higher benzene selectivity and less coke formation after dealumination, in comparison to untreated Mo-ZSM-5, because the strong Brønsted acid sites that favor aromatic carbonaceous deposits were destroyed *(494)*.

Silylation of Mo-ZSM-5 also proved to be an effective method of decreasing coke formation during the MDA reaction. Recently, Tempelman et al. varied the degree of silylation as well as the sequence of silylation and molybdenum introduction *(385)*. Silylation of Mo-ZSM-5

resulted in higher molybdenum dispersion; however, a higher severity of silylation increased the hydrophobicity, decreasing the molybdenum dispersion. Because of the high molybdenum dispersion, a high methane conversion rate was recorded and little coke formed. However, in a further investigation, it was discovered that severe silylation reduces the amount of hard coke produced, since acid sites on the zeolite surface are disabled *(495)*. In contrast, if silylation is performed before introduction of molybdenum, a poor catalytic performance was obtained.

The creation of hierarchical ZSM-5, or in other words, the creation of a mesopores system in addition to the micropore system already available, has also shown to be effective in enhancing catalyst performance and stability. Liu *et al.* used ordered mesoporous carbon and disordered carbon rods as the hard templates when synthesizing Mo–ZSM-5 catalysts *(496)*. The generation of secondary mesopores within the zeolite crystals led to unhindered access of reactants to the active sites, as well as to favorable diffusion of larger molecules formed in the micropores. A similar result was reported by Martínez *et al.* who also created intracrystalline mesopores (ca. 10–20 nm) by using a carbon template, with the resulting Mo–ZSM-5 catalyst achieving a higher and more stable aromatics yield *(497)*. The authors attributed the improved performance to trapping of coke molecules in the intracrystalline mesopores, which allowed a larger fraction of acid sites to remain accessible for aromatization reactions.

One of the most effective ways to increase catalyst performance, particularly conversion rate, aromatics selectivity, and catalyst stability, is the introduction of co-reactants to the methane feed. Ma *et al.* co-fed H_2 (5.4%) and H_2O (1.8%) with methane and found that coke formation on a Mo–ZSM-5 catalyst was suppressed in comparison to the situation when only methane was fed *(498)*. The same group found a similar result when co-feeding CO and/or CO_2 with methane, noting that the amount of coke formed on the catalyst surface was reduced *(499)*. Choudhary *et al.* investigated the effect of co-feeding of alkenes and/or higher alkanes with methane, noting that the temperature needed to activate methane was reduced, as a result of a hydrogen transfer mechanism between methane and alkene molecules *(500)*. Moreover, the benzene selectivity was higher (reaching more than 90%), as was the methane conversion (20–50%).

We know that the thermodynamic limitation of the nonoxidative MDA reaction is a big stumbling block when considering commercial application, because of the high temperatures that are required and the vulnerability of the catalyst to coking. Enhancing the catalyst design to resist coking is one

possible solution; alternatively, the reactor design can be altered to accomplish a more efficient process, which can be a more effective solution. Nearly all of the catalytic testing performed in the literature described so far in this review article is based on fixed-bed reactor designs, but alternative designs are showing promising results.

Membrane reactors are excellent to remove H_2 produced during the reaction, thereby shifting the chemical equilibrium toward the formation of benzene. This approach was pursued by Kinage *et al.* who used a palladium membrane (Figure 45) and successfully removed 50 to 60% of the H_2, thus enhancing the rate of formation of benzene, naphthalene, and toluene *(501)*. However, it has also been shown that an increase in benzene yield corresponding to the H_2 removal from equilibrium is accompanied by rapid deactivation, because less H_2 is available to suppress carbon formation *(502)*.
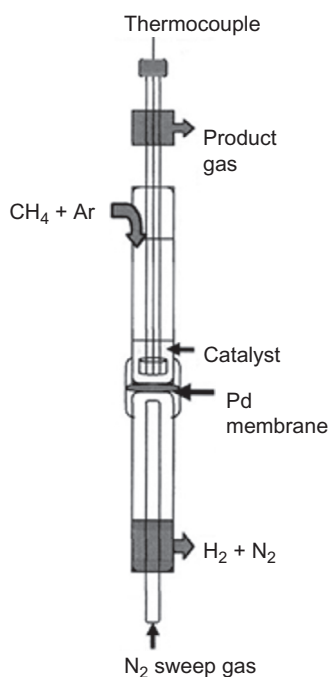
Figure 45 Palladium membrane reactor, consisting of upper and lower parts, made from stainless steel pipes of 40 mm i.d. and 300 mm length. A palladium membrane sheet (20 μm thickness) is mounted on a mesh plate, situated in between the upper and lower parts. Catalyst charged is in contact with the palladium membrane in the upper part of the reactor, with a thermocouple situated at the center of the reactor to monitor reaction temperature. *Reproduced with permission from Ref.* (501).
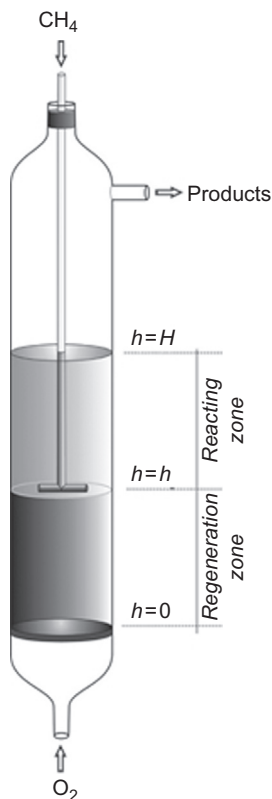
Figure 46 Scheme of a two-zone fluidized bed reactor (TZFBR). *Reprinted with permission from Ref.* (503). *Copyright (2010) American Chemical Society.*

Another unique reactor design is that of the two-zone reactor, where methane is fed to the center of the reactor bed, which creates two zones of differing environments: a reducing atmosphere in the top part and an oxidizing atmosphere in the bottom part (503) (Figure 46). This design is based on the fact that, as the catalyst deactivates over time, it becomes denser and falls to the lower region of the reactor bed, where it is regenerated. It could be demonstrated that employing 1% CO_2 for regeneration, the regenerated catalyst rises back to the upper section of the reactor bed, achieving 90% benzene and hydrocarbon selectivity, with a methane conversion of 8%.

Since the discovery by Wang *et al*. in 1993, remarkable improvements in catalyst performance and process design have been achieved. Notwithstanding these successes, some issues are still debated, most notably the MDA reaction mechanism. Further investigations are required to elucidate the

exact mechanism, the knowledge of which could lead to better strategies to further improve catalyst or reactor design. Although the performance to date does not suffice to make MDA a viable industrial process, there is enough potential to justify further research on this topic.

4.2 Alcohol-to-Hydrocarbon Conversion Processes

Olefins are an indispensable and versatile feedstock in chemical industry, but are much less naturally abundant than alkanes *(504)*. As explained above, conversion processes, like FCC and HC, are mainly responsible for the transformation of heavy fractions of the fossil feedstock, in particularly crude oil fractions, to the lighter and higher valued diesel, gasoline, and kerosine (jet fuel) *(505)*. In addition to being converted to transportation fuels, crude oil can also be processed to various unsaturated hydrocarbons, that contain one or two C=C bonds. The primary sources of such olefins have been various fossil fuel derivatives, such as natural gas condensate and petroleum distilled naphtha derivatives *(504,505)*. A large portion of the ethylene produced originates from steam cracking of naphtha and natural gas liquids, while about two thirds of the propylene is obtained as a co-product of steam cracking *(505,506)*. The current worldwide production of the two most important olefinic building blocks, ethylene and propylene, is more than 150 million tons and more than 85 million tons per annum, respectively *(506)*. These two molecules are the precursor materials for the production of plastics, fibers, and various important chemical intermediates, such as ethylene oxide, ethylene dichloride, propylene oxide, acrylonitrile, and cumene *(506)*. For instance, more than 60% of the ethylene and propylene are consumed for the production of polyethylene (like HDPE: high-density polyethylene and LDPE: low-density polyethylene) and polypropylene (PP). Moreover, the demand for propylene is growing at a much faster rate compared to that of ethylene (6% vs. 4% per year) *(506)*. The main reason behind this trend is the increasing popularity of propylene-based polymers, especially in the automobile industry *(506)*. This rapid rise in propylene demand could lead to supply chain problems. At this growth rate, the cracking processes alone, such as FCC, are probably not sufficient to cover the anticipated demand. Thus, in the coming decades, the balance between demand and supply of light olefins should be restored from other sources, such as selective dehydrogenation of propane (see Section 5.2) *(507)* and higher olefin cracking *(508)*, and maybe most significantly, the alcohol-to-(light)olefin technologies *(509)*. The environmental concerns over the recent shale gas revolution (in particular in the UK and EU region, see

Section 4.1) *(510,511)* and the depletion of fossil fuels in the long run are steering the interest of the chemical community toward the development of new and improved catalytic technologies for the selective conversion of alcohols (e.g., methanol or ethanol) to very important raw materials for chemical industries, namely ethylene and propylene *(512–515)*.

An additional advantage of these alcohol–to–olefin (ATO) technologies is that they can potentially reduce the dependency of ethylene production on petroleum feedstocks, as methanol is currently being produced from natural gas, coal, and (to a small extent) carbon dioxide, while ethanol is produced from lingo-cellulosic and starchy feedstock. Moreover, these ATO processes can (in principle) be "CO_2 neutral" and fit into the popular concepts of "coal to chemicals" and, perhaps more importantly, "biomass to chemicals" *(506)*. For instance, China has vast coal resources, which have the potential to replace crude oil and natural gas as raw materials for chemicals production. More than 20 such plants have already been established across China by various companies (General Electric Co., Royal Dutch Shell, Celanese, Praxair, and Dow) with the goal of achieving a "more energy-intense chemical industry" *(516)*. In Brazil, four different companies (Braskem, Dow, Solvay, and Mitsui) are collectively producing more than 600 kt bioethylene per year for the subsequent production of completely green chemicals, mostly polymers *(517,518)*. Alternatively, the long-term significance of ATO technologies may be rationalized in terms of the current prices of crude materials, alcohols, light olefins, and their derived products (Table 8).

Table 8 Cost Comparison of Various Crude Materials, Olefins, and Olefin-Derived Essential Chemicals

	Price in \$/mt (2014)		Price in \$/mt (2014)
Oil	470	Naphtha	550
Ethane	500	Propane	756
Coal	53	Sugarcane	24
Methanol	442	Ethanol	485
1-Butanol	1890	Ethylene	984
Propylene	1550	Butene	1996
Butadiene	1300	Polyethylene	1041
Polypropylene	1354	Butadiene rubbers	1456

The prices listed in the table are based on December 2014 U.S. prices.

4.2.1 Methanol-to-Olefin and Methanol-to-Gasoline Processes

The conversion of alcohols to olefins or other hydrocarbons has been widely investigated during the past 50 years, and the technology for commercial operation has been developed. The pioneering work in the 1970s and 1980s mainly focused on gasoline range products, and accordingly the MTG process operated with ZSM-5-type zeolites as catalysts *(519,520)*. However, the MTG process favors the formation of highly branched hydrocarbons and aromatics over formation of lighter olefins. The MTG process was later (1979) commercialized by Mobil as "Mobil MTG process" in New Zealand. In this process, methanol is produced from synthesis gas (derived from natural gas) *(509)*. The MTG part of this plant was shut down permanently in the 1990s after the oil prices became low (compared to the price of methanol) in the 1980s, which continued for the next decade. Unfortunately, this shutdown prompted chemical companies to explore fossil fuels for the production of important olefins (e.g., C_2–C_4 olefins). In the meantime, that is, during the mid-1980s, Union Carbide (now Honeywell UOP) discovered silicoaluminophosphate zeotype materials (SAPO). In the 1990s, UOP and Norsk Hydro A.S. developed a SAPO-34-catalyzed MTO process, known as UOP/HYDRO MTO process. The unique pore size, acidity, and geometry of SAPO materials are responsible for the selective production of ethylene and propylene with reduced amounts of side products. The relatively small-pore size of SAPO-34 (CHA) compared to that of ZSM-5 (MFI) prohibits the diffusion of heavy and branched hydrocarbons and, hence, favors higher selectivity toward the desired light olefins (see Section 2.1). An additional advantage of the SAPO-34-based MTO process over the ZSM-5-based MTG process is that a major part of the C_4–C_6 fraction in the product is olefinic in nature; this distribution makes olefin cracking necessary (*vide infra*). However, one of the major limitations of the UOP/HYDRO MTO process is the relatively fast deactivation of the catalyst compared with the analogous Mobil MTG process. Therefore, the removal of coke by combustion in a catalyst regenerator is absolutely essential for maintaining the catalytic activity for a longer period of time.

During the development of MTO in the 1990s, ATOFINA (later a part of Total) was developing their olefin cracking technology. In the last decade, further improvement of light olefin selectivity in the UOP/HYDRO MTO process was achieved by combining this process with the olefin cracking process developed jointly by Total Petrochemicals and UOP. The performance of these combined processes was successfully demonstrated in 2009 at a semicommercial unit in Feluy (Belgium), which is capable of

processing up to 10 t per day of methanol feed. Simultaneously in 2010, another MTO plant was constructed and started its operation in Baotou, China, based on the technology developed by Dalian Institute of Chemical Physics *(521)*. The construction of another 295 kt/year plant based on similar technology is presently being completed in Nanjing, China *(522)*. Currently, several MTO plants based on coal–derived syngas are being constructed in China *(523)*. The plant built by the Shenhua Company in Baotou includes a 1.8 million ton methanol unit and a 600 kt MTO unit along with the facilities for simultaneous production of PE and PP directly from syngas. All these developments eventually make processes, such as the UOP/HYDRO MTO process, more economically viable than conventional naphtha cracking, while also promoting the concept of "coal-to-chemicals."

Over the last half century, a comprehensive screening of a large variety of zeolite materials has been performed to identify catalysts for the MTO reaction. The zeolite and zeotype materials investigated differ from each other by their topologies, compositions, and morphologies. However, to the best of our knowledge, SAPO–34 and ZSM–5 are the only two zeolitic materials used in industrial MTH processes up to now. The smaller pore size of SAPO–34 effectively controls the size of the olefin molecules that can emerge from the cages (Figure 47). Therefore, diffusion of larger olefins is expected to be slow in SAPO–34 compared with diffusion in ZSM–5, and diffusion is not at all possible for simple aromatics or paraffins (Figure 47B and D). Therefore, SAPO–34 is selectively producing smaller olefins (e.g., ethylene and propylene) as the predominant products in the industrial MTO process. However, the diffusion limitation for larger molecules in SAPO–34 eventually leads to faster deactivation associated with coke formation, as observed in the UOP/HYDRO MTO process (Figure 48). An additional catalyst regenerator is used in the UOP/HYDRO MTO process to maintain the stability of the catalyst for longer periods of time. In contrast, ZSM–5 has high product selectivity toward propylene and butylene (but lower yield) and a relatively long catalyst life (because of the slower deactivation and/or the larger pore size) compared with SAPO–34. Among the other zeolites, SSZ–13 (an aluminosilicate zeolite of CHA topology patented by Chevron) is also considered as a potential candidate catalyst for industrial MTO processes in the near future. There are also nonzeolitic materials; for example, Olah *et al.* reported on bifunctional supported acid–base catalysts (e.g., WO_3/Al_2O_3) for the conversion of methanol into ethylene and propylene at temperatures of 250–350 °C. It is remarkable that
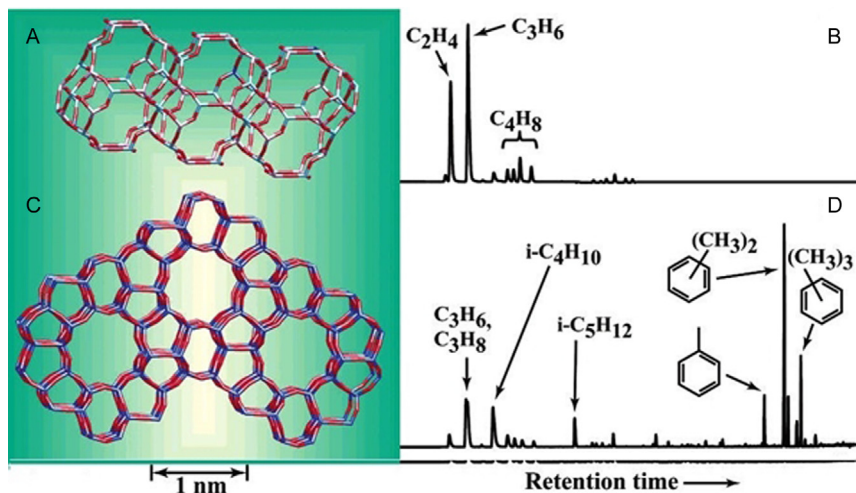
Figure 47 Structures of the two most commonly used zeolite materials in MTG/MTO and GC–MS total ion chromatograms illustrating product selectivity during methanol conversion: (A) The CHA topology of SAPO-34. (B) The products of methanol conversion on SAPO-34. (C) The MFI structure of ZSM-5. (D) The products of methanol conversion on ZSM-5. In each experiment, 300 mg of catalyst was used, the reactor was operated at 450 °C, and products were sampled 1.5 s following pulsed introduction of 10.2 μl of methanol. *Reprinted with permission from Ref.* (525). *Copyright (2003) American Chemical Society.*
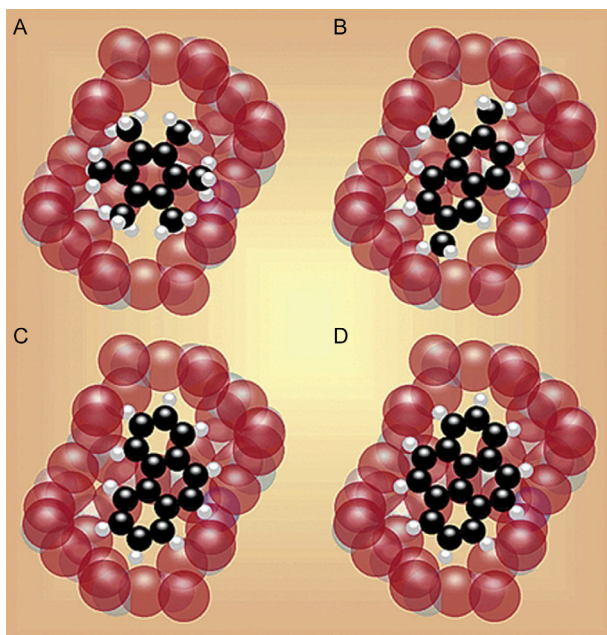
Figure 48 Molecular view of MTO catalyst deactivation shown for the specific case of SAPO-34. (A) Hexamethylbenzene and other methylbenzenes are present in a few percent of the cages in an active MTO catalyst. (B) With increasing time on stream, some of the methylbenzenes grow to give methylnaphthalenes. (C) Further growth to phenanthrene causes a loss of MTO activity in SAPO-34. (D) The largest ring system to form in SAPO-34 is pyrene. *Reprinted with permission from Ref.* (525). *Copyright (2003) American Chemical Society.*

such nonzeotype heterogeneous bifunctional catalysts were found to be active for MTO conversion although they lack the well-defined 3D structures characterizing zeolites and zeotype materials *(506,524)*.

The MTO reaction is now being considered to be a valuable option for the valorization of stranded gas reserves, and therefore several investigations were devoted to the elucidation of the reaction mechanism or to the improvement of the present technology *(526)*. The key reaction steps of the MTO/MTG process are summarized in Scheme 15. Methanol is first
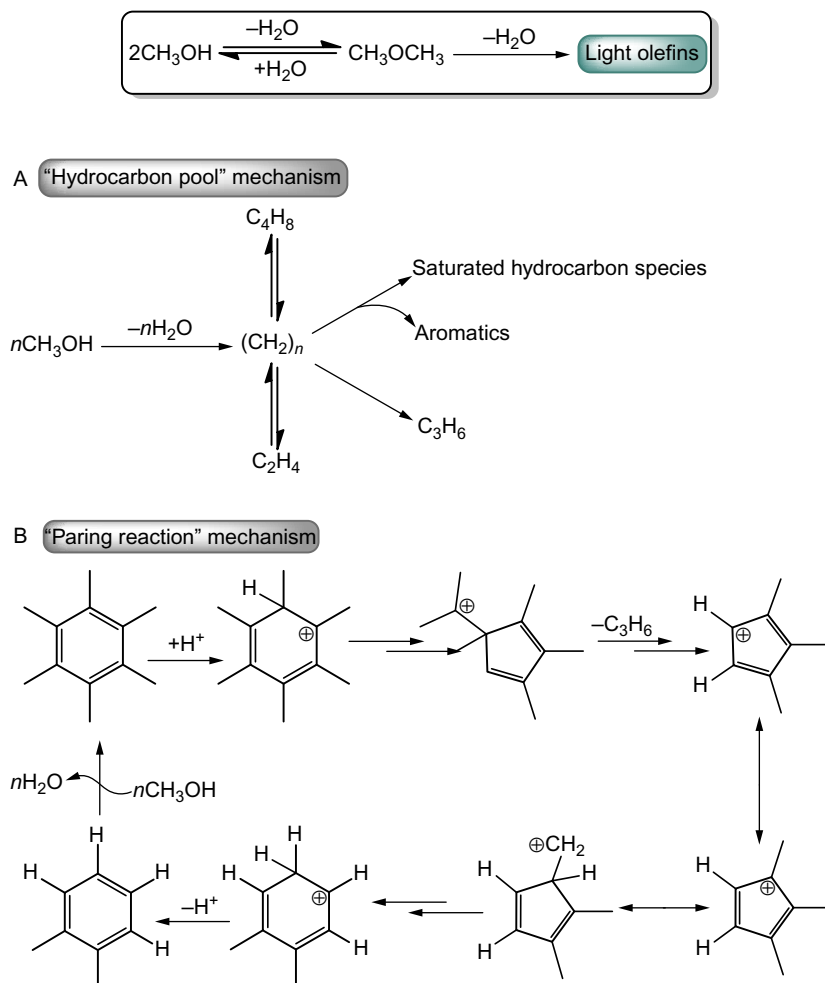
Scheme 15 Two most popular postulated mechanisms for the MTO reaction: (A) hydrocarbon pool mechanism and (B) paring reaction mechanism. *Adapted with permission from Refs.* (527,528).

dehydrated on a solid acid catalyst (Scheme 15). This step produces an equi-
librium mixture consisting of methanol, dimethyl ether, and water, which
is then converted into either light olefins (MTO) or gasoline (MTG),
depending on the nature of the catalyst topology and reaction conditions.
The larger pore zeolites (like ZSM-5) promote the MTG route. During
the course of the MTO/MTG reaction, light olefins can be transformed
into higher olefins, various paraffins, and polyaromatics via alkylation and
polycondensation reactions (Figure 48).

Since the discovery of MTO conversion, there has been extensive
research to elucidate the mechanistic aspects. Unfortunately, there is no con-
sensus in the scientific community regarding the MTO mechanism. So far,
more than 20 different mechanisms (two of which are shown in Scheme 15)
have been postulated for this chemistry *(526,529)*. The majority of the pro-
posed mechanisms were rejected by the scientific community because they
failed to describe the experimentally observed initial kinetic induction
period. However, a protonated surface methoxy, which is prone to further
nucleophilic attack by methanol, is commonly considered as the most prob-
able intermediate in the initial dehydration of methanol to DME on solid
acid catalysts. The oxonium ylide structure formed after nucleophilic attack
by methanol is shown in Figure 49. For instance, dimethyl oxonium
methylide can be formed in the zeolite cage after deprotonation of a
trimethyl oxonium ion by a nearby basic site (Figure 49) *(529)*.
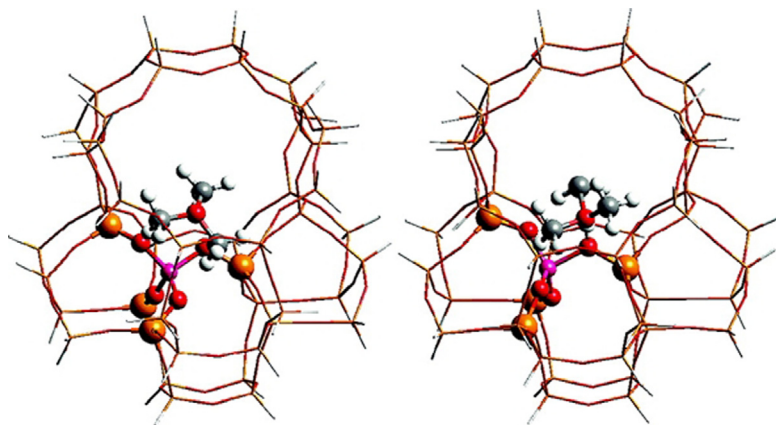
Figure 49 Computed trimethyl oxonium ion and dimethyl oxonium methylide formed
in ZSM-5 cage (46T cluster). *Reprinted with permission from Ref. (530). Copyright (2007)
American Chemical Society.*

Most of the past debate of MTO chemistry is related to two issues: (i) the origin of the first C—C bond and (ii) the MTO catalytic cycle. The key intermediates in the various proposed mechanisms are oxonium ylides (Figure 49), carbenes, carbocations, and free radicals *(529–534)*. The formation of the "first C—C bond" through a direct mechanism requires participation of two (from two different methanol molecules) or four (from two different DME molecules) carbon atoms during the conversion of methanol or DME to hydrocarbon. However, the probability of such direct coupling to form the first C—C bond is negligible. It has been established that adsorbed methanol is not able to couple directly inside zeolite pores at an appreciable rate under MTO reaction conditions. An ONIOM calculation by Lesthaeghe *et al.* reveals that the activation energy barrier for direct C—C coupling is very high (≈ 200 kJ/mol) *(530)*.

Work by Song *et al. (535)* led to the conclusion that impurities are actually responsible for the formation of the first C—C bond in the MTO process. These impurities could originate from the methanol feed (or even the carrier gas) and/or from the catalyst, as a result of incomplete combustion reactions during removal of the SDA from the zeolite synthesis, or during removal of carbonaceous deposits in a regeneration step. Song *et al.* made two comparisons: they compared yields obtained with a commercially available methanol feed (which contained 36 ppm ethanol) with those obtained with fractionally distilled methanol (which contained 1 ppm ethanol); and they compared yields obtained after a conventional calcination procedure with those obtained after rigorous calcination. In both scenarios, the olefin yields were higher in the presence of more organic impurities. According to Haw *et al.*, "H-SAPO-34 is highly sensitive to the impurity concentration in the methanol feed, indicating that if even direct C_1 coupling does occur, it operates at a rate significantly slower compared with the rate at which trace impurities initiate the reaction" *(537)*.

Regarding the catalytic cycle for the formation of olefin from methanol, indirect routes (routes involving organic moieties in addition to the catalyst sites and not directly involving the participation of two different molecules of methanol/DME) have been proposed for over three decades. Already in 1983, Mole *et al.* observed that toluene (intentionally introduced as an impurity) acted as co-catalyst during the MTO process on ZSM-5 *(531,532)*. According to the mechanism that they proposed, the MTO reaction was facilitated via side-chain alkylation of toluene followed by olefin elimination. Also the NMR spectroscopic analysis of the mechanism by Haw and coworkers *(535–537)* suggests an indirect route of olefin formation.

Based on the experimental evidence in support of an indirect route for olefin formation from methanol or dimethyl ether, Kolboe and co-workers proposed a "hydrocarbon pool" mechanism where (as yet) unspecified hydrocarbon moieties are formed *in situ* and undergo successive methylation and finally olefin elimination (Scheme 15) *(527,538–541)*. Though the exact nature of the active hydrocarbon moieties in MTO cycle is yet to be confirmed, results from various spectroscopies suggest the presence of various four- or five-membered carbocationic methylated rings *(525,527,529–548)*. For instance, a very recent investigation by Wulfers and Jentoft found cyclopentadienium ions with 4–5 alkyl substituents to be predominant hydrocarbon pool species on ZSM-5 during the MTO reaction *(533)*. Since it has been supported by various mechanistic investigations over the last two decades *(509,515,525,527,529–548)*, Dahl and Kolboe's "hydrocarbon pool" mechanism is now the widely accepted MTO mechanism (Scheme 15A). Also, the statement that the "first C–C bond (or olefins) formed from impurities in methanol" has found acceptance in that it is frequently cited.

In addition to the general idea of a "hydrocarbon pool" mechanism, specific proposals for individual steps of olefin formation have been made, such as the "paring reaction," referring to a 1961 paper by Sullivan *et al.* (Scheme 15B) *(509,515,525,528,529,547)*. In this reaction, hexamethylbenzene (HMB) is regarded as the active intermediate, which undergoes successive ring contraction and expansion via isomerization after the initial protonation step on the acid sites of the catalyst. In this way, an extended alkyl side chain is formed, which cracks; thus an olefin is eliminated and a methylated benzene is left behind. Next, this methylated benzene reacts with methanol or dimethyl ether and HMB is again created, hence completing the catalytic cycle. Although there is no consensus regarding a complete mechanism, HMB is a commonly acknowledged intermediate in the various proposals of a zeolite–catalyzed MTO reaction mechanism. In this regard, Van Speybroeck *et al.* recently proposed the full computed catalytic cycle for the SAPO-34–catalyzed MTO process, starting from HMB as intermediate (Scheme 16) *(549)*. For the detailed mechanistic insights along with the current status of the MTO process, various excellent reviews can be consulted *(509,525,529,542–547,550–552)*.

4.2.2 Ethanol-to-Olefin Conversion Process

To decrease the dependency on petroleum as a feedstock and in response to the demand for CO_2-neutral transportation fuels, bioethanol production
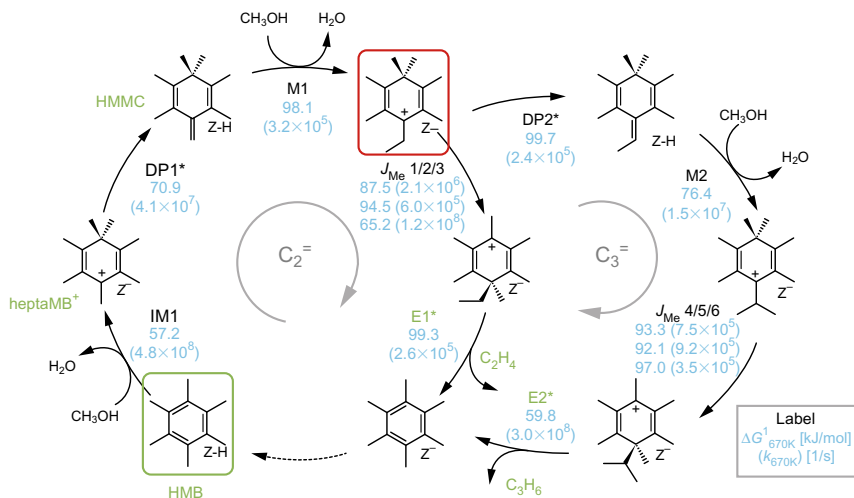
Scheme 16 The proposed side-chain mechanism in SAPO-34 for ethylene ($C_2^=$) and propylene ($C_3^=$) formation starting from HMB. Reactions indicated with an asterisk are water assisted. Free energy barriers in kJ/mol and intrinsic rate coefficients in 1/s (in parentheses) at 400 °C are displayed in blue (light gray in the print version). The products of E1* and E2* still contain a H_3O^+ cation resulting in the presence of Z^- at the end of the cycle. The intermediate where the ethylene- and propylene-producing cycles bifurcate is indicated with a red (light gray in the print version) box. *Reprinted with permission from Ref. (549).*

(e.g., from fermentation of biomass) has increased significantly *(513)*. The U.S. Energy Information Administration reports that the current ethanol production is about 947,000 barrels per day *(553)*. This high volume of bioethanol is not only contributing to the CO_2-neutral production of transportation fuels; it is also used as a feedstock for the production of various bulk chemicals of higher value. The total amounts of ethanol and ethylene produced in 2014 exceeded 773 billion tons and 115 million tons, respectively, while the respective prices (as of December 2014 in the USA) were \$485/ton and \$984/ton (Table 8) *(513,554)*. Considering the production scales and values, it is also logical to convert ethanol (and higher alcohols) to corresponding olefins by dehydration, which also connects the biorefinery to the petrochemical industry, as proposed by Rass-Hansen et al. *(513)*.

It is important to recall that almost 100 years ago, most of the ethylene was produced via the dehydration of ethanol with good activity and selectivity in fluidized bed reactors on activated alumina *(555)*. The first commercial plant was built by Elektrochemische Werke GmbH in Bitterfeld,

Germany in 1913. However, as the initial MTO process, this process was discontinued during the rise of the petrochemical industry, since the steam-cracking process was preferred. Very recently, the low cost of sugarcane in Brazil has encouraged several chemical companies (e.g., Solvay, Dow, Mitsui, and in particular Braskem) to build and operate bioethylene plants, which use ethanol (derived from sugarcane) as feedstock, with a collective total capacity of over 600 kt/year (Figure 50) *(555–558)*.

Enzymes (*Saccharomyces cerevisiae* yeast) are used in the fermentation process in Brazil to convert sugarcane juice and molasses into ethanol, which is subsequently dehydrated to ethylene *(560)*. For the dehydration step, acid catalysts of various kinds are typically employed (e.g., alumina, silica–alumina, zeolites, and other metal oxides, variations of the cited catalysts impregnated with metals as well as mixtures of two or more such catalysts). The nature of the actual catalyst utilized in Braskem's technology is a secret; however, a few reports suggest that the catalyst is based on a modified zeolite (phosphorus, gallium, or lanthanum), mordenite, zeolite beta, and several SAPO variants (e.g., SAPO-34, SAPO-11, and NiSAPO-34) have been explored as catalysts for the dehydration step *(559,561–566)*.

Notwithstanding the industrial breakthrough of the ethanol-to-ethylene technology, there is no consensus regarding the mechanism of the dehydration step. Ethanol can be either intramolecularly dehydrated directly to ethylene or intermolecularly to diethyl ether (Scheme 17). In principle, three different reaction mechanisms are plausible *(559,567)*. In the E1 reaction pathway, a carbocationic intermediate is first generated, followed by β-hydride elimination to produce ethylene. The E2 reaction pathway is a single-step second-order reaction characterized by simultaneous proton
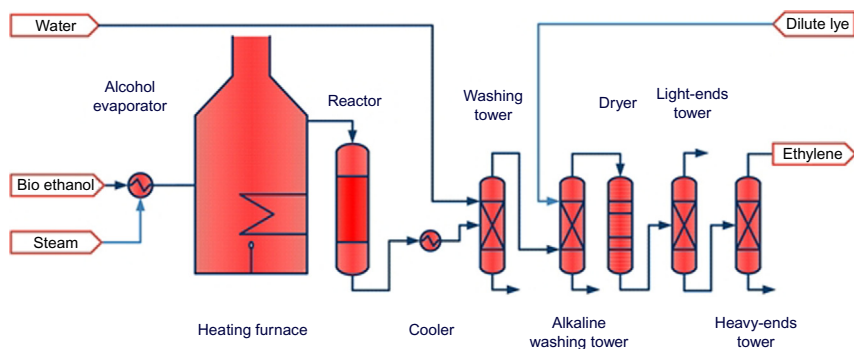
Figure 50 A simplified process diagram of a bioethanol-based ethylene plant. *Reprinted with permission from Ref.* (559). *Copyright (2013) American Chemical Society.*
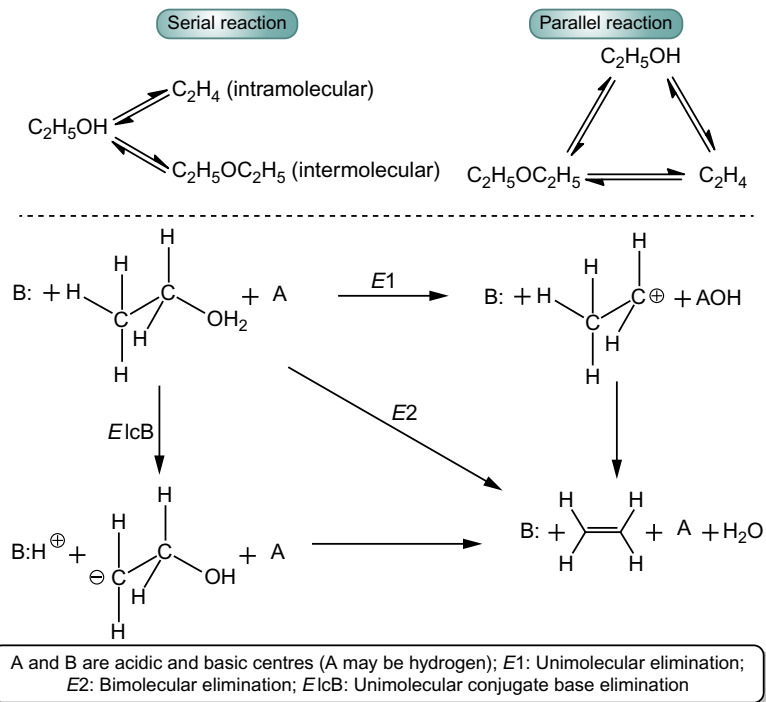
Scheme 17 Plausible reaction steps of ethylene formation by catalytic dehydration of ethanol. *Adapted with permission from Ref. (559).*

abstraction and hydride elimination. However, the rate depends on the concentration of both species, the substrate C_2H_5OH and carbocationic $C_2H_5^+$ intermediates (similar to the intermediate depicted in the E1 route). In the E1cB reaction pathway, the acidic β-hydrogen is abstracted and the conjugate base, a carbanion, is formed. Subsequently, a conjugate base-assisted dehydroxylation leads to olefin formation. However, a very recent investigation indicates the possibility of an MTO-like hydrocarbon pool mechanism (Scheme 15) and rejects the possibility of endothermic dehydration steps *(568)*. In essence, the actual ethylene formation pathway on zeolite catalysts is still unclear and requires more investigation.

Inspired by the success of their bioethylene plant, Brazil's Braskem has recently invested $100 million to produce 30,000 mt/year of propylene from sugarcane-derived ethanol *(569–571)*. The intent is to make polypropylene with the same properties as conventional fossil fuel-derived PP (Scheme 18). In the future, it may be more advantageous to use
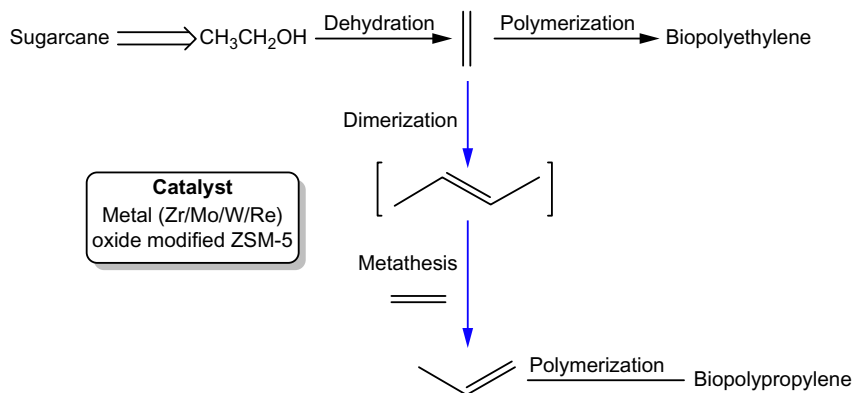
Scheme 18 Role of Braskem's bioethanol-to-olefin process in the overall scheme for production of biopolyethylene and biopolypropylene.

hydrolyzed cellulose and hemicellulose from nonedible biomass for possibly less expensive production of ethanol (instead of sugarcane). However, this technology is currently under development and has not yet been commercialized *(560)*.

The ethanol-to-propylene conversion technology is similar to the ethanol-to-ethylene conversion technology. The difference in the mechanism is that metathesis between ethylene and butene (formed via dimerization of ethylene) produces the propylene monomer for the production of polypropylene (Scheme 18). Various bifunctional catalysts consisting of a zeolite (i.e., ZSM-5, ZSM-11, ZSM-12, ZSM-23, and ZSM-35) with Si/Al ratio larger than 40 exchanged with a transition metal with metathesis activity (e.g., zirconium, molybdenum, tungsten, and rhenium) are effective for the production of propylene directly from ethanol *(572,573)*. To the best of our knowledge, rhenium oxide–modified zeolite ZSM-5 is currently the most active reported catalyst *(573)*.
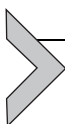
5. BINDER–MATRIX EFFECTS IN ZEOLITE-BASED CATALYSTS

While for research purposes, typically pure zeolites in powder form are used, industrially employed zeolite-based catalysts often contain a combination of other components in addition to the catalytically active zeolite phase *(574–578)*. In fact, components, such as binders, matrix, and fillers, usually make up the majority of the final material, which is often shaped to the desired needs; for example, there exist fluidized bed catalyst particles, pellets, granules, or extrudates. Fillers, such as clay, are added to reduce the catalyst

cost, act as a heat sink, and maintain activity, as well as for other purposes. However, binders, such as silica or alumina, are known to introduce mechanical strength and alter many other physicochemical properties. Mainly physical attributes are believed to be affected, and binders are often thought of as "inert" in the final catalyst material; however, recent literature has shown this assumption to be incorrect *(575)*.

In a recent perspective article, Hargreaves and Munnoch *(578)* highlight the beneficial and deleterious effects of binder materials in shaped catalyst bodies, noting that they can (i) modify coking characteristics; (ii) trap poisons; (iii) influence transfer of chemical species; (iv) modify thermal characteristics; (v) modify porosity characteristics; and (vi) enhance physical durability. The article is complemented by a recent review by Mitchell *et al.* which gives an excellent summary of the available literature on "binder effects" *(574)*. In general, this topic is scarcely researched in academia. There are two main reasons for the absence of academic research activity: limited availability of relevant detail needed to replicate catalysts produced on an industrial scale, and the (previous) lack of advanced techniques required to investigate shaped materials with large-scale variations of properties. However, there is progress in understanding the influences of binders and other matrix components on the activity and selectivity of industrial zeolite-based catalysts, with some past and recent examples discussed below. To clarify, we make a distinction between fluidized bed catalyst particles and shaped catalyst bodies.

5.1 Binder–Matrix Effects in Fluidized Bed Catalyst Particles

FCC particles, which are designed for a fluidized bed, are a well-known example of a composite catalyst; and the situation encountered can be considered as representative: binder–matrix effects are abundant, but are not well understood. As discussed above and illustrated in Figure 51, FCC catalyst particles mainly consist of USY and also contain matrix components, such as amorphous silica, alumina, or silica–alumina, and clay (kaolin). The role of the matrix is, presumably, to support the active zeolite phase and also to transfer heat from the regenerator to the riser reactor *(579)*; however, the matrix is known to also assist with the diffusion of molecules to and from the active phase. One of the main reasons for not being able to generally designate matrix components as "inert" is their function in the FCC process, where they actually operate as a precracking catalyst, breaking up the larger feed molecules to products that are further reacted at the Brønsted acid sites of the zeolite *(580,581)*.
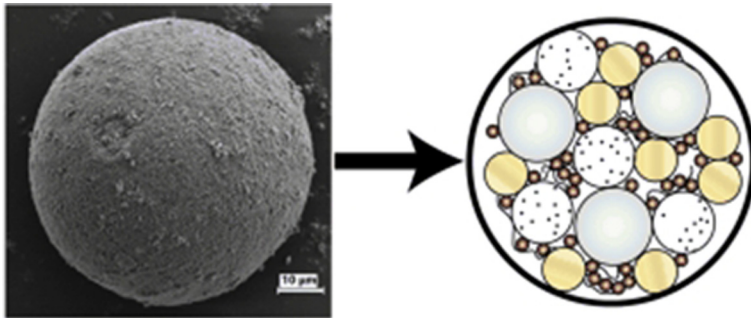
Figure 51 Left: Scanning electron micrograph of a single fluid catalytic cracking particle (scale bar = 10 μm) together with a pictorial view (right) of its various components such as active phase (gold spheres; light gray with stripe in the print version), matrix (large white/gray spheres), binder (white), and fillers (small brown (dark gray in the print version) spheres). *Adapted from Ref.* (582).

One reason for deactivation of the zeolite contained in working FCC particles is dealumination because of the hydrothermal conditions within the industrial reactor system. Gelin and Gueguen *(583)* observed that during severe steaming, crystallinity of RE–Y and H–offerite particles is maintained up to a temperature of 810 °C when they are bound with silica–alumina sol. In a further investigation, Gelin and Des Courieres *(584)* noted that in the absence of a silica–alumina-based matrix, LaY zeolites lose 55% of their crystallinity (in comparison to preservation of the crystallinity when the matrix is present). The enhanced stability was associated with the migration and reincorporation of silicon-containing species from the matrix to the zeolite framework, the healing defects in the framework, and with the interaction of zeolite silicon species with those of the matrix.

The acidic properties of the clay allow for a minor catalytic contribution of this material during the FCC process. For example, Buurmans *et al.* reported clay to be slightly active for the oligomerization of thiophene, as observed by using optical microspectroscopy on single FCC particles *(585)*. The clay component is also useful for the entrapment of metal poisons from the reactant feed. Some metals are prevalent in heavy crude oil and are known to remain on the catalyst surface, where they act as poisons and reduce both catalytic activity and selectivity. Specifically, vanadium is known to form metavanadic acid, which irreversibly damages the zeolite framework, and nickel is increasing the selectivity to coke because it promotes dehydrogenation reactions *(586–590)*. Liu *et al.* investigated the interactions of nickel and vanadium with two types of kaolin clay

matrices: acid–modified kaolin (AMK) and caustic–modified kaolin (CMK) *(591)*. Although the amounts of vanadium and nickel (1–5 wt.%) were not comparable with those found in spent commercial catalysts (ppm range), a positive effect of the clay could be demonstrated. After heating to temperatures between 660 and 700 °C, a vanadium mullite phase formed through reaction with the clay. The insertion of vanadium into the mullite structure by replacement of silicon or aluminum atoms completely prevented zeolite deactivation by vanadium poisoning. The presence of CMK led to the formation of a stable $NiAl_{10}O_{16}$ compound, and trapping of the nickel through this reaction protected the zeolite phase from deactivation. Occelli *et al.* reported the effective use of an acid-leached kaolin clay, which was characterized by lattice vacancies and could host metal impurities and form inert nickel silicate compounds, which increased the catalyst's resistance to metal poisoning *(592)*.

In addition to the clay component, several other matrix compounds, such as silica, alumina, and silica–alumina have been investigated for their potential to increase resistance toward metal poisoning in FCC particles. In the late 1970s, Swift *et al.* produced a number of patents pertaining to the use of magnesia–alumina–aluminum phosphate (MgAAP) as a matrix, which led to highly selective gasoline production and improved metal tolerance *(593–595)*. These effects remained initially unexplained. In the mid-1990s, Yang *et al.* attempted to shed light on these effects by employing alumina, magnesia–alumina ($MgO–Al_2O_3$), alumina–aluminum phosphate (AAP), and MgAAP as matrices for USY *(596)*. The authors characterized the materials by XRD and N_2-physisorption and applied *n*-hexane cracking as a test reaction. It was concluded that the presence of the matrix increased the resistance of USY toward steam deactivation, and the type of matrix influenced the degree of metal poisoning. $MgO–Al_2O_3$, because of it basicity, reacts with H_3VO_4, effectively "capturing" vanadium species, which prevents their migration to the zeolite USY surface. The effect of the matrix on the catalytic activities of vanadium-poisoned catalysts decreased in the order: $MgO·Al_2O_3 > MgAAP > AAP > Al_2O_3$ *(596)*.

The presence of alumina (as a matrix or binder) in an FCC catalyst is thought to play a significant role in determining catalytic activity and selectivity. De la Puente *et al.* investigated the influence of the alumina content in silica–alumina matrices in FCC catalysts subjected to hydrothermal treatment, by means of conversion of cyclohexene at a temperature of 300 °C *(597)*. The cyclohexane yield was shown to increase when the relative amount of octahedrally coordinated aluminum atoms decreased. Aluminum

extracted from the zeolite during the hydrothermal treatment (and thus in octahedral coordination) reacted with silica in the matrix, producing a new silica–alumina phase. Such reactions have also been noted by other researchers, who find evidence of the formation of a new silica–alumina phase after dealumination of the zeolite in conjunction with the conditions in the FCC process (598,599). A similar result was also obtained by Pinto et al. who employed two model FCC catalysts modified with nickel and vanadium, one consisting of zeolite USY, kaolin, and silica; and a second with alumina as an additional component (600). Three model reactions, namely, ethane hydrogenolysis, *n*-hexane cracking, and cyclohexane transformation, were used to characterize the effect of the binder–matrix components on the catalytic activity and selectivity. When alumina was present in the matrix, the microporosity and *n*-hexane activity were better maintained after vanadium introduction, with vanadium non-homogeneously distributed throughout the particle, in contrast to the homogeneous distribution observed in the absence of alumina. Data obtained from the cyclohexane and ethane hydrogenolysis reactions suggest that alumina limited the coke formation on nickel particles, because the nickel interacted with the alumina.

Two recent investigations by Meirer et al. show how our understanding of metal poisoning in FCC particles is advancing, by using noninvasive X-ray-based high spatial resolution characterization techniques, in this case at the Stanford Synchrotron Radiation Lightsource (SLAC). Full-field transmission X-ray microscopy, specifically, "absorption mosaic imaging," was used to investigate a single whole, commercially used (E-cat) FCC catalyst particle. The macrostructure and its availability for mass transport were visualized, and the distribution of nickel and iron species was determined (Figure 52) (601). By using multienergy tomography at the relevant metal K-edges and correlating with the distributions of porosity and permeability in the E-cat particle, both metals were found to accumulate in the outer layers of the particle, decreasing porosity (clogging the pores) and restricting access for reactant molecules. It was discovered that nodules and valleys formed at the surface of the particle, with iron distributed along these, showing the largest concentration within 1 μm distance from the surface. In contrast, nickel species were not only found near the surface, but they penetrated more deeply into the particle (≈ 7 μm from surface). Meirer et al. went one step further, by applying the techniques of X-ray nanotomography to a series of commercially used FCC particles, deactivated
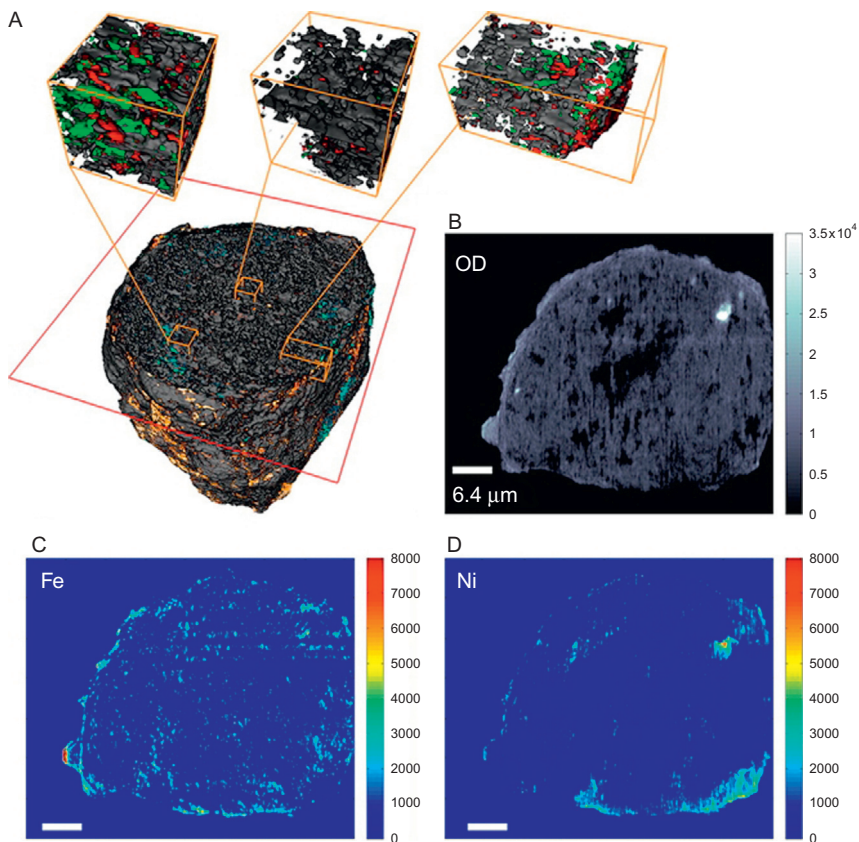
Figure 52 Relative iron and nickel distributions within an FCC particle. (A) Cut-through of the reconstructed FCC particle and selected subvolumes showing the 3D distribution of particle matrix (dark gray), iron (red), and nickel (green). (B–D) Slices in the *xz*-plane of the reconstructed volume display (B) the optical density at 7060 eV, (C) relative iron distribution, and (D) relative nickel distribution. *Reproduced with permission from Ref.* (601).

to differing degrees (equivalent to different life stages) *(602)*. It was observed that most of the nickel and iron accumulation occurs in the early stages of the FCC particles' cycle life and that these elements are concentrated near the surface layers (Figure 53). The inner core and pore system remain clear of metals (similar to a fresh particle). The presence of meso– and micropores allows some access for reactant molecules to the inside of the particle, but transport is less efficient. With this knowledge, it could be possible to design more efficient FCC catalyst particles.
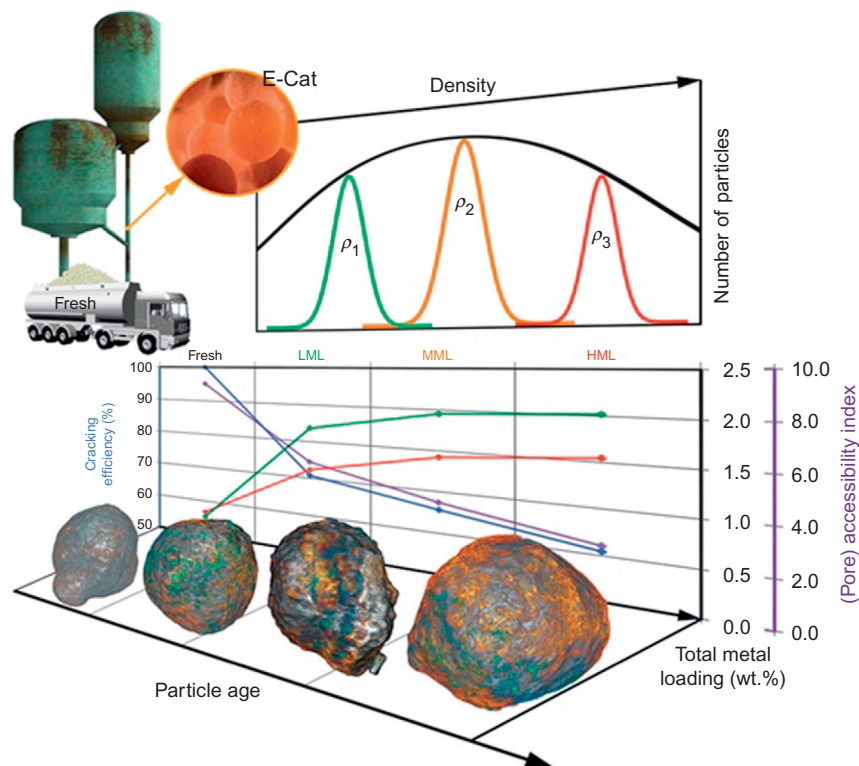
Figure 53 Bulk analysis results of fluid catalytic cracking particles at varying "life" stages in an industrial reactor. Top: Fresh catalyst particles and calcined E-Cat particles separated into three age groups according to their skeletal density (ρ_1 to ρ_3). Middle: Catalytic cracking activity (%) (blue) of vacuum gas oil (VGO) and accessibility index (purple) are anticorrelated with the total metal content of Fe and Ni (summed Fe and Ni concentrations in wt.%) for particle surface (green) and bulk (red). Bottom: Catalytic particles imaged by TXM tomography at 64 nm 3D voxel size. Red to orange colors indicate Fe concentration, whereas Ni is visualized using the blue to green color range. *Reproduced with permission from Ref.* (602).

5.2 Binder–Matrix Effects in Zeolite-Based Shaped Catalyst Bodies

Recently, Whiting *et al*. investigated the effects of amount and type of binder on the performance of zeolite ZSM-5-based catalysts (575,576). Either a pure zeolite ZSM-5 pellet or a series of zeolite ZSM-5-based extrudates, containing silica or alumina binder (20, 50, or 80 wt.% active phase), were taken and their catalytic performances in the oligomerization of thiophene were determined by using microspectroscopy. It was found that the amount of binder present

plays a significant role for reactivity and product selectivity. Increasing binder contents favors the formation of larger oligomers, probably because reactant species are stored in the binder and can react with intermediates bound to acid sites in the zeolite crystallites. Furthermore, the type of binder selected has a substantial impact on the product selectivity. Silica–bound zeolite ZSM-5 extrudates produced higher oligomers, whereas alumina-bound zeolite ZSM-5 extrudates preferentially produced ring-opened thiol-like species. As both binders were effectively inactive for this reaction, further tests were carried out to determine the role of the binder. Using a silicalite-Al_2O_3-bound extrudate (where both components are individually inactive for this reaction), reactivity was recorded for the oligomerization of thiophene, and it was found that formation of thiol–like oligomer species was favored. This result shows that aluminum species migrated from the Al_2O_3 binder to the silicalite, creating additional acid sites Therefore, the binder type should be carefully selected when forming shaped zeolite-based catalyst bodies. Finally, it was also noted, by using confocal fluorescence microscopy, that larger oligomer species appear to extend from the external surface of the zeolite crystallites or agglomerates outward into the surrounding binder material (Figure 54), suggesting that the interface between the zeolite material and the binder material offers a significant volume for reactions that leads to an altered product selectivity (Figure 55).

Conversion of MTO is another zeolite-catalyzed reaction for which binders have been shown influence performance, specifically conversion of methanol and selectivity to olefins *(603,604)*. Lee *et al.* have probed the effect of several different binders, namely silica, alumina, and aluminum phosphate sol (APS) on the catalytic performance of zeolite ZSM-5 in methanol conversion, with the desired product molecule being propylene *(605)*. The addition of an alumina binder increased the number of strong acid sites on the catalyst, but the opposite effect was noted with silica and APS binders. As the density and strength of Brønsted acid sites are known to be factors determining selectivity *(606)*, the binder contribution had obvious implications for the propylene selectivity. Although the alumina-bound zeolite showed a slight increase in strong acidity, its performance was similar to that of the silica–bound zeolite material. However, the performance of the APS-bound zeolites was dependent on the AAP content. A high content (>20 wt.%) produced mainly DME, the dehydration product of methanol, without further reaction to hydrocarbons. A low content of APS (<10 wt.%) resulted in a significantly enhanced propylene selectivity, because of fewer strong acid sites.
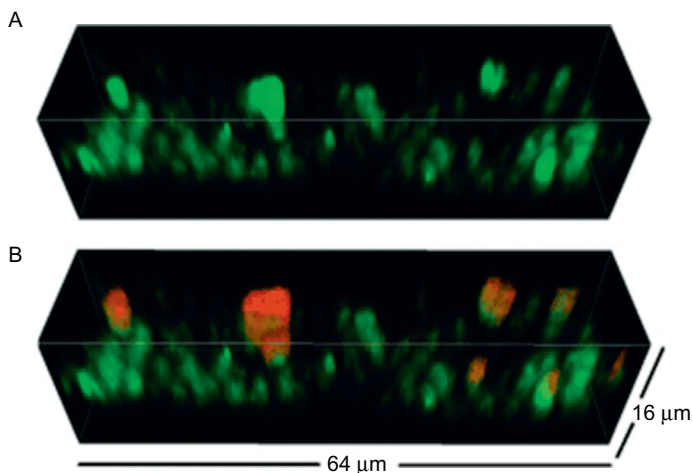
Figure 54 3D confocal fluorescence microscopy images of (A) a volume of a silica-bound ZSM-5-containing (80 wt.%) extrudate reacted with thiophene and subsequently excited with a 488 nm laser, showing fluorescent green oligomers present in the ZSM-5 crystals/agglomerates; (B) same volume as in (A), excited simultaneously with 488 and 561 nm laser, showing the "growth" of larger oligomers (in red) outward from the surface of ZSM-5 crystals/agglomerates. *Reproduced with permission from Ref.* (575).
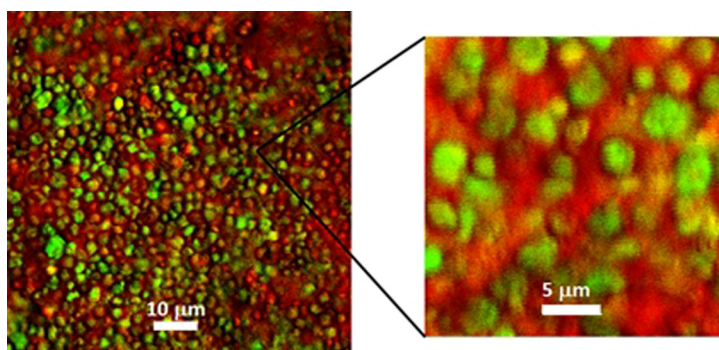
Figure 55 2D confocal fluorescence microscopy images of a silica-bound ZSM-5-containing (80 wt.%) extrudate reacted with thiophene and impregnated with Nile blue chloride (too large to enter zeolite pores, and so remains in the binder material). Simultaneous excitation with 488 and 642 nm lasers produced a green fluorescence attributed to ZSM-5 domains and a red fluorescence attributed to surrounding binder. Enlargement of the marked area in the left image is shown on the right. *Reproduced with permission from Ref.* (575).

Michels *et al.* investigated the effects of the type of binder and preparation method selected to form zeolite-based shaped bodies for the MTO process *(607)*. The authors used physical, extruded, or milled admixtures of MFI zeolites with either silica, alumina, or a clay binder and analyzed the properties and the performance of the obtained bodies. Extrusion with attapulgite and kaolin clay resulted in a larger particle size, producing enhanced macroporosity and related mass transfer properties. However, because of partial dealumination or ion exchange with the zeolite, the number of Brønsted acid sites was diminished, in turn reducing the intrinsic activity of the catalysts (with no significant correlation with selectivity or stability). Attapulgite offers unique advantages over silica or alumina binders, by neutralizing the zeolite framework with magnesium species, which promotes light-olefin selectivity and catalyst lifetime.

The migration of binder species to the active zeolite phase is not uncommon in zeolite-based shaped bodies, and the type of binder should be chosen carefully. Although it is difficult to find low cost, abundant, nontoxic, and efficient binders, Lee *et al.* discovered a base binder, namely flash-calcined hydrotalcite, for MTO catalysts. This binder, granulated with MFI zeolite, produces effective catalysts for the MTO process with high mechanical crush strength, and there is no loss in catalytic activity, because of the neutral to basic nature of the binder surface *(608)*. Kim *et al.* also demonstrated that the type of binder material plays a profound role in determining catalytic activity and stability of catalysts in the conversion of methanol *(609)*. The authors determined that the addition of a γ-alumina binder to sodium-modified zeolite ZSM-5 lowered the conversion of methanol to DME (target product), while broadening the operating temperature range and producing a more stable catalyst. This effect was associated with a dilution of the strong acid sites of the zeolite; however, other scenarios such as aluminum migration from the alumina binder to the zeolite cannot be ruled out, based on the available data.

The dispersion of the active zeolite phase in shaped catalyst bodies also determines the catalytic activity and selectivity in the MTO reaction and, ideally, should be controlled. Castaño *et al.* workers focused on determining the impact of heterogeneities in the spatial distribution of ZSM-5 aggregates in shaped catalyst bodies on catalyst selectivity and stability in MTH conversion (Figure 56) *(610)*. It was observed that shaped bodies containing smaller ZSM-5 aggregates yielded more olefins, fewer paraffins, and much less coke than shaped bodies containing ill-dispersed ZSM-5 crystals (Figure 57). The behavior of the catalyst with the finely dispersed ZSM-5 was associated with
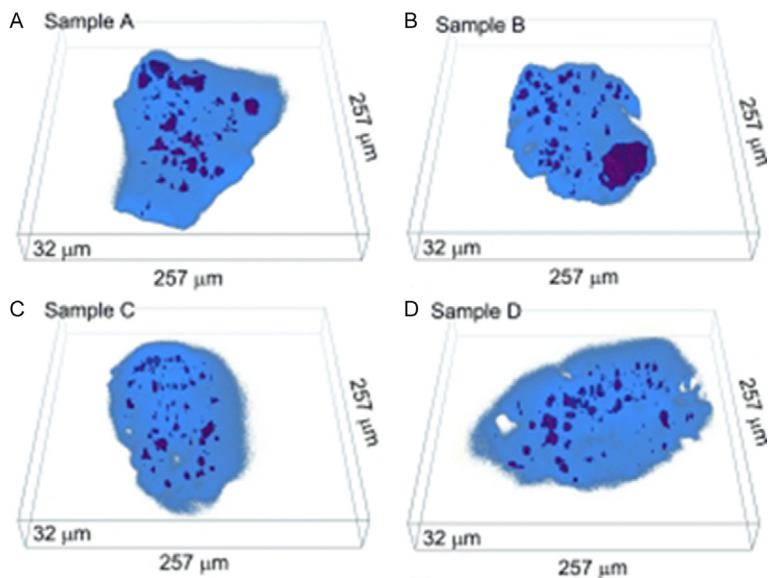
Figure 56 Confocal fluorescence microscopic images of four different zeolite ZSM-5-containing catalyst bodies stained with 4-fluorostyrene at a temperature of 100 °C. The binder is depicted in blue, whereas the ZSM-5 aggregates embedded are visualized in purple. A direct link between the zeolite ZSM-5 aggregate size and their intrinsic performances during the MTH reaction was found. *Adapted from Ref.* (610).

an increased number of hydrogen transfer reactions and lower diffusivity of coke precursors in close proximity to the aggregated zeolite domains. In a follow-up investigation, Ibanez *et al.* probed the effect of bentonite and α–Al_2O_3 as binders of ZSM-5-based catalysts during the transformation of chloromethane into light olefins (611). By using a combination of XPS, ^{29}Si NMR spectroscopy, TG–TPO, SEM, FT-IR, and UV–vis spectroscopy to analyze fresh and spent catalysts, the physicochemical properties and nature of the coke species were elucidated. The authors found that two deactivation mechanisms exist: irreversible dealumination at temperatures above 450 °C by HCl, and reversible coking (Figure 58). Coke formation was reported to result from condensation of polyalkylbenzenes, which are intermediates to olefin production.

To meet the increasing demand for propylene, catalytic propane dehydrogenation (PDH) can be applied, in addition or as an alternative to the MTO process (612). However, as PDH is an endothermic process, it requires relatively high temperature. Hence, cracking reactions occur,
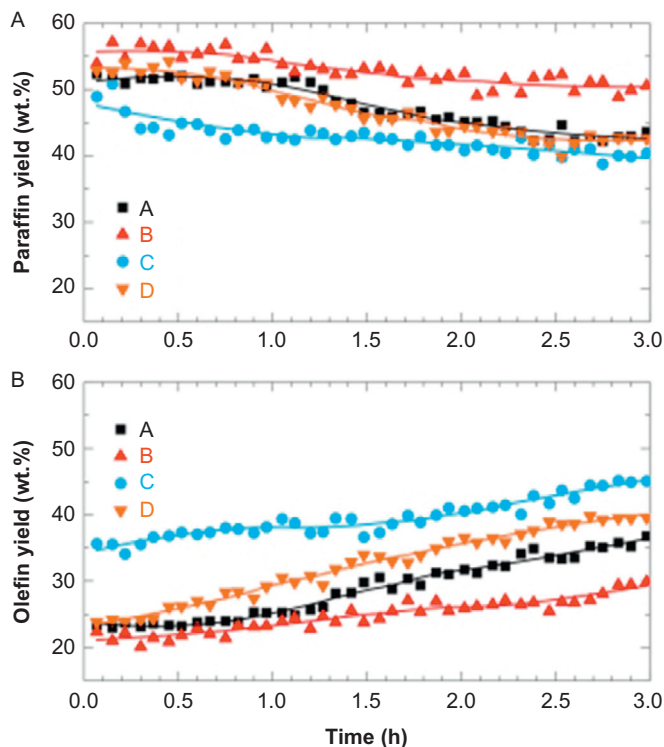
Figure 57 Catalytic performance of the ZSM-5-containing catalyst bodies A–D from Figure 56 in MTH conversion as a function of time on stream, yields of paraffins (A) and olefins (B). Reaction performed at a temperature of 400 °C in a fixed-bed reactor. *Reproduced with permission from Ref.* (610).

producing light alkanes and coke, which leads to catalyst deactivation and decreased propylene yields. Catalyst design is thus of vital importance. Chromium-based and platinum-based catalysts are commonly reported for PDH *(613–616)*, but do not exhibit stable performance because of coke formation. Zeolites can possibly improve stability, together with a binder, to make these catalysts more suitable for industrial application. Zhang *et al.* investigated the influence of an alumina binder on the performance of pelletized PtSnNa–ZSM-5 catalysts for PDH *(617)*. Not only was it observed that the binder decreases the surface area of the catalyst, with an enhancement in particle intensity (measured by catalytic grain intensity), but aluminum species from the binder migrated toward the zeolite ZSM-5 framework during the shaping process, producing additional acid sites. The binder content was also found to impact catalytic activity; a small amount of alumina
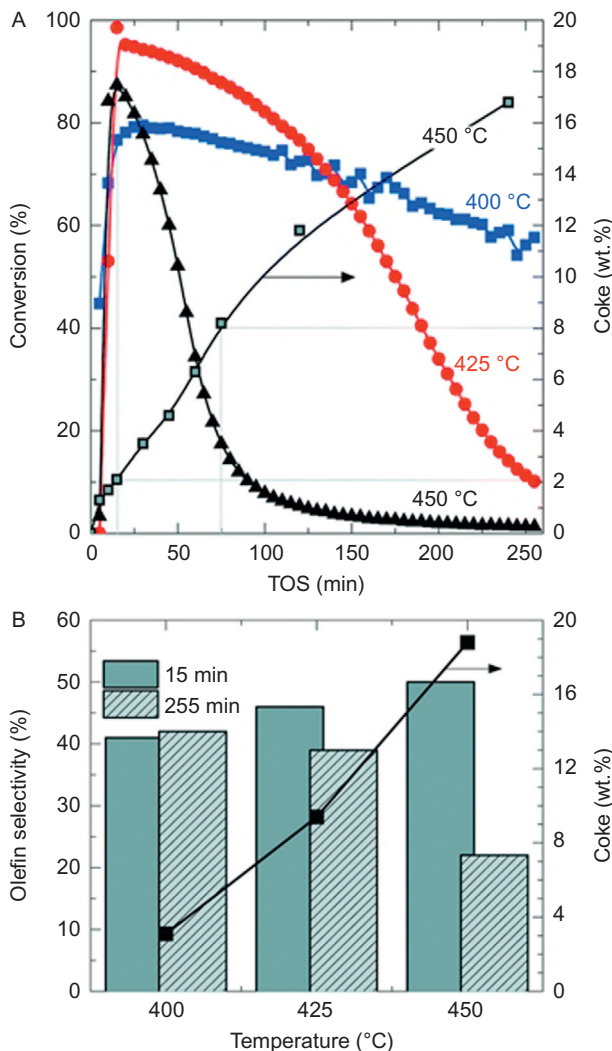
Figure 58 Evolution of chloromethane conversion with time on stream at different temperatures and coke content at 450 °C (A), and effect of temperature on the selectivity for light olefins at 15 and 255 min time on stream and coke content at 255 min time on stream (B). *Reproduced from Ref.* (611). *Published by The Royal Society of Chemistry.*

had a positive effect, associated with enhanced metal dispersion, and an increased number of acid sites, whereas a large amount of alumina resulted in a lower catalytic activity. Finally, the binder also aided in the transport of carbon deposits away from the tin species. Liu *et al.* investigated how the type of binder, that is, alumina, silica sol, or montmorillonite, influenced

the structure and performance of PtSnNa–ZSM-5 on PDH to propylene
(618). As expected, the mechanical strength of all catalyst particles agglom-
erated with binder was higher than that of the nonagglomerated catalysts,
and the dispersion of platinum was enhanced by differing degrees,
depending on the binder selected. ^{27}Al MAS NMR spectra of each material
showed that aluminum migration can occur from the binder to the zeolite
framework, with the highest degree of aluminum migration in the alumina-
bound catalysts. This catalyst also showed the highest propane conversion
and selectivity to propylene.

Propane aromatization is also of commercial importance and is an inter-
esting reaction to investigate binder effects on acidity and catalytic perfor-
mance in zeolite-based catalysts (see Section 3.1.6) *(619)*. Aromatization
activity and selectivity, and the ratios of dehydrogenation to cracking and
aromatization to cracking are of diagnostic value. Choudhary *et al.* investi-
gated the use of alumina or kaolin as a binder in H–GaZSM-5 catalysts, not-
ing that kaolin produced an appreciable decrease in acidity and catalytic
activity in comparison with the alumina-bound catalyst *(620)*. The alumina
binder produced a drastically increased zeolite intercrystalline acidity but did
not significantly influence the catalytic activity; however, catalyst deactiva-
tion and coke deposition were more pronounced. The addition of either
binder promoted the formation of aromatics in the zeolite; however, the
product selectivity is also strongly influenced by the degree of catalyst
deactivation.

Sodium montmorillonite (a clay) is often chosen as a binder in zeolite-
based catalysts, because of its excellent agglomerating properties, abundant
availability in nature, low cost, and its high mechanical resistance in the final
catalyst. However, it also has a major impact on the acidic properties of the
zeolite active phase, which affects the catalytic performance. *n*-Butane trans-
formation is an ideal reaction to investigate such effects, as acid properties of
the catalyst influence the initial conversion of butane as well as the product
selectivity. *n*-Butane isomerization is a highly attractive industrial process, as
isobutane can be used in alkylation units, or dehydrogenated to isobutylene
for use in MTBE production *(621)*. Cañizares *et al.* investigated the effect of
sodium montmorillonite content on pelletized zeolites, namely ZSM-5 and
mordenite *(622)*. The presence of sodium in the binder led to an overall loss
of strong acidity of the pelletized H–ZSM-5 catalysts (predicted value pro-
portionally calculated from the contribution of the zeolite and the binder if
they were not agglomerated). This loss was found to be due to solid–state ion
exchange between the H^{+} ions of the zeolite and Na^{+} ions in the clay.

However, by performing additional proton–exchange steps, the overall strong acidity of the pelletized material could be recovered. Because of the high number of Na^+ ions in Na–ZSM-5-based catalysts with a high binder content (65 wt.%), their strongly acid sites were found to be diminished to a greater extent than those of the Na–ZSM-5-based material bound with a lower binder content (35 wt.%), as expected. However, since the Na–mordenite-based catalysts had a higher sodium content (4.21 wt.%) at the outset than Na–ZSM-5 (2.61 wt.%) and the binder (2.90 wt.%) alone, a higher binder content in Na-mordenite pelletized catalysts led to an increase in the density of strong acid sites. These differences in strong acidity of the zeolite ZSM-5- and mordenite-montmorillonite pelletized catalysts had a clear influence on the catalytic performance. A lower initial activity was obtained with the zeolite ZSM-5-bound catalyst, compared with mordenite-bound catalyst materials. The main reaction occurring on the latter catalysts was disproportionation, forming propane and pentanes, whereas zeolite ZSM-5-bound catalyst materials produced typical cracking products, with no major changes in product distribution compared to mordenite samples as stated in the previous paragraph, because of reduced hydrogen transfer activity. Dorado *et al.* investigated how the addition of montmorillonite and bentonite as binders influenced the performance of Pd–ZSM-5 zeolites in the hydroisomerization of *n*–butane *(623)*. The results were similar to those of Canizares *et al.*; agglomeration of zeolite Pd–ZSM-5 with binder led to a neutralization of the acid sites of the zeolite, as a result of solid–state ion exchange between the two materials. This neutralization, of course, implied lower *n*–butane conversion with a differing product selectivity (as compared with unbound catalysts). The change in catalytic behavior was again explained with a modified hydrogen transfer activity (i.e., decrease in conversion accompanied by increase in isobutane selectivity), and also with the balance between metal and acid sites, and product diffusion. By selecting a catalyst consisting of Pd–ZSM-5 (Si/Al ratio of 25) and bentonite (65 wt.%), a high isobutane selectivity (87 mol.%) and yield (24 mol.%) was achieved, compared with the unbound Pd–ZSM-5 catalyst (47% isobutane selectivity and 18.5 mol.% yield).

Hydroisomerization of C_7 and C_8 compounds such as *n*–octane to (multi) branched high octane isomers is an interesting alternative to produce gasoline-type compounds and replace other environmentally harmful compounds such as aromatic, lead, and oxygenated compounds. The industrial hydro-isomerization of *n*–paraffins commonly employs bifunctional zeolite catalysts containing a metal, which offers the hydrogenation–dehydrogenation

function to accompany the isomerization function of the acid sites in the zeolite *(624,625)*. Currently, no industrial hydroisomerization process exists for *n*-octane; however, to make these bifunctional catalysts viable for this reaction in industrial reactors, binders should be added. de Lucas *et al.* investigated the influence of a bentonite (clay) binder on palladium-containing zeolites during the liquid–phase hydroisomerization of *n*-octane *(626)*. Following the general trend observed when using clay as a binder in zeolite-based catalysts, the acidity decreased as a result of solid-state ion exchange between H^+ and Na^+ ions, which led to a lower catalytic activity, in comparison with unbound catalysts. However, it was also noted that the porosity of the samples was affected during the agglomeration process, since EFAL species were created that caused partial blocking of the micropore mouths, thus increasing the diffusion lengths. Sanchez *et al.* *(627)* also used a bentonite−zeolite agglomerated catalyst and noticed that the presence of EFAL species made a more active *n*-octane hydroisomerization catalyst. This effect was explained with the strong Lewis acidity of EFAL in interaction with Brønsted acid sites, which can be considered as a synergistic effect. Regarding product selectivity, higher selectivity toward mono-branched isomers and lower selectivity to multibranched isomers were obtained with the agglomerated catalysts because of fewer strongly acidic Brønsted sites.

Lucas *et al.* investigated the influence of a bentonite binder on Pd-doped zeolites with three different framework types (MFI, MOR, and BEA) during the hydroisomerization of *n*-octane *(628)*. As seen previously, solid-state ion exchange between the binder and the zeolite led to a decrease in number of strongly acidic sites in the materials, which produced a lower conversion for both zeolite ZSM-5- and mordenite-based catalysts. The meso- and macroporosity introduced by adding the binder led to a higher selectivity toward branched isomers for both ZSM-5 (increase from 14 to 35 mol.%) and mordenite (27 to 49 mol.%). The activity of the zeolite beta–agglomerated catalyst was improved by the presence of EFAL species, producing higher selectivity to branched isomers (49 to 77.5 mol.%).

TDP is an old industrial process (see Section 3.2.1) that is still important because of the demand for C_8 aromatics such as xylene, which is essential for the production of polyesters and plastics *(629–631)*. Solid acid catalysts such as SiO_2–Al_2O_3 were used initially in this industrial process, but the product yield was low. Since then, zeolites have become the catalyst class of choice, but as in most cases, the addition of a binder is required to obtain an efficient industrial catalyst. Chen *et al.* investigated the effects of the binder on

coking characteristics during the TDP reaction *(632)* by analyzing fresh, spent, or regenerated α–alumina–bound mordenite–based commercial catalysts. Focusing on the fresh and spent catalyst, it was discovered that the concentration of strong acid sites (originating from the zeolite) initially decreased rapidly upon coking, but the catalyst remained active even after significant coke deposition. This behavior was explained by the location of the coke, which was believed to reside on the external surface of the zeolite (between zeolite and binder), rather than in the intracrystalline channels.

Coke formation on zeolite–based catalysts is a well–researched topic, but little is known about the effects of binders on coke characteristics. The work of Misk *et al.* is a rare example of work on this topic. The authors investigated the formation of coke from propylene on a catalyst containing zeolite 5A (80 wt.%) as active phase and kaolinite as binder (20 wt.%) *(633)*. The location and composition of the coke as a function of time on stream were analyzed, and the presence of the binder was found to significantly reduce the amount of coke on the zeolite (relative to coke formation on the unbound zeolite), because coke (precursor) molecules were trapped in the binder. By using a physical mixture of the zeolite and the binder (both having different dimensions), the authors could separate the components after the reaction and characterize them. Polyaromatic coke species were found to reside in the binder, while the zeolite contained mainly mono–, bi–, tri–, and tetra–alkyl aromatic compounds. Because of their size, these compounds sterically hindered access to the α–cages of the zeolite material. As observed by Chen *et al.*, high coke contents implied heavy polyaromatic compounds, which are located on the external surface of the zeolite crystallites *(632)*.

Although the addition of binder during the formation of shaped bodies is the common method to produce bound zeolite–based catalysts, relatively recent research teaches us that binders can be tailor–made with great detail.

van der Bij *et al.* recently investigated the formation of aluminum phosphate in four different zeolite framework topologies, namely, MOR, FAU, FER *(634)*, and MFI *(635)*, and, further, how the phosphate can act as a binder in the final catalyst material. By using steam dealumination of each industrially relevant zeolite prior to reaction with a phosphate precursor, EFAL species were created that in the first step reacted to form an $AlPO_4$ phase (Figure 59). However, a variety of results were obtained depending on the zeolite topology. In mordenite, an amorphous $AlO(OH)$ phase created upon dealumination readily reacted with phosphoric acid to form
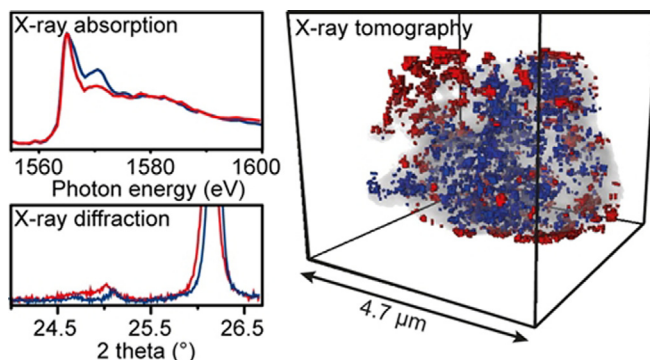
Figure 59 A combination of X-ray absorption spectroscopy, X-ray diffraction, and X-ray tomography to investigate the ability of three industrially relevant zeolite frameworks (MOR, FAU, and FER) to form an $AlPO_4$ binder phase after steam dealumination and reaction with phosphoric acid. Framework Si/Al ratio, stability of the framework aluminum, pore dimensionality, and accessibility of EFAL species are all parameters that affect the formation of the binder phase. *Reprinted with permission from Ref.* (634). *Copyright (2014) American Chemical Society.*

mainly amorphous $AlPO_4$ inside the zeolite channel system, but also $AlPO_4$ islands that crystallized on the outside. During a milder phosphatation step, the ultrastable Y (FAU) formed an α-cristobalite/tridymite $AlPO_4$ phase in the pores of the framework. However, when employing FER, aluminum species could not be extracted and reaction with phosphoric acid did not result in the formation of an $AlPO_4$ binder phase.

Lercher and coworkers explored the creation of a binder by surface modification of medium-pore-size zeolites (i.e., ZSM-5). The motivation was to enhance the sorption properties, which can also play a role in catalysis, as demonstrated by the shape-selective nature of zeolites in many industrial applications *(636–638)*. By depositing tetraethyl orthosilane (TEOS) on zeolite ZSM-5 crystals, a hierarchical pore system with enhanced sorption properties was formed on the outside of the zeolite. This modification can be thought of as introducing a binder. The transfer of reactant molecules to the active phase was enhanced. By using a number of aromatic molecules, namely, benzene, toluene, and *p*–xylene, in combination with fast, time-resolved IR spectroscopy, it was found that the mesoporous silica overlayer significantly increases the sorption rates for benzene (Figure 60), whereas the sorption rates for alkyl-substituted aromatics decreased with increasing radius of gyration. The change in sorption rates was ascribed to enhanced sticking probability of the aromatic molecules on the modified surface (which
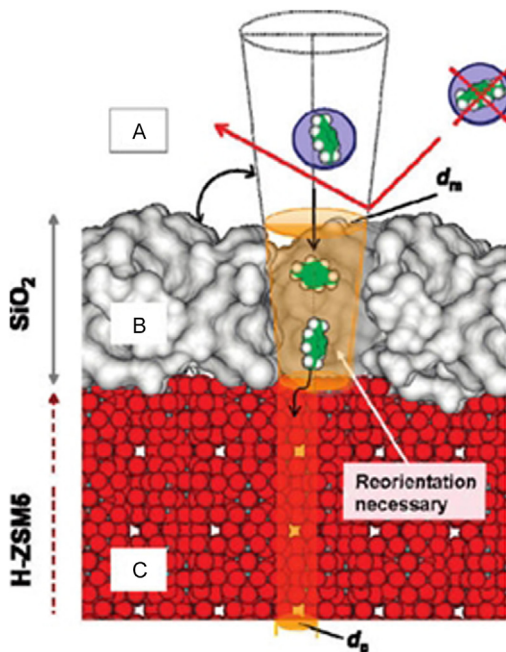
Figure 60 Scheme of a cross-section of a typical zeolite ZSM-5-3m crystal surface coated with a silica overlayer, with an average thickness of 3.0 nm. Such overlayers contain large micropores with an average pore diameter of 1.5 nm, which direct the sorbing molecules with the appropriate radius of gyration into the zeolite micropores. The *p*-xylene molecules can directly enter the overlayer pores; however, they must undergo reorientation before they access the zeolite micropores. *Reproduced with permission from Ref.* (637).

enhanced mass transfer), as well as to the intrinsic size exclusion properties of the micropores in the zeolite ZSM–5 crystals. This innovative method allows the kinetic separation of molecules based on their dimensions.

The porous overlayer created by Lercher and coworkers was not the first of this kind of "binder." Bellussi and coworkers reported on the use of tetrapropylammonium ions (TPA$^+$) during the shaping of silica–bound sub-micron TS-1 aggregates in an industrial catalyst. By organizing the silica oligomers around the TPA$^+$ clusters (and subsequent calcination), a meso-porous amorphous "sponge" binder is created *(639–641)*. Combination of this sponge with the micropores of the titanium–silicalite structure leads to a micromesoporous hierarchical material that is used for many important industrial processes such as the hydroxylation of phenol *(642)* and the epox-idation of propylene *(643)* (see Section 3.3.5).

6. CONCLUDING REMARKS AND FUTURE PERSPECTIVES

This review article illustrates the enormous versatility of zeolites and zeotypes as catalysts. Because of their properties, they are applied in a wide range of catalytic processes and have tremendous impact, providing our main transportation fuels, raw materials for petrochemicals, monomers, and fine chemicals and allowing the use of a variety of fossil and renewable feedstocks as starting materials. In an era characterized by the need and desire to implement alternatives to fossil feedstocks, such as biomass and natural gas, we can expect an increasing role for zeolites and zeotypes in future catalytic processes.

Whereas previous review papers have focused on "the Big Five" zeolites (FAU, MFI, MOR, BEA, and FER), a literature search based on the 13 structures with catalytic applications listed in the introduction, as summarized in Figure 61, shows that RHO, CHA, TON, MWW, and LTL are gaining increasing interest, not only in academia but also in the chemical industry. Consequently, the list of "the Big Five" zeolites should perhaps be expanded and renamed to include some of these structures, in
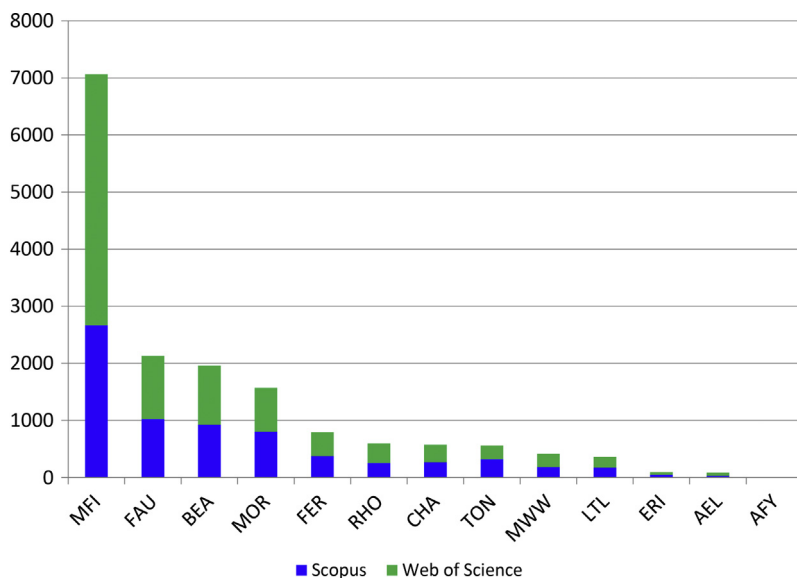
Figure 61 Literature references related to zeolite structures from Web of Science and Scopus. The figure shows the number of articles in which the combination of "zeolite" and the three letter IUPAC structure code for each structure was found in Web of Science and Scopus.

particular CHA, given the widespread application of CHA–based catalysts in MTO processes in China (644).

The timeline in Figure 62 shows a number of important discoveries and commercial applications in the field of zeolites and related materials. The
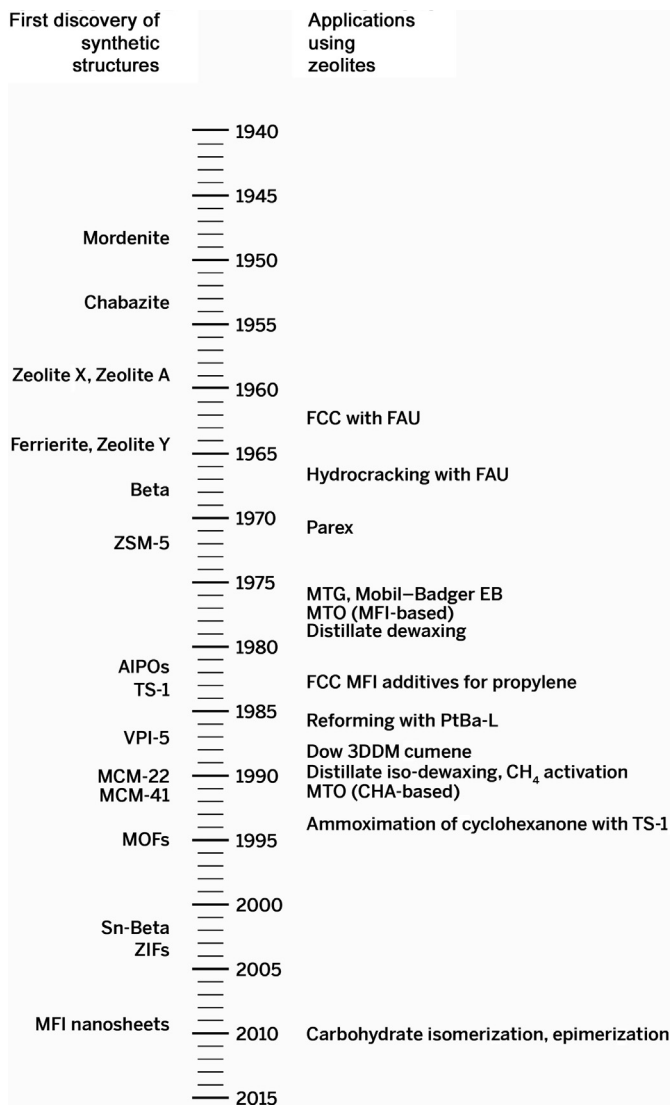
Figure 62 Timeline indicating milestones in zeolite synthesis and application. The year of invention or first publication for zeolite structures is mentioned on the left; on the right, a number of important applications are listed, based on date of first publication or date of first commercial use as discussed earlier in this review.

continuing synthesis efforts taking place at a global scale both in industrial and in academic laboratories are not reflected in this graph, but will continue to yield interesting new porous materials with catalytic functionalities. It is evident from the figure that there is a continuous flow of new materials and new process designs. In addition, as this review shows, mechanistic understanding based on both theory and experiments keeps improving.

More specifically, we have recently seen promising developments in the field of characterization of zeolite-based catalyst materials. New microspectroscopy tools have been developed and are continuously improved, which will allow us to better understand the catalysis on zeolites both at a molecular level as well as on the mesoscale. Accessible information includes pore structures of zeolite-based catalysts, matrix effects in zeolite deactivation, and spatial determination of activity hot spots in zeolite-based catalysts.

The databases of hypothetical framework structures show that many more zeolite and zeotype structures may be within reach of our synthetic efforts, and synthesis routes may be discovered through structured efforts involving both theory and experiment. High-throughput experimental techniques will certainly accelerate both the design of zeolite synthesis and the screening of catalytic properties for various applications, while improved theoretical models of (the early stages of) zeolite synthesis and the reactions of molecules within the confined space of the zeolite structures will guide experimental work on zeolite synthesis. The increased understanding may allow not only the design of new structures and chirality but also the exact placement of framework atoms (for instance aluminum or transition metals) within the structure, which may allow the design of even more selective and active catalysts *(645)*.

Design of successful new processes will require a fundamental understanding of the catalytic processes at the molecular level, combined with a thorough understanding of the interaction of the various constituents of the final catalyst (of which the zeolite is only a part) at the mesoscale, and finally a reactor design that allows the full potential of the new process to be exploited at a commercial scale. This problem requires a multiscale scientific approach, which will only be realized when scientists with different backgrounds join forces.

The inherent stability and chemical versatility of zeolites and zeotypes, which can be applied as acid catalysts (Brønsted and Lewis), base catalysts, redox catalysts, and bifunctional catalysts, will ensure that they remain the primary candidates for active materials in many future applications, including the catalytic conversion of renewables as well as advanced photo- and electrocatalytic processes.

REFERENCES

1. Breck, D. W. *Zeolite Molecular Sieves—Structure, Chemistry and Use*; Robert E. Krieger Publishing Company: Malabar, FL, **1984**; p 29.
2. Cronstedt, A. F. *Akad. Handl. Stockholm* **1756**, *18*, 120–123.
3. Cejka, J.; Corma, A.; Zones, S., Eds. *Zeolites and Catalysis: Synthesis, Reactions, and Applications*; Wiley-VCH: Weinheim, **2010**.
4. Ertl, G.; Knözinger, H.; Schüth, F.; Weitkamp, J., Eds. *Handbook of Heterogeneous Catalysis,* 8 vol. 2nd ed.; Wiley-VCH: Weinheim, **2014**.
5. van Bekkum, H.; Jacobs, P. A.; Flanigen, E. M.; Jansen, J. C., Eds.; *Introduction to Zeolite Science and Practice*; Studies in Surface Science and Catalysis; Vol. 137, Elsevier: Amsterdam, **2001**.
6. Smith, J. V. *Zeolites* **1984**, *4*, 309–310.
7. Wilson, S. T.; Lok, B. M.; Messina, C. M.; Cannan, T. R.; Flanigen, E. M. *J. Am. Chem. Soc.* **1982**, *104*, 1146–1147.
8. Yaghi, O. M.; Li, G.; Li, H. *Nature* **1995**, *378*, 703–706.
9. Tian, Y.-Q.; Cai, C.-X.; Ren, X.-M.; Duan, C.-Y.; Xu, Y.; Gao, S.; You, X.-Z. *Chem. Eur. J.* **2003**, *9*, 5673–5685.
10. Phan, A.; Doonan, C. J.; Uribe-Romo, F. J.; Knobler, C. B.; O'Keeffe, M.; Yaghi, O. *Acc. Chem. Res.* **2010**, *43*, 58–67.
11. Weitkamp, J. *Solid State Ion.* **2000**, *131*, 175–188.
12. Liebau, F. *Zeolites* **1983**, *3*, 191–193.
13. Dyer, A. *An Introduction to Zeolite Molecular Sieves*; John Wiley and Sons: Chichester, **1988**; p 1.
14. Li, J.; Corma, A.; Yu, J. *Chem. Soc. Rev.* **2015**, *44*, 7112–7127. http://dx.doi.org/10.1039/c5cs00023h.
15. Sherman, J. D. *Proc. Natl. Acad. Sci. U. S. A.* **1999**, *96*, 3471.
16. Maesen, T. *Introduction to Zeolite Science and Practice*, 3rd revised ed.; Elsevier: Amsterdam, **2007**; pp 1–12.
17. Janshekar, H.; Inoguchi, Y.; Greiner, E. Chemical Economics Handbook Zeolites (599.1000); IHS Chemical, **2013**; and previous versions by Lacson *et al.* (2002) and Lauriente *et al.* (2005) (SRI Consulting).
18. Association of Detergent Zeolite Producers. *Zeolites for detergents*, **2000**. http://www.zeolites.eu/downloads/Zeolites.pdf (accessed June 28, 2015).
19. Adams, C. J.; Araya, A.; Carr, S. W.; Chapple, A. P.; Franklin, K. R.; Graham, P.; Minihan, A. R.; Osinga, T. J.; Stuart, J. A. *Stud. Surf. Sci. Catal.* **1997**, *105*, 1667–1674.
20. Vermeiren, W.; Gilson, J. P. *Top. Catal.* **2009**, *52*, 1131–1161.
21. Rabo, J. A.; Schoonover, M. W. *Appl. Catal. A* **2001**, *222*, 261.
22. Martínez, C.; Corma, A. *Coord. Chem. Rev.* **2011**, *255*, 1558–1580.
23. Baerlocher, C.; McCusker, L. B.; Olson, D. H. *Atlas of Zeolite Framework Types*; Elsevier: Amsterdam, **2007**. http://www.iza-structure.org/databases/.
24. Bull, I. U.S. Patent 7,601,662, **2009**.
25. Andersen, P. J. WO Patent Appl. 2008/132452 A2, **2008**.
26. Deka, U.; Lezcano-Gonzalez, I.; Weckhuysen, B. M.; Beale, A. M. *ACS Catal.* **2013**, *3*, 413–427.
27. Gao, F.; Kwak, J. H.; Szanyi, J.; Peden, C. H. F. *Top. Catal.* **2013**, *56*(15–17), 1441–1459.
28. Kwak, J. H.; Tran, D.; Szanyi, J.; Peden, C. H. F.; Lee, J. H. *Catal. Lett.* **2012**, *142*, 295–301.
29. Ellmers, I.; Vélez, R. P.; Bentrup, U.; Brückner, A.; Grünert, W. *J. Catal.* **2014**, *311*, 199–211.
30. Johnson, T. V. In: *Urea-SCR Technology for deNOx After Treatment of Diesel Exhausts, Fundamental and Applied Catalysis*; Nova, I., Tronconi, E., Eds.; Springer Science + Business Media: New York, **2014**; pp 3–31.

31. Chen, H.-Y. In: *Urea-SCR Technology for deNOx After Treatment of Diesel Exhausts, Fundamental and Applied Catalysis*; Nova, I., Tronconi, E., Eds.; Springer Science +Business Media: New York, **2014**; pp 123–147.
32. Brandenberger, S.; Kröcher, O.; Tissler, A.; Althoff, R. *Catal. Rev.* **2008**, *50*, 492–531.
33. de Rezende Pinho, A.; de Almeida, M. M. B.; Leal Mendes, F.; Loureiro Ximenes, V.; Carlos Casavechia, L. *Fuel Process. Technol.* **2015**, *131*, 159–166.
34. http://www.kior.com (accessed July 2015).
35. Bridgewater, A. V. *Biomass Bioenergy* **2012**, *38*, 68–94.
36. *Chem. Eng. News*, **2013**, 91, http://cen.acs.org/articles/91/i45/Race-Create-Pyrolysis-Biofuels-Hot.html (accessed July 2015).
37. Huber, G. W.; Iborra, S.; Corma, A. *Chem. Rev.* **2006**, *106*, 4044–4098.
38. Huber, G. W.; Corma, A. *Angew. Chem. Int. Ed. Engl.* **2007**, *46*, 7184–7201.
39. Climent, M. J.; Corma, A.; Iborra, S. *Green Chem.* **2014**, *16*, 516–547.
40. Corma, A.; Iborra, S.; Velty, A. *Chem. Rev.* **2007**, *107*, 2411–2502.
41. Stöcker, M. *Angew. Chem. Int. Ed. Engl.* **2008**, *47*, 9200–9211.
42. Al-Sabawi, M.; Chen, J.; Ng, S. *Energy Fuel* **2012**, *26*, 5355–5372.
43. Kubicka, D.; Kikhtyanin, O. *Catal. Today* **2015**, *243*, 10–22.
44. Degnan, T. F. *Top. Catal.* **2000**, *13*, 349–356.
45. Sun, J.; Bonneau, C.; Cantin, A.; Corma, A.; Diaz-Cabañas, M. J.; Moliner, M.; Zhang, D.; Li, M.; Zou, X. *Nature* **2009**, *458*, 1154–1157.
46. Jiang, J.; Jorda, J. L.; Diaz-Cabañas, M. J.; Yu, J.; Corma, A. *Angew. Chem. Int. Ed. Engl.* **2010**, *49*, 4986–4988.
47. Effenberger, H.; Giester, G.; Krause, W.; Bernhardt, H. J. *Am. Mineral.* **1998**, *83*, 607–617.
48. Baerlocher, C.; Gramm, F.; Massüger, L.; McCusker, L. B.; He, Z.; Hovmöller, S.; Zou, X. *Science* **2007**, *315*, 1113–1116.
49. Xie, D.; Baerlocher, C.; McCusker, L. B. *J. Appl. Crystallogr.* **2011**, *44*, 1023–1032.
50. Smeets, S.; McCusker, L. B.; Baerlocher, C.; Mugnaioli, E.; Kolb, U. *J. Appl. Crystallogr.* **2013**, *46*, 1017–1023.
51. Treacy, M. M. J.; Newsam, J. M.; Deem, M. *J. Proc. R. Soc. Lond.* **1991**, *433*, 499–520.
52. McCusker, L. B.; Baerlocher, C. *Chem. Commun.* **2009**, 1439–1451.
53. Sun, J.; Hovmöller, S.; Zou, X.; Gramm, F.; Baerlocher, C.; McCusker, L. B. *Z. Kristallogr.* **2010**, *225*, 77–85.
54. McCusker, L. B. *Stud. Surf. Sci. Catal.* **2008**, *174* (Part A), 3–12.
55. Li, Y.; Yu, J. *Chem. Rev.* **2014**, *114*, 7268–7316.
56. Haag, W. O.; Lago, R. M.; Weisz, P. B. *Nature* **1984**, *309*, 589.
57. Miale, J. N.; Chen, N. Y.; Weisz, P. B. *J. Catal.* **1966**, *6*, 278–287.
58. Derouane, E. G.; André, J.-M.; Lucas, A. A. *Chem. Phys. Lett.* **1987**, *137*, 336–340.
59. Derouane, E. G.; André, J. M.; Lucas, A. A. *J. Catal.* **1988**, *110*, 58–73.
60. Frillette, V. J.; Haag, W. O.; Lago, R. M. *J. Catal.* **1981**, *67*, 218–222.
61. Zones, S. I.; Harris, T. V. *Microporous Mesoporous Mater.* **2000**, *35–36*, 31–46.
62. Chu, Y. F. U.S. Patent 4,927,525, **1990**.
63. Butter, S. A.; Chester, A. W.; Schwartz, A. B. U.S. Patent 4,354,963, **1982**.
64. Carpenter, J. R. In: *Synthesis and Testing of a Supported Shilov Oxidation Catalyst & II. Influence of Structural Features on Zeolite Characterization by Constraint Index Testing*; California Institute of Technology: Pasadena, **2010**. PhD thesis.
65. Zones, S. I.; Chen, C.; Corma, A.; Cheng, M. T.; Kibby, C. L.; Chan, I. Y.; Burton, A. W. *J. Catal.* **2007**, *250*, 41–54.
66. Wagner, P.; Nakagawa, Y.; Lee, G. S.; Davis, M. E.; Elomari, S.; Medrud, R. C.; Zones, S. I. *J. Am. Chem. Soc.* **2000**, *122*, 263–273.
67. Baerlocher, C.; Weber, T.; McCusker, L. B.; Palatinus, L.; Zones, S. I. *Science* **2011**, *333*, 1134–1137.

68. Camblor, M. A.; Diaz-Cabañas, M.-J.; Perez-Pariente, J.; Teat, S. J.; Clegg, W.; Shannon, I. J.; Lightfoot, P.; Wright, P. A.; Morris, R. E. *Angew. Chem. Int. Ed. Engl.* **1998**, *37*, 2122–2126.
69. Corma, A.; Diaz-Cabañas, M. J.; Jorda, J. L.; Rey, F.; Sastre, G.; Strohmaier, K. G. *J. Am. Chem. Soc.* **2008**, *130*, 16482.
70. Castañeda, R.; Corma, A.; Fornés, V.; Martínez-Triguero, J.; Valencia, S. *J. Catal.* **2006**, *238*, 79–87.
71. Xu, Y.; Li, Y.; Han, Y.; Song, X.; Yu, J. *Angew. Chem. Int. Ed. Engl.* **2013**, *52*, 5501–5503.
72. Willhammar, T. *Structural Study of Zeolites Utilizing Novel Electron Crystallographic Methods—A Voyage into the World of Zeolite Structures*; Stockholm University: Stockholm, **2013**. Doctoral Thesis.
73. Corma, A.; Díaz-Cabañas, M. J.; Rey, F.; Afeworki, M.; Dorset, D. L.; Soled, S. L.; Strohmaier, K. G. *Proc. Natl. Acad. Sci. U. S. A.* **2010**, *107*, 13997–14002.
74. Martinez-Franco, R.; Moliner, M.; Yun, Y.; Sun, J.; Wan, W.; Zou, X.; Corma, A. *Proc. Natl. Acad. Sci. U. S. A.* **2013**, *110*, 3749–3754.
75. Moliner, M.; Díaz-Cabañas, M. J.; Fornés, V.; Martínez, C.; Corma, A. In: *Zeolites and Related Materials: Trends, Targets and Challenges*; *Proceedings of 4th International FEZA Conference*, **2008**; pp 155–160.
76. Jang, J.; Yun, J.; Zou, X.; Jorda, J. L.; Corma, A. *Chem. Sci.* **2015**, *6*, 480–485.
77. Jiang, J.; Jorda, J. L.; Baumes, L. A.; Mugnaioli, E.; Diaz-Cabanas, M. J.; Kolb, U.; Corma, A. *Science* **2011**, *333*, 1131–1134.
78. Tang, L.; Shi, L.; Bonneau, C.; Sun, J.; Yue, H.; Ojuva, A.; Lee, B.-L.; Kritikos, M.; Bell, R. G.; Bacsik, Z.; Mink, J.; Zou, X. *Nat. Mater.* **2008**, 7, 381–385.
79. Song, X. W.; Li, Y.; Gan, L.; Wang, Z. P.; Yu, J. H.; Xu, R. R. *Angew. Chem. Int. Ed. Engl.* **2009**, *48*, 314–317.
80. Broach, R. W.; Kirchner, R. M. *Microporous Mesoporous Mater.* **2011**, *143*, 398–400.
81. Moliner, M.; González, J.; Portilla, M. T.; Willhammar, T.; Rey, F.; Llopis, F. J.; Zou, X.; Corma, A. *J. Am. Chem. Soc.* **2011**, *133*, 9497–9505.
82. Wilhammar, T.; Sun, J.; Wan, W.; Oleynikov, P.; Zhang, D.; Zou, X.; Moliner, M.; Gonzalez, J.; Martinez, C.; Rey, F.; Corma, A. *Nat. Chem.* **2013**, *4*, 188–194.
83. Jackowski, A.; Zones, S. I.; Hwang, S. J.; Burton, A. W. *J. Am. Chem. Soc.* **2009**, *131*, 1092–1100.
84. Afeworki, M.; Dorset, D. L.; Kennedy, G. J.; Stromaier, K. G. *Chem. Mater.* **2006**, *18*, 1697–1704.
85. Dorset, D. L.; Strohmaier, K. G.; Kliewer, C. E.; Corma, A.; Diaz-Cabanas, M. J.; Rey, F.; Gilmore, C. J. *Chem. Mater.* **2008**, *20*, 5325–5331.
86. Dorset, D. L.; Kennedy, G. J.; Strohmaier, K. G.; Diaz-Cabanas, M. J.; Rey, F.; Corma, A. *J. Am. Chem. Soc.* **2006**, *128*, 8862–8867.
87. Hernandez-Rodriguez, M.; Jorda, J. L.; Rey, F.; Corma, A. *J. Am. Chem. Soc.* **2012**, *134*, 13232–13235.
88. Simancas, R.; Dari, D.; Velamazán, N.; Navarro, M. T.; Cantin, A.; Jordá, J. L.; Sastre, G.; Corma, A.; Rey, F. *Science* **2010**, *330*, 1219–1222.
89. Wagner, P.; Zones, S. I.; Davis, M. E.; Medrud, R. C. *Angew. Chem. Int. Ed. Engl.* **1999**, *38*, 1269–1272.
90. Simancas, R.; Jorda, J. L.; Rey, F.; Corma, A.; Cantin, A.; Peral, I.; Popescu, C. *J. Am. Chem. Soc.* **2014**, *136*, 3342–3345.
91. Smeets, S.; McCusker, L. B.; Baerlocher, C.; Xie, D.; Chen, C.-Y.; Zones, S. I. *J. Am. Chem. Soc.* **2015**, *137*, 2015–2020.
92. Zones, S. I. *Zeolites* **1989**, *9*, 458–467.
93. Barrett, P. A.; Boix, T.; Puche, M.; Olson, D. H.; Jordan, E.; Köller, H.; Camblor, M. A. *Chem. Commun.* **2003**, 2114–2115.

94. Lorgouilloux, Y.; Dodin, M.; Paillaud, J.-L.; Caullet, P.; Michelin, L.; Josien, L.; Ersen, O.; Bats, N. *J. Solid State Chem.* **2009**, *182*, 622–629.
95. Dodin, M.; Paillaud, J.-L.; Lorgouillous, Y.; Caullet, P.; Elkaim, E.; Bats, N. *J. Am. Chem. Soc.* **2010**, *132*, 10221–10223.
96. Rojas, A.; Camblor, M. A. *Angew. Chem. Int. Ed. Engl.* **2012**, *51*, 3854–3856.
97. Balkus, K. J.; Gabrielow, A. G. Jr. U.S, Patent 5,489,424, **1996**.
98. Han, Y.; Li, Y.; Yu, J.; Xu, R. *Angew. Chem. Int. Ed. Engl.* **2011**, *50*, 3003–3005.
99. Xu, Y.; Li, Y.; Han, Y.; Song, X.; Yu, J. *Angew. Chem. Int. Ed. Engl.* **2013**, *52*, 5501–5503.
100. Martínez-Franco, R.; Moliner, M.; Thogersen, J. R.; Corma, A. *ChemCatChem* **2013**, *5*, 3316–3323.
101. Martínez-Franco, R.; Moliner, M.; Frach, C.; Kustov, A.; Corma, A. *Appl. Catal. B* **2012**, *127*, 273–280.
102. Martínez-Franco, R.; Moliner, M.; Concepcion, P.; Thogersen, J. R.; Corma, A. *J. Catal.* **2014**, *314*, 73–82.
103. Martínez-Franco, R.; Moliner, M.; Corma, A. *J. Catal.* **2014**, *319*, 36–43.
104. Ren, L.; Zhu, L.; Yang, C.; Chen, Y.; Sun, Q.; Zhang, H.; Li, C.; Nawaz, F.; Meng, X.; Xiao, F. *Chem. Commun.* **2011**, *47*, 9789–9791.
105. Shao, L.; Li, Y.; Yu, J.; Xu, R. *Inorg. Chem.* **2012**, *51*, 225–229.
106. Liu, Z.; Song, X.; Li, J.; Li, Y.; Yu, J.; Xu, R. *Inorg. Chem.* **2012**, *51*, 1969–1974.
107. Schnick, W.; Lücke, J. *Angew. Chem. Int. Ed. Engl.* **1992**, *31*, 213–215.
108. Stock, N.; Irran, E.; Schnick, W. *Chem. Eur. J.* **1998**, *4*, 1822–1828.
109. Correl, S.; Oeckler, O.; Stock, N.; Schnick, W. *Angew. Chem. Int. Ed. Engl.* **2003**, *42*, 3549–3552.
110. Leonowicz, M. E.; Lawton, J. A.; Lawton, S. L.; Rubin, M. K. *Science* **1994**, *264*, 1910–1913.
111. Richardson, J. W., Jr.; Vogt, E. T. C. *Zeolites* **1992**, *12*, 13–19.
112. Dessau, R. M.; Schlenker, J. L.; Higgins, J. B. *Zeolites* **1990**, *10*, 522–524.
113. Treacy, M. M. J.; Rao, S.; Rivin, I. In: von Ballmoos, R., Higgins, J. B., Treacy, M. M. J., Eds.; *Proceedings of the 9th International Zeolite Conference Montreal 1992* Butterworth-Heinemann: Stoneham, Massachusetts, **1993**; pp 381–388.
114. Li, Y.; Yu, J.; Xu, R. *Angew. Chem. Int. Ed. Engl.* **2013**, *52*, 1673–1677.
115. Foster, M. D.; Treacy, M. M. J. A database of hypothetical zeolite structures, **2010**. http://www.hypotheticalzeolites.net.
116. Li, Y.; Yu, J.; Xu, R. Hypothetical zeolite database. http://mezeopor.jlu.edu.cn/hypo.
117. Thomas, J. M.; Lewis, D. W. *Z. Phys. Chem.* **1996**, *197*, 37–48.
118. Lewis, D. W.; Sankar, G.; Wyles, J. K.; Thomas, J. M.; Catlow, C. R. A.; Willock, D. J. *Angew. Chem. Int. Ed. Engl.* **1997**, *36*, 2675–2677.
119. Bushuev, Y. G.; Sastre, G. *Microporous Mesoporous Mater.* **2010**, *129*, 42–53.
120. Moliner, A.; Rey, F.; Corma, A. *Angew. Chem. Int. Ed. Engl.* **2013**, *52*, 13880–13889. http://dx.doi.org/10.1002/anie.201304713.
121. Yu, J.; Xu, R. *Acc. Chem. Res.* **2010**, *43*, 1195–1204.
122. Derouane, E. G.; Gabelica, Z. *J. Catal.* **1980**, *65*, 486–489.
123. Moliner, M.; Willhammar, T.; Wan, W.; González, J.; Rey, F.; Jorda, J. L.; Zou, X.; Corma, A. *J. Am. Chem. Soc.* **2012**, *134*, 6473–6478.
124. Vogt, E. T. C.; Weckhuysen, B. M. *Chem. Soc. Rev.* **2015**, *44*, 7342–7370. http://dx.doi.org/10.1039/c5cs00376h.
125. Breck, D. W. U.S. Patent 3,130,007, **1964**.
126. Reichle, A. D. *Chem. Eng. Prog.* **1990**, 70–74.
127. Arguaer, R. J.; Landolt, G. R. U.S. Patent 3,702,886, **1973**.
128. Biswas, J.; Maxwell, I. E. *Appl. Catal.* **1990**, *63*, 197–258.
129. Fu, J.; Kim, S.; Rodgers, R. P.; Hendrickson, C. L.; Marshall, A. G.; Qian, K. *Energy Fuel* **2006**, *20*, 661–667.

130. Ma, X.; Sakanishi, K.; Isoda, T.; Mochida, I. *Fuel* **1997**, *76*, 329–339.
131. Vogt, E. T. C.; Kresge, C. T.; Vartuli, J. C. *Stud. Surf. Sci. Catal.* **2001**, *137*, 1003–1027.
132. Mitchell, S.; Michels, N.-L.; Perez-Ramirez, J. *Chem. Soc. Rev.* **2013**, *42*, 6094–6112.
133. Greensfelder, B. S.; Voge, H. H.; Good, G. M. *Ind. Eng. Chem.* **1949**, *41*, 2573–2584.
134. Corma, A.; Planelles, J.; Sánchez-Marín, J.; Tomás, F. *J. Catal.* **1985**, *93*, 30–37.
135. Kotrel, S.; Knözinger, H.; Gates, B. C. *Microporous Mesoporous Mater.* **2000**, *35–36*, 11–20.
136. Corma, A.; Ochillés, A. V. *Microporous Mesoporous Mater.* **2000**, *35–36*, 21–30.
137. Dupain, X.; Makkee, M.; Moulijn, J. A. *Appl. Catal.* **2006**, *297*, 198–219.
138. Haag, W. O.; Dessau, R. M. *Proceedings of the 8th International Congress on Catalysis, Berlin*; Vol. 2, **1984**; pp 305–316.
139. Plank, C.; Rosinky, E. H. W. *Ind. Eng. Chem. Prod. Res. Dev.* **1964**, *3*, 165–169.
140. Li, C. W.; Rees, L. V. C. *Zeolites* **1986**, *6*, 60–65.
141. Flanigen, E. M.; Khatami, H.; Szymanksi, H. A. *Adv. Chem. Ser.* **1971**, *101*, 201–209.
142. Roelofsen, J. W.; Mathies, H.; de Groot, R. L.; van Woerkom, P. C. M.; Angad Gaur, H. *Stud. Surf. Sci. Catal.* **1988**, *28*, 337–344.
143. Breck, D. W.; Flanigen, E. M. *Molecular Sieves*; Soc. Chem. Ind. London, **1968**; p 47.
144. Scherzer, J.; Bass, J. L.; Hunter, F. D. *J. Phys. Chem.* **1975**, *79*, 1194–1199.
145. Scherzer, J.; Bass, J. L. *J. Phys. Chem.* **1975**, *79*, 1200–1205.
146. Falabella Sousa-Aguiar, E.; Doria Camorim, V. L.; Zanon Zotin, F. M.; Correa dos Santos, R. L. *Microporous Mesoporous Mater.* **1998**, *25*, 25–34.
147. Schüßler, F.; Pidko, E. A.; Kolvenbach, R.; Sievers, C.; Hensen, E. J. M.; van Santen, R. A.; Lercher, J. A. *Phys. Chem.* **2011**, *115*, 21763–21776.
148. van Bokhoven, J. A.; Roest, A. L.; Koningsberger, D. C.; Miler, J. T.; Nachtegaal, G. H.; Kentgens, A. P. M. *J. Phys. Chem.* **2000**, *104*, 6743–6754.
149. Vezzalini, G.; Quartieri, S.; Galli, E.; Alberti, A.; Cruciani, G.; Kvick, A. *Zeolites* **1997**, *19*, 323–325.
150. Xue, N.; Olindo, R.; Lercher, J. A. *J. Phys. Chem.* **2010**, *114*, 15763–15770.
151. van der Bij, H. E.; Weckhuysen, B. M. *Chem. Soc. Rev.* **2015**, *44*, 7406–7428. http://dx.doi.org/10.1039/c5cs00109A. Advance Article.
152. van der Bij, H. E.; Weckhuysen, B. M. *Phys. Chem. Chem. Phys.* **2014**, *16*, 9892–9903.
153. van der Bij, H. E.; Aramburo, L. R.; Arstad, B.; Dynes, J. J.; Wang, J.; Weckhuysen, B. M. *ChemPhysChem* **2014**, *15*, 283–292.
154. van der Bij, H. E.; Meirer, F.; Kalirai, S.; Wang, J.; Weckhuysen, B. M. *Chem. Eur. J.* **2014**, *20*, 16922–16932.
155. van der Bij, H. E.; Cicmil, D.; Wang, J.; Meirer, F.; de Groot, F. M. F.; Weckhuysen, B. M. *J. Am. Chem. Soc.* **2014**, *136*, 17774–17787.
156. Fletcher, R. *Hydrocarbon Eng.* **2011**, 39–43 (January issue).
157. Oil Producing and Exporting Countries (OPEC). World Oil Outlook **2014**.
158. Rigutto, M. *Zeolites and Catalysis: Synthesis, Reactions and Applications,* Vol. 2; Wiley-VCH: Weinheim, **2010**; pp 547–584.
159. Hansen, A.; Humphries, A.; McGovern, S.; Speronello, B. *PTQ Catal.* **2014**, 37–41.
160. Kung, H. H.; Babitz, S. M.; Miller, J. T.; Haag, W. O.; Snurr, R. Q. *Top. Catal.* **2000**, *10*, 59–64.
161. Meima, G. R.; van der Aalst, M. J. M.; Samson, M. S. U.; Garcés, J. M.; Lee, J. G. In Proceedings of the 9th International Zeolite Conference, Montreal, Vol. 2; **1992**; p 327.
162. Garcés, J. M.; Olken, M. M.; Lee, G. J.; Meima, G. R.; Jacobs, P. A.; Martens, J. A. *Top. Catal.* **2009**, *52*, 1175–1181.
163. Li, X.; Prins, R.; van Bokhoven, J. A. *J. Catal.* **2009**, *262*, 257–265.

164. Park, D. H.; Kim, S. S.; Wang, H.; Pinnavaia, T. J.; Papapetrou, M. C.; Lappas, A. A.; Triantafyllidis, K. S. *Angew. Chem. Int. Ed. Engl.* **2009**, *48*, 7645–77648.
165. Holm, M. S.; Taarning, E.; Egeblad, K.; Christensen, C. H. *Catal. Today* **2011**, *168*, 3–16.
166. Janssen, A. H.; Koster, A. J.; de Jong, K. P. *J. Phys. Chem. B* **2002**, *106*, 11905–11909.
167. Groen, J. C.; Peffer, L. A. A.; Moulijn, J. A.; Pérez-Ramírez, J. *Microporous Mesoporous Mater.* **2004**, *69*, 29–34.
168. Groen, J. C.; Moulijn, J. A.; Pérez-Ramírez, J. *Ind. Eng. Chem. Res.* **2007**, *46*, 4193–4201.
169. Verboekend, D.; Pérez-Ramírez, J. *Catal. Sci. Technol.* **2011**, *1*, 879–890.
170. Verboekend, D.; Vilé, G.; Pérez-Ramírez, J. *Cryst. Growth Des.* **2012**, *12*, 3123–3132.
171. Kresge, C. T.; Leonowicz, M. E.; Roth, W. J.; Vartuli, J. C.; Beck, J. S. *Nature* **1992**, *359*, 710–712.
172. García-Martínez, J.; Li, K.; Krishnaiah, G. *Chem. Commun.* **2012**, *48*, 11841–11843.
173. Martens, J. A.; Thybaut, J. W.; Denayer, J. F. M.; Sree, S. P.; Aerts, A.; Reyniers, M.-F.; van Speybroeck, V.; Waroquier, M.; Buekenhoudt, A.; Vankelecom, I.; Buijs, W.; Persoons, J.; Baron, G. V.; Bals, S.; van Tendeloo, G.; Marin, G. B.; Jacobs, P. A.; Kirschhock, C. E. A. *Catal. Today* **2011**, *168*, 17–27.
174. Choi, M.; Na, K.; Kim, J.; Sakamoto, Y.; Terasaki, O.; Ryoo, R. *Nature* **2009**, *461*, 246–249.
175. Kim, J. C.; Ryoo, R.; Opanasenko, M. V.; Maksym, V.; Shamzhy, M. V.; Cejka, J. *ACS Catal.* **2015**, *5*, 2596–2604.
176. Ng, E. P.; Chateigner, D.; Bein, T.; Valtchev, V.; Mintova, S. *Science* **2012**, *335*, 70–73.
177. Awala, H.; Gilson, J. P.; Retoux, R.; Boulley, P.; Goupil, J. M.; Valtchev, V.; Mintova, S. *Nat. Mater.* **2015**, *14*, 447–451.
178. Ruiz-Martinez, J.; Beale, A. M.; Deka, U.; O'Brien, M. G.; Quinn, P. D.; Mosselmans, J. F. W.; Weckhuysen, B. M. *Angew. Chem. Int. Ed. Engl.* **2013**, *52*, 5983–5987.
179. Meirer, F.; Morris, D. T.; Kalirai, S.; Liu, Y.; Andrews, J. C.; Weckhuysen, B. M. *J. Am. Chem. Soc.* **2015**, *137*, 102–105.
180. Meirer, F.; Kalirai, S.; Morris, D.; Soparawalla, S.; Liu, Y.; Mesu, G.; Andrews, J. C.; Weckhuysen, B. M. *Sci. Adv.* **2015**, *1*, e1400199.
181. Meirer, F.; Kalirai, S.; Nelson Weker, J.; Liu, Y.; Andrews, J. C.; Weckhyusen, B. M. *Chem. Commun.* **2015**, *51*, 8097–8100.
182. Kalirai, S.; Boesenberg, U.; Falkenberg, G.; Meirer, F.; Weckhuysen, B. M. *ChemCatChem* **2015**. http://dx.doi.org/10.1002/cctc.201500710.
183. Bare, S. R.; Charochak, M. E.; Kelly, S. D.; Lai, B.; Wang, J.; Chen-Wiegart, Y.-C. K. *ChemCatChem* **2014**, *6*, 1427–1437.
184. Da Silva, J. C.; Mader, K.; Holler, M.; Haberthur, D.; Diaz, A.; Guizar-Sicairos, M.; Cheng, W.-C.; Shu, Y.; Raabe, J.; Menzel, A.; Van Bokhoven, J. A. *ChemCatChem* **2015**, *7*, 413–416.
185. Buurmans, I. L. C.; Ruiz-Martinez, J.; Knowles, W. V.; van der Beek, D.; Bergwerff, J. A.; Vogt, E. T. C.; Weckhuysen, B. M. *Nat. Chem.* **2011**, *3*, 862–867.
186. Buurmans, I. L. C.; Ruiz-Martinez, J.; van Leeuwen, S. L.; van der Beek, D.; Bergwerff, J. A.; Knowles, W. V.; Vogt, E. T. C.; Weckhuysen, B. M. *Chem. Eur. J.* **2012**, *18*, 1094–1101.
187. Karreman, M. A.; Buurmans, I. L. C.; Geus, J. W.; Agronskaia, A. V.; Ruiz-Martinez, J.; Gerritsen, H. C.; Weckhuysen, B. M. *Angew. Chem. Int. Ed. Engl.* **2012**, *51*, 1428–1431.
188. Karreman, M. A.; Buurmans, I. L. C.; Agronskaia, A. V.; Geus, J. W.; Gerritsen, H. C.; Weckhuysen, B. M. *Chem. Eur. J.* **2013**, *19*, 3846–3859.

189. Sprung, C.; Weckhuysen, B. M. *Chem. Eur. J.* **2014**, *20*, 3667–3677.
190. Ristanovic, Z.; Kerssens, M. M.; Kubarev, A. V.; Hendriks, F. C.; Dedecker, P.; Hofkens, J.; Roeffaars, M. B. J.; Weckhuysen, B. M. *Angew. Chem. Int. Ed. Engl.* **2015**, *54*, 1836–1840.
191. Worldwide Refining Report. *Oil Gas J.* **2013**, 2–59.
192. IG Farben GB Patent 247,587, **1927**.
193. IG Farben GB Patent 247,582, **1927**.
194. Scherzer, J.; Gruia, A. J. *Hydrocracking Science and Technology*; Marcel Dekker: New York, **1996**.
195. Scherzer, J. *ACS Symp. Ser.* **1984**, *284*, 157–200.
196. Szostak, R. *Stud. Surf. Sci. Catal.* **2001**, *137*, 261–297.
197. Minderhout, J. K.; van Veen, J. A. R.; Hagen, A. P. In: Stud. Surf. Sci. Catal., Vol. 127; *Hydrotreatment and Hydrocracking of Oil Fractions: Proceedings of the 2nd International Symposium/7th European Workshop*, **1999**; pp 3–20.
198. Weitkamp, J. *ACS Symp. Ser.* **1975**, *20*, 1–27.
199. Martens, J. A.; Jacobs, P. A.; Weitkamp, J. *Appl. Catal.* **1986**, *20*, 239–281.
200. Ward, J. W. *Fuel Process. Technol.* **1993**, *35*, 55–85.
201. Zečević, J.; Meeldijk, J. D.; Vanbutsele, G.; Martens, J.; de Jong, K. P. In: *24th NAM, Pittsburgh*, **2015**. Abstract O-ATh-403-14.
202. Zhang, T.; Leyva, C.; Froment, G. *Ind. Eng. Chem. Res.* **2015**, *54*, 858–868.
203. Olsen, C. W.; Shifflet, W. K.; Torchia, D.; Brossard, D. *Hydrocarbon Process.* **2013**, *92*, 91–96.
204. Naber, J. E.; Stork, W. H. J.; Blauwhoff, P. M. M.; Groeneveld, K. J. W. *Oil Gas Eur. Mag.* **1991**, *1*, 26–34.
205. De Jong, K. P.; Zečević, J.; Friedrich, H.; de Jongh, P. E.; Van Donk, S.; Kenmogne, R.; Finiels, A.; Hulea, V.; Fajula, F. *Angew. Chem. Int. Ed. Engl.* **2010**, *49*, 10074–10078.
206. Agudelo, J. L.; Mezari, B.; Hensen, E. J. M.; Giraldo, S. A.; Hoyos, L. J. *Appl. Catal. A Gen.* **2014**, *488*, 219–230.
207. Agudelo, J. L.; Hensen, E. J. M.; Giraldo, S. A.; Hoyos, L. J. *Fuel Process. Technol.* **2015**, *133*, 89–96.
208. Griesman, K.; et al. *Ullmann's Encyclopedia of Chemical Industry*; Vol. 18, **2012**; pp 133–189.
209. Bradley, J.-C.; Lang, A. S. I. D.; Williams, A. J.; Curtin, E. ONS Open Melting Point Collection. http://precedings.nature.com/documents/6229/version/1, 2011. (accessed July, 2015)
210. https://en.wikipedia.org/wiki/Higher_alkanes, **2015** (accessed July, 2015).
211. http://www.chemistry-reference.com/alkanes/. (accessed July, 2015)
212. Hancsók, J.; Kasza, T.; Kovács, S.; Solymosi, P.; Holló, A. *J. Clean. Prod.* **2012**, *34*, 76–81.
213. http://science.csustan.edu/almy/3012/AlkaneBP.htm. (accessed July, 2015)
214. http://webbook.nist.gov/. (accessed July, 2015)
215. Burch, K. J.; Wakefield, D. K.; Whitehead, E. G. *Commun. Math. Comp. Chem.* **2003**, *47*, 25–52.
216. ASTM International—Standard D6890, 2015. http://www.astm.org/Standards/D6890.htm. (Accessed July, 2015)
217. Chen, N. Y.; Gorring, L. R.; Irland, H. R.; Stein, T. R. *Oil Gas J.* **1977**, *75*, 165.
218. Chen, N. Y.; Degnan, T. F. *Chem. Eng. Prog.* **1988**, *84*, 32–41.
219. Homan Free, H. W.; Schockaert, T.; Sonnemans, J. W. M. *Fuel Process. Technol.* **1993**, *35*, 111–117.
220. LaPierre, R. B.; Partridge, R. D.; Chen, N. Y.; Wong, S. S. U.S. Patent 4,419.220, **1982**.

221. LaPierre, R. B.; Partridge, R. D.; Chen, N. Y.; Wong, S. S. U.S. Patent 4,501,926, **1985**.
222. Miller, S. J. U.S. Patent 5,135,638, **1992**.
223. Martens, J. A.; Verboekend, D.; Thomas, K.; Vanbutsele, G.; Gilson, J.-P.; Pérez-Ramiréz, J. *ChemSusChem* **2013**, *6*, 421–425.
224. Hanaoka, T.; Miyazawa, T.; Shimura, K.; Hirata, S. *Chem. Eng. J.* **2015**, *263*, 178–185.
225. Seo, M.; Lee, D.-W.; Lee, K.-Y.; Moon, D. J. *Fuel* **2015**, *143*, 63–71.
226. Pölczmann, G.; Valyon, J.; Szegedi, Á.; Mihályi, R. M.; Hancsók, J. *Top. Catal.* **2011**, *54*, 1079–1083.
227. Sartipi, S.; Parashar, K.; Valero-Romero, M. J.; Santos, V. P.; van der Linden, B.; Makkee, M.; Kapteijn, F.; Gascon, J. *J. Catal.* **2013**, *305*, 179–190.
228. Xing, C.; Yang, G.; Wu, M.; Yang, R.; Tan, L.; Zhu, P.; Wei, Q.; Li, J.; Mao, J.; Yoneyama, Y.; Tsubaki, N. *Fuel* **2015**, *148*, 48–57.
229. Kim, J.-C.; Lee, S.; Cho, K. *ACS Catal.* **2014**, *4*, 3919–3927.
230. Tamm, P. W.; Mohr, D. H.; Wilson, C. R. *Stud. Surf. Sci. Catal.* **1987**, *38*, 335–353.
231. Bernard, J. R. In: Rees, L. V. C. Ed.; *Proc. Fifth Int. Conf. Zeolites* Heyden: London, **1980**; pp 686–695.
232. Lane, G. S.; Modica, F. S.; Miller, J. T. *J. Catal.* **1991**, *129*, 145–158.
233. Derouane, E. G.; Vanderveken, D. J. *Appl. Catal.* **1988**, *45*, L15–L22.
234. Tauster, S. J.; Steger, J. J. *J. Catal.* **1990**, *125*, 387–389.
235. Davis, R. J.; Derouane, E. G. *Nature* **1991**, *349*, 313–315.
236. Vaarkamp, M.; van Grondelle, J.; Miller, J. T.; Sajkowski, D. J.; Modica, F. S.; Lane, G. S.; Gates, B. C.; Koningsberger, D. C. *Catal. Lett.* **1990**, *6*, 369–382.
237. Vaarkamp, M.; van Grondelle, J.; van Santen, R. A.; Miller, J. T.; Meyers, B. L.; Modica, F. S.; Lane, G. S.; Koningsberger, D. C. In: *Proceedings of the 9th International Zeolite Conference, Montreal*, **1993**; pp 433–440.
238. Vaarkamp, M.; Miller, J. T.; Modica, F. S.; Lane, G. S.; Koningsberger, D. C. In *New Frontiers in Catalysis?* Guczi, L., Solymosi, F., Tétényi, P., Eds., *Studies in Surface Science and Catalysis*, *Vol. 75; Proc. 10th Int. Conf. Catal., Budapest, 1992*, **1993**; pp 809–820.
239. Philippou, A.; Naderi, M.; Pervaiz, N.; Rocha, J.; Anderson, M. W. *J. Catal.* **1998**, *178*, 174–181.
240. Rainis, A. U.S. Patent 5,328,595, **1992**.
241. Zones, S. I.; Holtermann, D. L.; Rainis, A. PCT WO Patent Appl. 91/11501, **1991**.
242. Rosin, R. R.; Stine, M. A.; Anderson, G.; Hunter, M. J. In: *NPRA Annual Meeting, Washington, DC* **2004**. AM-04-46.
243. Montgomery, C. W.; McAteer, J. H.; Franke, N. W. *J. Am. Chem. Soc.* **1937**, *59*, 1768–1769.
244. Hidalgo, J. M.; Zbuzek, M.; Černý, R.; Jíša, P. *Cent. Eur. J. Chem.* **2014**, *12*, 1–13.
245. Wulfers, M. J.; Tzolova-Müller, G.; Villegas, J. I.; Murzin, D. Y.; Jentoft, F. C. *J. Catal.* **2012**, *296*, 132–142.
246. Wulfers, M. J.; Jentoft, F. C. *J. Catal.* **2015**, *330*, 507–519. http://dx.doi.org/10.1016/j.jcat.2014.12.035.
247. Yadav, R.; Sakthivel, A. *Appl. Catal. A Gen.* **2014**, *481*, 143–160.
248. Smolikov, M. D.; Shkurenok, V. A.; Yablokova, S. S.; Kir'yanov, D. I.; Belopukhov, E. A.; Zaikovski, V. I.; Belyi, A. S. *Catal. Ind.* **2014**, *6*, 223–230.
249. Moulijn, J. A.; Sheldon, R. A.; van Bekkum, H.; van Leeuwen, P. W. M. N. *Catalysis. An Integrated Approach to Homogeneous, Heterogeneous and Industrial Catalysis*, *Studies in Surface Science and Catalysis*, Vol. 79; **1999**; p 33. Chapter 2.
250. Sie, S. T. In: Jansen, J. C., Stöcker, M., Karge, H. G., Weitkamp, J., Eds.; *Studies in Surface Science and Catalysis,* Vol. 85; **1994**; pp 587–632.
251. Tran, M. T.; Gnep, N. S.; Szabo, G.; Guisnet, M. *J. Catal.* **1998**, *174*, 185–190.
252. Ono, Y. *Catal. Today* **2003**, *81*, 3–16.

253. Brouwer, D. M.; Hoogeveen, H. In: Streitwieser, A., Jr., Taft, R. W., Eds.; Prog. Phys. Org. Che., Vol. 9; Wiley-Interscience: New York, **1972**; p 179.
254. Boronat, M.; Viruela, P.; Corma, A. *J. Phys. Chem. A* **1998**, *102*, 982.
255. Boronat, M.; Viruela, P.; Corma, A. *J. Phys. Chem.* **1996**, *100*, 633–637.
256. van Donk, S.; Bus, E.; Broersma, A.; Bitter, J. H.; de Jong, K. P. *J. Catal.* **2002**, *212*, 86–93.
257. van Donk, S.; Bus, E.; Broersma, A.; Bitter, J. H.; de Jong, K. P. *Appl. Catal. A Gen.* **2002**, *237*, 149–159.
258. Jo, D.; Hong, S. B.; Camblor, M. A. *ACS Catal.* **2015**, *5*, 2270–2274.
259. Cavani, F.; Girotti, G.; Terzoni, G. *Appl. Catal.* **1993**, *97*, 177–196.
260. de Klerk, A.; Furimski, E. *Catalysis in the Refining of Fischer-Tropsch Syncrude*; Royal Society of Chemistry: Cambridge, UK, **2010** (chapter 5).
261. Maxwell, I. E. In van Bekkum, H., Flanigen, E. M., Jansen, J. C., Eds.; Stud. Surf. Sci. Cat., Vol. 58; **1991.** Chapter 12.
262. van den Berg, J. P.; Roebschlaeger, K. H. W.; Maxwell, I. E. In: *The Shell PolyGasoline and Kero (SPGK) Process*; *11th North Am. Catal. Soc. Meeting, Dearborn, MI,* **1989.**
263. Finiels, A.; Fajula, F.; Hulea, V. *Catal. Sci. Technol.* **2014**, *4*, 2412–2426.
264. Lapidus, A. L.; Avetisyan, R. V.; Isakov, Y. I.; Minachev, K. M.; Eidus, Y. T. *Pet. Chem. U.S.S.R.* **1970**, *10*, 185–193.
265. Lapidus, A. L.; Mal'tsev, V. V.; Loktev, M. I.; Mishin, I. V.; Slinkin, A. A. *Bull. Acad. Sci. USSR Div. Chem. Sci.* **1978**, *27*, 196–198.
266. Heveling, J.; van der Beek, A.; de Pender, M. *Appl. Catal.* **1988**, *42*, 325–336.
267. Lallemand, M.; Finiels, A.; Fajula, F.; Hulea, V. *Appl. Catal. A Gen.* **2006**, *301*, 196–201.
268. Lallemand, M.; Rusu, O. A.; Dimitriu, E.; Finiels, A.; Fajula, F.; Hulea, V. *Appl. Catal. A Gen.* **2008**, *338*, 37–43.
269. Hulea, V.; Fajula, F. *J. Catal.* **2004**, *225*, 213–222.
270. Dutta, P.; Roy, S. C.; Nandi, L. N.; Samuel, P.; Muthukumaru Pillai, S.; Bhat, B. D.; Ravidranathan, M. *J. Mol. Cat. A Chem.* **2004**, *223*, 231–235.
271. Feller, A.; Lercher, J. A. *Adv. Catal.* **2004**, *48*, 229–295.
272. http://transportpolicy.net/index.php?title=EU:_Fuels:_Diesel_and_Gasoline#Highway_Gasoline. (accessed July, 2015)
273. Peterson, J. R. In: *Preprints of Papers, American Chemical Society, Division of Fuel Chemistry, 212*; *National Meeting of the American Chemical Society (ACS), Orlando, FL, USA, 25–30 August* **1996**; pp 916–921.
274. Primo, A.; Garcia, H. *Chem. Soc. Rev.* **2014**, *43*, 7548–7561.
275. Corma, A.; Martínez, A. *Catal. Rev. Sci. Eng.* **1993**, *35*, 483–570.
276. Rao, P.; Vatcha, S. R. *Oil Gas J.* **1996**, *94*(37), 56.
277. D'Amico, V.; van Broekhoven, E. H.; Nat, P. J.; Nousiainen, H.; Jakkula, J. In: *NPRA Annual Meeting, San Antonio,* **2002**. Paper AM-02-19.
278. Barthe, P.; Chaugny, M.; Roudier, S.; Delgado Sancho, L. In: *Best Available Techniques (BAT) Reference Document for the Refining of Mineral Oil and Gas*; **2015**; pp 158–159. European Commission Industrial Emissions Directive 2010/75/EU.
279. van Broekhoven, E.; van Rooijen, E. *PTQ Mag.* **2008**, *Q4*, 87–93.
280. Weitkamp, J.; Traa, Y. *Catal. Today* **1999**, *49*, 193–199.
281. Kirsch, F. W.; Potts, J. D.; Barmby, D. S. *J. Catal.* **1972**, *27*, 142–150.
282. Hattori, H.; Ono, Y. *Solid Acid Catalysts. From Fundamentals to Applications*; CRC Press, Boca Raton, FL, **2015** (chapter 1).
283. Hommeltoft, S. I. *Appl. Catal. A Gen.* **2001**, *221*, 421–428.
284. Hommeltoft, S. I. *Ind. Eng. Chem. Res.* **2003**, *42*, 5526–5534.
285. de Jong, K. P.; Mesters, C. M. A. M.; Peferoen, D. G. R.; van Brugge, P. T. M.; de Groot, C. *Chem. Eng. Sci.* **1996**, *51*, 2053–2060.

286. Buchold, H.; Dropsch, H.; Eberhart, J. In: *17th World Petroleum Congress, Brazil*, **2002**.
287. *Hydrocarbon Eng.* **2007**, *12*(5), 105.
288. Black, S. M.; Gosling, C. D.; Steigleder, K. Z.; Shields, D. J. In: *NPRA Annual Meeting 2000, San Antonio, TX, USA*, **2000**.
289. McBride, T. K.; Bricker, M. L.; Steigleder, K. Z. U.S. Patent 5,883,039, **1999**.
290. D'Amico, V.; Gieseman, J.; Nousiainen, H.; van Broekhoven, E.; van Rooijen, E. *Hydrocarbon Process.* **2006**, *85*, 65.
291. D'Amico, V.; Gieseman, J. C.; van Broekhoven, E.; van Rooijen, E.; Nousiainen, H. In: *NPRA National Meeting, Salt Lake City*, **2006**. Paper AM-06-41.
292. van Broekhoven, E. R.; Mas Cabré, F. R.; Bogaard, P.; Klaver, G.; Vonhof, M. U.S. Patent 5,986,158, **1999**.
293. van Broekhoven, E. R.; Mas Cabré, F. R. U.S. Patent 6,855,856, **2005**.
294. Hydrocarbon Processing **2013**, April 4. http://www.hydrocarbonprocessing.com/Article/3198828/CB-I-licenses-process-technology-for-new-China-acid-alkylation-project.html
295. Meyers, R. A. *Handbook of Petroleum Refining Processes*, 2nd ed.; McGraw-Hill: New York, **1996**.
296. Dupraz, C.; Rault, J.; Alario, F.; Ramsey, S. Maximizing Paraxylene Production with Paramax. http://www.axens.net/document/90/paramax-suite—article/english.html (accessed July 20, 2015).
297. Degnan, T. F.; Smith, C. M.; Venkat, C. R. *Appl. Catal. A Gen.* **2001**, *221*, 283–294.
298. Perego, C.; Ingallina, P. *Catal. Today* **2002**, *73*, 3–22.
299. Chen, N. Y.; Garwood, W. A.; Dwyer, F. G. *Shape Selective Catalysis in Industrial Applications*; Marcel Dekker: New York, **1996**; p 208.
300. Cheng, J. C.; Degnan, T. F.; Beck, J. S.; Huang, Y. Y.; Kalyanaraman, M.; Kowalski, J. A.; Loehr, C. A.; Mazzone, D. N. *Stud. Surf. Sci. Catal.* **1999**, *121*, 53–60. Elsevier.
301. Holderich, W.; Hesse, M.; Naumann, F. *Angew. Chem. Int. Ed. Engl.* **1988**, *27*, 226–246.
302. Shimizu, S.; Abe, N.; Iguchi, A.; Dohba, M.; Sato, H.; Hirose, K. *Microporous Mesoporous Mater., 21*, **1998**; pp 447–451.
303. Krishna Mohan, K. V. V.; Reddy, K. S. K.; Narender, N.; Kulkarni, S. J. *J. Mol. Catal. A Chem.* **2009**, *298*, 99–102.
304. Climent, M. J.; Corma, A.; Iborra, S. In *Zeolites and Catalysis: Synthesis, Reactions and Applications*; Cejka, J., Corma, A., Zones, S., Eds.; Wiley-VCH Verlag GmbH & Co: Weinheim, **2010**; pp 775–826.
305. Venuto, P. B.; Landis, P. S. *J. Catal.* **1966**, *6*, 237–244.
306. Moreau, C.; Fajula, F.; Finiels, A.; Razigade, S.; Gilbert, L.; Jacquor, R.; Spagnol, M. *Chem. Ind.* **1998**, *75*, 51–57.
307. Lecomite, J.; Finiels, A.; Geneste, P.; Moreau, C. *J. Mol. Catal. A* **1998**, *133*, 283–288.
308. Jaenicke, S.; Chuah, G. K.; Lin, X. H.; Hu, X. C. *Microporous Mesoporous Mater.* **2000**, *35*, 143–153.
309. Climent, M. J.; Corma, A.; Velty, A.; Susarte, M. *J. Catal.* **2000**, *196*, 345–351.
310. Hoelderich, W. F.; Heitmann, G. *Catal. Today* **1997**, *38*, 227–364.
311. Yilmaz, S.; Ucar, S.; Artok, L.; Gulec, H. *Appl. Catal. A Gen.* **2005**, *287*, 261–266.
312. Gunduz, G.; Dimitrova, R.; Yilmaz, S.; Dimitrov, L. *Appl. Catal. A Gen.* **2005**, *282*, 61–65.
313. Clerici, M. G. *Top. Catal.* **2000**, *13*, 373–386.
314. Hoelderich, W. F.; Roselar, J.; Heitmann, G.; Liebens, A. T. *Catal. Today* **1997**, *37*, 353.

315. Kunkeler, P. J.; van der Waal, J. C.; Bremmer, J.; Zuurdeeg, B. J.; Downing, R. S.; van Bekkum, H. *Catal. Lett.* **1998**, *53*, 135–138.
316. Moliner, M.; Roman-Leshkov, Y.; Davis, M. E. *Proc. Natl. Acad. Sci. U. S. A.* **2010**, *107*, 6164–6168.
317. Nikolla, E.; Roman-Leshkov, Y.; Moliner, M.; Davis, M. E. *ACS Catal.* **2011**, *1*, 408–410.
318. Gunther, W. R.; Wang, Y.; Ji, Y.; Michaelis, V. K.; Hunt, S. T.; Griffin, R. G.; Roman-Leshkov, Y. *Nat. Commun.* **2012**, *3*, 1109–1122.
319. Corma, A.; Domine, M. E.; Nemeth, L.; Valencia, S. *J. Am. Chem. Soc.* **2002**, *124*, 3194–3195.
320. Corma, A. *Chem. Rev.* **1995**, *95*, 559–614.
321. Venuto, P. B.; Landis, P. S. *Adv. Catal.* **1968**, *18*, 259–371.
322. Chiche, B.; Finiels, A.; Gauthier, C.; Geneste, P.; Graille, J.; Pioch, D. *J. Org. Chem.* **1986**, *51*, 2128–2130.
323. Harvey, G.; Vogt, A.; Kouwenhoven, H. W.; Prins, R. *Performance of Zeolite Beta in Friedel-Crafts Reactions of Functionalized Aromatics*; Butterworth-Heinemann: Boston, **1993**.
324. Smith, K.; Zhenhua, Z.; Hodgson, P. K. G. *J. Mol. Catal.* **1998**, *134*, 121–128.
325. Spagnol, M.; Benazzi, E.; Marcilly, C. U.S. 5817878, Rhône-Poulenc, 1998.
326. Botella, P.; Corma, A.; Navarro, M. T.; Rey, F.; Sastre, G. *J. Catal.* **2003**, *217*, 406–416.
327. Alvaro, V. F. D.; Brigas, A. F.; Derouane, E. G.; Lourenco, J. P.; Santos, B. S. *J. Mol. Catal. A Chem.* **2009**, *305*, 100–103.
328. Pedro, C. L.; Apesteguia, C. R. *J. Catal.* **2004**, *226*, 308–320.
329. Sheldon, R. S.; Downing, R. S. *Appl. Catal. A Gen.* **1999**, *189*, 163–183.
330. Gunnewegh, E. A.; Downing, R. S.; van Bekkum, H. *Stud. Surf. Sci. Catal.* **1995**, *97*, 447–452.
331. Elings, J. A.; Downing, R. S.; Sheldon, R. S. *Stud. Surf. Sci. Catal.* **1997**, *105*, 1125–1132.
332. Gunnewegh, E. A.; Hoefnagel, A. J.; van Bekkum, H. *J. Mol. Catal.* **1995**, *100*, 87–92.
333. March, J.; Smith, K. *Advanced Organic Chemistry*; John-Wiley & Sons: New York, **2001**.
334. Landis, P.S. U.S. Patent 3,359,285, **1968**.
335. Durand, R.; Geneste, P.; Joffre, J.; Moreau, C. *Stud. Surf. Sci. Catal.* **1993**, *78*, 647–652.
336. de Vyver, S. V.; Roman-Leshkov, Y. *Angew. Chem. Int. Ed. Engl.* **2015**, 54. http://dx.doi.org/10.1002/anie.201503701.
337. Corma, A.; Renz, M. *Chem. Commun.* **2004**, 550–551.
338. Sheldon, R. A.; van Vliet, M. C. A. *Fine Chemicals Through Heterogeneous Catalysis*; Wiley-VCH: New York, **2001**; pp 473–551.
339. Bellussi, G.; Carati, A.; Millini, R. In *Zeolites and Catalysis: Synthesis, Reactions and Applications*, Vol. 107; Wiley-VCH Verlag GmbH & Co. KGaA: Weinheim, **2010**; pp 449–491.
340. Nemeth, L.; Bare, S. R. *Adv. Catal.* **2014**, *57*, 1–97.
341. Clerici, M. G.; Ingallina, P. *J. Catal.* **1993**, *140*, 71–83.
342. Clerici, M. G. *Rend. Fis. Acc. Lincei.* **2007**, *18*, 221–234.
343. Gallo, E.; Lamberti, C.; Glatzel, P. *Phys. Chem. Chem. Phys.* **2011**, *13*, 19409–19419.
344. Clerici, M. G.; Bellussi, G.; Roamno, U. *J. Catal.* **1991**, *129*, 159–167.
345. Huybrechts, D. R. C.; Bruycker, L. D.; Jacobs, P. A. *Nature* **1990**, *345*, 240–242.
346. Bellussi, G.; Carati, A.; Clerici, M. G.; Maddinelli, G.; Millini, R. *J. Catal.* **1992**, *133*, 220–230.
347. Hutter, R.; Mallat, T.; Baiker, A. *J. Catal.* **1995**, *153*, 177–189.

348. Hermann, W. A.; Kratzer, R. M.; Fischer, R. W. *Angew. Chem. Int. Ed. Engl.* **1997**, *36*, 2652–2654.
349. Corma, A.; Iglesias, M.; Sanchez, F. *J. Chem. Soc. Chem. Commun.* **1995**, 1653.
350. Kumar, R.; Pais, G. C. G.; Pandey, B.; Kumar, P. *J. Chem. Soc. Chem. Commun.* **1995**, 1315–1316.
351. Fischer, J.; Holderich, W. F. *Appl. Catal. A Gen.* **1999**, *180*, 435–443.
352. Bhaumik, A.; Kumar, P.; Kumar, R. *Catal. Lett.* **1996**, *40*, 47–50.
353. Corma, A.; Nemeth, L. T.; Renz, M.; Valencia, S. *Nature* **2001**, *412*, 423–425.
354. Peregot, G.; Bellussi, G.; Corno, C.; Taramasso, M.; Buonomot, F.; Esposito, A. *Stud. Surf. Sci. Catal.* **1986**, *28*, 129–136.
355. Bianchi, D.; Balducci, L.; Bortolo, R.; D'Aloisio, R.; Ricci, M.; Spano, G.; Tassinari, R.; Tonini, C.; Ungarelli, R. *Adv. Synth. Catal.* **2007**, *349*, 979–986.
356. Wu, P.; Komatsu, T.; Yashima, T. *J. Phys. Chem. B* **1998**, *102*, 9297–9303.
357. Dimitrova, R.; Spassova, M. *Catal. Commun.* **2007**, *8*, 693–696.
358. Sobolev, V. I.; Kharitnov, A. S.; Paukshtis, Y. A.; Panov, G. I. *J. Mol. Catal.* **1993**, *84*, 117–124.
359. Sobolev, V. I.; Panov, G. I.; Kharitonov, A. S.; Romannikov, V. N.; Volodin, A. M.; Ione, K. G. *J. Catal.* **1993**, *139*, 435–443.
360. Dubkov, K. A.; Ovanesyan, N. S.; Shteinman, A. A.; Starokon, E. V.; Panov, G. I. *J. Catal.* **2002**, *207*, 341–352.
361. Panov, G. I.; Kharitonov, A. S.; Sobolev, V. I. *Appl. Catal. A Gen.* **1993**, *98*, 1–20.
362. Perez-Ramirez, J.; Groen, J. C.; Bruckner, A.; Kumar, A. S.; Bentrup, U.; Debbagh, M. N.; Villaescusa, L. A. *J. Catal.* **2005**, *232*, 318–334.
363. Lee, J. K.; Kim, Y. J.; Lee, H.-J.; Kim, S. H.; Cho, S. J.; Nam, I.-S.; Hong, S. B. *J. Catal.* **2011**, *284*, 23–33.
364. Tuel, A.; Moussa-Khouzami, S.; Ben Taarit, Y.; Naccache, C. *J. Mol. Catal.* **1991**, *68*, 45–52.
365. Ramaswamy, A. V.; Sivasankar, S.; Ratnasamy, P. *Microporous Mater.* **1994**, *2*, 452–458.
366. Chang, C. D.; Lang, W. S. U.S. Patent 4,220,783, **1980**.
367. Chang, C. D.; Perkins, P. D. European Patent 0082613, **1983**.
368. Martin, A.; Lucke, B. *Stud. Surf. Sci. Catal.* **1994**, *84*, 1965–1972.
369. Romano, V.; Esposito, A.; Maspero, F.; Neri, C.; Clerici, M. G. *Chim. Ind. (Milan)* **1990**, *72*, 610–616.
370. Clerici, M. G.; Ricci, M.; Rivetti, F. *Encyclopedia of Hydrocarbons*; Vol. 3; Instituto Della Enciclopedia Italiana: Rome, Italy, **2006**; pp 661–686.
371. Kitamura, M.; Ichihashi, H.; Suzukamu, G.; Nakamura, Y. U.S. Patent 4,968,793, **1990**.
372. Barthomeuf, D. *Catal. Rev.* **1996**, *38*, 521–612.
373. Kloetstra, K. R.; van Bekkum, H. *J. Chem. Soc. Chem. Commun.* **1995**, 1005–1006.
374. Kloetstra, K. R.; van Laren, M.; van Bekkum, H. *J. Chem. Soc. Faraday Trans.* **1997**, *47*, 235–242.
375. Corma, A.; Fornes, V.; Martin-Aranda, R. M.; Garcia, H.; Primo, J. *Appl. Catal.* **1990**, *59*, 237–248.
376. Kloetstra, K. R.; van Laren, M.; van Bekkum, H. *J. Chem. Soc. Faraday Trans.* **1997**, *93*, 1211–1220.
377. Saravanamurugan, S.; Palanichamy, M.; Arabindoo, B.; Murugesan, V. *J. Mol. Catal. A Chem.* **2004**, *218*, 101–106.
378. Kunkeler, P. J.; Zuurdeeg, B. J.; van der Waal, J. C.; van Bokhoven, J. A.; Koningsberger, D. C.; van Bekkum, H. *J. Catal.* **1998**, *180*, 234–244.
379. van der Waal, J. C.; Tan, K.; van Bekkum, H. *Catal. Lett.* **1996**, *41*, 63–67.
380. Smith, K.; Musson, A.; DeBoos, G. A. *J. Org. Chem.* **1998**, *63*, 8448.
381. Esakkidurai, T.; Pitchumani, K. *J. Mol. Catal. A Chem.* **2000**, *185*, 305–309.

382. Ma, X. M.; Li, B. D.; Chen, L.; Lu, M.; Lv, C. X. *Chin. Chem. Lett.* **2012**, *23*, 809–812.
383. Kim, J.-C.; Ryoo, R.; Opanasenko, M. V.; Shamzhy, M. V.; Cejka, J. *ACS Catal.* **2015**, *5*, 2596–2604.
384. Abdelsayed, V.; Shekhawat, D.; Smith, M. W. *Fuel* **2015**, *139*, 401–410.
385. Tempelman, C. H. L.; de Rodrigues, V. O.; van Eck, E. R. H.; Magusin, C. M. M.; Hensen, E. J. M. *Microporous Mesoporous Mater.* **2015**, *203*, 259–273.
386. Asche, F.; Oglend, A.; Osmundsen, P. *Energy Policy* **2012**, *47*, 117–124.
387. Ma, S.; Gao, X.; Zhao, L.; Scott, S.; Bao, X. *J. Energy Chem.* **2013**, *22*, 1–20.
388. Keller, G. E.; Bhasin, M. M. *J. Catal.* **1982**, *73*, 9–19.
389. Holmen, A. *Catal. Today* **2009**, *142*, 2–8.
390. Lunsford, J. H. *Catal. Today* **2000**, *2–4*, 165–174.
391. Choudhary, V.; Aksoylu, E.; Goodman, D. W. *Catal. Rev.* **2003**, *45*, 151–203.
392. Horn, R.; Schlögl, R. *Catal. Lett.* **2015**, *145*, 23–29.
393. Lunsford, J. H. *Catal. Today* **2000**, *63*, 165–174.
394. Panov, G. L.; Sobolev, V. I.; Kharitonov, A. S. *J. Mol. Catal.* **1990**, *61*, 85–97.
395. Sobolev, V. I.; Dubkov, K. A.; Panna, O. V.; Panov, G. I. *Catal. Today* **1995**, *24*, 251–252.
396. Dubkov, K. A.; Ovamesyan, N. S.; Shteinman, A. A.; Starokon, E. V.; Panov, G. I. *J. Catal.* **2002**, *207*, 341–352.
397. Taboada, J.; Overweg, A. R.; Kooyman, P. J.; Arends, I. W. C. E.; Mul, G. *J. Catal.* **2005**, *231*, 56–66.
398. Sazama, P.; Wichterlova, B.; Tabor, E.; Statsny, P.; Stathu, N. K.; Sobalik, Z.; Dedecek, J.; Sklenak, S.; Klein, P.; Vondrova, A. *J. Catal.* **2014**, *312*, 123–138.
399. Gao, Z. X.; Kim, H. S.; Sun, Q.; Stair, P. C.; Sachtler, W. M. H. *J. Phys. Chem. B.* **2001**, *105*, 6186–6190.
400. Starokon, E. V.; Perfenov, M. V.; Arzumanov, S. S.; Pirutko, L. V.; Stepanov, A. G. *J. Catal.* **2013**, *300*, 47–54.
401. Parfenov, M. V.; Starokon, E. V.; Pirutko, L. V.; Panov, G. I. *J. Catal.* **2014**, *318*, 14–21.
402. Groothaert, M. H.; Smeets, P. J.; Sels, B. F.; Jacobs, P. A.; Schoonheydt, R. A. *J. Am. Chem. Soc.* **2005**, *127*, 1394–1395.
403. Balasubramanian, R.; Smith, S. M.; Rawat, S.; Yatsunyk, L. A.; Stemmler, T. L.; Rosenzweig, A. C. *Nature* **2010**, *465*, 115–119.
404. Smeets, P. J.; Groothaert, M. H.; Schoonheydt, R. A. *Catal. Today* **2005**, *110*, 303–309.
405. Woertink, J. S.; Smeets, P. J.; Groothaert, M. H.; Vance, M. A.; Sels, B. F.; Schoonheydr, R. A.; Solomon, E. I. *Proc. Natl. Acad. Sci. U. S. A.* **2009**, *106*, 18908–18913.
406. Vanelderen, P.; Hadt, R. G.; Smeets, P. J.; Solomon, E. I.; Schoonheydt, R. A.; Sels, B. F. *Catal. Today* **2011**, *284*, 157–164.
407. Smeets, P. J.; Hadt, R. G.; Woertink, J. S.; Vanelderen, P.; Schoonheydt, R. A.; Sels, B. F.; Solomon, E. I. *J. Am. Chem. Soc.* **2010**, *132*, 14736–14738.
408. Beznis, N. V.; Weckhuysen, B. M.; Bitter, J. H. *Catal. Lett.* **2010**, *138*, 14–22.
409. Vanelderen, P.; Snyder, B. E. R.; Tsai, M. L.; Hadt, R. G.; Vancauwenbergh, J.; Coussens, O.; Schoonheydt, R. A.; Sels, B. F.; Solomon, E. I. *J. Am. Chem. Soc.* **2015**, *137*, 6383–6392.
410. Alayon, E. M.; Nachtegaal, M.; Ranocchiari, M.; van Bokhoven, J. A. *Chem. Commun.* **2012**, *48*, 404–406.
411. Alayon, E. M.; Nachtegaal, M.; Bodi, A.; van Bokhoven, J. A. *ACS Catal.* **2013**, *4*, 16–22.

412. Alayon, E. M. C.; Nachtegaal, M.; Kleymenov, E.; van Bokhoven, J. A. *Microporous Mesoporous Mater.* **2013**, *166*, 131–136.

413. Alayon, E. M. C.; Nachtegaal, M.; Bodi, A.; Ranocchiari, M.; van Bokhoven, J. A. *Phys. Chem. Chem. Phys.* **2015**, *17*, 7681–7693.

414. Grundner, S.; Markovits, M. A. C.; Li, G.; Tromp, M.; Pidko, E. A.; Hensen, E. J. M.; Jentys, A.; Sanchez-Sanchez, M.; Lercher, J. A. *Nat. Commun.* **2015**, *6*, 7546.

415. Chan, S. I.; Lu, Y. J.; Nagababu, P.; Maji, S.; Hung, M. C.; Lee, M. M.; Hsu, I. J.; Minh, P. D.; Lai, J. C. H.; Ng, K. Y.; Ramalingam, S.; Yu, S. S. F.; Chan, M. K. *Angew. Chem. Int. Ed. Engl.* **2013**, *52*, 3731–3823.

416. Wulfers, M. J.; Teketel, S.; Ipek, B.; Lobo, R. F. *Chem. Commun.* **2015**, *51*, 4447–4450.

417. Shappard, T.; Hamill, C. D.; Goguet, A.; Rooney, D. W.; Thompson, J. M. *Chem. Commun.* **2014**, *50*, 11053–11055.

418. Beznis, N. V.; Weckhuysen, B. M.; Bitter, J. H. *Catal. Lett.* **2010**, *136*, 52–56.

419. Beznis, N. V.; van Laak, A. N. C.; Weckhuysen, B. M.; Bitter, J. H. *Microporous Mesoporous Mater.* **2011**, *138*, 176–183.

420. Kung, M. C.; Lin, S. S. Y.; Kung, H. H. *Top. Catal.* **2012**, *55*, 108–115.

421. Shan, J. J.; Huang, W. X.; Nguyen, L.; Yu, Y.; Zhang, S. R.; Li, Y. Y.; Frenkel, A. I.; Tao, F. *Langmuir* **2014**, *30*, 8558–8569.

422. Xu, J.; Zheng, A. M.; Wang, X. M.; Qi, G. D.; Su, J. H.; Du, J. F.; Gan, Z. H.; Wu, J. F.; Wang, W.; Deng, F. *Chem. Sci.* **2012**, *3*, 2932–2940.

423. Narsimhan, K.; Michalies, V. K.; Mathies, G.; Gunther, W. R.; Griffin, R. G.; Roman-Leshkov, Y. *J. Am. Chem. Soc.* **2015**, *137*, 1825–1832.

424. Wu, J. F.; Yu, S. M.; Wang, W. D.; Fan, Y. X.; Bai, S.; Zhang, C. W.; Gao, Q.; Huang, J.; Wang, W.; Wu, J. F.; Yu, S. M.; Wang, W. D.; Fan, Y. X.; Bai, S.; Zhang, C. W.; Gao, Q.; Huang, J.; Wang, W. *J. Am. Chem. Soc.* **2013**, *135*, 13567–13573.

425. Hammond, C.; Forde, M. M.; Ab Rahim, M. H.; Thetford, A.; He, Q.; Jenkins, R. L.; Dimitratos, N. M.; Lopez-Sanchez, J. A.; Dummer, N. F.; Murphy, D. M.; Carley, A. F.; Taylor, S. H.; Willock, D. J.; Stangland, E. E.; Kang, J.; Hagen, H.; Kiely, C. J.; Hutchings, G. J. *Angew. Chem. Int. Ed. Engl.* **2012**, *51*, 5129–5133.

426. Hammond, C.; Jenkins, R. L.; Dimitratos, N.; Lopez-Sanchez, J. A.; Ab Rahim, M. H.; Forde, M. M.; Thetford, A.; Murphy, D. M.; Hagen, H.; Stangland, E. E.; Moulijn, J. A.; Taylor, S. H.; Willock, D. J.; Hutchings, G. J. *Chem. Eur. J.* **2012**, *18*, 15735–15745.

427. Hammond, C.; Dimitratos, N.; Jenkins, R. L.; Lopez-Sanchez, J. A.; Kondrat, S. A.; Ab Rahim, M. H.; Forde, M. M.; Thetford, S. H.; Hagen, H.; Stangland, E. E.; Kang, J. H.; Moulijn, J. A.; Willock, D. J.; Hutchings, G. J. *ACS Catal.* **2013**, *3*, 689–699.

428. Hammond, C.; Dimitratos, N.; Lopez-Sanchez, J. A.; Jenkins, R. L.; Whiting, G.; Kondrat, S. A.; Ab Rahim, M. H.; Forde, M. M.; Thetford, A.; Hagen, H.; Stangland, E. E.; Moulijn, J. A.; Taylor, S. H.; Willock, D. J.; Hutchings, G. J. *ACS Catal.* **2013**, *3*, 1835–1844.

429. Hammond, C.; Hermans, I.; Dimitratos, N. *ChemCatChem* **2015**, *7*, 434–440.

430. Forde, M. M.; Armstrong, R. D.; Hammond, C.; He, Q.; Jenkins, R. L.; Kondrat, S. A.; Dimitratos, N.; Lopez-Sanchez, J. A.; Taylor, S. H.; Willock, D. J.; Kiely, C. J.; Hutchings, G. J. *J. Am. Chem. Soc.* **2013**, *135*, 11087–11099.

431. Armstrong, R. D.; Freakley, S. J.; Forde, M. M.; Peneau, V.; Jenkins, R. L.; Taylor, S. H.; Moulijn, J. A.; Morgan, D. J.; Hutchings, G. J. *J. Catal.* **2015**, *330*, 84–92.

432. Wang, L. S.; Tao, L. X.; Xie, M. S.; Xu, G. F.; Huang, J. S.; Xu, Y. D. *Catal. Lett.* **1993**, *21*, 35–41.

433. Bruijnincx, P. C. A.; Weckhuysen, B. M. *Angew. Chem. Int. Ed. Engl.* **2013**, *52*, 11980–11987.
434. Ismailov, E. G.; Aliev, S. M.; Sivleimanov, S. S.; Dadashev, B. A.; Sokolovskii, V. D. *React. Kinet. Catal. Lett.* **1991**, *45*, 185–189.
435. Abasov, S. J.; Babaeva, F. A.; Dadashev, B. A. *Kinet. Catal.* **1991**, *32*, 178–181.
436. Claridge, J. B.; Gree, M. L. H.; Tsang, S. C.; York, A. P. E. *Appl. Catal. A* **1992**, *89*, 103–116.
437. Guo, X.; Fang, G.; Li, G.; Ma, H.; Fan, H.; Yu, L.; Ma, C.; Wu, X.; Deng, D.; wei, M.; Tan, D.; Si, R.; Zhang, S.; Li, J.; Sun, L.; Tang, Z.; Pan, X.; Bao, X. *Science* **2014**, *344*, 616–619.
438. Ruitenbeek, M. R.; Weckhuysen, B. M. *Angew. Chem. Int. Ed. Engl.* **2014**, *53*, 11137–11139.
439. Spivey, J. J.; Hutchings, G. J. *Chem. Soc. Rev.* **2014**, *43*, 792–803.
440. Weckhuysen, B. M.; Wang, D.; Rosynek, M. P.; Lunsford, J. H. *Angew. Chem. Int. Ed. Engl.* **1997**, *36*, 2374–2379.
441. Weckhuysen, B. M.; Wang, D.; Rosynek, M. P.; Lunsford, J. H. *J. Catal.* **1998**, *175*, 338–346.
442. Weckhuysen, B. M.; Wang, D.; Rosynek, M. P.; Lunsford, J. H. *J. Catal.* **1998**, *175*, 347–351.
443. Alvarez-Galvan, M. C.; Mota, N.; Ojeda, M.; Rojas, S.; Navarro, R. M.; Fierro, J. L. G. *Catal. Today* **2011**, *171*, 15–23.
444. Diang, W.; Li, S.; Meitzner, G. D.; Inglesia, E. *J. Phys. Chem. B* **2001**, *105*, 506–513.
445. Solymosi, F.; Cserenyi, J.; Szoke, A.; Bansagi, T.; Oszko, A. *J. Catal.* **1997**, *165*, 150–161.
446. Wang, D.; Rosynek, M. P.; Lunsford, J. H. *Top. Catal.* **1996**, *3*, 289–297.
447. Wang, D.; Lunsford, J. H.; Rosynek, M. P. *J. Catal.* **1997**, *169*, 347–358.
448. Majhi, S.; Mohanty, P.; Wang, H.; Pant, K. K. *J. Energy Chem.* **2013**, *22*, 543–554.
449. Xu, Y.; Lin, L. *Appl. Catal. A.* **1999**, *188*, 53–67.
450. Xu, Y. D.; Bao, X. H.; Lin, L. W. *J. Catal.* **2003**, *216*, 386–395.
451. Mestl, G.; Knözinger, H. *Handbook of Heterogeneous Catalysis*; Wiley-VCH Weinheim, **2008**; pp 932–971.
452. Mosqueira, L.; Gomez, S. A.; Fuentes, G. A. *J. Phys. Cond. Mater.* **2004**, *16*, S2319.
453. Xu, Y.; Shu, Y.; Liu, S.; Huang, J.; Guo, X. *Catal. Lett.* **1995**, *25*, 233–243.
454. Borry, R. W.; Kim, Y. H.; Huffsmith, A.; Reimer, J. A.; Iglesia, E. *J. Phys. Chem. B* **1999**, *103*, 5787–5796.
455. Ding, W. P.; Li, S. Z.; Meitzner, G. D.; Iglesia, E. *J. Phys. Chem. B* **2001**, *191*, 506–513.
456. Li, W.; Meitzner, G. D.; Borry, R. W.; Iglesia, E. *J. Catal.* **2000**, *191*, 373–383.
457. Kim, Y. H.; Borry, R. W.; Iglesia, E. *Microporous Mesoporous Mater.* **2000**, *35–36*, 496–509.
458. Tessonnier, J. P.; Louis, B.; Rigolet, S.; Ledoux, M. J.; Pham-Huu, C. *Appl. Catal. A* **2008**, *336*, 79–88.
459. Tessonnier, J. P.; Louis, B.; Walspurger, S.; Sommer, J.; Ledoux, M. J.; Pham-Huu, C. *J. Phys. Chem. B.* **2006**, *110*, 10390–10395.
460. Chen, L. Y.; Lin, L. W.; Xu, Z. S.; Li, X. S.; Zhang, T. *J. Catal.* **1995**, *157*, 190–200.
461. Xu, Y. D.; Liu, S. T.; Wang, L. S.; Xie, M. S.; Guo, X. X. *Catal. Lett.* **1995**, *30*, 135–149.
462. Wang, D. J.; Lunsford, J. H.; Rosynek, M. P. *Top. Catal.* **1996**, *3*, 289–297.
463. Jiang, H.; Wang, L. S.; Cui, W.; Xu, Y. D. *Catal. Lett.* **1999**, *57*, 95–102.
464. Solymosi, F.; Bugyi, L.; Oszko, A. *Catal. Lett.* **1999**, *57*, 103–107.
465. Li, B.; Li, S. J.; Li, N.; Chen, H. Y.; Zhang, W. J.; Bao, X. H.; Lin, B. X. *Microporous Mesoporous Mater.* **2006**, *88*, 244–253.
466. Liu, H. M.; Shen, W. J.; Bao, X. H.; Xu, Y. D. *J. Mol. Catal. A* **2006**, *244*, 229–236.

467. Liu, H. M.; Bao, X. H.; Xu, Y. D. *J. Catal.* **2006**, *239*, 441–450.
468. Ding, W.; Meitzner, G. D.; Iglesia, E. *J. Catal.* **2002**, *206*, 14–22.
469. Liu, S.; Wang, L.; Ohnishi, R.; Ichikawa, M. *Kinet. Catal.* **2000**, *41*, 132–144.
470. Li, S.; Ma, D.; Kan, Q. B.; Wu, P.; Peng, Y. B.; Zhang, L. C.; Li, M. S.; Fu, Y. H.; Shen, J. Y.; Wu, T. H.; Bao, X. H. *React. Kinet. Catal. Lett.* **2000**, *70*, 349–356.
471. Weckhuysen, B. M.; Rosynek, J. H.; Lunsford, J. H. *Catal. Lett.* **1998**, *52*, 31–36.
472. Ma, D.; Wang, D. Z.; Su, L. L.; Shu, Y. Y.; Xu, Y. D.; Bao, X. H. *J. Catal.* **2002**, *208*, 260–269.
473. Karge, H. G. *Stud. Surf. Sci. Catal.* **1991**, *58*, 531–570.
474. Lee, K. Y.; Kang, M. Y.; Ihm, S. K. *J. Phys. Chem. Solids* **2012**, *73*, 1542–1545.
475. Liu, H.; Shen, W.; Bao, X.; Xu, Y. *Appl. Catal. A* **2005**, *295*, 79–88.
476. Liu, H.; Li, T.; Tian, B.; Xu, Y. *Appl. Catal. A* **2001**, *213*, 103–112.
477. Lu, Y. A.; Xu, Z. S.; Tian, Z. J.; Zhang, T.; Lin, L. W. *Catal. Lett.* **1999**, *62*, 215–220.
478. Gao, J.; Zheng, Y.; Jehng, M.; Tang, Y.; Wachs, I. E.; Podkolzin, S. G. *Science* **2015**, *348*, 687–690.
479. Ma, H.; Kojima, R.; Ohnishi, R.; Ichikawa, M. *Appl. Catal. A* **2004**, *275*, 183–187.
480. Ismagilov, Z. R.; Tsykoza, L. T.; Matus, E. V.; Litvak, G. S.; Ismagilov, I. Z.; Sukhova, O. B. *Eurasian Chem. Technol.* **2005**, 7, 115–121.
481. Shu, Y. Y.; Ma, H. T.; Ohnishi, R.; Ichikawa, M. *Chem. Commun.* **2003**, *1*, 86–87.
482. Zhang, L.; Li, S.; Yuan, Y.; Zhang, X.; Wu, H.; Lin, W. *Catal. Lett.* **1998**, *56*, 207–213.
483. Xu, Y.; Wang, J.; Suzuki, Y.; Zhang, G. *Appl. Catal. A* **2011**, *409–410*, 181–193.
484. Li, S. T.; Dong, Q.; Ohnishi, R.; Ichikawa, M. *Chem. Commun.* **1997**, *15*, 1455–1456.
485. Aboul-Gheit, A. K.; El-Masry, M. S.; Awadallah, A. E. *Fuel Process. Technol.* **2012**, *102*, 24–29.
486. Kojima, R.; Kikuchi, S.; Ma, H. T.; Bai, J.; Ichikawa, M. *Catal. Lett.* **2006**, *110*, 15–21.
487. Liu, B. S.; Yang, Y.; Sayari, A. *Appl. Catal. A* **2001**, *214*, 95–102.
488. Tshabalala, T. E.; Coville, N. J.; Scurrell, M. S. *Appl. Catal. A* **2014**, *485*, 218–244.
489. Abdelsayed, V.; Shekhawat, D.; Smith, M. W. *Fuel* **2015**, *139*, 401–410.
490. Xu, Y.; Wang, J.; Suzuki, Y.; Zhang, G. *Catal. Today* **2012**, *185*, 41–46.
491. Zeng, J. L.; Xiong, Z. T.; Zhang, H. B.; Lin, G. D.; Tsai, K. R. *Catal. Lett.* **1998**, *53*, 119–124.
492. Burns, S.; Hargreaves, J. S. J.; Pal, P.; Parida, K. M.; Parija, S. *Catal. Today* **2006**, *114*, 383–387.
493. Honda, K.; Chen, X.; Zhang, Z. G. *Catal. Commun.* **2004**, *5*, 557–561.
494. Ma, D.; Lu, Y.; Xu, Z.; Tian, Z.; Xu, Y.; Lin, L.; Bao, X. *J. Phys. Chem. B* **2002**, *106*, 8524–8530.
495. Tempelman, C. H. L.; Hensen, E. J. M. *Appl. Catal. B* **2015**, *176–177*, 731–739.
496. Liu, H.; Yang, S.; Hu, J.; Shang, F.; Li, Z.; Xu, C.; Guan, J.; Kan, Q. *Fuel Process. Technol.* **2012**, *96*, 195–202.
497. Martinez, A.; Peris, E.; Derewinski, M.; Burkat-Dulak, A. *Catal. Today* **2011**, *169*, 75–84.
498. Ma, H. T.; Kojima, R.; Kikuchi, S.; Ichikawaw, M. *Catal. Lett.* **2005**, *104*, 63–66.
499. Liu, S. T.; Dong, Q.; Ohnishi, R.; Ichikawa, M. *Chem. Commun.* **1998**, 1217–1218.
500. Choudhary, V. R.; Kinage, A. K.; Choudhary, T. V. *Science* **1997**, *275*, 1286–1288.
501. Kinage, A. K.; Ohnishi, R.; Ichikawa, M. *Catal. Lett.* **2003**, *88*, 199–202.
502. Rival, O.; Grandjean, B. P. A.; Guy, C.; Sayari, A.; Larachi, F. *Ind. Eng. Chem. Res.* **2001**, *40*, 2212–2219.
503. Gimeno, M. P.; Soler, J.; Herguido, J.; Menendez, M. *Ind. Eng. Chem. Res.* **2010**, *49*, 996–1000.
504. Choi, J.; McArthur, A. H. R.; Brookhart, M.; Goldman, A. S. *Chem. Rev.* **2011**, *111*, 1761–1779.

505. Caspery, K. J.; Gehrke, G.; Heinritz-Adrian, M.; Schwefer, M. *Handbook of Heterogeneous Catalysis*; Wiley-VCH: Weinheim, **2008**.

506. Olah, G. A.; Goeppert, A.; Prakash, G. K. S. *Beyond Oil and Gas: The Methanol Economy*, 2nd Updated and Enlarged Ed; Wiley-VCH: Weinheim, **2009**.

507. Bruijnincx, P. C. A.; Weckhuysen, B. M. *Angew. Chem. Int. Ed. Engl.* **2013**, *52*, 11980–11987.

508. Tullo, A. H. *Chem. Eng. News* **2007**, *85*, 27–29.

509. Olsbye, U.; Svelle, S.; Bjørgen, M.; Beato, P.; Janssens, T. V. W.; Joensen, F.; Bordiga, S.; Lillerud, K. P. *Angew. Chem. Int. Ed. Engl.* **2012**, *51*, 5810–5831.

510. Howarth, R. W.; Santoro, R.; Ingraffea, A. *Clim. Change* **2011**, *106*, 679–690. and references therein.

511. MacKay, D.; Stone, T. J. Potential Greenhouse Gas Emissions Associated with Shale Gas Extraction and Use. https://www.gov.uk/government/publications/potential-greenhouse-gas-emissions-associated-with-gas-production-and-use (accessed July 2015).

512. Kunkes, E. L.; Simonetti, D. A.; West, R. M.; Serrano-Ruiz, J. C.; Gärtner, C. A.; Dumesic, J. A. *Science* **2008**, *322*, 417–421.

513. Rass-Hansen, J.; Falsig, H.; Jorgensen, B.; Christensen, C. H. *J. Chem. Technol. Biotechnol.* **2007**, *82*, 329–333.

514. Olah, G. A. *Angew. Chem. Int. Ed. Engl.* **2005**, *44*, 2636–2639.

515. Bellussi, G.; Pollesel, P. *Stud. Surf. Sci. Catal.* **2005**, *158*, 1201–1212.

516. Campoy, A.; Oster, H. Coal-to-Chemicals Projects Boom in China: Western Firms Fight to Keep Edge Among Asia Counterparts; Ease Natural-Gas Dependence **2007**. http://www.wsj.com/articles/SB119906071914658457 (accessed June 2015).

517. Braskem Ethanol-to-Ethylene Plant. http://www.chemicals-technology.com/projects/braskem-ethanol/ (accessed June 2015).

518. Dow and Mitsui to Create Platform for Biopolymers to Serve Packaging; Hygiene & Medical Markets **2011**. http://newsroom.dow.com/press-release/company-news/dow-and-mitsui-create-platform-biopolymers-serve-packaging-hygiene-medica (accessed June 2015).

519. Olsbye, U.; Svelle, S.; Lillerud, K. P.; Wei, Z. H.; Chen, Y. Y.; Li, J. F.; Wang, J. G.; Fan, W. B. *Chem. Soc. Rev.* **2015**, http://dx.doi.org/10.1039/C5CS00304K. Advance Article.

520. Maiden, C. J. *Stud. Surf. Sci. Catal.* **1988**, *36*, 1–16.

521. Tian, P.; Wei, Y.; Ye, M.; Liu, Z. *ACS Catal.* **2015**, *5*, 1922–1938.

522. Honeywell's UOP Helping Meet Petrochemicals Demand in China with Breakthrough Coal-to-Plastics Technology. http://www.uop.com/?press_release=honeywells-uop-helping-meet-petrochemicals-demand-in-china-with-breakthrough-coal-to-plastics-technology (accessed June 2015).

523. Tullo, A. H.; Trembly, J. F. *Chem. Eng. News* **2008**, *86*, 15–22.

524. Olah, G. A.; Doggweiler, H.; Felberg, J. D.; Frohlich, S.; Grdina, M. J.; Karpeles, R.; Keumi, T.; Inaba, S.; Ip, W. M.; Lammertsma, K.; Salem, G.; Tabor, D. *J. Am. Chem. Soc.* **1984**, *106*, 2143–2149.

525. Haw, J. F.; Song, W. G.; Marcus, D. M.; Nicholas, J. B. *Acc. Chem. Res.* **2003**, *36*, 317–326.

526. Stöcker, M. In Cejka, J., Corma, A., Zones, S., Eds.; Zeolites and Catalysis. Synthesis, Reactions and Applications, Vol. 2,; Wiley-VCH, Weinheim, **2010**; pp 687–711.

527. Dahl, I. M.; Kolboe, S. *J. Catal.* **1994**, *149*, 458–464.

528. Sullivan, R. F.; Egan, C. J.; Langlois, G. E.; Sieg, R. P. *J. Am. Chem. Soc.* **1961**, *83*, 1156–1160.

529. Stöcker, M. *Microporous Mesoporous Mater.* **1999**, *29*, 3–48.

530. Lesthaeghe, D.; van Speybroeck, V.; Marin, G. B.; Waroquier, M. *Ind. Eng. Chem. Res.* **2006**, *417*, 309–315. *Chem. Phys. Lett.* **2006**, *417*, 309–315.

531. Mole, T.; Bett, G.; Seddon, D. *J. Catal.* **1983**, *84*, 435–455.
532. Mole, T.; Whiteside, J. A.; Seddon, D. *J. Catal.* **1983**, *82*, 261–266.
533. Wulfers, M. J.; Jentoft, F. C. *ACS Catal.* **2014**, *4*, 3521–3532.
534. Qian, Q.; Ruiz-Martinez, J.; Mokhtar, M.; Asiri, A. M.; Al-Thabaiti, S. A.; Basahel, S. N.; Weckhuysen, B. M. *ChemCatChem* **2014**, *6*, 772–783.
535. Song, W.; Marcus, D. M.; Fu, H.; Ehresmann, J. O.; Haw, J. F. *J. Am. Chem. Soc.* **2002**, *124*, 3844–3845.
536. Haw, J. F.; Nicholas, J. B.; Song, W.; Deng, F.; Wang, Z.; Heneghan, C. S. *J. Am. Chem. Soc.* **2000**, *122*, 4763–4775.
537. Song, W.; Haw, J. F.; Nicholas, J. B.; Heneghan, K. *J. Am. Chem. Soc.* **2000**, *122*, 10726–10727.
538. Kolboe, S. *Acta Chem. Scand.* **1986**, *A-40*, 711–713.
539. Dahl, I. M.; Kolboe, S. *J. Catal.* **1996**, *161*, 304–309.
540. Mikkelsen, Ø.; Ronning, P. O.; Kolboe, S. *Microporous Mesoporous Mater.* **2000**, *40*, 95–113.
541. Arstad, B.; Kolboe, S. *J. Am. Chem. Soc.* **2001**, *123*, 8137–8138.
542. Haw, J. F.; Marcus, D. M. *Top. Catal.* **2005**, *34*, 41–48.
543. Chen, D.; Moljord, K.; Holmen, A. *Microporous Mesoporous Mater.* **2012**, *164*, 239–250.
544. Froment, G. F. *Catal. Rev.* **2005**, *47*, 83–124.
545. Wang, W.; Jiang, Y.; Hunger, M. *Catal. Today* **2006**, *113*, 102–114.
546. Chang, C. D.; Silvestri, A. J. *J. Catal.* **1977**, *47*, 249–259.
547. Ilias, S.; Bhan, A. *ACS Catal.* **2013**, *3*, 18–31.
548. Langner, B. E. *Appl. Catal.* **1982**, *2*, 289–302.
549. Wispelaere, K. D.; Hemelsoet, K.; Waroquier, M.; van Speybroeck, V. *J. Catal.* **2013**, *305*, 76–80.
550. Kolboe, S. In: *Methane Conversion*; Bibby, D. M., Chang, C. D., Howe, R. F., Yurchak, S., Eds.; Elsevier Science Publishers: Amsterdam, **1988**; pp 189–193.
551. van Speybroeck, V.; de Wispelaere, K.; van der Mynsbrugge, J.; Vandichel, M.; Hemelsoet, K.; Waroquier, M. *Chem. Soc. Rev.* **2014**, *43*, 7326–7357.
552. Hemelsoet, K.; van der Mynsbrugge, J.; de Wispelaere, K.; Waroquier, M.; van Speybroeck, V. *Chem. Phys. Chem.* **2013**, *14*, 1526–1545.
553. Voegele, E. EIA increases 2015, 2016 ethanol production forecasts, **2015**. http://www.ethanolproducer.com/articles/12025/eia-increases-2015-2016-ethanol-production-forecasts (accessed July 2015).
554. Gray, K. A.; Zhao, L. S.; Emptage, M. *Curr. Opin. Chem. Biol.* **2006**, *10*, 141–146.
555. Bozell, J. J.; Petersen, G. R. *Green Chem.* **2010**, *12*, 539–554.
556. Brazilian SolVin PVC Produced from Salt and Sugar, **2007**. http://www.solvayplastics.com/sites/solvayplastics/EN/news/Pages/Solvin_07_12_20_Brasilian_SolVin_PVC_produced_from_salt_and_sugar.aspx (accessed July 2015).
557. Lange, K.–B. *Bioplastics to Pass the One Million Tonne Mark in 2011: European Bioplastics Presents Data on Production Capacity at Interpack.* http://www.en.european-bioplastics.org/wp-content/uploads/2011/press/pressreleases/PR_market_study_bioplastics_ENG.pdf, **2011** (accessed July 2015).
558. Shen, L.; Worrell, E.; Patel, M. *Biofuels Bioprod. Biorefin.* **2010**, *4*, 25–40.
559. Zhang, M.; Yu, Y. *Ind. Eng. Chem. Res.* **2013**, *52*, 9505–9514.
560. Morschbacker, A. *J. Macromol. Sci. Polym. Rev.* **2009**, *49*, 79–84.
561. Fan, D.; Dai, D. J.; Wu, H. S. *Materials* **2013**, *6*, 101–115.
562. Morschbacker, A.; Castro, A. L. R. D. WO Patent Appl. 2008/067627, **2008**.
563. Roza, L.; Faleiros, E. L. WO Patent Appl. 2014127436 A1, **2014**.
564. Barrocas, H. V.; Lacerda, A. I. WO Patent Appl. 2007134415 A2, **2007**.
565. Kagyrmanova, A. P.; Chumachenko, V. A.; Korotkikh, V. N.; Kashkin, V. N.; Noskov, A. S. *Chem. Eng. J.* **2011**, *176–177*, 188–194.

566. Zhang, X.; Wang, R.; Yang, X.; Zhang, F. *Microporous Mesoporous Mater.* **2008**, *116*, 210–215.

567. Smith, M. B.; March, J. *March's Advanced Organic Chemistry: Reactions, Mechanisms, Structure*, 6th ed.; John Wiley & Sons, Inc: USA, **2006**.

568. Casbeer, E.; Geiger, R. A.; Davison, B. H.; Szybist, J. P.; Keller, M.; Narula, C. K. In: *American Chemical Society International Fall Meeting, Indianapolis, September*, **2014**.

569. Tullo, A. *Braskem to Make Propylene From Ethanol.* http://cenblog.org/the-chemical-notebook/2010/10/braskem-to-make-propylene-from-ethanol/, **2010** (accessed July 2015).

570. Gotro, J. *Bio-Based Polypropylene; Multiple Synthetic Routes Under Investigation.* http://polymerinnovationblog.com/bio-based-polypropylene-multiple-synthetic-routes-under-investigation/, **2013** (accessed July 2015).

571. Braskem's process. http://www.braskem.com/site.aspx/How-it-is-produced (accessed July 2015).

572. Almanza, L. O.; Chanaga, Q. T. M.; Ramirez, S. I. B. WO Patent Appl. 2012085690 A1, **2012**.

573. Liu, Y.; Malek, A. M.; Schweizer, A. E. U.S. Patent Appl. 20120330080 A1, **2012**.

574. Mitchell, S.; Michels, N.-L.; Perez-Ramirez, J. *Chem. Soc. Rev.* **2013**, *42*, 6094–6112.

575. Whiting, G. T.; Meirer, F.; Mertens, M. M.; Bons, A.-J.; Weiss, B. M.; Stevens, P. A.; de Smit, E.; Weckhuysen, B. M. *ChemCatChem* **2015**, 7, 1312–1321.

576. Whiting, G. T.; Meirer, F.; Valencia, D.; Mertens, M. M.; Bons, A.-J.; Weiss, B. M.; Stevens, P. A.; de Smit, E.; Weckhuysen, B. M. *Phys. Chem. Chem. Phys.* **2014**, *16*, 21531–21542.

577. Mitchell, S.; Michels, N.-L.; Kunze, K.; Perez-Ramirez, J. *Nat. Chem.* **2012**, *4*, 825–831.

578. Hargreaves, J. S. J.; Munnoch, A. L. *Catal. Sci. Technol.* **2013**, *3*, 1165–1171.

579. Scherzer, J. *Catal. Rev. Sci. Eng.* **1989**, *31*, 215–354.

580. O'Connor, P.; van Houtert, F. In: *Proceedings of the Ketjen Catalysis Symposium '86 on the Role of Diffusion in Bottoms Conversion, Scheveningen*, **1986**.

581. Von Ballmoos, R.; Hayward, C. M. T. In: *Catalysis and Adsorption by Zeolites*; Ohlmaan, G., Pfeifer, H., Fricke, R., Eds.; Elsevier: Amsterdam, **1991**; p 171.

582. Buurmans, I. L. C.; Ruiz-Martinez, J.; van Leeuwen, S. L.; van der Beek, D.; Bergwerff, J. A.; Knowles, W. V.; Vogt, E. T. C.; Weckhuysen, B. M. *Chem. Eur. J.* **2012**, *18*, 1094–1101.

583. Gelin, P.; Gueguen, C. *Appl. Catal.* **1988**, *38*, 225–233.

584. Gelin, P.; Des Courieres, T. *Appl. Catal.* **1991**, *72*, 179–192.

585. Buurmans, I. L. C.; Ruiz-Martinez, J.; Knowles, W. V.; van der Beek, D.; Bergwerff, J. A.; Vogt, T. C.; Weckhuysen, B. *Nat. Chem.* **2011**, *3*, 862–867.

586. Mitchell, M. M., Jr.; Hoffman, J. F.; Moore, H. F. *Stud. Surf. Sci. Catal.* **1993**, *76*, 293–338.

587. Cerqueira, H. S.; Caeiro, G.; Costa, L.; Ramoa Ribero, F. J. *Mol. Catal. A Chem.* **2008**, *292*, 1–13.

588. Xu, M.; Liu, X.; Madon, R. J. *J. Catal.* **2002**, *207*, 237–246.

589. Trujillo, C. A.; Uribe, U. N.; Knops-Gerrits, P.-P.; Oviedo, L. A.; Jacobs, P. A. *J. Catal.* **1997**, *168*, 1–15.

590. Cadet, V.; Raatz, F.; Lynch, J.; Marcilly, C. *Stud. Surf. Sci. Catal.* **1989**, *49*, 1377–1386.

591. Liu, C.; Deng, Y.; Pan, Y.; Zheng, S.; Gao, X. *Appl. Catal. A Gen.* **2004**, *257*, 145–150.

592. Occelli, M.; Kowalczyk, D.; Kibby, C. *Appl. Catal.* **1985**, *16*, 227–236.

593. Swift, H. E.; Stanulonis, J. T.; Reynolds, E. H. U.S. Patent 4,179,358, **1979**.

594. Swift, H. E.; Stanulonis, J. T.; Reynolds, E. H. U.S. Patent 4,222,896, **1980**.

595. Swift, H. E.; Stanulonis, J. T.; Reynolds, E. H. U.S. Patent 4,228,036, **1980**.

596. Yang, S.-J.; Chen, Y.-W.; Li, C. *Appl. Catal. A Gen.* **1994**, *115*, 59–68.

597. de la Puente, G.; Sousa-Aguiar, E. F.; Costa, A. F.; Sedran, U. *Appl. Catal. A Gen.* **2003**, *242*, 381–391.

598. Corma, A.; Grande, M.; Fornes, V.; Cartlidge, S.; Shatlock, M. P. *Appl. Catal.* **1990**, *66*, 45.

599. Souza-Aguair, E. F.; de Almeida, M. B. B.; Maurta Valle, L. *Latin Am. Appl. Res.* **1996**, *26*, 99.

600. Pinto, V.; Escobar, A. S.; de Oliveira, B. G.; Lam, Y. L.; Cerqueira, H. S.; Louis, B.; Tessonnier, J. P.; Su, D. S.; Pereira, M. M. *Appl. Catal. A Gen.* **2010**, *388*, 15–21.

601. Meirer, F.; Morris, D. T.; Kalirai, S.; Liu, Y.; Andrews, J. C.; Weckhuysen, B. M. *J. Am. Chem. Soc.* **2015**, *137*, 102–105.

602. Meirer, F.; Kalirai, S.; Morris, D.; Soparawalla, S.; Liu, Y.; Mesu, G.; Andrews, J. C.; Weckhuysen, B. M. *Sci. Adv.* **2015**, *1*(3), e1400199.

603. Shibabi, D. S.; Garwood, W. E.; Chu, P.; Miale, J. N.; Lago, R. M.; Chu, C. T.-W.; Chang, C. D. *J. Catal.* **1985**, *93*, 471–474.

604. Patcas, F. C. *J. Catal.* **2005**, *231*, 194–200.

605. Lee, K.-Y.; Lee, H.-K.; Ihm, S.-K. *Top. Catal.* **2010**, *53*, 247–253.

606. Olysbe, U.; Syelle, S.; Biorgen, M.; Beato, P.; Janssens, T. V. W.; Joensen, F.; Bordiga, S.; Lillerud, K. P. *Angew. Chem. Int. Ed. Engl.* **2012**, *51*, 5810–5831.

607. Michels, N.-L.; Mitchell, S.; Perez-Ramirez, J. *ACS Catal.* **2014**, *4*, 2409–2417.

608. Lee, H.-J.; Kim, J. H.; Park, D.-W.; Cho, J. *Appl. Catal. A Gen.* **2015**, *502*, 42–47.

609. Kim, S. D.; Baek, S. C.; Lee, Y.-J.; Jun, K.-W.; Kim, M. J.; Yoo, I. S. *Appl. Catal. A Gen.* **2006**, *309*, 139–143.

610. Castano, P.; Ruiz-Martinez, J.; Epelde, E.; Gayubo, A. G.; Weckhuysen, B. M. *ChemCatChem* **2013**, *5*, 2827–2831.

611. Ibanez, M.; Gamero, M.; Ruiz-Martinez, J.; Weckhuysen, B. M.; Aguayo, A. T.; Bilbao, J.; Castano, P. *Catal. Sci. Technol.* **2015**. http://dx.doi.org/10.1039/C5CY00784D (advance article) Online.

612. Sattler, J. J. H. B.; Ruiz-Martinez, J.; Santillan-Jimenez, E.; Weckhuysen, B. M. *Chem. Rev.* **2014**, *20*, 10613–10653.

613. Bhasin, M. M.; McCain, J. H.; Vora, B. V.; Imai, T.; Puiado, P. R. *Appl. Catal. A Gen.* **2001**, *221*, 397–419.

614. Gascon, J.; Tellez, C.; Herguido, J.; Menendez, M. *Appl. Catal. A Gen.* **2003**, *248*, 105–116.

615. Takehira, K.; Ohishi, Y.; Shishido, T.; Kawabata, T.; Takaki, K.; Zhang, Q.; Wang, Y. *J. Catal.* **2004**, *224*, 404–416.

616. De Rossi, S.; Ferraris, G.; Fremiotti, S.; Cimino, A.; Indovina, V. *Appl. Catal. A Gen.* **1992**, *81*, 113–132.

617. Zhang, Y.; Zhou, Y.; Qiu, A.; Wang, Y.; Xu, Y.; Wu, P. *Ind. Eng. Chem. Res.* **2006**, *45*, 2213–2219.

618. Liu, H.; Zhou, Y.; Zhang, Y.; Bai, L.; Tang, M. *Ind. Eng. Chem. Res.* **2008**, *47*, 8142–8147.

619. Bhan, A.; Delgass, W. N. *Catal. Rev.* **2008**, *50*, 19–151.

620. Choudhary, V. R.; Devas, P.; Kinage, A. K.; Guisnet, M. *Appl. Catal. A Gen.* **1997**, *162*, 223–233.

621. Ono, Y. *Catal. Today* **2003**, *81*, 3–16.

622. Cañizares, P.; Duran, A.; Dorado, F.; Carmona, M. *Appl. Clay. Sci.* **2000**, *16*, 273–287.

623. Dorado, F.; Romero, R.; Canizares, P. *Ind. Eng. Chem. Res.* **2001**, *40*, 3428–3434.

624. Taylor, R. J.; Petty, R. H. *Appl. Catal. A Gen.* **1994**, *119*, 121–138.

625. Deldari, H. *Appl. Catal. A Gen.* **2005**, *293*, 1–10.

626. de Lucas, A.; Sanchez, P.; Funez, A.; Ramos, M. J.; Valverde, J. L. *J. Mol. Catal.* **2006**, *259*, 259–266.

627. Sanchez, P.; Dorado, A.; Funez, A.; Jimenez, V.; Ramos, M. J.; Valverde, J. L. *J. Mol. Catal.* **2007**, *273*, 109–113.

628. de Lucas, A.; Valverde, J. L.; Sanchez, P.; Dorado, F.; Ramos, M. J. *Ind. Eng. Chem. Res.* **2004**, *43*, 8217–8225.

629. Kaeding, W. W.; Chu, C.; Young, L. N.; Butter, S. A. *J. Catal.* **1981**, *69*, 392–398.

630. Chen, N. Y.; Kaeding, W. W.; Dwyer, F. G. *J. Am. Chem. Soc.* **1979**, *101*, 6783–6784.

631. Kubu, M.; Zilkova, N.; Zones, S. I.; Chen, C.-Y.; Al-Khattaf, S.; Cejka, J. *Catal. Today* **2016**, *259*, 97–106. http://dx.doi.org/10.1016/j.cattod.2015.05.019. Online.

632. Chen, W.-H.; Huang, S.-J.; Lai, C.-S.; Tsai, T.-C.; Lee, H.-K.; Liu, S.-B. *Res. Chem. Intermed.* **2003**, *29*, 761–772.

633. Misk, M.; Joly, G.; Magnoux, P.; Guisnet, M.; Jullian, S. *Microporous Mesoporous Mater.* **2000**, *40*, 197–204.

634. van der Bij, H.; Cicmil, D.; Wang, J.; Meirer, F.; de Groot, F. M. F.; Weckhuysen, B. M. *J. Am. Chem. Soc.* **2014**, *136*, 17774–17787.

635. van der Bij, H. E.; Aramburo, L. R.; Arstad, B.; Dynes, J. J.; Wang, J.; Weckhyusen, B. M. *Chem. Phys. Chem.* **2014**, *15*, 283–292.

636. Reitmeier, J.; Gobin, O. C.; Jentys, A.; Lercher, J. A. *J. Phys. Chem. Chem. Phys.* **2009**, *113*, 15255–15363.

637. Reitmeier, S. J.; Gobin, O. C.; Jentys, A.; Lercher, J. A. *Angew. Chem. Int. Ed. Engl.* **2009**, *48*, 533–538.

638. Gobin, O. C.; Reitmeier, S. J.; Jentys, A.; Lercher, J. A. *J. Phys. Chem. Chem. Phys.* **2011**, *115*, 1171–1179.

639. Buonomo, F.; Bellussi, G.; Notari, B. It. Pat. 20115 MI A83, **1983**.

640. Bellussi, G.; Buonomo, F.; Esposito, A.; Clerici, M. G.; Romano, U.; Notari, B. It. Pat. 20457 MI A85, **1983**.

641. Bellussi, G.; Perego, C.; Carati, A.; Peratello, S.; Previde Massara, E.; Perego, G. *Stud. Surf. Sci. Catal.* **1994**, *84A*, 85–92.

642. Esposito, A.; Neri, C.; Buonomo, F., It. Pat. 20262 MI A82, **1982**.

643. Neri, C.; Anfossi, B.; Esposito, A.; Buonomo, F.; It. Pat. 22608 MI A82, **1982**.

644. Tian, P.; Wei, Y.; Ye, M.; Liu, Z. *ACS Catal.* **2015**, *5*, 1922–1938.

645. Davis, M. E. *Chem. Mater.* **2014**, *26*, 239–245.

646. Rabo, J. A.; Angell, C. L.; Schomaker, V. In: *Proceedings of the IVth International Congress on Catalysis, Moscow*, **1968**; pp 966–993.